University of Sheffield

Characterisation of Thermally Treated Products

D.Parkes

PhD Thesis

2024

Characterisation of Thermally Treated Products

Daniel Parkes

PhD Thesis

Department of Materials Science and Engineering

April 2024

Acknowledgements

This thesis and project would not have been possible without the vision and support of my supervisors initially Professor Claire Corkhill and Dr Clare Thorpe and laterally Professor Russell Hand. I would like to express my deepest appreciation to all three of these people for initially giving me the opportunity to undertake the project and then for giving me advice and support during the project. This project would also not have been possible without the funding from the TRANSCEND project and the Nuclear Decommissioning Agency (NDA) and industrial support and sample provision from both Veolia and Tectonics during the COVID period. The University of Sheffield, in particular the Immobilisation Science Laboratory through funding from the PLEIADES and HADES, Quarrell Lab and Royce Discovery Centre have allowed access to equipment that have made this project possible as well as giving me access to a range of other facilities including an office space and libraries that have been vital for project completion.

Thanks, should also go to the many other people that have given me advice and help during the project. This includes my industrial supervisor Mike Harrison that has provided context and industrial knowledge throughout the project and the many members of staff and students at the University of Sheffield that have provided support, training, analysis, and knowledge throughout the project. Special mention goes to Dr Daniel Bailey, Dr Martin Stennett, Dr Sam Walling, Dr Lewis Blackburn, Dr Amber Mason, Dr Colleen Mann, Odey Hussain, Dr Sarah Pepper, Dr Josh Rashford, Dr James Mansfield, Dr Malin Wilkins, Dr Clemence Gausse, Dr Lisa Hollands, Neil Hind, Rachel Crawford, and Jenny Ayling. Outside of the University of Sheffield I am also grateful to both members of staff, in particular Dr Anjali Menakath, at the UK High-Field Solid State NMR Facility and the Warwick Analytical Science Centre (WASC) Seedcorn funding (EP/V007688/1) for NMR spectroscopy and members of staff at both the National Synchrotron Light Source II at the Brookhaven National Laboratory, New York, USA and at the Beamline B18 (Diamond Light Source, Harwell Science and Innovation Campus, Oxfordshire, UK) for XAS spectroscopy.

Finally, outside of the University I'd like to mention my parents for providing emotional and practical support that has been a major help in giving me the time and space to complete the project.

Abstract

Nuclear waste requires management and disposal and often requires treatment/conditioning, so it is safe for transport and disposal. Thermal treatment uses heat to change the characteristics of the waste package to improve its structure and durability. It is widely used to vitrify HLW but there are opportunities for ILW treatment including using Geomelt and Plasma technology. Four wasteforms from Geomelt trials [1-3] using waste simulants from the Hanford Site, USA and the Fukushima Site, Japan are analysed in this project. Results show glassy wasteforms with mixed levels of radionuclide retention and crystallisation. All glasses were chemically durable in comparison to other HLW and ILW wasteforms. The chemical composition and presence of crystalline phases has affected the durability of the wasteforms. Element incorporation and redox state effects glass structure, but generally high silica glasses had higher polymerisation and durability, with preferential crystalline dissolution in one Japanese wasteform effecting durability by inducing acidic conditions. In the UK the focus of ILW thermal treatment is on using Plasma vitrify Plutonium Contaminated Material (PCM) using Calcium-Alumino-Silicate glass (CAS). Two samples were analysed from inactive Tectronics trials [4, 5]. Glassy wasteforms had extensive anorthite crystallisation, high Fe contents incorporated as Fe^{2+} had minor effect on the glass structure and dissolution tests showed high durability compared to other HLW and ILW glasses. Building on this work and using the trials base CAS composition a series of CAS + PCM waste constituents were produced. All glasses processed at ~1450 °C were highly viscous and with mostly good waste incorporation. CASM5 compositionally was closest to the PCM trial (1A_glass) but an increased Fe^{3+} percentage altered the glass structure, Hf^{4+} incorporation increased polymerisation. Variable Fe oxidation along with several other factors illustrate differences between supposedly representative lab and industry trials that require investigation and improvement in the future.

1. Finucane, K.G., et al. The Development of GeoMeltR In-Container Vitrification (ICV)TM for Fukushima Daiichi Water Treatment Secondary Wastes - 21347. in WM2021: 47 Annual Waste Management Conference. 2021. United States.
2. AMEC, Bulk Vitrication Treatment of K Basin Sludge Simulant Final Report. 2003.
3. Witwer.S.K, D.J.E., Garfiled.S.J, Beck.H.T. Hanfords Supplemental Treatment Project: Full-Scale Integrated Testing of In-Container-Vitrification and 10,000 Liter Dryer. in WM2008 Conference. 2008. Phoenix, AZ.
4. Tetronics, 1107 COSTAIN Plasma Trials Procedure for Nuclear Demonstration Furnace. 2019.
5. Tetronics, 1107 Plasma PCM Trials Report for Nuclear Demonstration Furnace. 2020.

Table of Contents

Figures (for references see individual chapters)

Tables (for references see individual chapters)

Equations

1 Introduction

The nuclear industry uses the heat mostly generated from the radioactive decay of Uranium-235 to generate power. Nuclear is seen as a green source of energy due to its low carbon emissions which could help countries reach emissions targets, however it is restricted due to the production of nuclear waste during the operation and decommissioning of the power plant [1]. The waste is harmful to the environment and people, the correct handling, treatment, and disposal of the nuclear waste is a major challenge for the nuclear industry with the UK waste inventory already standing at 137,000 m^3 [2]. To aid management nuclear waste is classified primarily upon its radioactivity, classifications do vary between countries with an additional focus in this project on the USA and Japan but are based upon a division into High Level (HLW), Intermediate (ILW) and Low Level (LLW) waste [2-6]. A multibarrier approach is seen as a working concept for disposal of nuclear waste of all levels separating the harmful radionuclides from the environment via several protective layers that prevent their escape. The multi barrier approach works on several scales to isolate the radionuclide. Large scale isolation in a geological facility uses natural rock properties to isolate the waste, within the geological facility waste packages are isolated in specially designed canisters and surrounded by impermeable clay or cement [7-10]. Finally, the waste itself provides a defence against the escaper of radionuclides, development of optimised waste forms and treatments that can convert the original waste into a form that is safe and stable is a major focus of the nuclear industry and this project. Treatment for HLW is well developed in the UK with vitrification in borosilicate glass using induction melting at Sellafield, before storage, awaiting deep geological disposal, with options for USA and Japanese HLW waste [11-17]. Spent fuel and stockpiles of Pu and U in the UK and USA are currently awaiting a management decision but could become HLW if MOX production is not chosen, Japan is committed and implementing reprocessing and MOX production [16-22]. LLW is mostly cemented and disposed of the shallow storage facility at Drigg in the UK and similar facilities in the USA and Japan, with other additional treatment techniques such as incineration offering potential optimisation [2, 14, 16, 23-40].

ILW and equivalent categories in the USA and Japan offer the biggest disposal challenge due to their broad inventory. In the UK ILW waste is currently processed via a range of techniques including volume reduction, liquid waste evaporation, dewatering, solid waste compaction and mechanical size reduction all followed by conditioning via cement encapsulation [3, 41-45]. Cement solidification and chemical immobilisation is also common particularly for liquid wastes and sludges such as ion exchange material, here waste solidified and contracted via evaporated, emulsified, or absorption and is mixed with cement forming material and chemically immobilised [44-46]. This process has several issues including durability of the final waste, increased volumes and specific wasteform compatibility there is potential for review and development of the treatment and conditioning of some ILW and LLW waste streams [41, 44, 45, 47, 48]. In the UK, the NDA as part of the HAW framework reviewed potential other options for the ILW waste category [49]. This included thermal treatment that uses heat to either pretreat waste removing organics and reducing waste volume and/or final treatment techniques that involve heating the waste and additives to produce a glass, glass-ceramic or ceramic that chemically immobilises the radionuclide ready for long term geological disposal [27, 45, 50-52]. It is less clear on the direct plans for ILW equivalent disposal in the

USA and Japan where ILW is not a specific category, but ILW equivalents include TRU and the upper categories of LLW, some of these such as TRU in the USA and Japan have a clear treatment and disposal path, with most utilising cement and varying depths of geological storage, recently the use thermal treatment has been proposed for a several sites and wasteforms [39, 40, 53-61].

Thermal treatment offers a few general advantageous as it reduces waste volumes, is cost saving, can deal with a range of ILW compositions and produces a stable and durable wasteform [41, 45, 50, 51, 62]. A range of different thermal technologies including Hot Isostatic Pressing (HIP), Plasma Vitrification, Joule Heated Ceramic Melting (JHCM) and In Can/Geomelt [50, 63] have been proposed to treat ILW.

In the UK there is a major focus on the vitrification of Plutonium Contaminated Waste (PCM) waste [64] due potential for large volume reductions and incompatibility with cementation [41, 45, 50, 51, 65-67]. Plasma vitrification has been suggested as the method for thermal treatment due to the high operating temperature that can deal with the heterogeneous and high metal composition of the PCM [41, 64-66, 68]. A Calcium-Alumino-Silicate (CAS) glass frit matrix has been studied for PCM vitrification as it can incorporate significant amounts of the PCM waste including the PuO_2 and at elevated temperatures it has medium melt viscosity, lower volatility, and reduced corrosiveness. Recent inactive vitrification trials for Plasma vitrification have been carried out by Tetronics on a range of PCM waste compositions using CAS glass frit [41, 65, 69-79]..

In the USA, Hanford is a nuclear site in the Pacific Northwest associated with the production of Pu [80]. It is a large site with a major nuclear legacy that requires clean up and decommissioning [81] with thermal treatment being used to treat HLW and LAW via JHCM [15, 56, 82, 83] with potential for the use of other mechanisms and technologies including Geomelt due to ensure vitrification targets are met by 2028 [56, 59, 60, 82, 84, 85] . Two waste streams from the KBasin and Tank-24-S-109 have been used in trials for additional vitrification using Veolia’s geomelt technology [84, 86-99] . In Japan the Fukushima Daichii nuclear power plant was badly damaged during the 2011 Tsunami [100]. It has left a legacy site that requires clean up and decommissioning. The site has an issue with the contamination of large volumes of infiltrating of groundwater that requires treatment before it can be disposed of to the ocean. [100-104] Treatment using a range of different ion exchange materials has left a large legacy of solid waste that requires treatment with trials using Veolia/s Geomelt technology [57, 104-109].

The structure of this project is split into 8 major chapters. Chapter 2 is a review of the literature to better understand the context of the thesis and to identify where the gaps in the academic literature are. The review briefly looks at the production of nuclear power including the advancement in nuclear power stations before moving onto the waste they generate. The review explores the different waste types focusing in on ILW waste streams from the UK, USA, and Japan. A discussion of past treatments concludes that thermal treatment is a good future option with different thermal technologies and final waste types, including glass, glass ceramics and ceramics discussed. Lastly final waste disposal options are explored alongside glass durability and the mechanics of dissolution as the release of radionuclides to the environment post disposal is critical to the long term safety case.

Chapter 3 describes the samples analysed in this project and the methods used to investigate the different samples. Samples were supplied by industry and come from larger industrial trials including material from PCM plasma trials carried out by Tectonics in Swindon, UK by and from Geomelt trials carried out at the Veolia Nuclear Solutions Federal Services (VNSFS) in

Richland, USA. A suite of lab CAS glass samples that built upon the analysis of the Tetronics samples were also created at the University of Sheffield. A standard set of characterisation techniques were used to analyse the industry and lab samples including Laser ablation ICP-MS (at the British Geological Survey), X-ray Diffraction (XRD), Scanning Electron Microscopy (SEM), Differential Scanning Calorimetry (DSC), Mossbauer Spectroscopy, X-ray absorption near edge structure (XANES) spectroscopy, Nuclear Magnetic Resonance (NMR) spectroscopy. Durability of the industrial samples was investigated using two standard techniques, PCT-B tests looked at short term dissolution behaviour whereas MCC-1 tests looked at longer term dissolution behaviour including alteration layer development. Chapter 4-6 describes the results from the analysis of the different industrial and lab glasses. Chapter 4 focuses on 4 samples, 2 from Hanford and 2 from Fukushima, the chapter is split into two main areas: firstly, understanding the composition, radionuclide (surrogate) distribution and elemental structure of the wasteforms and secondly understanding the durability of the wasteforms. Chapter 5 follows the same format of Chapter 4 but focuses on samples of vitrified simulant waste from the inactive Valingar trials. CAS glass frit was added to the plasma trials to immobilise the PCM waste components, previous work has shown that the glass in mixed vitrified PCM waste is likely to accommodate most of the waste components therefore the compositions of frit additive was taken as a base glass composition for a series of lab glasses that are described and analysed in Chapter 6. In addition to the base glass the important individual PCM waste component were added to the CAS base glass in increased waste loadings to create a series of glasses, PCM waste elements included Hf and Ce (surrogates for Pu), mixed metals (Pb, Steel, Al, and Cu) and PVC. Chapter 6 describes the results of a suite of techniques that investigated how these indiuvial elements are incorporated into the CAS glass and how they affect its structure and properties. Chapter 7 and 8 conclude the thesis by summarising the results from the proceeding chapters and offering remarks to their wider impact, in addition to suggesting future work that could build upon this project.

1.1 References

1. Whittle, K., Nuclear Materials Science (Second Edition). 2020, IOP Publishing.
2. NDA, 2022 UK Radioactive Waste Inventory. 2023.
3. NDA, An Overview of NDA Higher Activity Waste. 2015, Nuclear Decomissioning Agency.
4. Ojovan, M.I. and W.E. Lee, Glassy Wasteforms for Nuclear Waste Immobilization. Metallurgical and Materials Transactions A, 2011. **42**(4): p. 837-851.
5. Classification of Radioactive Waste. 2009, Vienna: INTERNATIONAL ATOMIC ENERGY AGENCY.
6. Ojovan.I.M, L.E.W.a.K.N., An Introduction to Nuclear Waste Immobilisation. 2019: Elsevier.
7. NDA, Integrated Waste management NDA Higher Activity Waste Strategy. 2016, Nuclear Decommissioning Authority.
8. NDA, Integrated Waste Managment - Radioactive Waste Strategy. 2019.
9. Government, U., Implememting Geological Disposal - Working With Communities, E.a.I.S. Business, Editor. 2018.
10. Government, U., Implementing Geological Disposal, E.a.C. Change, Editor. 2014.
11. Harrison, M.T., Vitrification of High Level Waste in the UK. Procedia Materials Science, 2014. **7**: p. 10-15.
12. Board, U.S.N.W.T.R., Vitrified High-Level Radioactive Waste 2017.
13. Sakai, A. and S. Ishida, Reflective reviews on Japanese high-level waste (HLW) vitrification – Exploring the obstacles encountered in active tests at Rokkasho. Annals of Nuclear Energy, 2024. **196**: p. 110175.
14. (NEA), N.E.A. Radiaoctive waste management and decomissioning programmes in NEA member countries.
15. Plant, H.V.
16. Limited, J.N.F.; Available from: https://www.jnfl.co.jp/en/.
17. Association, W.N. World Nuclear Association: Nuclear Fuel Cycle.
18. Hyatt, N.C., Safe management of the UK separated plutonium inventory: a challenge of materials degradation. npj Materials Degradation, 2020. **4**(1): p. 28.
19. Hyatt, N.C., Plutonium management policy in the United Kingdom: The need for a dual track strategy. Energy Policy, 2017. **101**: p. 303-309.
20. (Postnote), P.O.o.S.a.T., Managing the UK Plutonium Stockpile Febuary 2005.
21. NDA, 2022 UK Radioactive Material Inventory. 2023.
22. Orano. MOX, Recycling Nuclear Energy. Available from: https://www.orano.group/country/china/en/our-stories/mox-recycling-nuclear-energy.
23. Vanbrabant, R., et al., 40 years of experience in incineration of radioactive waste in Belgium. 1999: International Atomic Energy Agency (IAEA). p. 5.
24. Vehmas, T., et al., Geopolymerisation of gasified ion-exchange resins, mechanical properties and short-term leaching studies. IOP Conference Series: Materials Science and Engineering, 2020. **818**: p. 012017.
25. Mason, J.B. and D. Bradbury, Pyrolysis and its potential use in nuclear graphite disposal. 2001: International Atomic Energy Agency (IAEA). p. 8.
26. Agency, I.A.E., Treatment of Off-gas from Radioactive Waste Incinerators. 1989, IAEA: Vienna.

27. Scourfield, S.J., et al., Thermal treatment for radioactive waste minimisation and hazard reduction: overview and summary of the EC THERAMIN project. IOP Conference Series: Materials Science and Engineering, 2020. **818**: p. 012001.
28. THERAMIN, Characterisation of thermally treated waste products. 2020.
29. THERAMIN, D3.2 Summary of Demonstration Trials Carried Out Under WP3. 2020.
30. THERAMIN, Gasification based waste treatment. 2019, VTT.
31. Nieminen, M., J. Laatikainen-Luntama, and M. Olin, Gasification-based thermal treatment of Low and Intermediate Level Waste containing organic matter. IOP Conference Series: Materials Science and Engineering, 2020. **818**: p. 012007.
32. Hansen, J. and J. Deckers, Pyrolysis of Radioactive Spent Resins in the PRIME Installation. IOP Conference Series: Materials Science and Engineering, 2020. **818**: p. 012008.
33. EDF. Cyclife-France/our-solutions. Available from: https://www.cyclife-edf.com/en/cyclife/governance/cyclife-france/our-solutions.
34. Vincent.J.J, L.T., Cartier.R, Chaudon.L. Incineration Process For Plutonium Contaminated Waste. in Incineration Conference. 1992. Albuquerque, New Mexico.
35. Research, I.f.E.a.E. Incineration of Radioactive and Mixed Waste. Available from: https://ieer.org/resource/factsheets/incineration-radioactive-mixed/.
36. Perkins.L.B, Incineration Facilities for Treatment of Radioactive Waste: A Review. 1976, Los Alamos Scientific Laboratory.
37. EnergySolutions, Barnwell Disposal Facility. 2016.
38. EnergySolutions, Clive Disposal Facilty. 2016.
39. Nakarai, K., et al., Low-Level Radioactive Waste Disposal in Japan and Role of Cementitious Materials. Journal of Advanced Concrete Technology, 2022. **20**: p. 359-374.
40. (IAEA), I.A.A., National Example Japan.
41. Hyatt, N.C., et al., Thermal treatment of simulant plutonium contaminated materials from the Sellafield site by vitrification in a blast-furnace slag. Journal of Nuclear Materials, 2014. **444**(1): p. 186-199.
42. NuSAC, Plutonium Contaminated Material (PCM). 2005.
43. NDA, Packaging of Plutonium Contaminated Material at the Waste Treatment Complex. 2013.
44. Glasser, F.P., Cements in Radioactive Waste Disposal.
45. Walling, S., L. Gardner, and N. Hyatt, ILW conditioning and performance. 2021.
46. Li, J., L. Chen, and J. Wang, Solidification of radioactive wastes by cement-based materials. Progress in Nuclear Energy, 2021. **141**: p. 103957.
47. Corkhill, C.L.
48. Hyatt, N.C. and M.I. Ojovan, Special Issue: Materials for Nuclear Waste Immobilization. LID - 10.3390/ma12213611 [doi] LID - 3611. (1996-1944 (Print)).
49. NDA, NDA Higher Activity Waste Treatment Framework. 2015.
50. RWM, Geological Disposal Review of Alternative Radioactive Waste Managment Options 2017, Radioactive Waste Management.
51. NNL, Thermal Processes for Immoblilising Intermediate Level Wastes - Position Paper. 2015, National Nulcear Laboratory.
52. McCloy, J.S. and A. Goel, Glass-ceramics for nuclear-waste immobilization. MRS Bulletin, 2017. **42**(3): p. 233-240.
53. A Study of WIPP Radiological Tranuranic Waste Charaterization Requirements and Activities. 2010, Pecos Mangement Services, INC.
54. Energy, T.U.S.D.o., Disposal of Greater-Than-Class C (GTCC) Low-Level Radioactive Waste abd GTCC-Like Waste 2016.

55. Department of Energy, U., Annual Transuranic Waste Inventory Report. 2021.
56. Washington State Department of Ecology, U.S.E.P.A.a.U.S.D.o.E. Amended March 6, 2024.
57. Finucane, K.G., et al. The Development of GeoMeltR In-Container Vitrification (ICV)TM for Fukushima Daiichi Water Treatment Secondary Wastes - 21347. in WM2021: 47 Annual Waste Management Conference. 2021. United States.
58. (NUMO), N.W.M.O.o.J., Geological Disposal of TRU Waste. 2008.
59. Raymond, R.E. INITIAL SELECTION OF SUPPLEMENTAL TREATMENT TECHNOLOGIES FOR HANFORDS LOW ACTIVITY TANK WASTE. 2004. United States.
60. Medicine, Review of the Continued Analysis of Supplemental Treatment Appraoches of Low-Activity Waste at Hanford Nculear Reservation: Review #2 Consensus Study Report. 2022.
61. Witwer, K.S., et al. Hanford bulk vitrification technology status. in WM'07: 2007 Waste Management Symposium - Global Accomplishments in Environmental and Radioactive Waste Management: Education and Opportunity for the Next Generation of Waste Management Professionals. 2007. United States.
62. Mason.C, Sellafield Ltd and LLW Repository Ltd Joint Waste Mangement Plan. 2019.
63. NNL, Thermal Processes for Immobilising Intermediate Level Wastes. 2015, National Nuclear Laboratory.
64. Harrison.T.M, Personal Communication.
65. Schwarz.R, B.P.a., Thermal Treatment of Plutonium Contaminated Materials Phase 2: Vitrification Study Final Report. 31st May 2012.
66. Boast.L, Investigation of the Thermal Treatment of Higher Activity Waste., in Material Science. 2018, Sheffield.
67. Group, B.N., Treatment of Plutonium Contaminated Material at Sellafield - Best Practicale Environmental Option Study. 2007.
68. Report, A., Sellafield Thermal Treatment Phase 2: Geomelt trials on high metallic waste. January 2012.
69. Schofield, J.M., P.A. Bingham, and R.J. Hand, The Immobilisation of a Chloride Containing Actinide Waste Surrogate in Calcium Aluminosilicate Glasses, in Environmental Issues and Waste Management Technologies in the Materials and Nuclear Industries XII. 2009. p. 69-80.
70. Connelly.A.J, B.P.A., Hyatt.N.C and Hand.R.J, Thermal Treatment of plutonium contaminated materails: Phase 1, Report. March 2010, Immobilisation Science Laboratory, University of Sheffield. p. 60pp.
71. Connelly.A. J, B., .P.A, Hyatt.N.C, Hand.R.J, Thermal treatment of plutonium contmainated materials: Phase 1, Appendix. March 2010, Immobilisation Science Laboratory, University of Sheffield. p. 162pp.
72. Owen.E.D, F.E.J. 1981, Idaho National Labaratory.
73. Reimann.A.G, K.C.P. 1993, Idaho National Laboratory.
74. Reimann.A.G, G.D.J., Eddy.L.T, Anderson.L.G. 1992, Idaho National Laboratory.
75. Hyatt, N.C., et al., Characterisation of Plasma Vitrified Simulant Plutonium Contaminated Material Waste. MRS Proceedings, 2006. **985**: p. 0985-NN10-06.
76. Ltd, T., Sellafield Ltd High Metallic ILW Trials Technical Report. June 2011.
77. Tetronics, 1107 COSTAIN Plasma Trials Procedure for Nuclear Demonstration Furnace. 2019.
78. Tetronics, 1107 Plasma PCM Trials Report for Nuclear Demonstration Furnace. 2020.
79. Tetronics, Drum Preparation - R01. 2019.

80. Gephart.E.R, A Short History of Hanford Waste Generation, Storage, and Release. 2003.
81. Gephart, R.E. and R.E. Lundgren, Hanford tank clean up: A guide to understanding the technical issues. 1995: United States.
82. National Academies of Sciences, E., and Medicine Review of the Continued Analysis of Supplemental Tretament Approaches of Low-Activity Waste at the Hanford Nuclear Reservation Review #3 Consensus Study Report. 2023.
83. Energy, U.S.D.o. The Hanford Site: Integrated Disposal Facility Available from: https://www.hanford.gov/page.cfm/idf.
84. Witwer, S.K., Dysland.J.E. Hanford Bulk Vitrification Technology Status. in WM'07 Conference. 2007. Tucson, AZ.
85. Veolia, Our GeoMelt Vitrification Technologies to Stabilize Waste.
86. Bagaasen, L.M., et al. Transport of Technetium and Rhenium into Refractory Materials during Bulk Vitrification. 2006. United States.
87. Bagaasen, L.M., et al. Method to Reduce Molten Salt Penetration into Bulk Vitrification Refractory Materials. 2008. United States: WM Symposia, Phoenix, AZ, United States(US).
88. Witwer, S.K., Woolery.W.D, Dysland.J.E. Progress of the Hanford Bulk Vitrification Project ICV Testing Program in WM'06. 2006. Tucson, AZ.
89. Group, C.M.H., Technical Assessment of Bulk Vitrification Process/Product for Tank Waste Treatment at the Department of Energy Hanford Site. 2006.
90. Witwer.K. Preliminary Demonstration Of Geomelt Treatment Of Hanfords K-Basin Sludge. in ICEM - Internation Conference on Environmental Remediation and Radioactive Waste Managment. 2011. Reims, France.
91. AMEC, Bulk Vitrication Treatment of K Basin Sludge Simulant Final Report. 2003.
92. Kim.S.D, V.D.J., Hrma.R.P, Schweiger.J.M, Matyas.J, Crum.V.J, SMith.E.D, Sevigny.J.G, Buchmiller.C.W, Jr.Tixier.S.J, Yeager.D.J, Belew.B.K, Development and Testing of ICV Glasses for Hanford LAW. 2003, PNNL.
93. Hrma.R.P, K.S.D., Vienna.D.J, Matyas.J, Smith.E.D, Schweiger.J.M, Yeager.J.D, Testing of Large Scale ICV Glasses with Hanford LAW Simulant. 2005, PNNL.
94. L.E. Thompson, L.M., and D. Hamilton., Status and Direction of the Bulk Vitrification Program for the Supplemental Treatment of Low Activity Tank Waste at Hanford. Proceedings of WM’05 Symposia. WM-5138, AMEC Earth and Environmental, Inc., Richland, Washington., 2005.
95. Mahoney.A.L, V.D.J., Feed Variability and Bulk Vitrication Glass Performance Assessment. 2005, PNNL.
96. Rassat.S.D, M.A.L., Russell.L.R, Bryan.A.S, Sell.R.L, Cold Dissolved Saltcake Waste Simulant Development, Preparation, and Anlaysis. 2003, PNNL.
97. Kim.et.al, Matrix Crucible Testing of Bulk Vitrification Glasses for Hanford Low Activity Waste. 2005, AMEC Earth amnd Environmetal.
98. AMEC, Demonstration and Test Plan in AMEC Proposal to Bulk Vitirifcation RFP #93505 to CH2M Hill Hanford Group, November 2002. 2002.
99. Witwer, K.S., et al. Hanford's Supplemental Treatment Project: Full-Scale Integrated Testing of In-Container-Vitrification and a 10,000-Liter Dryer. in 2008 Waste Management Symposium - WM2008/WM'08: HLW, TRU, LLW/ILW, Mixed, Hazardous Wastes and Environmental Management - Phoenix Rising: Moving Forward in Waste Management. 2008. United States.
100. The Fukushima Daiichi Accident. 2015, Vienna: INTERNATIONAL ATOMIC ENERGY AGENCY.

101. Gallardo, A.H. and A. Marui, The aftermath of the Fukushima nuclear accident: Measures to contain groundwater contamination. (1879-1026 (Electronic)).
102. Marui, A. and A.H. Gallardo, Managing Groundwater Radioactive Contamination at the Daiichi Nuclear Plant. Int J Environ Res Public Health, 2015. **12**(7): p. 8498-503.
103. Kurion, Managment Measures to Block Grounwater from Flowing into the Site Using an Underground Geomelt Barrier. IRID - International Research Institute For Nuclear Decommisiong.
104. Tokyo Electric, T. Status of Contamined Water Measures.
105. Lehto, J., et al., Removal of Radionuclides from Fukushima Daiichi Waste Effluents. Separation & Purification Reviews, 2019. **48**(2): p. 122-142.
106. Triplett.M, Cesium Removal and Storage Update on Fukushima Daiichi Status. 2015, PNNL.
107. Mertz, J., et al., Development of a Reactive Transport Model for the Optimization of Ion Specific Media Used at the Fukushima Dai-ichi Nuclear Power Plant – 14579. 2014.
108. Saito, N., Current Status of Solid Waste Management on Fukushima Daiichi Nuclear Power Station. 2021: International Atomic Energy Agency (IAEA). p. 89.
109. Kurion Japan K.K, V.N.S.I., Project of Decommissioning and Contaminated Water Management (Research and Development of Processing and Disposal of Solid Waste) - The Holistic Evaluation of Applicability of GeoMelt® ICV™ for Treatment of 1F Water Treatment Secondary Waste Fiscal Year 2019-2020. 2021.

2 Literature Review and Project Aims

2.1 Background Literature

This project is focused on the thermal treatment of intermediate level nuclear waste (ILW), and specifically the composition of the resultant waste form, the distribution and speciation of radionuclides within that wasteform and its long-term durability. Thermal treatment includes any process that changes the physical characteristics of a material using heat. Meanwhile ILW can mean different things to different nations with no single global classification scheme adopted. In this chapter the origin and classification all UK nuclear wastes are described before focusing in on the current treatment and disposal options for ILW. There is also a focus on nuclear waste and management of ILW equivalents from two other major nuclear nations: the USA and Japan where some of the samples studied in this project originated.

2.1.1 Source of Nuclear Waste

Radioactivity is the natural phenomenon that occurs within isotopes of elements that have unstable numbers of neutrons and protons that decay to become stable. The nuclear industry takes advantages of this process in using the release of excess energy and particles during the decay in several different applications, most commonly the generation of power (electricity). Several different nuclear power station and reactor designs exist that use fabricated nuclear fuel to create power (Figure 2.1). A few other applications including weapons manufacturing and medical isotopes also utilise nuclear material but in the scope of utilised resources and waste generation (see later) these are very minor [1]. During operation and then decommissioning these nuclear power stations generate large volumes of nuclear waste that is contaminated with radioactive material that requires analysis and classification to allow for the correct treatment and disposal mechanism.

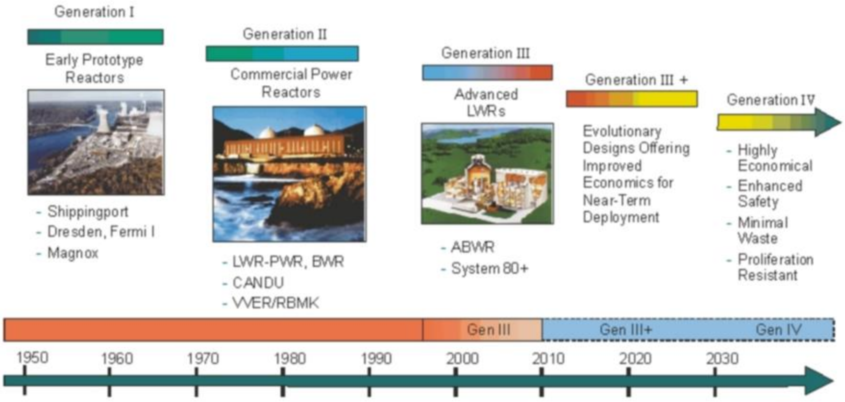

Figure 2.1 History, development, and examples of the different generation power station designs [2].

2.1.2 Nuclear Waste and Classification

2.1.2.1 Nuclear Waste Types

Nuclear waste is in many different forms and has different levels of radioactivity, toxicity and potential harmfulness therefore requires classification and characterisation so that the correct disposal process and path can be identified. Variations of a general classification system are globally used to categorise nuclear waste with several major categories: High Level Waste (HLW), Intermediate Level Waste (ILW) and Low-Level Waste (LLW), Very Low-Level Waste (VLLW) and Exempt Waste (EX). For disposal purposes (Chapter 2.3.1) these categories are often grouped based on activity: HLW, IWL and a very small amount of LLW are classified as HAW (High Activity Waste) and the majority of LLW and VLLW as LAW (Low Activity Waste) [3-6].

2.1.2.2 Waste Classification and Inventory

The UK nuclear waste inventory is dominated by waste from the civil nuclear power industry. The decommissioning of legacy power stations and the disposal of associated waste poses the largest challenge to the UK. Advances in technology mean that volumes created from future nuclear power plants (Table 2.1) will only increase the current UK waste volume by around 10% over their 60 year life span [7]. The UK inventory is classified following the general classification [3, 6]. Some waste streams such as UK HLW already have established treatment pathways that contribute or reduce the waste volumes at nuclear sites with future planned disposal options.

High Activity Waste (HAW):

HAW is waste that has an activity that exceeds 4Gbq per tonne alpha activity or 12 GBq per tonne beta/gamma activity. For disposal purposes the HAW is subdivided into two categories based upon the radionuclide heat generation of the waste, H (high) and L (low) HGW (heat generating waste) [8, 9] which is further divided into several subcategories.

Table 2.1 Categorisation of High Activity Waste (HAW) [8]

Waste Category	Sub-division
Low Heat Generating Waste (LHGW)	Low Level Waste (LLW)
	Intermediate Level Waste (ILW) – shielded and unshielded
	Depleted, natural and low enriched uranium (DNLEU)
High Heat Generating Waste (HHGW)	High Level Waste (HLW)
	Plutonium
	Legacy and Mixed Oxide (MOX) spent fuel (SF)
	Highly enriched uranium (HEU)

More details on the main subdivisions are given below:

High Heat Generating Waste (HHGW):

*High Level Waste (HLW).*This waste type dominates activity of the UK nuclear waste inventory but accounts for a small fraction of its volume (Figure 2.2 and Table 2.1). The primary source of this material is from the processing of spent nuclear fuel creating a Highly Active Liquor (HAL). There is currently about 1,990 m^3 of HLW at Sellafield which is being treated currently via evaporation of the Highly Active Liquor (HAL), vitrification in borosilicate glass and emplacement into stainless steel canisters [10]; waste is then emplaced in long-term storage awaiting the development of a GDF (Geological Disposal Facility) (Chapter 2.2.2.2). From 2022 this volume will change (Table 2.1) due to reductions during vitrification and exportation and potential additions from areas such as Post Operational Clean Out (POCO) [6, 11-14].

Plutonium, Spent Fuel (Legacy and Mixed Oxide (MOX) and Highly Enriched Uranium (HEU). These are yet to be classified as waste as a final decision on there management has not been decided but currently they would be heat generating. They have the potential to become waste (rather than reporcessing and recycling) and to be immobilised in a suitable wasteform including glass, ceramic or glass-ceramic. It is likely that these wasteforms will then be disposed of as a type of ILW or possibly HLW as all disposal concepts do mitigate for some AGR and Sizewell spent fuels [6, 13, 15, 16].

Low Heat Generating Waste (LHGW):

*Intermediate Level Waste (ILW). I*LW tends to have lower activity than HLW but is still significant and due to material type and cement conditioning it has higher than HLW but still proportionally total low waste volumes (Figure 2.2 and Table 2.1). In the UK this waste is mostly contaminated steel, graphite, and concrete from nuclear plant decommissioning as well as sludges, ion exchange resins and flocculants from waste processing (Table 2.3). Waste volumes have been increased by cement encapsulation during conditioning and as of 2022 there is about 102,000 m^3 of ILW mostly (75%) at Sellafield (Table 2.2), some of which is currently in long-term storage (mild steel drums) awaiting a suitable disposal route for this waste which may include for some items for near-surface disposal but mostly emplacement in a GDF. Volumes of ILW (Table 2.1, 2.2 and 2.3), are overestimates for ILW because it is expected

1,440 m^3 at 01.04.2022 will be reclassified as LLW due to decontamination and decay storage this rises to 11,200 m^3 for future arising volumes.

Low Level Waste (LLW): This is a very minor category for LLW that is not suitable for near surface disposal [9].

Low Activity Waste (LAW):

Low Level Waste (LLW). Exceeds the limits of VLLW due to higher concentrations of both long- and short-lived radionuclides, but never high concentrations with activity levels never exceeding < 4 GBq per tonne alpha activity or 12 GBq per tonne beta/gamma activity. This waste consists of mostly rubble, steel, and soil from the operational, decommissioned and dismantled nuclear sites. As of 2022 there was about 32,100 m^3 of LLW mostly at Dounreay (64%) nuclear site, it is mostly stored in temporary storage awaiting disposal at either the Low-Level Waste Repository at Drigg or landfill. This means it dominates the inventory by volume but barely registers in term of activity (Table 2.1 and Figure 2.2).

Very Low-Level Waste (VLLW). The level of activity is low and rarely contains longer lived radionuclides, but activity is present and at higher levels than for exempt waste, for low volume VLLW activity levels must not exceed for a single item 40 kBq or 0.1m^3 of VLLW having < 400kBq and for high volume VLLW a maximum activity of 4 MBq per tonne of total activity, the latter is typically material such as soil or dismantled building material. This is a minor waste category in the UK with 1490 m^3 of waste mostly at the Harwell (69%) awaiting treatment or disposal, although there are expected to be major increases in volumes due to decommissioning projects although at this point it is unclear as the classification of decommissioned waste so projected volumes are pure estimates but it is expected to dominate the inventory by volume but barely register in term of activity (Table 2.1 and Figure 2.2).

Exempt Waste (EW). Waste that has a very low concentration of radionuclides and does not regulatory control for radiation protection it can be disposed of in general landfill and/or recycled.

A further category is *Very Short-Lived Waste (VSLW).* Waste that contains radionuclides with very short (few years) half-life that can be stored for decay storage and then disposed of in a controlled manner, this often includes medical and research waste.

Disposal of nuclear waste is a global issue with many other countries also having nuclear programs and waste legacies. Two of the most prominent nuclear countries outside the UK are the USA and Japan. Although similar the USA and Japan categorise their waste slightly differently to the UK and thus it is important to understand these classifications so that comparisons can be made. For some waste types there is already treatment and disposal pathways that have been developed.

In the USA waste is generally classified by source rather than type [17-23]: spent fuel, HLW, Transuranic Waste (TRU) and categorised Low Level Waste (LLW). Detailed inventories are less well summarised than in the UK, but details can be found in [18, 24-27]. Current HLW from reprocessing for defence in the USA has historically and is currently being vitrified and stored awaiting a decision on disposal with vitrification at Hanford starting to be used for LAW but with others (Savannah River) using a encapsulation process, traditionally the lower levels of LLW are treated, conditioned and disposed of at several shallow storage facilities across the USA [12, 13, 22, 23, 25, 28-30]. Higher than C low level waste (GTTC) (analogous to ILW) does not have a treatment or storage plan, except defence generated TRU from across the USA which, after suitable treatment and conditioning, is repackaged into steel drums and emplaced in salt caverns at the WIPP facility in Texas for long term storage [20, 21, 26]. ILW from the UK would be divided into the upper categories of LLW and TRU waste. The classifications scheme in the USA is subject to change because it appears that type classification is a more efficient and cost-effective way of dealing with nuclear waste. [19, 31]. Japan divides its waste into HLW and categorised LLW based upon its activity [18, 32-34]. Detailed inventories are less well summarised then in the UK, but details can be found in [18]. UK ILW would fall mostly into the upper categories of LLW and TRU waste.

Japan has sent spent fuel for reprocessing, MOX production and borosilicate vitrification in the UK and France, and has now developed its own reprocessing and treatment facility including joule heated ceramic melting technology (see Chapter 2.3.3) at the JNFL facility at Rokkasho, with returned and self-generated vitrified HLW, along with untreated TRU (a category of LLW), stored awaiting deep geological disposal [11, 18, 32, 33, 35-37]. Following appropriate treatment and conditioning L1-L3 waste is disposed of at several active and trial shallow to intermediate depth (depending on activity) disposal facilities [18, 33-35].

Table 2.2 The UK nuclear waste inventory divided up by waste type including forecasted waste production up to 2136. Most of the nuclear waste in the inventory comes from the civil nuclear power industry with minor producers including the Ministry of Defence, universities and hospitals [4, 6].

Waste Type	Reported Volume (m^3)	Packaged Volume (m^3)	Activity (TBq) at 01.04.2200
HLW	1,670	1,470	1,900,000
ILW	249,000	496,000	430,000
LLW	1,580,000	1,340,000	81
VLLW (subcatagory)	2,750,000	2,610,000	14
Total	4,580,000	4,450,000	2,300,000

Table 2.3 ILW waste volumes and activities at the different NDA sites across the UK [6].

Site	Current Volume (01.04.2022) (m^3)	Future Arising Volumes (2136)	Current Activity (TBq)
Sellafield	76,300	71,600	2,200,000
Magnox Power Stations	10,700	42,500	72,000
AGR Power Stations	3,570	20,200	1,200,000
Dounreay	4,840	DNA	240,000
Aldermaston (Defence Site)	4,590	DNA	1,500
Harwell	895	DNA	DNA
Other (unspecified)	DNA	DNA	18,000

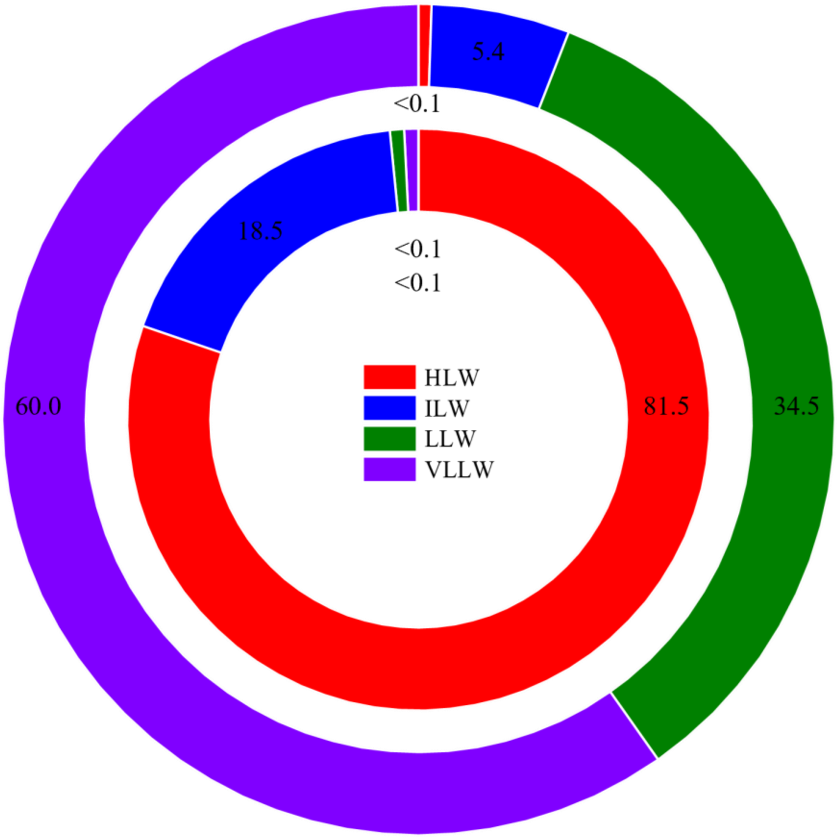

Figure 2.2 UK waste inventory for volume (outer) and activity (inner) at 01.04.2200 [6]. Discrepancy between the two causes several issues for storage, treatment, and disposal.

Table 2.4 Volumes of different ILW waste types based on future operations and waste generation up to 2136 [6].

Waste Type	Volume (m^3)
Graphite	65,800
Plutonium contaminated waste (PCM)	37,100
Conditioned	27,300
Contaminated metals	26,100
Activated metals	22,200
Contaminated other materials	17,200
Others	14,500
Fuel cladding and miscellaneous waste	12,500
Flocs	15,400
Mixed wastes	11,300

2.1.3 Waste Treatment

As mentioned above in both the UK and globally some waste types such as HLW in the UK already have a well-planned or even implemented treatment and disposal pathway. As part of the integrated waste management development programme (IWMDP) the NDA however see that there are improvements and optimisation to be had in the ILW category of nuclear waste [38, 39].

As part of the IWMDP the NDA will still follow the multibarrier approach where a series of protective layers including the waste(form) itself prevents the escape of harmful radionuclides [38-41]. To optimise the waste to provide the best protection requires some form of treatment and/or conditioning to convert it into a safe and stable wasteform before it can be transported and disposed of [38]. Various techniques are under consideration, or are currently used, to encapsulate the waste by surrounding it by another material such as a cement or chemically immobilising the radionuclides within the structure of an optimised wasteform such as a glass, glass-ceramic, or ceramic.

The ILW inventory in the UK and abroad is very varied and diverse providing one of the major challenges in developing treatment and conditioning techniques. It is likely that a complex selection process for each waste type is required considering factors such as waste loading, volume reduction, ease of production, durability (to reduce the release of radioactive and/or toxic elements), chemically flexibility (to deal with waste heterogeneity and form a consistent wasteform without secondary phase formation), existence of natural analogues (to help predict future waste performance) and good final waste compatibility with the local disposal environment.

2.1.4 Treatment options for ILW

Traditionally in the UK and abroad, ILW (and LLW) have been pre-treated via processes such as volume reduction, liquid waste evaporation, dewatering, solid waste compaction and mechanical size reduction. These have been followed by conditioning via cement encapsulation. This has issues however including the large volumetric increase of the waste volume increasing storage costs, the long term waste passivity as some ILW streams are incompatible with cement as they have high metal, salt and organic contents which can react with cementitious alkaline water to produce hydrogen and decompose to form various gaseous species, radon release, increased porosity allowing water ingress, the availability and supply of raw cement materials, cement additions to greenhouse emissions and a low retention of some radioactive elements including fission and activation products [30, 42-46]. In the UK to combat these and look at other options the NDA as part of the IWMDP produced a HAW treatment framework [3] to try and find the best options for the treatment/conditioning of the ILW inventory and focuses on the opportunities for integrated and optimised management of HAW, focusing in areas of significant risk (e.g. Sellafield Legacy Waste) or opportunity (e.g. boundary ILW/LLW waste) [3, 38, 47]. Potential alternative treatments and conditioning techniques include thermal treatment, wet oxidation, decay storage, polymer encapsulation, decontamination and use of innovative container designs and problematic waste [44, 48]. Other countries including Japan, and the USA are also looking at alternatives including thermal treatment for some ILW equivalent wastes particularly at the Hanford and Fukushima nuclear sites.

The focus of this study is on the development of final treatment technologies that act to treat and immobilise ILW waste streams in the UK and abroad. Thermal treatment involves the use of heat to alter the form of a waste product. The term can describe pretreatment techniques that reduce waste volume and remove organics requiring further treatment including pyrolysis, incineration, calcination, and thermal gasification. Thermal treatment can also refer to final treatment technologies that apply heat to produce final products (glass, glass ceramic or ceramic) that chemically incorporate the radionuclides and can be stored long-term with no further treatment [44, 48-51].

General key advantages of thermal treatment are the reduction in waste volume due to the removal of water and organics and co-immobilisation, a final wasteform with high aqueous durability and radiation tolerance, reduced radionuclide mobility due to organics destruction and cost saving due to reduction in storage volumes. For heterogeneous ILW waste streams, thermal treatment offers the chemical flexibility to incorporate a range of elements into the same wasteform, this is particularly true if targeting a glass wasteform [42, 44, 48, 51, 52]. Consideration is required as thermal treatment can cause/ has a few issues including the release of volatile elements (e.g. tritium, I-129 and C-14) control, concentration of the fissile material, immature technologies, high temperature operation and the long-term waste compatibility with the GDF conditions [48].

There are a range of different thermal treatment technologies available that each produce different thermal products. Each thermal treatment is aiming to produce a type of waste product, either a glass (type1), a ceramic or a glass-ceramic (type 2 and 3) that each have different advantages and disadvantages and applications [50].

This project focuses on a series of ILW waste types and treatment techniques that are currently at the forefront of the thermal treatment of ILW this includes the use of Geomelt® and Plasma technology and the vitrification of PCM (plutonium contaminated material) in the UK and a range of ILW waste products from the USA and Japan.

2.1.5 Current Target Waste Types for Active Large Scale Thermal Treatment Development

Sellafield in west Cumbria, is the UK's largest nuclear site and is currently undergoing a major clean up and decommissioning project and is where most of the nuclear waste is stored and processed in the UK. [53]. Along with pumpable waste and miscellaneous beta and gamma waste, Plutonium Contaminated Material (PCM) is a major form of ILW onsite that currently requires treatment [30]. Plutonium Contaminated Waste (PCM) waste is composed of a whole range of material that is packaged in PVC bags before being stored in 200 L drums. Drum composition can vary and include a mix of metals, organics (wood, rubber, paper, PVC (from storage bags and PVC clothing), masonry material (brick, concrete and glass) and plutonium (Pu) complicating the disposal process [3, 42, 54-59].

Of particular importance are the high levels of PVC (56 wt. % suppling up to 20 wt% Cl^-) and low levels of Pu (<0.1wt% or 50 g in an 80 Kg drum) [42, 57, 58, 60]. Sellafield has by far the largest PCM waste volume (Table 2.4). Current disposal involves super compaction to reduce volume before cement encapsulation [3, 42, 57, 59, 61, 62]. Some PCM is non-compactable, compaction can create Pu 'hotspots' late stage deformation and the inability to deal with liquids along with cementation issues (see above) [42, 57, 59] mean that this process is disadvantages and alternatives are being investigated. Thermal treatment is advantageous as a lot of the organic and plastic material is burnt off and the masonry waste can co-immobilise the waste reducing waste volume[42, 44, 48, 58, 63], with plasma technology regarded as a very promising candidate for PCM vitrifcation based upon the high operating temperature that can deal with the heterogeneous and high metal composition of the PCM waste.

Table 2.5 PCM waste volumes at the different UK storage sites [61].

Site	Existing volume (m^3)	Total future arising (m^3)
Sellafield	7975	22000
Dounreay	840	1250
Harwell	1230	1390
Aldermaston	3400	6500
Total	13445	31140

In the USA there is a drive to expand the use of vitrification of waste as a treatment method including at Hanford, a major nuclear site in the USA that is developing its own onsite vitrification plant to treat both HLW and LAW via JHCM technology with the melters currently in the second phase of melter heat up [29, 64, 65]. Hanford is located on the Columbia River in Washington State, USA, and is currently in the process of a major site clean-up [66], under the Tri Party Agreement this current involves the vitrification of ~56 million gallons of high level and low activity radioactive waste at the Hanford Waste Treatment Plant (WTP) to produce stable broadly borosilicate glass (some optimisation) wasteforms [29, 67-70] .The target of the Tri-Party agreement is to treat all of Hanford's waste by 2028, but calculations suggest the WTP only has capacity to treat a third of the LAW by this date. To meet the 2028 target and treat the supplementary LAW or (S)LAW research into alternative technologies has begun including grouting, fluidized bed stream reforming and of interest to this project AMEC's Bulk In-Container Vitrification System or Geomelt® an alternative thermal treatment technology that is currently operated by Veolia Nuclear Solutions Federal Services (VNSFS) [67, 68, 71-74].

Various projects and trials at crucible and engineering scale level were undertaken beginning in 2004 demonstrating the bulk vitrification process for two different simulant Hanford waste streams: Hanford's K-Basin and Tank-24-S-109 [72, 75-90]. The K-Basins were used to store cool irradiated reactor fuel from the K-East/West and N-reactors and, over the time of operation, accumulated approx. 50 m^3 of radioactive sludge accumulated on the basin floors [91, 92]. Between 2007 and 2019 sludge was transferred to the T-Plant facility in the 200 West Area of the Hanford Site before planned vitrification [93]. Tank-24-S-109 simulant was based on waste from one of 177 tanks built bet ween 1943 and 1964 to store radioactive liquid waste and sludge [88]. Tank S-109 currently has a basal sludge layer and an upper saltcake layer amounting to 533 kgal of waste [94].

In Japan, thermal treatment is under consideration for ILW from the treatment of contaminated water at the Fukushima Daiichi Nuclear Power Site, where a major earthquake caused a tsunami and damage to the facility in 2011 [95-97]. Influx and contamination of groundwater water on site is a major issue as the water encounters the reactor fuel and is contaminated with radioactive isotopes Cs-134, Cs-137, tritium, Sr-90, and Sr-89 and requires treatment before a constant amount can be recycled back to the reactor to aid with cooling or the excess can be released to the environment [97-101]. Treatment of water to remove Cs and Sr, the most active radionuclides, has included several systems including ion exchange zeolites and coprecipitation of barium sulphate ($BaSO_4$) to remove Sr and nickelcyanoferrate ($M_2NiFe(CN)_6$) to remove Cs [101-104]. These methods of water treatment have generated large volumes of solid waste [105], equivalent of ILW, that requires treatment and disposal, with thermal treatment being considered as a viable option and tests undertaken using AMEC's Bulk In-Container Vitrification System or Geomelt® [95, 96].

2.1.6 Thermal treatment technologies and examples for trials of ILW vitrification.

This project focuses on the use of In Can/Container Vitrification (ICV) and Plasma Vitrification as these have been identified as potential treatment options for the wasteforms in the project. Other thermal treatment options do exist that all provide heat and for some pressure to melt and solidify the waste and precursors [48, 51]. A good summary of thermal treatment options for ILW is in the THERAMIN (**THER**mal treatment for **RA**dioactive waste **MIN**imisation and hazard reduction) project, a 2017-2020 European Commission project looking at the thermal processing of ILW and LLW [49, 106, 107].

Geomelt® is the current major ICV system and is currently operated by Veolia [74] after initial developed at PNNL in 1980 [74, 100, 108]. In ICV glass former and waste is added to a cast refractory (sand/silica lined) box. Resistive heating is initiated by passing a current along a conductive starter path between two submerged sacrificial graphite electrodes. Further material can be added to the box during processing as the volume reduces, with typical operating temperatures of 1000°C -1800°C [109]. The vitrified waste remains in the sacrificial box for disposal, any volatile releases are managed in an off-gas system [110-112]. Alongside the in-can vitrification the conductive technology was used to develop in-situ vitrification (ISV) or Subsurface Planar Vitrification (SPV) for coping with contaminated land. In SPV long electrodes are placed in the ground and the material is vitrified onsite, either remaining there or later removed for disposal [74, 112-114]. Veolia and proceeding companies (AMEC, Geosafe and Kurion) have demonstrated a whole range of lab, pilot, and full scale Geomelt® test on IWL (or simulants) and other materials in the USA, UK, Australia and Japan [49, 58, 72, 75-79, 81, 82, 84-87, 89, 90, 106, 107, 109-111, 115-138]. Some samples were analysed as part of the THERAMIN project [106, 132]. SPV trials and operations have been completed in Australia, Fukushima, Japan, and USA [100, 112, 116, 139-143].

In addition to the general thermal treatment advantages (Geomelt® can achieve up to 80% volume reduction often due to co-immobilisation and organics destruction) ICV can accept a wide range of LLW and ILW compositions including difficult and problem waste like asbestos, contaminated and orphan waste. An advantage over Joule Heated Ceramic Melting (JHCM) is that the final glass melt does not require pouring, which is a problem for JHCM as it promotes crystallisation [48, 51] and possible blocking of the melter by unmelted waste and metallic Fe [58], Geomelt® also has lower concerns with refractory corrosion expanding the range of waste types and loadings. In this project the Geomelt® system has been considered to vitrify legacy waste and Hanford and Fukushima, but it has also been looked at for the UK's major ILW vitrification waste stream, PCM. Geomelt® could also be beneficial for PCM as it has been shown to be successful in previous trials even with high metal wastes [134], reduces Ce escape to the offgas especially with the use of a cold cap and requires no pouring [58, 134-138]. Despite this plasma is seen as a better alternative for PCM vitrification due to its higher operating temperature, ability to accommodate waste drums and potential continuous process [58].

Plasma is a high temperature (20,000+ °C) form of matter formed when an electrical current is passed through a gas and it used to transfer heat energy via plasma torches [66, 68, 194-200]. Plasma vitrification is used to immobilize a wide range of industrial waste types and there are currently active and developing plants in Switzerland, Bulgaria, South Korea and Japan for treating LLW, with trials and development for ILW including PCM, Sellafield sludges, concretes, and bitumen [49, 51, 54, 55, 106, 107, 137, 138, 144-168].

The focus on plasma vitrification in the UK is the vitrification of PCM waste with several lab and industry trials completed often by the Valingar (now Tetronics) at their non-active demonstration facility at Swindon, mostly focused on using a Calcium Aluminium Silica based frit (Chapter 2.3.4) to demonstrate the simulated, full sized PCM drum loading and plasma melting [42, 54, 55, 57, 58, 137, 138, 151, 153, 168, 169]. CAS compositions can accommodate PCM waste (Chapter 2.3.4) with high plasma temperatures dealing with metallic waste elements causing increased homogenisation and removing the requirement for drum pre-treatment increasing safety and reducing cost [30, 42, 57, 58]. Trials have shown radionuclide retention in the slag phase, high glass partitioning, high volume reduction without the risk of reaching critical levels and low radionuclide volatilisation levels, although this could be improved to mirror Geomelt® levels [30, 42, 57, 58, 134, 137, 138, 151, 153]. A potential major issue with Plasma vitrification of PCM is the low temperature pyrolysis and thermal degradation of PVC packaging that could release large amounts Cl prior to there being a molten waste phase to incorporate it causing a large release of harmful and corrosive gases such as HCl and Cl_2 to the off-gas phase [62]. The formation of oxychlorides is particularly concerning as these can incorporate and facilitate the release of actinides along with the “puffing” pressure releases from the system although HEPA filters have been shown to limit this release [58, 170]. Issues with plasma include the requirement for large amounts of electricity which elevate the cost, the immaturity of the technology in comparison to other thermal treatment techniques with a relatively low number of experimental trials [42, 57, 58, 134, 137, 138, 151, 153] and finally issues with melt pours, although recent designs remove this issue as sacrificial crucibles allow multiple drums to be continuously melted after a process of degassing, this however raises the issues of radionuclide accumulation and requires further investigation [42, 57, 58, 137, 138, 159]. These are key questions that form a major part of this thesis looking at important elements of PCM vitrification such as Cl retention and radionuclide saturation in CAS glass (Chapter 6). Another part of the thesis looks at recent industry trials (Chapter 5) looking at the challenges and waste products of vitrifying PCM using CAS glass. Development of these trials has now moved forward with some designs and concepts put forward, with the idea that Costain and Cavendish Ltd could potentially build an active plasma trial facility at Sellafield in the future [30, 54, 55, 171].

2.1.7 Products of Thermal Treatment

Irrespective of the thermal treatment type the process can produce a range of different wasteform products that it is important to understand can be created from thermal treatment based around ceramics, glass, and a mixture of the two in glass-ceramics. As defined by The US National Research Council (US NRC), Type 1 (Figure 2.3) products are where the radionuclide is incorporated into the glass structure, is what was targeted and expected in the waste elements of this project; therefore, it is important to understand glass structure. If there is any crystalline behaviour (Type 2 and 3) it is important to understand if this has any effect on waste behaviour including radionuclide retention and durability [50, 172].

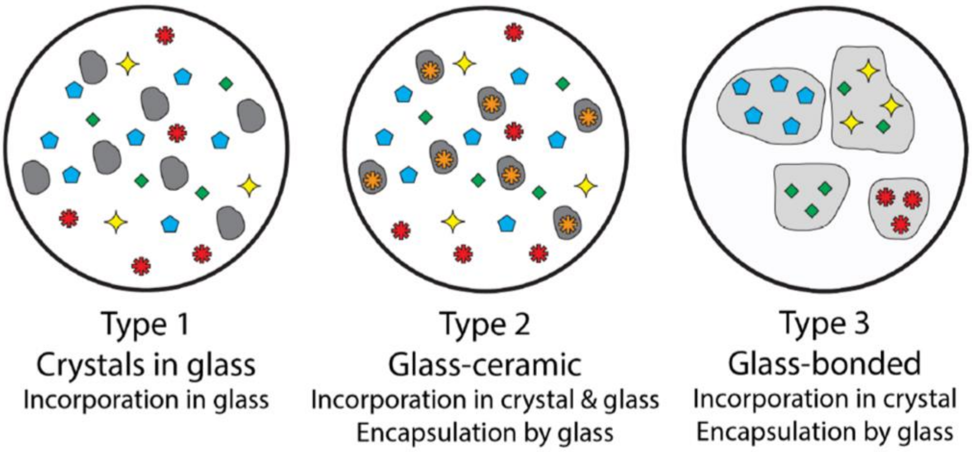

Figure 2.3 The US National Research Council (US NRC) classification of waste forms based upon radionuclide retention [50].

In general terms, a glass is defined as an amorphous solid that displays a region of glass transformation and lacks any long range periodic atomic structure [173-175]. Except for the sol-gel method [173], glasses are produced when a liquid is cooled below its temperature of crystallization quickly enough to prevent crystal nucleation [175]. Upon cooling a glass is commonly defined in terms of their glass transition temperature (T_g), when a heated glass goes from a rigid state to a more flexible state and allows comparisons of different glass structural effects. Any material can effectively form a glass if cooled fast enough, with the formation of crystalline material controlled by the kinetics of crystal nucleation, growth and the cooling rate between the Tl (liquidus temperature) and Tg, a good glass forming material has a medium critical cooling rate. In industrial glasses it is unlikely there will be no crystallisation, and a glass definition is still accepted if the crystalline component is very low (<1 ppm), above this the product is a glass-ceramic [50, 175]. Glasses can have a range of different compositions, and a range of different glasses are currently used or are being trialled depending on the requirement of the waste and processing technique. Borosilicate glass is currently preferred for HLW immobilization [10], with a range of different glass types including borosilicates, alkali-silicates, alkali-borosilicate, alumino-silicates and phosphates under consideration for treatment of ILW, (see section 2.4). These glass types form the general base type for ILW glasses, so it is important to understand how the general elements of these glasses are incorporated in the glass structure along more unusual elements often found in ILW. These glasses often form the base composition however it is common through lab trials that for individual waste types of unique glass frit formulae are optimised [4, 79-81, 83, 176-179]. Geomelt® trials regularly use local soil to vitrify waste as it is cheap, Si rich and easily available at nuclear sites. Soil is generally silica rich and forms a silicate glass which is advantageous due to high durability but often requires addition of additives such as alkalis and boron to improve waste processing and final wasteforms properties by reducing melt temperature and viscosity, as mentioned above optimised lab trials are often used to finalise waste form composition and optimise the balance between durability and waste processing.

Plasma trials for vitrifying PCM waste have investigated a range of different glass formers based around the (calciumaluminosilicate (CAS) glass composition [42, 57, 58, 137, 138, 151] with a plan for uniform volume addition of glass forming material to waste drums removing the requirement for pre-inspection increasing safety and cost [12, 54, 55, 57, 58, 151, 171].

The structure of silicate and borosilicate glasses can be explained by the Random Network Model, first postulated by Zachariasen [180]. Pure silica glasses are the simplest of oxide glasses described by a network structure of corner sharing [SiO_4] tetrahedral units interconnected by Si-O-Si bonds, where the conjoining O is referred to as a bridging oxygen (BO). Silicate glasses due to their high degree of polymerisation and high number of strong Si-O-Si bonds have a high processing temperature, viscosity, and durability. Alkaline/alkaline earth elements such as Na and Ca are often added to glasses to reduce melt temperature and viscosity with the disadvantage of reducing durability they are referred to as modifiers (M). Modifier elements are present in 6-8 co-ordinated positions in the silicate framework and form Non-Bridging Oxygens that act to break up the silicate network and depolymerise the glass. The network connectivity is often discussed in term of Q (1-4) species: relating to the number of NBO's [174, 180-182]. In the Modified Random Network Model it has been suggested that alkali distribution is not totally random and there is grouping to form alkali channels [183]. The addition of divalent cations like Ca as network modifiers tend to increase durability when compared to monovalent cations like Na as they increase network connectivity as well as reducing the mobility of sodium [184].

Boron and Phosphorus can also exclusively act network formers based on the rules of the Random Network Theory [180], and commonly form their own glasses. In this project they are likely to form minor components added either to optimise the glass formulae or from the waste. Both borates and phosphates tend to have lower durability, viscosity and melt temperature than pure silicates due to the structural units in the glass (phosphorus, forms charge-neutral tetrahedron with 3 bonded oxygens and a terminal P=O double bond and boron, forms BO_3 trigonal units with a vacant p_z unit BO_4^- tetrahedral units if there is flow or modifiers added that has implications for the glass properties) and the super structures and complexes that these can from. Boron and phosphorous can be mixed with pure Silica glasses to form borosilicate and phosphosilicate glasses often due to operating and physical compromise, reduced melting temperatures, viscosity and increasing chemical incorporation of the glasses while maintaining high durability [174, 175, 181, 184-189]. Fe and Al form a major part of this project in the different wasteforms for example due to the high metallic element of the PCM and some of the USA waste and forming a major component of the CAS glass frit. Due to their atomic nature these as network intermediates or 'chameleon' elements, acting as both network formers and network modifiers. As network formers due to their trivalent nature, they require some form of charge balancing [174, 175, 180, 181, 187]. Aluminium (Al) can be accommodated in silicate glass Al in 4-, 5- and 6-fold co-ordination. 4-fold co-ordinated Al can act as a network former with [AlO_4]$^-$ tetrahedra replacing [SiO_4] in the glass framework and forming analogous corner-sharing bonds [190-198]. The [AlO_4]$^-$ tetrahedra have a net negative charge which require positive alkali and alkaline earth ions (modifiers- M) to associate with the tetrahedra and charge balance the system. In aluminasilicate systems the M can act as both a charge compensator and a network modifier depending on the Al:M ratio. If Al<M in a peralkaline system, the excess of M is not required for charge balancing and acts as a network modifier and depolymerises the network. In Al=M a metaluminous system the Al and M are equal, all the Al tetrahedron are charge balanced and the glass forms a fully polymerised network resembling vitreous silica glass. In Al>M a peraluminous system there is too much Al for the M to charge balance, in this case several possibilities have been suggested to charge balance and stabilise the network. Al can be present in tetrahedra, and the charge deficit is balanced with defects/vacancies in the structure. Alternatively, Al can be present in five or six fold co-ordination and acts as a network modifier. Recent work has also suggested that oxygen tri-clusters may form in contradiction with Loewenstein rule where oxygens form 3 bonds with 3 network formers and metastable positive charge is balanced by the negative charge of the Al tetrahedra, although these have only recently been tentatively confirmed with ^{17}O NMR and may not be required for Al stabilisation with the presence of increased Al[5] and there concentration maybe influenced by cation field strength and Al composition [190-195, 197-203]. In manufactured CAS glass relevant to this project the A:M is in the peralkaline region therefore the calcium will act as a charge compensator and a network modifier and will compensate two $[AlO_4]^-$ tetrahedra in the structure dominated by $[AlO_4]^-$ and $[SiO_4]$ tetrahedra which can be modelled in the New Modified Randon Network (NMRN) [197, 204]. The Ca^{2+} ion sits in distorted sites with 6-7 oxygen neighbours in interstitial gaps in the tetrahedral network [197, 205-207]. Higher co-ordinated $Al^{[5]}$ and $Al^{[6]}$ have also been suggested as present across the compositional range, with the Al avoidance principle violated with potentially some medium order in the form of two regions; $[SiO_3]^-$ - [1/2Ca] Q^3 rich regions and $[AlO_4]^-$ -[1/2Ca] - $[SiO_4]$ Q^4 tetrahedra charge compensated rich regions [190-198]. In other glasses, cationic field strength of the modifier can control the spatial distribution of modifier and regions meaning that as Si levels drop the glass becomes depolymerised as Al enters Q3 and Q2 units, after showing an initial affinity for Q4 species, although this can vary with temperature [197, 198, 204]. Iron (Fe) has multiple oxidation states depending on conditions. Fe is simpler and is mainly tetrahedral (although higher co-ordination has been reported) for Fe^{3+} and 4 (tetrahedral), 5 (trigonal bipyramidal) and 6 (octahedral) co-ordinated for Fe^{2+}. Fe^{3+} if charged balanced forms a weak network former and Fe^{2+} enters the system as a network modifier, similar patterns of charge balancing and network modification are expected as in Al although this is less well studied or calibrated and there is no evidence of the additional structures seen in Al glasses [187, 208-212]. The Fe in this project's glasses is expected to be Fe^{3+} due to the oxidising nature of the glasses and be amply charge balanced as network formers in the glass structure.

Some more exotic elements mostly sourced from the waste form a major part of the Geomelt®, PCM and PCM simulant melts, including Zirconium, Titanium, Vanadium, Zinc, Hafnium, Lead and Cerium (as a surrogate). Uranium and Plutonium behaviour is of interest due to future analogue or real PCM melts with comparison to surrogate (Ce) melts in this study. Zirconium models have shown Zr favouring negatively charged corner sharing octahedra increasing glass polymerisation that require charge balancing inducing competition with other network formers and between network modifiers. At increased levels of Zr there is evidence for higher (7 and 8) coordination environments[213-220]. Hf is an element analogous to Zr and is believed to have similar properties and behaviours in glass being incorporated in octahedral sites with increased solubility in aluminosilicates linked to the excess of non-charge balancing network modifiers [213, 221, 222]. Titanium has four-, five- and six-fold co-ordination, with the relative proportions related to glass composition. $^{[4]}$Ti acts as a glass former, $^{[6]}$ Ti acts as a modifier and $^{[5]}$ Ti is predicted as potentially having a dual role due to the similar structure as P with both double and single oxygen bonds [187, 223]. Vanadium also has variable oxidation with $^{[5]}$V a weak network former in variable $[VO_5]$ (analogues to P) and $[VO_4]^+$ units, $^{[4]}$V acting as an intermediate ion and $^{[3]}$V although rarely present a network modifier [224, 225]. Zinc can form tetrahedral or octahedral units based on charge compensation, in a recent trial of HLW glasses it was shown to form as a tetrahedral network former in the waste glass and improve durability at low concentrations [226]. Lead has been found at low content as a network modifier in silicate glasses and could although not confirmed be a network former at higher concentrations [227]. No experimental work could be found on the behaviour of Pu in glasses, surrogates can be used as predications, but care is required as many factors including oxidation state and elemental size influence their behaviour (see later). This is seen, with Ce independent of oxidation state acting as a network modifier in the structure of silicate and aluminosilicate glasses [228, 229], Hf acts as a network former in octahedral sites (see above) and U entering the glass in a high oxidation state as a network modifier in alkali channels [187, 230].

2.2 Project aims and previous work

In developing this project and its aims for analysing wasteforms there is a series of key questions and areas of analysis that build upon the knowledge and understanding of the information above and allow the assessing the suitability of the wasteforms for future waste treatment and disposal development.

2.2.1 Waste Composition and Texture

A key part of this project is to look at the waste composition and textural information the distribution and saturation of elements, formation of crystalline phases and the structural environment that the elements occupy in each phase. Crystallisation will occur in the glassy phase due to elemental saturation or heterogenous cooling in the wasteforms, it is important to understand the composition and distribution of the crystalline phases and any radionuclide partitioning into crystalline phases as they could have a major impact on waste effectiveness. Analysis of the glass and crystalline phases independently or as an average can show how the different waste elements including the radionuclides are distributed in the wasteforms and the structural environment (oxidation state and co-ordination) that they are occupying. This is critical as it provides information on how and why the waste form will physically perform including key factors such as durability, thermal performance and density (see later) and what could be improved in the future to optimise it for disposal.

Analysis of these key factor will be carried out using a variety of different techniques that will enable better understanding of the wasteforms composition and structure.

2.2.1.1 Geomelt® Glasses

From the trials above four different glasses for the analysis of the Geomelt® vitrification process. Two from the USA and Hanford waste stream (K Basin and DBVS) [72, 75-90] and two from the Japanese waste stream (MRI4 and 7) [95, 96] that form the basis of the analysis in Chapter 3. From these glasses it is important to understand and have information on the expectations of wasteform composition and structure as then key project aims can then be targeted by appropriate experimental work.

It is expected that silicate glasses will dominate the USA Geomelt® waste compositions as they have been vitrified with Hanford soil which is predominately silica rich. Additional elemental components will come from the initial wasteform and any additives which could have an impact on the structure and performance of the glass. The KBasin is a mixed waste rich in metallic elements with the wasteform expected to be rich in Fe with radioactivity coming from the Uranium with Misch Metal added to represent this in the Geomelt® trial including lathanides such as Ce. Previous analysis would expect a glassy wasteform with some metallic iron and high Ce retention with measured analysis as close as 5% to the batch analysis [75, 84, 90, 91, 231, 232]. DBVS has not been analysed before but the salt rich wasteform [88, 94] is expected to be rich in Na with radioactivity coming from Tc represented by Re as a surrogate, concentrations of this are expected to be low due to volatilisation, however cold cap management increased measured retention levels upto to 70.9 wt% in DBVS-38-C [72, 76-79, 82, 83, 87, 89].

In the two Japanese wasteforms the ion exchange material and waste sludge will strongly impact the wasteform composition due to high waste loading (67-76.6%) with the addition of more exotic elements like Titanium, Vanadium and Nickel, previous analysis supports this with moderate crystallisation in MRI4 of Rutile (Ti phase) and other Na, Ca, Zn and Ti phases, and in MRI7 Kareliniaite (V and Cr phase) crystallisation. In both MRI4 and MRI7 the radioactive elements were added as non-radioactive isotopes of Cs and Sr, they are notoriously volatile, and their retention is vital for the Geomelt® process. The Cs distribution is shown to be homogenous in both MRI 4 and 7 with levels at ~500 mg/kg which is supported by high retention levels over 98% calculated from off gas systems *[95, 96, 102]*.

An important part of this project is to confirm and build upon the knowledge and observations above. Specifically for these waste stream this involves the understanding the ability for the wasteforms to accommodate key waste elements including key non-radioactive elements such as silica, iron, vanadium, titanium and zirconium as these forms the basis of the wasteforms and the key radioactive elements or simulants as this is critical for safe disposal.

The critical waste composition and textural information that will be investigated in this project via several different experimental techniques includes the distribution and saturation of elements, formation of crystalline phases and the structural environment that the elements occupy in each phase. This can have a major impact on the waste properties including durability, thermal properties and density (see later)

Key research aims and questions that will form the basis part of the experimental work and results in Chapter 4 of the thesis are;

1. What is the structure of the waste including the distribution and abundance of crystalline phase?

2. What is the composition of the waste elements including glass and crystalline phases?

3. How much of the radionuclides is retained in each wasteforms, what phases are the radionuclides partitioned, are they saturated and what is there environment?

4. What is the structural role that key elemental phases play in the glass and crystalline phases?

2.2.1.2 PCM and Valingar Glasses

To investigate PCM vitrification a select set of samples from a series of Valingar industrial trials [54, 55] are to be analysed, from these glasses, in a similar vein to the Geomelt® glasses, it is important to understand and have information on the expectations of wasteform composition and structure then key project aims can then be targeted by appropriate experimental work.

The expected wasteform in the Valingar wasteform is expected to be based upon a Calcium-Alumino-Silicate glass frit that has be chosen as a vitrifying matrix for the PCM waste. CAS is advantageous at operating temperatures of 1400 + °C (required to ensure the melting of the steel component) as it has medium melt viscosity, lower volatility, has a high chemical durability (see later), compatibility with steel slags, previous operation success, low postulated Pu and Ce volatility and reduced corrosiveness over other glasses. CAS due to its composition and low density can also provide co-immobilisation with PCM that reduces waste volumes and can incorporate the primary waste elements of PCM including upto ca.40 wt% FeO_x, PuO_2 upto ca.20 wt% and >10wt% Cl. Industrial type CAS has been shown to be melt combatable and reduce metallic U and Ce contamination in mixed waste products partitioning upto 97% into the slag fraction making it more stable and potentially reducing costs as the metallic waste can be disposed of as LLW [42, 54, 55, 57, 58, 151, 168, 230, 233-238] – check if have time

In this project CAS glass frit was used to optimise the composition but in the past trials industrial type CAS and other alternatives are often used as they are cheap and available including GGBS (ground granulated blast furnace slag) and SLS (Soda Lime Silicate) [42, 54, 55, 57, 58, 137, 138, 151, 167] - check if have time

A major part of this project will be looking at the waste products composition in a similar way to the Geomelt® glasses including looking at the glass:crystalline ratio, glass and crystalline composition and glass and crystalline structure as these can have an impact on key general waste properties including waste ability to incorporate waste elements including radionuclide partitioning and saturation, density, thermal properties and durability (see later). Past industrial trials using GGBS and SLS [42, 57, 58, 137, 138, 151, 167] - check if have time can provide some information on the possible wasteforms that may be expected in the PCM vitrification trials including the crystallisation types and composition and the incorporation and partitioning of key waste elements including radionuclides and simulants, metallic elements and chlorine form the low temperature thermal degradation of PVC.

Focusing on the optimised samples that use the CAS alternative GGBS [42, 58] there is variable crystallisation in the samples that can be useful to understand for producing project aims and predictions including phase composition and partitioning on surrogate radionuclides. In the waste products of these trials there is variable crystalline phases including pyroxene phases like diopside and spinels. This is shown to be important as the CeO_2 shows differential concentration and partitioning when crystalline material is present between both the glass and different crystalline phases. Low crystalline samples have close to batch levels (1.2 wt%) whereas high crystallisation samples have much elevated values upto 4 wt% CeO_2 in the glass phase. In high crystalline phases pyroxene phases like diopside are shown to incorporate more CeO_2 than spinel phases (0.96-1.04 wt% compared to 0.18 wt%) [42, 58] .This could be important as it shows that there could be variable crystallisation in the CAS wasteforms that it is important to understand as it impacts factors such as radionuclide partitioning and solubility that could impact waste performance due to durability (see later) and criticality, although homogenous distribution and molar levels well below Pu_2O_3 saturation predict this a lesser issue [42, 58, 239-242].

Levels of PVC in PCM appear variable but are reported to be as high as 20 wt%, with the PVC , this is important as low temperature pyrolysis and thermal degradation of PVC produce high levels of the toxic gas Chlorine (Cl) as the PVC contains upto 20wt% Cl. Retention of the Cl is vitally important as chlorine is damaging to both people and equipment and through the formation of oxychlorides and other compounds aid the escape of radionuclides [58]. Previous analysis has shown variable Cl retention in CAS glasses and glass-ceramics with both lower [42, 58, 243, 244] and higher (>10 wt%) Cl values [238, 245, 246] indicating that different factors could be controlling Cl incorporation. CAS composition such as Ca:Al ratio could be impacting Cl incorporation, but also low temperature pyrolysis and thermal degradation of PVC prior to CAS frit melting could inhibit incorporation, although low Cl values in experimental trails where Cl was added as alkaline earth salts disputes this [243, 244]. This appears to show that the CAS composition and incorporation mechanism is vital to understand if Cl retention levels are to be optimised in PCM vitrification. In both aluminsilicates (and borosilicates) initial incorporation of Cl is controlled by the availability of network spaces associated with network modifiers with each Cl^- anion associating with a M^+ network modifier. There is a trend of increased retention with higher atomic number in the alkaline and alkali series, with a higher affinity for alkaline earths, with CAS glasses having the lowest retention and incorporation at 1400°C in aluminosilicate modifier series at 40% and 1.11 mol% [243, 247-253]. At increased levels of Cl, the increased instability of the network may create incorporation issues as higher CAS density with increased Cl levels suggests expansion and distortion of the glass network [243-245, 253]. Al levels in CAS glass have been shown to have a conflicting effect on Cl retention with elevated values in high Al glasses potentially explained by the presence of aluminium tri-clusters that provide an alternative charge compensation mechanism [245] [370], but higher values in Calcium Silicates [254, 255], and lower values in some CAS glasses and ceramics [42, 58, 243, 244] suggesting that Al supresses Cl incorporation via an undescribed mechanism. Further detailed understanding of the mechanisms of Cl incorporation into CAS glass is clearly required and will form a major part of this project.

Finally, in PCM there are high levels of metals including elements such as Fe (stainless steel), aluminium, lead and cooper in some of the PCM waste drums [42, 54, 55, 57-59, 137, 138, 151, 153, 168, 169, 234, 256]. Excluding lead (Pb) the metallic components don't necessarily present a safety or disposal issue however it has been shown that during the plasma treatment of PCM the metallic element can partition to a separate phase. This is important as if any radionuclides partition into the metallic phase it could provide durability, stability and safety issues. Incorporating the metallic elements into the glass or glass ceramic removes this threat, although an alternative is also to remove all the radionuclide from any metallic elements that could then be separated as disposed of as LLW reducing cost [42, 55, 57, 58, 137, 138, 151, 168, 169]. It is important to understand the metallic partitioning in the PCM waste elements so that future wasteforms and disposal routes can be optimised.

As for the Geomelt® glasses, it is important to understand how the Valingar PCM waste stream accommodates key waste elements including Cl and metals and this will be investigated via several different experimental techniques looking specifically at the distribution, partitioning and saturation of elements, formation of crystalline phases and the structural environment that the elements occupy in each phase. This can have a major impact on the waste properties including durability, thermal properties and density (see later). Radionuclides or simulants were not part of the Valingar study [54, 55, 234] so there are no predictions on their analysis. From previous work and analysis [42, 55, 57, 58, 137, 138, 151, 168, 169], the CAS glass component of the wasteform is important and predicted to form a large part of the wasteform and accommodate most of the PCM waste elements [37, 51, 53, 54, 133, 134, 147, 164, 165. For this reason, a series of CAS glasses will be produced that focuses on the CAS glass and the incorporation of the key waste elements including PVC (chlorine), metals and radionuclide simulants. Analysis of these glasses is critical as it will help unravel the complexness of the incorporation of the different waste elements. Similar experimental techniques will be used to investigate the glass structure, elemental distribution, partitioning and saturation of elements, formation of crystalline phases and structural environment that the elements occupy in the glass as these can impact glass properties including density and thermal properties.

As part of this analysis there are some key research aims and questions that will form the basis part of the experimental work and results in Chapter 5 and 6 are like the Geomelt® glasses and include.

1. What is the structure of the PCM waste including the distribution and abundance of any metallic or crystalline phase

2. What is the composition of the PCM waste elements including any glass, metallic and crystalline regions?

3. In what phases are the key waste elements of Cl and metal partitioned in the PCM waste?

4. What is the structural role that key elemental phases play in any metallic, glass or crystalline phases in the PCM waste?

5. Are the simulant CAS glasses pure glasses if not what elements, including any of the 3 key waste element groups (radionuclides, Cl and metals) are saturated and what crystalline phases are produced?

6. What is the structure of the CAS glass and how does the variable waste loading effect the roles of the different elements and the general glass structure?

2.2.2 Waste Properties

The composition and texture of the wasteform will control how it performs as a material, this is important as it can strongly affect how it performs during thermal processing and disposal. Important properties include density, glass thermal properties (glass transition temperature, crystallisation temperature and melting point) and durability.

2.2.2.1 Processing Properties

Thermal processing of the wasteform is important for a variety of reasons including power costs, manipulating and handling the wasteforms, damage to equipment via heat or volatilisation and operational safety. In this project experimental techniques will look at the thermal properties of the wasteforms including the industrial and synthetic CAS glass aiming to determine parameters such as melt temperature, crystalline temperature and glass transition temperature. Information about these parameters can be used to understand key properties (some of which were not measured in this project) such as viscosity and maximum thermal processing temperature. If these can be understood, then changes in composition or operational set up could optimise the processing procedure to improve safety and cost.

Glasses in the USA Geomelt® trials predominantly use local soil or glass additives to vitrify the waste, these along with the waste compositions will dominate the glass and are broadly expected to fall into the silicate-borosilicate region. PCM vitrification with CAS glass frit will produce CAS glasses. Predictions of the thermal behaviour of these glasses from previous studies [257-259] show that factors such as composition and network structure can have a major effect on the glass behaviour that could impact on key physical properties mentioned above. Similar factors are also likely to impact on density of the glass which can be an indicator of factors such as elemental incorporation, network distribution and distortion and is a key measure for other studies in the project including EXAF and durability studies.

The major questions regarding processing properties include,

1. What are the physical properties of the different waste glasses, and do they align with measurements of analogous glasses?

2. How do the physical properties align with the compositional and structural measurements from above and what else can be inferred from this interpretation?

3. What predictions can be made from the measured physical properties in reference to important processing parameters including viscosity and volatilisation?

2.2.2.2 Disposal Properties

For nuclear waste ideal end scenario is safe long term disposal in a suitable geological facility with the multibarrier approach, including the wasteform itself, isolating the waste components including radionuclides, from the geosphere. A major threat to the escape of these waste components is the ingress of water into the repository and the dissolution of the wasteform. The general dissolution of glass when contacted with water or water vapour is well understood and alters via 3 recognised stages (Figure 2.4), understanding these stages can help understand how the waste composition and structure and the environmental conditions impact the dissolution. The 3 stages of glass dissolution identified by changes in the rate of elemental release and are important as they will control elemental, including radionuclide, release rate to the environment, an overview is given in [260] and summarised below;

Stage I (Interdiffusion and network hydrolysis) [260, 261]:

After initial contact (few seconds) interdiffusion begins with post hydration ion exchange occurs between the network modifiers (alkali and alkali rare earths) and boron in the glass and H_3O^+ and H^+ ions in solution, forming silonal (Si-OH) groups (Equation 2.1), leading to non-congruent dissolution, a increase in pH and creates a microporous, alkali depleted, structurally modified hydrated glass layer.

$\equiv Si\text{-}O\text{-}M + H_3O^+ \leftrightarrow Si\text{-}OH + H_2O + M^+$ Equation 2.1

In tandem network hydrolysis is a direct attack on silica network by the water molecules (Equation 2.2), it will begin immediately after the initial hydration of the glass but is accelerated by interdiffusion due to the diffusion of H_3O^+ ions into the structure and the drop in pH. When network hydrolysis controls the rate the dissolution on a macroscopic level, appears congruent.

$SiO_2 + 2H_2O \leftrightarrow H_4SiO_4$ Equation 2.2

The rate of dissolution in this stage is controlled by either the interdiffusion or network hydrolysis which varies depending on dissolution progress and experimental conditions.

Rate Drop

This is not seen as a rate limiting regime; however, it is important in understanding the change between stage II and III. Evidence from the GLAMOR project [262, 263] attributes the rate drop to 2 major mechanisms:

a) Affinity Concept – H_4SiO_4 reaches saturation in solution meaning that there is no thermodynamic driving force for dissolution i.e. steady state [264].

b) Protective Layer Concept – H_4SiO_4 reaches saturation (1mg/L) and forms a gel layer either in situ or by reprecipitation, it can incorporate other glass components (Al, Zn and Ca) and can inhibit ion exchange and dissolution by being either ‘protective’ or by another mechanism [265, 266].

Stage II (Residual Rate)[260, 267]:

This regime is seen in nearly all static tests with nuclear glasses and is important as over geological time periods it is likely the regime that will control the dissolution rate and release of radionuclides. As the gel forming elements reach saturation, and the system approaches a steady state, the rate of network hydrolysis drops quickly, and the system enters a plateau or steadily decreasing residual rate regime. The residual rate can be 10^{-4} times lower than the initial rate. Although the rate is greatly reduced in the residual regime it is not zero and in a closed system is controlled by slow reactive diffusion through the gel layer and precipitation of secondary phases, which can alter the silica saturation levels and change the conditions required for achieving a ‘protective’ gel layer.

Stage III (Rapid Alteration/Rate Resumption)[260, 268]:

If secondary phase precipitation is rapid and on a large scale, then it can lead to the re-initiation of stage I/II behaviour. The increase in dissolution can be attributed to the decrease in silica saturation and/or alteration of the gel layer that is caused by the precipitation of phases like smectite-clay, rare earth phosphates and zeolites. Cycling between stages II and III as conditions change highlights the fact that all stages are occurring concurrently, and it just depends on the reaction progress to which is the rate limiting process.

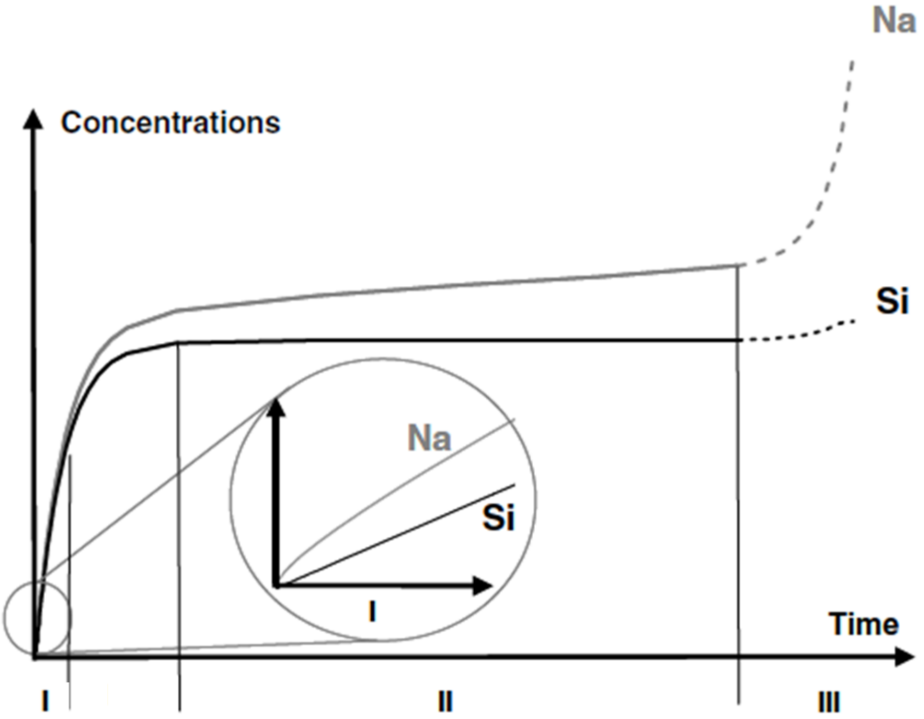

Figure 2.4 Graph of glass dissolution showing the 3 key stages. The difference in Si and Na can be attributed to the different mechanisms of dissolution for network modifiers and network formers in the early part of Stage I, modified from [260].

Major factors that can affect this profile of dissolution is the composition of the dissolution media and the composition and structure of the wasteforms. Discounting the buffering from the dissolution of the wasteform the design of the disposal facility, has a strong control on the composition of the dissolution media. In UK, USA and Japan there are plans to follow the multibarrier approach where additional barriers beyond the wasteform are present to protect the surrounding environment, these can include engineered barriers of clay and cement layers and natural barriers of local geology in either a deep (HLW/ILW) or shallow (LLW/some ILW) geological storage facility [21-23, 32-35, 37-41, 269, 270]. Groundwater infiltration through these barriers control the chemistry of the water that dissolve the wasteforms over the storage lifetime. Long term it would be ideal to understand wasteform disposal in either rock buffered or high pH (e.g. $Ca(OH)_2$ and KOH to represent saturated cement waters) solutions that the wasteform is likely to experience due to the dissolution of disposal facility protective barriers [264, 271-294]. In this project, as the site for the GDF has not yet been selected in any of the studied countries, dissolution have used pure UHQ water to ascertain the relative durability of wastes in comparison to each other. In this scenario the focus is on the wasteform that forms itself the initial barrier of defence against the escape of the waste elements. In the comparative UHQ experiments at a fixed temperature (elevated temperature will increase dissolution due to elevated kinetic (diffusion, bond breaking) and thermodynamic effects.) the composition and structure of the wasteform will control the dissolution profile. The effect can be direct with reduced dissolution due to with increased network connectivity, or indirectly by the release of elements: buffering the solution, changing the elemental affinity and/or pH and forming gel layers or secondary phases [264, 266, 285, 286, 295-302]. pH changes can have variable effects depending on other parameters like solution saturation, glass chemistry and protective layer formation, it can influence the initial dissolution mechanism promoting interdiffusion at low pH and network hydrolysis at high pH and can affect the solubility of elements like Ca in solution (Figure 2.5) [286, 303-306].

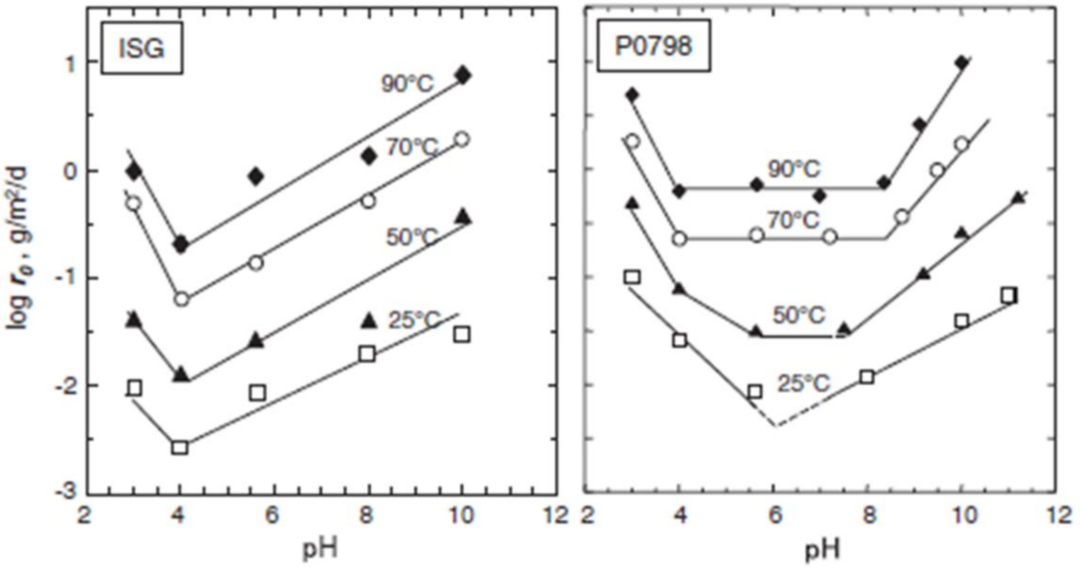

Figure 2.5 pH and temperature effects on the initial rate of dissolution of the international standard glass (ISG) and PO798 glass the variable behaviour is due to the increased alkali metal content in the PO798, meaning it is more effected by low pH promoted interdiffusion [303].

A good initial starting point is to look at previous analysis of ILW durability can provide an insight into how the different parameters effect the dissolution of ILW and help provide predictions and the basis for some project aims for this part of the project. There have been several studies into the performance of ILW glasses including in the THERAMIN project [49, 106], with a recent attempt to summarise these [307]. All elemental release provides vital information for the analysis of waste products however some elements don't participate in gel layer or formation of secondary phases so these provide the best estimate of network breakdown and waste dissolution. Boron is often used but is rarley present unless artifically added therefore alternatives, in this case Na or NL_{Na} are used to compare ILW waste types in standardised PCT powder dissolution tests. NL_x is the normalised mass loss of element x, it adjusts raw elemental concentration in solution to account for initial wasteform elemental concentration and allows for direct comparison of relative elemental mass loss that is more indicative of mechanisms of wasteform dissolution. More details and specific calculations can be found in chapter 3.2.11.5, with the different methods for measuring surface area in these comparison studies corrected using a simple multiplication factor of 2.5 (Figure 2.6 and Table 2.5) [96, 307, 308].

The major questions regarding the disolltuoon of the wasteform are:

1. What is the general pattern of dissolution for the different elements from the wasteforms?
2. What are the links of the dissolution trends to the wasteform structure?
3. What are the links of the dissolution trends with the pH and formation of dissolution features such as alteration layers and secondary mineralisation?
4. What of the factors from question 2 and 3 is controlling the dissolution at different periods?
5. What is the NL_{Na} and the initial and residual rates for the different wasteforms and how do they compare with the other ILW wasteforms?

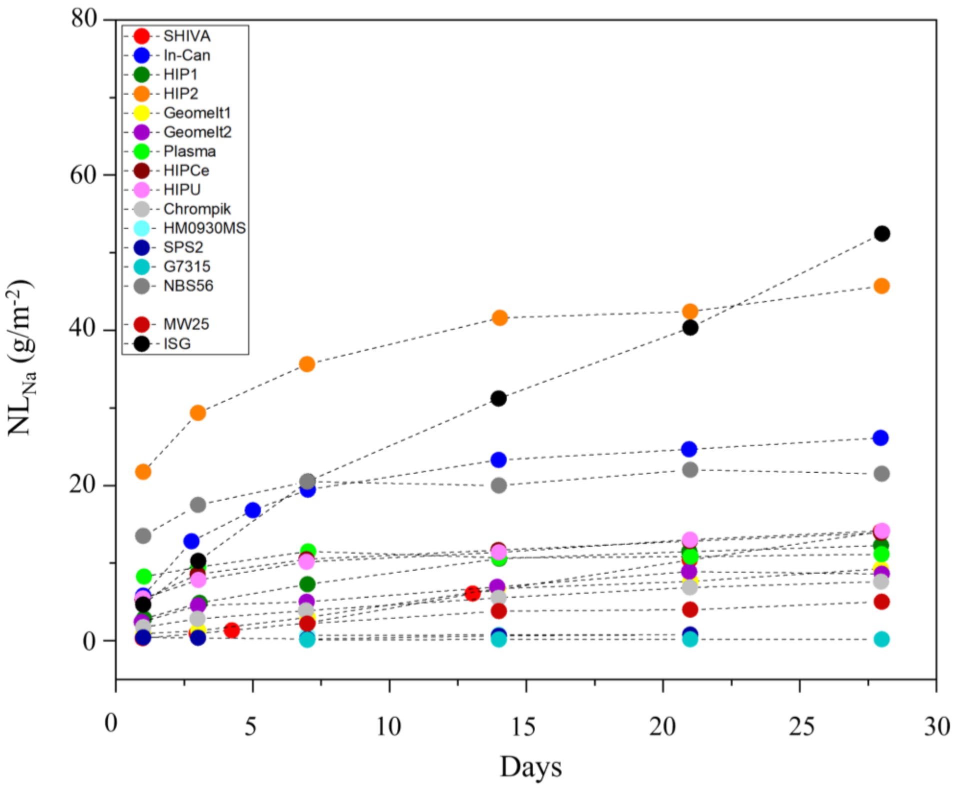

Figure 2.6 Comparative plot of NL_{Na} for PCT-B tests in UHQ at 90°C for a series of reference and ILW glasses.

Table 2.6 Details of the reference and ILW glasses and wasteforms from literature that have comparative NL_{Na} data and have been used to create the comparative plot in (Figure 2.6).

Name	Waste Type	Reference
SHIVA	Zeolites, diatoms, and ion exchange resins in alkali borosilicate glass frit.	[106, 107, 309]
In-Can	CEA IRIS ash in an alkali borosilicate glass frit.	[106, 107, 309]
HIP1	Magnox sludge and Cs-exchanged clinoptilolite in an alkali borosilicate glass frit.	[106, 107, 310]
HIP2	Magnox sludge and CS-exchanged clinoptilolite in borax glass frit.	[106, 107, 310]
Geomelt®1	PCM waste and SIXEP sand/clinoptilolite simulant with local soil.	[106, 107, 132, 133]
Geomelt®2	PCM waste and SIXEP sand/clinoptilolite simulant with local soil.	[106, 107, 132, 133]
Plasma	PCM waste in a calcium alumino silicate glass frit.	[106, 107, 151]
HIPCe	Magnox sludge and clinoptilolite with additional Ce surrogate.	[106, 107, 310, 311]
HIPU	Magnox sludge and clinoptilolite with additional Ce surrogate.	[106, 107, 310, 311]
Chrompik	Chrompik III waste form a legacy nuclear plant in Slovakia.	[106, 107, 312, 313]
ISG	International Simple Glass standard.	[106]
SPS2	Cs-exchanged chabazite waste created at Fukushima Daiichi NPP.	[314]
HM0930MS	Magnox sludge waste in alkali earth borosilicate glass.	[315]
G7315	Dounreay Prototype Fast Reactor (PFR) Raffinate in barium borosilicate glass.	[316]
NBS56	Clinoptilolite vitrified in a borax glass frit.	[317]
MW25	UK high level waste simulant glass.	[317]
HLP30	LAW waste glass simulant from Hanford, USA.	[120]

2.3 References

1. Whittle, K., Nuclear Materials Science (Second Edition). 2020, IOP Publishing.
2. Khalil.H, B.R., Versluis.R, The Generation IV Nuclear Energy Systems Technology Roadmap.
3. NDA, An Overview of NDA Higher Activity Waste. 2015, Nuclear Decomissioning Agency.
4. Ojovan.I.M, L.E.W.a.K.N., An Introduction to Nuclear Waste Immobilisation. 2019: Elsevier.
5. Classification of Radioactive Waste. 2009, Vienna: INTERNATIONAL ATOMIC ENERGY AGENCY.
6. NDA, 2022 UK Radioactive Material Inventory. 2023.
7. NIA, Nuclear Energy Facts, N.I.A. (NIA), Editor. 2018.
8. (RWM), R.W.M., Geological Disposal: Specifications for waste packages containing high heat generating waste 2016.
9. (RWM), R.W.M., Waste Package Specification and Guidance Documentation: Specification for Waste Packages Containing Low Heat Generating Waste: Part C - Fundamental Requirments. 2020.
10. Harrison, M.T., Vitrification of High Level Waste in the UK. Procedia Materials Science, 2014. 7: p. 10-15.
11. Association, W.N. World Nuclear Association: Nuclear Fuel Cycle.
12. Hyatt, N.C., Safe management of the UK separated plutonium inventory: a challenge of materials degradation. npj Materials Degradation, 2020. 4(1): p. 28.
13. Hyatt, N.C., Plutonium management policy in the United Kingdom: The need for a dual track strategy. Energy Policy, 2017. 101: p. 303-309.
14. (Postnote), P.O.o.S.a.T., Managing the UK Plutonium Stockpile Febuary 2005.
15. NDA. Managing nuclear materials and spent fuels. 2015; Available from: https://www.gov.uk/government/collections/managing-nuclear-materials-and-spent-fuels.
16. NDA, Progress on Plutonium Consolidation, Storage and Disposition. 2019.
17. Andrews.A, Radioactive Waste Streams:Waste Classification for Disposal. 2006: CRS Report for Congress.
18. (NEA), N.E.A. Radiaoctive waste management and decomissioning programmes in NEA member countries.
19. Future, B.R.C.O.A.s.N., Report to the Secretary of Energy. 2012.
20. A Study of WIPP Radiological Tranuranic Waste Charaterization Requirements and Activities. 2010, Pecos Mangement Services, INC.
21. Energy, T.U.S.D.o., Disposal of Greater-Than-Class C (GTCC) Low-Level Radioactive Waste abd GTCC-Like Waste 2016.
22. EnergySolutions, Barnwell Disposal Facility. 2016.
23. EnergySolutions, Clive Disposal Facilty. 2016.
24. Yancey, K. and P.V. Tsvetkov, Quantification of U.S. spent fuel inventories in nuclear waste management. Annals of Nuclear Energy, 2014. 72: p. 277-285.
25. Board, U.S.N.W.T.R., Vitrified High-Level Radioactive Waste 2017.
26. Department of Energy, U., Annual Transuranic Waste Inventory Report. 2021.
27. Energy, U.D.o., Integrated Data Base Report - 1996: U.S. Spent Nuclear Fuel and Radioactive Waste Inventories, Projections, and Characterisitics. 1997.
28. Swift, P.N. and E.J. Bonano, Geological Disposal of Nuclear Waste in Tuff: Yucca Mountain (USA). Elements, 2016. 12(4): p. 263-268.

29. Plant, H.V.
30. Harrison.T.M, Personal Communication.
31. J, C., High-Level Nuclear Waste Redefined - 10041. Transactions of the American Nuclear Society, 2014. Proceedings of the American Nucelar Society Annual Meeting, Reno, NV June 15-19, 2014.
32. (NUMO), N.W.M.O.o.J., Geological Disposal of TRU Waste. 2008.
33. Nakarai, K., et al., Low-Level Radioactive Waste Disposal in Japan and Role of Cementitious Materials. Journal of Advanced Concrete Technology, 2022. 20: p. 359-374.
34. (IAEA), I.A.A., National Example Japan.
35. Limited, J.N.F.; Available from: https://www.jnfl.co.jp/en/.
36. Sakai, A. and S. Ishida, Reflective reviews on Japanese high-level waste (HLW) vitrification – Exploring the obstacles encountered in active tests at Rokkasho. Annals of Nuclear Energy, 2024. 196: p. 110175.
37. (NEA), N.E.A., Japan's Siting Process for the Geological Disposal of High-level Radioactive Waste - An International Peer Review. 2016.
38. NDA, Integrated Waste management NDA Higher Activity Waste Strategy. 2016, Nuclear Decommissioning Authority.
39. NDA, Integrated Waste Managment - Radioactive Waste Strategy. 2019.
40. Government, U., Implememting Geological Disposal - Working With Communities, E.a.I.S. Business, Editor. 2018.
41. Government, U., Implementing Geological Disposal, E.a.C. Change, Editor. 2014.
42. Hyatt, N.C., et al., Thermal treatment of simulant plutonium contaminated materials from the Sellafield site by vitrification in a blast-furnace slag. Journal of Nuclear Materials, 2014. 444(1): p. 186-199.
43. Glasser, F.P., Cements in Radioactive Waste Disposal.
44. Walling, S., L. Gardner, and N. Hyatt, ILW conditioning and performance. 2021.
45. Hyatt, N.C. and M.I. Ojovan, Special Issue: Materials for Nuclear Waste Immobilization. LID - 10.3390/ma12213611 [doi] LID - 3611. (1996-1944 (Print)).
46. Corkhill, C.L.
47. AMEC, Upstream Optioneering - ILW/LLW Opportunities. 2014.
48. RWM, Geological Disposal Review of Alternative Radioactive Waste Managment Options 2017, Radioactive Waste Management.
49. Scourfield, S.J., et al., Thermal treatment for radioactive waste minimisation and hazard reduction: overview and summary of the EC THERAMIN project. IOP Conference Series: Materials Science and Engineering, 2020. 818: p. 012001.
50. McCloy, J.S. and A. Goel, Glass-ceramics for nuclear-waste immobilization. MRS Bulletin, 2017. 42(3): p. 233-240.
51. NNL, Thermal Processes for Immoblilising Intermediate Level Wastes - Position Paper. 2015, National Nulcear Laboratory.
52. Mason.C, Sellafield Ltd and LLW Repository Ltd Joint Waste Mangement Plan. 2019.
53. Association, W.N., Nuclear Development in the United Kingdom. 2016.
54. Tetronics, 1107 COSTAIN Plasma Trials Procedure for Nuclear Demonstration Furnace. 2019.
55. Tetronics, 1107 Plasma PCM Trials Report for Nuclear Demonstration Furnace. 2020.
56. Tetronics, Nuclear Plasma Trails Drum Preparation - R01. 2019.
57. Boast.L, Investigation of the Thermal Treatment of Higher Activity Waste., in Material Science. 2018, Sheffield.

58. Schwarz.R, B.P.a., Thermal Treatment of Plutonium Contaminated Materials Phase 2: Vitrification Study Final Report. 31st May 2012.
59. Group, B.N., Treatment of Plutonium Contaminated Material at Sellafield - Best Practicale Environmental Option Study. 2007.
60. Egan.M, P.A., Towler.G, Treatment of Plutomium Contaminated Material at Sellafield: Best Practical Environmnetal Option Study. 2008, Sellafield.
61. NuSAC, Plutonium Contaminated Material (PCM). 2005.
62. NDA, Packaging of Plutonium Contaminated Material at the Waste Treatment Complex. 2013.
63. NNL, Thermal Processes for Immobilising Intermediate Level Wastes. 2015, National Nuclear Laboratory.
64. Goel, A., et al., Challenges with vitrification of Hanford High-Level Waste (HLW) to borosilicate glass – An overview. Journal of Non-Crystalline Solids: X, 2019. 4: p. 100033.
65. Vienna, J.D., Nuclear Waste Vitrification in the United States: Recent Developments and Future Options. International Journal of Applied Glass Science, 2010. 1(3): p. 309-321.
66. Gephart, R.E. and R.E. Lundgren, Hanford tank clean up: A guide to understanding the technical issues. 1995: United States.
67. Washington State Department of Ecology, U.S.E.P.A.a.U.S.D.o.E. Amended March 6, 2024.
68. National Academies of Sciences, E., and Medicine Review of the Continued Analysis of Supplemental Tretament Approaches of Low-Activity Waste at the Hanford Nuclear Reservation Review #3 Consensus Study Report. 2023.
69. Energy, U.S.D.o. The Hanford Site: Integrated Disposal Facility Available from: https://www.hanford.gov/page.cfm/idf.
70. Marcial, J., et al., Hanford low-activity waste vitrification: A review. Journal of Hazardous Materials, 2024. 461: p. 132437.
71. Medicine, Review of the Continued Analysis of Supplemental Treatment Appraoches of Low-Activity Waste at Hanford Nculear Reservation: Review #2 Consensus Study Report. 2022.
72. Witwer, S.K., Dysland.J.E. Hanford Bulk Vitrification Technology Status. in WM'07 Conference. 2007. Tucson, AZ.
73. Raymond, R.E. INITIAL SELECTION OF SUPPLEMENTAL TREATMENT TECHNOLOGIES FOR HANFORDS LOW ACTIVITY TANK WASTE. 2004. United States.
74. Veolia, Our Geomelt® Vitrification Technologies to Stabilize Waste.
75. Witwer, K. Preliminary Demonstration of Geomelt® Treatment of Hanford’s K-Basin Sludge. in Waste Managment Conference. 2011. USA.
76. Witwer, S.K., Woolery.W.D, Dysland.J.E. Progress of the Hanford Bulk Vitrification Project ICV Testing Program in WM'06. 2006. Tucson, AZ.
77. Bagaasen, L.M., et al. Method to Reduce Molten Salt Penetration into Bulk Vitrification Refractory Materials. 2008. United States: WM Symposia, Phoenix, AZ, United States(US).
78. Bagaasen, L.M., et al. Transport of Technetium and Rhenium into Refractory Materials during Bulk Vitrification. 2006. United States.
79. Kim.S.D, V.D.J., Hrma.R.P, Schweiger.J.M, Matyas.J, Crum.V.J, SMith.E.D, Sevigny.J.G, Buchmiller.C.W, Jr.Tixier.S.J, Yeager.D.J, Belew.B.K, Development and Testing of ICV Glasses for Hanford LAW. 2003, PNNL.

80. Kim, D.S., et al. Glass Formulations for Immobilizing Hanford Low-Activity Wastes. in Waste Management 2006 Symposium - WM'06 - Global Accomplishments in Environmental and Radioactive Waste Management: Education and Opportunity for the Next Generation of Waste Management Professionals. 2006. United States.
81. Kim.et.al, Matrix Crucible Testing of Bulk Vitrification Glasses for Hanford Low Activity Waste. 2005, AMEC Earth amnd Environmetal.
82. Group, C.M.H., Technical Assessment of Bulk Vitrification Process/Product for Tank Waste Treatment at the Department of Energy Hanford Site. 2006.
83. Hrma.R.P, K.S.D., Vienna.D.J, Matyas.J, Smith.E.D, Schweiger.J.M, Yeager.J.D, Testing of Large Scale ICV Glasses with Hanford LAW Simulant. 2005, PNNL.
84. AMEC, Bulk Vitrication Treatment of K Basin Sludge Simulant Final Report. 2003.
85. Witwer.S.K, D.J.E., Garfiled.S.J, Beck.H.T. Hanfords Supplemental Treatment Project: Full-Scale Integrated Testing of In-Container-Vitrification and 10,000 Liter Dryer. in WM2008 Conference. 2008. Phoenix, AZ.
86. AMEC, Demonstration and Test Plan in AMEC Proposal to Bulk Vitirifcation RFP #93505 to CH2M Hill Hanford Group, November 2002. 2002.
87. L.E. Thompson, L.M., and D. Hamilton., Status and Direction of the Bulk Vitrification Program for the Supplemental Treatment of Low Activity Tank Waste at Hanford. Proceedings of WM’05 Symposia. WM-5138, AMEC Earth and Environmental, Inc., Richland, Washington., 2005.
88. Rassat.S.D, M.A.L., Russell.L.R, Bryan.A.S, Sell.R.L, Cold Dissolved Saltcake Waste Simulant Development, Preparation, and Anlaysis. 2003, PNNL.
89. Mahoney.A.L, V.D.J., Feed Variability and Bulk Vitrication Glass Performance Assessment. 2005, PNNL.
90. Witwer.K. Preliminary Demonstration Of Geomelt® Treatment Of Hanfords K-Basin Sludge. in ICEM - Internation Conference on Environmental Remediation and Radioactive Waste Managment. 2011. Reims, France.
91. Knollmeyer, P., C. Phillips, and P. Townson, PROGRESS WITH K BASINS SLUDGE RETRIEVAL STABILIZATION & PACKAGING AT THE HANFORD NUCLEAR SITE. 2006.
92. Energy, U.S.D.o., The Hanford Site 100 K Area Fact Sheet, U.S.D.o. Energy, Editor. 2022.
93. French.M, K Basin Sludge Retrival Update. 2018, Richland Operations Office, Department of Energy.
94. Tingey.M.J, B.H.G., Deschane.R.J, Dangerous Waste Charaterisitics of Waste from Hanford Tank 241-S-109. 2004, PNNL.
95. Finucane, K.G., et al. The Development of Geomelt®R In-Container Vitrification (ICV)TM for Fukushima Daiichi Water Treatment Secondary Wastes - 21347. in WM2021: 47 Annual Waste Management Conference. 2021. United States.
96. Kurion Japan K.K, V.N.S.I., Project of Decommissioning and Contaminated Water Management (Research and Development of Processing and Disposal of Solid Waste) - The Holistic Evaluation of Applicability of Geomelt®® ICV™ for Treatment of 1F Water Treatment Secondary Waste Fiscal Year 2019-2020. 2021.
97. The Fukushima Daiichi Accident. 2015, Vienna: INTERNATIONAL ATOMIC ENERGY AGENCY.
98. Gallardo, A.H. and A. Marui, The aftermath of the Fukushima nuclear accident: Measures to contain groundwater contamination. (1879-1026 (Electronic)).
99. Marui, A. and A.H. Gallardo, Managing Groundwater Radioactive Contamination at the Daiichi Nuclear Plant. Int J Environ Res Public Health, 2015. 12(7): p. 8498-503.

100. Kurion, Managment Measures to Block Grounwater from Flowing into the Site Using an Underground Geomelt® Barrier. IRID - International Research Institute For Nuclear Decommisiong.
101. Tokyo Electric, T. Status of Contamined Water Measures.
102. Lehto, J., et al., Removal of Radionuclides from Fukushima Daiichi Waste Effluents. Separation & Purification Reviews, 2019. 48(2): p. 122-142.
103. Triplett.M, Cesium Removal and Storage Update on Fukushima Daiichi Status. 2015, PNNL.
104. Mertz, J., et al., Development of a Reactive Transport Model for the Optimization of Ion Specific Media Used at the Fukushima Dai-ichi Nuclear Power Plant – 14579. 2014.
105. Saito, N., Current Status of Solid Waste Management on Fukushima Daiichi Nuclear Power Station. 2021: International Atomic Energy Agency (IAEA). p. 89.
106. THERAMIN, Characterisation of thermally treated waste products. 2020.
107. THERAMIN, D3.2 Summary of Demonstration Trials Carried Out Under WP3. 2020.
108. Businesswire. Kurion Aquires Geomelt® to Expand Vitrification Solutions. 2012; Available from: https://www.businesswire.com/news/home/20120529005380/en/Kurion-Acquires-Geomelt®%C2%AE-Expand-Vitrification-Solutions.
109. Witwer, K., et al. Thermal treatment of UK intermediate and low level radioactive waste: a demonstration of the Geomelt® process towards treatment of Sellafield waste. in Paper 10507 at Waste Management Conference, 7–11 March. 2010.
110. Clarke, S., et al., Active demonstration of the thermal treatment of surrogate sludge and surrogate drums using the Geomelt®™ In Container Vitrification (ICV) melter installed in NNL Central Laboratory. IOP Conference Series: Materials Science and Engineering, 2020. 818: p. 012004.
111. THERAMIN, Test Report on Demonstration of Geomelt® for THERAMIN project. 2020, NNL.
112. Thompson, L.E. Mixed Waste Treatment Cost Analysis for a Range of Geomelt® Vitrification Process Configurations. 2002. United States: WM Symposia, Inc., Tucson, Arizona.
113. Corporation, G., Innovative Technology Evaluation Report. 1995.
114. Geosafe, Treatability Study for Planar In Situ Vitrification of INEEEL Test Area North V-Tanks. 1998, Geosafe Corporation.
115. Finucane, K., et al., Treatment of Asbestos Wastes Using the Geomelt® Vitrification Process. 2008.
116. Vijgen.J, M.R., POPs Technology Specification and Data Sheet. Basel Convention.
117. Wire, B. Kurion Signs New Licensing Agreement with ISV Japan to Expand Applications for Geomelt® Vitrification across Japan. 2015; Available from: https://www.businesswire.com/news/home/20151209005299/en/Kurion-Signs-New-Licensing-Agreement-ISV-Japan.
118. Veolia, Support US Departmnet of Energy (DOE) cleanup mission at the Hanford site. 2003.
119. Witwer, K., et al. Geomelt® ICV Treatment of Sellafield Pond Solids Waste - 13414. 2013. United States.
120. Vienna.J. D, H.P., Jiricka.A, Smith.D.E, Lorier.T.H, Schulz.R.I, Reamer.I.A, Hanford Immobilized LAW Product Acceptance Testing: Tanks Focus Area Results. 2001, Pacific Northwest National Laboratory.
121. Veolia, New Geolmelt Vitrification System Successfully Completes Hot Commisioning and its First Demonstration Melt 2019.

122. NNL. NNL and Kurion Complete Initial Commissioning of Geomelt® Vitrification System Prior ro Deployment at NNL's Central Laboratory, Sellafield. NNL Blog 2015; Available from: https://www.nnl.co.uk/blog/2015/11/17/nnl-and-kurion-complete-initial-commissioning-of-Geomelt®-vitrification-system-prior-to-deployment-at-nnls-central-laboratory-sellafield/.
123. Services, P.F.E. Perma-Fix Announces New Geomelt® Vitrification System Successfully Completes Hot Commissioning and First Demonstaration Melt. 2019; Available from: https://ir.perma-fix.com/press-releases/detail/4787/perma-fix-announces-new-Geomelt®-vitrification-system.
124. Veolia, Veolia Nuclear Solutions works with Idaho National laboratory (INL) to Demonstrate New Disposition Path for Radioactive Contaminated Reactive Metal Waste Streams. 2016.
125. NDA, Geomelt® Vitrification of ILW (Preliminary Stage). 2008.
126. News, W.N. Inauguration of Geomelt® system at Sellafield. 2016; Available from: https://www.world-nuclear-news.org/WR-Inauguration-of-Geomelt®-system-at-Sellafield-2507164.html.
127. Veolia, At Sellafield, UK, We tackle a Historic Challenge.
128. Veolia, Overview of Geomelt® Processing of Spent Fuel Components and Sludges.
129. Veolia, Veolia Nuclear Solutions to Highlight Geomelt® Capabilities in Agreement with the INL. 2018.
130. Fuller, A., et al. Radionuclide Behaviour During Thermal Treatment of LLW and ILW Using In-Container Vitrification - 19239. 2019. United States.
131. Wickham, S., et al. Strategic Implications of Active In-Container Vitrification Trials on Thermal Treatment of UK LLW and ILW - 19240. 2019. United States.
132. THERAMIN, D3.5 Geomelt® Operational Report. 2019.
133. Walling, S.A., et al., Characterisation and disposability assessment of multi-waste stream in-container vitrified products for higher activity radioactive waste. Journal of Hazardous Materials, 2021. 401: p. 123764.
134. Report, A., Sellafield Thermal Treatment Phase 2: Geomelt® trials on high metallic waste. January 2012.
135. Impact Services, I., Sellafield Thermal Vitrification Project: Geomelt® Trial 1 Feasibility Report. June 2009.
136. Impact Services, I., Sellafield Thermal Vitrification Project: Geomelt® Trial 2 Feasibility Report. August 2009.
137. Connelly.A.J, B.P.A., Hyatt.N.C and Hand.R.J, Thermal Treatment of plutonium contaminated materails: Phase 1, Report. March 2010, Immobilisation Science Laboratory, University of Sheffield. p. 60pp.
138. Connelly.A. J, B., .P.A, Hyatt.N.C, Hand.R.J, Thermal treatment of plutonium contmainated materials: Phase 1, Appendix. March 2010, Immobilisation Science Laboratory, University of Sheffield. p. 162pp.
139. Rawson, R., P. Davoren, and C. Perkins. Status of rehabilitation of the Maralinga and Emu sites. in Second conference on nuclear science and engineering in Australia, 1997 Conference handbook. 1997. Australia.
140. Parkinson.A, Maralinga: The Clean-Up of a Nuclear Test Site. Medicine and Global Survival, 2002. 7(2).
141. Thompson, L.E., et al. FINAL RESULTS FROM THE IN SITU VITRIFICATION TREATMENT AT MARALINGA. 2000.
142. Morse, M., B. Nowack, and L. Thompson, Subsurface Planar Vitrification Treatment of Problematic TRU Wastes: Status of a Technology Demonstration Program. 2006.
143. New Angles on in situ vitrification, in Initiatives Online. 1999.

144. Nachtrodt.F, Development of a method for plasma - induced combustion of intermediate to low-level radioactive waste. 2013, University of Bologna.
145. Boulos, M., P. Fauchais, and E. Pfender, High-Power Plasma Torches and Transferred Arcs. 2016. p. 1-55.
146. Wise.M, Plasma Processing of Nuclear Wastes, in The Role of Radiochemistry in the Sentencing and Disposal of Radioactive Wastes. 2008: Royal Society of Chemistry
147. R.F. Schumacher, A.L.K., D.F. Bickford, A. Applewhite-Ramsey, C.A. Cicero, T.L. Spatz, and J.C. Marra, HIGH-TEMPERATURE VITRIFICATION OF LOW-LEVEL RADIOACTIVE AND HAZARDOUS WASTES, in WSRC-MS-95-0082. 1995.
148. Scales.C, D.D.a., The role of Tetronics plasma vitrification technology in the management and conditioning of ILW nuclear waste sludges, in Proceedings of the UK Decommissioning and Waste Management Conference. 2007: Rheged.
149. Scales.C, D.D.a., The role of Tetronics plasma vitrification technology in the management and conditioning of nuclear waste, in ICEM2007: Proceedings of the 11th International Conference on Environmental Remediation and Radioactive Waste Management. 2007. p. 1179-1189.
150. Deckers, J., Plasma Technology to Recondition Radioactive Waste: Tests with Simulated Bitumen and Concrete in a Plasma Test Facility. IOP Conference Series: Materials Science and Engineering, 2020. 818: p. 012006.
151. Hyatt, N.C., et al., Characterisation of Plasma Vitrified Simulant Plutonium Contaminated Material Waste. MRS Proceedings, 2006. 985: p. 0985-NN10-06.
152. Deegan.D, M.A., Slaney.B, Wise.M. Plasma vitrification of ILW sludge. in Uk Decommisioning and Waste Management. 2007.
153. Deegan, D. and C. Scales, The Role of Tetronics Plasma Vitrification Technology in the Management and Conditioning of Nuclear Waste. 2007.
154. Deegan.D, C.C., Ismail.S, Treatment of Nuclear Sludge. 2013, Tetronics Limited.
155. Engineer, T. Sellafield nuclear site to trial DC plasma waste recovery 2011; Available from: https://www.theengineer.co.uk/sellafield-nuclear-site-to-trial-dc-plasma-waste-recovery/.
156. Solutions, P. PSC Plasma Torches Available from: https://www.phoenixsolutionsco.com/psctorches.html.
157. News, E.L., Costain wins hot contract to treat Sellafield waste with heat. 2019.
158. Ferrand, K., et al., Dissolution of plasma treated non-radioactive surrogate cemented concentrates and ion exchange resins in KOH solution at 40 °C. IOP Conference Series: Materials Science and Engineering, 2020. 818: p. 012016.
159. Heberlein, J. and A. Murphy, Thermal Plasma Waste Treatment. Journal of Physics D Applied Physics, 2008. 41: p. 053001.
160. Heep, W., The Zwilag Plasma Facility: Five Years of Successful Operation. 2010.
161. Development, E.B.f.R.a. Plasma plant at Bulgaria's Kozloduy nuclear power plant starts operations 2018; Available from: https://www.ebrd.com/news/2018/plasma-plant-at-bulgarias-kozloduy-nuclear-power-plant-starts-operations.html.
162. Newswire, P. EUROPLASMA: Delivery of the Plasma Facility for the Treatment of Low-Level Radioactive Waste Treatment in Bulgaria. 2017; Available from: https://www.prnewswire.co.uk/news-releases/europlasma-delivery-of-the-plasma-facility-for-the-treatment-of-low-level-radioactive-waste-treatment-642892133.html.
163. News, W.-W.N. Plasma plant starts operations in Bulgaria. 2018.
164. SeeNews. Europlasma Industries delivers plasma system to Bulgaria·s Kozloduy NPP 2017; Available from: https://seenews.com/news/europlasma-industries-delivers-plasma-system-to-bulgarias-kozloduy-npp-582504.

165. Harrison, M.T., Costain to build an active plasma trial facility at Sellafield for PCM. 2020.
166. Shuey, M.W. and P.P. Ottmer. LLW Processing and Operational Experience using a Plasma ARC Centrifugal Treatment (PACT{sup TM}) System. 2006. United States.
167. Byeong-Yeon, M., Low & Intermediate Level Radioactive Waste Vitrification Using Plasma Arc Melting Technology. Nuclear Engineering and Technology, 2003. 35.
168. Ltd, T., Sellafield Ltd High Metallic ILW Trials Technical Report. June 2011.
169. Boast, L., M.C. Stennett, and N.C. Hyatt, Thermal treatment of plutonium contaminated material (PCM) waste. MRS Advances, 2017. 2(13): p. 735-740.
170. Bingham, P., et al., Corrosion of Glass Contact Refractories for the Vitrification of Radioactive Wastes: A Review. International Materials Reviews, 2011. 56: p. 226-242.
171. Morgan, S., Personal Communication.
172. Jostsons.A, V.R.E., Hutchings.R. Hanford HLW Immobilisation in Synroc. in Waste Managment. 1996. Tucson, Arizona.
173. Sakka, S., Sol–Gel Formation of Bulk Glasses, in Handbook of Sol-Gel Science and Technology, L. Klein, M. Aparicio, and A. Jitianu, Editors. 2017, Springer International Publishing: Cham. p. 1-24.
174. Mauro.J.C, V.A.K.a., Fundamentals of Inorganic Glass. 2019.
175. Shelby.E.J, Introduction to Glass Science and Technology. 2 ed. 2005: Royal Soceity of Chemistry.
176. Bingham, P., et al., Glass Development for Vitrification of Wet Intermediate Level Waste (WILW) from Decommissionning of the Hinkley Point ‘A’ Site. Materials Research Society symposia proceedings. Materials Research Society, 2009. 1124: p. 161-166.
177. Bingham, P., N. Hyatt, and R. Hand, Vitrification of UK Intermediate Level Radioactive Wastes Arising from Site Decommissioning: Property Modelling and Selection of Candidate Host Glass Compositions. Glass Technology: European Journal of Glass Science and Technology Part A, 2012. 53: p. 83-100.
178. Bingham, P., et al., Vitrification of UK intermediate level radioactive wastes arising from site decommissioning. Initial laboratory trials. Glass Technology: European Journal of Glass Science and Technology Part A, 2013. 54: p. 1-16.
179. Vienna, J.D., et al. Preliminary Glass Development and Testing for In-Container Vitrification of Hanford Low-Activity Waste. 2004. United States: American Ceramic Society, Westerville, OH, United States(US).
180. Zachariasen, W.H., THE ATOMIC ARRANGEMENT IN GLASS. Journal of the American Chemical Society, 1932. 54(10): p. 3841-3851.
181. Ojovan, M.I. and W.E. Lee, Glassy Wasteforms for Nuclear Waste Immobilization. Metallurgical and Materials Transactions A, 2011. 42(4): p. 837-851.
182. Shelby, J., Introduction to Glass Science and Technology. Vol. 35. 2005.
183. Greaves, G.N., EXAFS and the structure of glass. Journal of Non-Crystalline Solids, 1985. 71(1): p. 203-217.
184. Hand.R.
185. Du, L.-S. and J.F. Stebbins, Site Preference and Si/B Mixing in Mixed-Alkali Borosilicate Glasses: A High-Resolution 11B and 17O NMR Study. Chemistry of Materials, 2003. 15(20): p. 3913-3921.
186. Grammes.T, Structure and mechanical properties of aluminosilicate glasses. 2020.
187. Calas, G., et al., Structure–property relationships in multicomponent oxide glasses. Comptes Rendus Chimie, 2002. 5(12): p. 831-843.

188. Wright, A., et al., Borate Versus Silicate Glasses: Why Are They So Different? Physics and Chemistry of Glasses - European Journal of Glass Science and Technology Part B, 2010. 51: p. 233-265.
189. Wright, A.C., N.M. Vedishcheva, and B.A. Shakhmatkin, Vitreous borate networks containing superstructural units: a challenge to the random network theory? Journal of Non-Crystalline Solids, 1995. 192-193: p. 92-97.
190. Neuville, D.R., L. Cormier, and D. Massiot, Al coordination and speciation in calcium aluminosilicate glasses: Effects of composition determined by 27Al MQ-MAS NMR and Raman spectroscopy. Chemical Geology, 2006. 229(1): p. 173-185.
191. Neuville, D.R., L. Cormier, and D. Massiot, Al environment in tectosilicate and peraluminous glasses: A 27Al MQ-MAS NMR, Raman, and XANES investigation. Geochimica et Cosmochimica Acta, 2004. 68(24): p. 5071-5079.
192. Neuville, D.R., et al., Local Al site distribution in aluminosilicate glasses by 27Al MQMAS NMR. Journal of Non-Crystalline Solids, 2007. 353(2): p. 180-184.
193. Neuville, D., V. Montouillout, and D. Massiot, Local environment of Al in aluminosilicate glasses: A NMR point of view. Journal of Non-Crystalline Solids, 2007. 353: p. 180-185.
194. Neuville, D., et al., Structure of Mg- and Mg/Ca Aluminosilicate Glasses: 27Al NMR and Raman Spectroscopy Investigations. American Mineralogist - AMER MINERAL, 2008. 93: p. 1721-1731.
195. Drewitt, J., L. Hennet, and D. Neuville, From Short to Medium Range Order in Glasses and Melts by Diffraction and Raman Spectroscopy. Reviews in Mineralogy and Geochemistry, 2022. 87(1): p. 55-103.
196. Chen, Z., et al., Insight into the Relationship Between Viscosity and Structure of CaO-SiO2-MgO-Al2O3 Molten Slags. Metallurgical and Materials Transactions B, 2019. 50.
197. Cormier, L., Glasses: Aluminosilicates. Encyclopedia of Materials: Technical Ceramics and Glasses, 2021.
198. Mysen, B., Structure of Aluminosilicate Melts. ISIJ International, 2021. 61(12): p. 2866-2881.
199. Lacy, E., Aluminium in glass and in melts Physics and Chemistry of Glasses, 1963. 4 (6): p. 234-238.
200. Loewenstein, W., The distribution of aluminum in the tetrahedra of silicates and aluminates. American Mineralogist, 1954. 39(1-2): p. 92-96.
201. Toplis, M.J., D.B. Dingwell, and T. Lenci, Peraluminous viscosity maxima in Na2O□Al2O3□SiO2 liquids: The role of triclusters in tectosilicate melts. Geochimica et Cosmochimica Acta, 1997. 61(13): p. 2605-2612.
202. Lee, S.K. and J.F. Stebbins, The degree of aluminum avoidance in aluminosilicate glasses. American Mineralogist, 1999. 84(5-6): p. 937-945.
203. Mysen, B.O. and M.J. Toplis, Structural behavior of Al3+ in peralkaline, metaluminous, and peraluminous silicate melts and glasses at ambient pressure. 2007. 92(5-6): p. 933-946.
204. Allu, A.R., et al., Structure and Crystallization of Alkaline-Earth Aluminosilicate Glasses: Prevention of the Alumina-Avoidance Principle. The Journal of Physical Chemistry B, 2018. 122(17): p. 4737-4747.
205. Neuville, D.R., et al., Al speciation and Ca environment in calcium aluminosilicate glasses and crystals by Al and Ca K-edge X-ray absorption spectroscopy. Chemical Geology, 2004. 213(1): p. 153-163.

206. Neuville, D.R., et al., Environments around Al, Si, and Ca in aluminate and aluminosilicate melts by X-ray absorption spectroscopy at high temperature. American Mineralogist, 2008. 93(1): p. 228-234.
207. Cormier, L. and D.R. Neuville, Ca and Na environments in Na2O–CaO–Al2O3–SiO2 glasses: influence of cation mixing and cation-network interactions. Chemical Geology, 2004. 213(1): p. 103-113.
208. Cochain, B., et al., Effects of the Iron Content and Redox State on the Structure of Sodium Borosilicate Glasses: A Raman, Mössbauer and Boron K-Edge XANES Spectroscopy Study. Journal of the American Ceramic Society, 2012. 95(3): p. 962-971.
209. Ciżman, A., et al., The effect of Fe on the structure and electrical conductivity of sodium borosilicate glasses. Physical Chemistry Chemical Physics, 2017. 19(34): p. 23318-23324.
210. Mysen, B.O., The structural behavior of ferric and ferrous iron in aluminosilicate glass near meta-aluminosilicate joins. Geochimica et Cosmochimica Acta, 2006. 70(9): p. 2337-2353.
211. Le Losq, C., et al., Determination of the oxidation state of iron in Mid-Ocean Ridge basalt glasses by Raman spectroscopy. American Mineralogist, 2019. 104.
212. Le Losq, C., M. Cicconi, Rita, and D. Neuville, R, Iron in Silicate Glasses and Melts: Implications for Volcanological Processes, in Magma Redox Geochemistry, M. Roberto and R.N. Daniel, Editors. 2021, Wiley. p. 233 - 253.
213. Bergeron, B., et al., First investigations of the influence of IVB elements (Ti, Zr, and Hf) on the chemical durability of soda-lime borosilicate glasses. Journal of Non-Crystalline Solids, 2010. 356(44): p. 2315-2322.
214. Jollivet, P., et al., An enhanced resolution of the structural environment of zirconium in borosilicate glasses. Journal of Non-Crystalline Solids, 2013. 381: p. 40-47.
215. Farges, F., C.W. Ponader, and G.E. Brown, Structural environments of incompatible elements in silicate glass/melt systems: I. Zirconium at trace levels. Geochimica et Cosmochimica Acta, 1991. 55(6): p. 1563-1574.
216. Ficheux, M., et al., Structural evolution of high zirconia aluminosilicate glasses. Journal of Non-Crystalline Solids, 2020. 539: p. 120050.
217. Lu, X., L. Deng, and J. Du, Effect of ZrO2 on the structure and properties of soda-lime silicate glasses from molecular dynamics simulations. Journal of Non-Crystalline Solids, 2018. 491: p. 141-150.
218. Lu, X., et al., Structural role of ZrO2 and its impact on properties of boroaluminosilicate nuclear waste glasses. npj Materials Degradation, 2018. 2(1): p. 19.
219. Dargaud, O., et al., In Situ study of Nucleation of Zirconia in an MgO–Al2O3–SiO2 Glass. Journal of the American Ceramic Society, 2010. 93(2): p. 342-344.
220. Dargaud, O., et al., Structural role of Zr4+ as a nucleating agent in a MgO–Al2O3–SiO2 glass-ceramics: A combined XAS and HRTEM approach. Journal of Non-Crystalline Solids, 2010. 356(52): p. 2928-2934.
221. Chevreux, P., et al., Hafnium solubility determination in soda-lime aluminosilicate glass. Journal of Non-Crystalline Solids, 2017. 457: p. 13-24.
222. Strachan.D, V.R.E., Shuh.K.D, Ewing.C.R, Distribution & Solubility of Radionuclides & Neutron Absorbers in Waste Forms for Disposition of Plutonium Ash & Scraps, Excess Plutonium, and Miscellaneous Spent Nuclear Fuels. 1998: Environmental Management Science Program.
223. Nienhuis, E.T., et al., Effect of Ti4+ on the structure of nepheline (NaAlSiO4) glass. Geochimica et Cosmochimica Acta, 2020. 290: p. 333-351.

224. Laorodphan, N., et al., Boron and pentavalent vanadium local environments in binary vanadium borate glasses. Journal of Non-Crystalline Solids, 2016. 453: p. 118-124.
225. Lu, X., et al., Vanadium Oxidation States and Structural Role in Aluminoborosilicate Glasses: An Integrated Experimental and Molecular Dynamics Simulation Study. The Journal of Physical Chemistry B, 2021. 125(44): p. 12365-12377.
226. Cassingham, N., et al., The Structural Role of Zn in Nuclear Waste Glasses. International Journal of Applied Glass Science, 2011. 2: p. 343-353.
227. Ben Kacem, I., et al., Structure and properties of lead silicate glasses and melts. Chemical Geology, 2016. 461.
228. Aboelwafa, M.A., et al., Influence of Cerium oxide on the structural aspects of soda-lime aluminosilicate glasses synthesized by sol-gel route. Materials Chemistry and Physics, 2023. 305: p. 127930.
229. el Damrawi, G. and A. Behairy, Structural Role of Cerium Oxide in Lead Silicate Glasses and Glass Ceramics. Journal of Minerals and Materials Characterization and Engineering, 2018. 06: p. 438-447.
230. Connelly, A.J., et al., The effect of uranium oxide additions on the structure of alkali borosilicate glasses. Journal of Non-Crystalline Solids, 2013. 378: p. 282-289.
231. Schmidt, A.J., Hanford Spent Nuclear Fuel Project Databook.
232. Energy, D.o., Hanford K-Basin Sludge Chararcterization Overview. 2005.
233. Reimann.G, Technical Assessment of Processes to Enable Recycling of Low-Level Contaminated Metal Waste. 1991.
234. Tetronics, Drum Preparation - R01. 2019.
235. Reimann.A.G, G.D.J., Eddy.L.T, Anderson.L.G. 1992, Idaho National Laboratory.
236. Reimann.A.G, K.C.P. 1993, Idaho National Laboratory.
237. Owen.E.D, F.E.J. 1981, Idaho National Labaratory.
238. Schofield, J.M., P.A. Bingham, and R.J. Hand, The Immobilisation of a Chloride Containing Actinide Waste Surrogate in Calcium Aluminosilicate Glasses, in Environmental Issues and Waste Management Technologies in the Materials and Nuclear Industries XII. 2009. p. 69-80.
239. Caurant, D., et al., Glasses, glass-ceramics and ceramics for immobilization. Glasses, Glass-Ceramics and Ceramics for Immobilization, 2009: p. 1-359.
240. Donald.W.I, Waste Immobilisation in Glass and Ceramic Based Hosts 2010, Chichester Wiley Publishing.
241. Lopez, C., et al., Solubility of actinide surrogates in nuclear glasses. Journal of Nuclear Materials, 2003. 312(1): p. 76-80.
242. Bingham, P.A., et al., The Use of Surrogates in Waste Immobilization Studies: A Case Study of Plutonium. MRS Proceedings, 2008. 1107: p. 421.
243. Tan, S. and R.J. Hand, Incorporation and phase separation of Cl in alkaline earth aluminosilicate glasses. Journal of Nuclear Materials, 2018. 507: p. 135-144.
244. Thornber, S.M., et al., Solubility, speciation and local environment of chlorine in zirconolite glass–ceramics for the immobilisation of plutonium residues. RSC Advances, 2020. 10(54): p. 32497-32510.
245. Siwadamrongpong, S., M. Koide, and K. Matusita, Prediction of Chloride Solubility in CaO-Al2O3-SiO2 Glass Systems. Journal of Non-crystalline Solids - J NON-CRYST SOLIDS, 2004. 347: p. 114-120.
246. Schofield, J.M., Vitrification of a chloride containing actinide waste surrogate. 2011, University of Sheffield: Dpeartment of Materials and Science and Engineering.
247. Sandland, T., et al., Structure of Cl-containing silicate and aluminosilicate glasses: A 35Cl MAS-NMR study. Geochimica Et Cosmochimica Acta - GEOCHIM COSMOCHIM ACTA, 2004. 68: p. 5059-5069.

248. Ojovan, M. and O. Batyukhnova, Glasses for Nuclear Waste Immobilization. 2007.
249. Donald, I.W., et al., A glass-encapsulated calcium phosphate wasteform for the immobilization of actinide-, fluoride-, and chloride-containing radioactive wastes from the pyrochemical reprocessing of plutonium metal. Journal of Nuclear Materials, 2007. 361(1): p. 78-93.
250. Webster, J.D., R.J. Kinzler, and E.A. Mathez, Chloride and water solubility in basalt and andesite melts and implications for magmatic degassing. Geochimica et Cosmochimica Acta, 1999. 63: p. 729-738.
251. Webster, J.D. and B. De Vivo, Experimental and modeled solubilities of chlorine in aluminosilicate melts, consequences of magma evolution, and implications for exsolution of hydrous chloride melt at Mt. Somma-Vesuvius. American Mineralogist, 2002. 87: p. 1046 - 1061.
252. Stebbins, J. and L.-S. Du, Chloride ion sites in silicate and aluminosilicate glasses: A preliminary study by 35Cl solid-state NMR. American Mineralogist, 2002. 87.
253. Jolivet, V., et al., Incorporation of chlorine in nuclear waste glasses using high-pressure vitrification: Solubility, speciation, and local environment of chlorine. American Mineralogist, 2023. 108(6): p. 1032-1042.
254. Chen, X., et al., High chloride content calcium silicate glasses. Physical Chemistry Chemical Physics, 2017. 19(10): p. 7078-7085.
255. Zimova, M., The effect of chlorine on the viscosity of Na2O-Fe2O3Al2O3SiO2 melts. American Mineralogist - AMER MINERAL, 2006. 91: p. 344-352.
256. NDA, NDA Higher Activity Waste Treatment Framework. 2015.
257. Avramov, I., T. Vassilev, and I. Penkov, The glass transition temperature of silicate and borate glasses. Journal of Non-Crystalline Solids, 2005. 351(6): p. 472-476.
258. Fokin, V.M., M.L.F. Nascimento, and E.D. Zanotto, Correlation between maximum crystal growth rate and glass transition temperature of silicate glasses. Journal of Non-Crystalline Solids, 2005. 351(10): p. 789-794.
259. Cormier, L., D.R. Neuville, and G. Calas, Relationship Between Structure and Glass Transition Temperature in Low-silica Calcium Aluminosilicate Glasses: the Origin of the Anomaly at Low Silica Content. Journal of the American Ceramic Society, 2005. 88(8): p. 2292-2299.
260. Frugier, P., et al., SON68 Nuclear Glass Dissolution Kinetics: Current State of Knowledge and Basis of the New GRAAL Model. Journal of Nuclear Materials, 2008. 380: p. 8-21.
261. Doremus, R.H., Interdiffusion of hydrogen and alkali ions in a glass surface. Journal of Non-Crystalline Solids, 1975. 19: p. 137-144.
262. Van Iseghem.P, A.M., Gin.S, Deneele.D, Grambow.B, McGrail.P, Strachan.D, Wicks.G, A Critical Evaluation of the Dissolution Mechanisms of High-level Waste Glasses in Condirions of Relevance for Geological Disposal (GLAMOR). 2007.
263. Van Iseghem, P., et al., Glamor- or how we achieved a common understanding on the decrease of glass dissolution kinetics through international cooperation. Journal of the South Carolina Academy of Science, 2011. 9: p. 9+.
264. Corkhill, C.L., et al., Dissolution of UK High-Level Waste Glass Under Simulated Hyperalkaline Conditions of a Colocated Geological Disposal Facility. International Journal of Applied Glass Science, 2013. 4(4): p. 341-356.
265. Gin, S., et al., Nuclear Glass Durability: New Insight into Alteration Layer Properties. The Journal of Physical Chemistry C, 2011. 115(38): p. 18696-18706.
266. Gin, S., I. Ribet, and M. Couillard, Role and properties of the gel formed during nuclear glass alteration: importance of gel formation conditions. Journal of Nuclear Materials, 2001. 298: p. 1.

267. Frugier, P., et al., Son68 Glass Dissolution Kinetics at High Reaction Progress: Mechanisms Accounting for The Residual Alteration Rate. MRS Proceedings, 2006. 932: p. 94.1.
268. Fournier, M., S. Gin, and P. Frugier, Resumption of nuclear glass alteration: State of the art. Journal of Nuclear Materials, 2014. 448(1): p. 348-363.
269. Government, S., Scotland's Higher Activity Radioactive Waste Policy 2011. 2011.
270. NDA, Near-Surface Disposal Strategic Position Paper. 2020.
271. Bamforth, P., et al., Cement materials for use as backfill, sealing and structural materials in geological disposal concepts. A review of current status. Serco Report for NDA, 2012. SERCO/005125/001 Issue 3.
272. Utton, C., et al., Dissolution of Vitrified Wastes in a High-pH Calcium-Rich Solution. Journal of Nuclear Materials, 2013. 435: p. 112–122.
273. Utton, C.A., et al., Chemical durability of vitrified wasteforms: effects of pH and solution composition. Mineralogical Magazine, 2012. 76(8): p. 2919-2930.
274. Mann, C., et al., Dissolution of glass in cementitious solutions: An analogue study for vitrified waste disposal. MRS Advances, 2018. 3(21): p. 1147-1154.
275. Mann, C., et al., The dissolution of simulant vitrified intermediate level nuclear waste in young cement water. MRS Advances, 2020. 5(3-4): p. 131-140.
276. Mann, C., et al., Interactions between Simulant Vitrified Nuclear Wastes and high pH solutions: A Natural Analogue Approach. MRS Advances, 2017. 2(12): p. 669-674.
277. Backhouse, D.J., et al., Corrosion of the International Simple Glass under acidic to hyperalkaline conditions. npj Materials Degradation, 2018. 2(1): p. 29.
278. Backhouse.D, A Study of the Dissolution of Nuclear Waste Glasses in Highly-Alkaline Conditions. 2016, University of Sheffield.
279. C.Mann, A study of the Dissolution of UK Nuclear Waste Glass in Cement Waters. 2018.
280. Gin, S., et al., French SON 68 Nuclear Glass Alteration Mechanisms on Contact with Clay Media. Applied Geochemistry, 2001. 16: p. 861-881.
281. Gin, S., F. Thierry, and Y. Minet, Nuclear Glass Alteration in Clay: Assessment of the Effect of Direct Contact between the Materials through Experimental and Modeling Approach. MRS Proceedings, 2011. 807.
282. de Combarieu, G., et al., Glass–iron–clay interactions in a radioactive waste geological disposal: An integrated laboratory-scale experiment. Applied Geochemistry, 2011. 26(1): p. 65-79.
283. Fisher, A.J., et al., Short communication : the dissolution of UK simulant vitrified high-level-waste in groundwater solutions. Journal of Nuclear Materials, 2020.
284. Utton, C.A., et al., Formation of alteration products during dissolution of vitrified ILW in a high-pH calcium-rich solution. Journal of Nuclear Materials, 2013. 442(1): p. 33-45.
285. Mercado-Depierre, S., et al., Antagonist effects of calcium on borosilicate glass alteration. Journal of Nuclear Materials, 2013. 441(1): p. 402-410.
286. Gin, S., et al., The fate of silicon during glass corrosion under alkaline conditions: A mechanistic and kinetic study with the International Simple Glass. Geochimica et Cosmochimica Acta, 2015. 151: p. 68-85.
287. RWM, Geological Disposal Waste Package Evolution Status Report. 2016, Radioactive Wasre Management.
288. AMEC, Understanding the long-term evolution of cement backfills: alteration of NRVB due to reaction with groundwater solutes. 2017.
289. Andriambololona, Z., N. Godon, and E. Vernaz, R7T7 glass alteration in the presence of mortar: effect of the cement grade. 1991: France. p. 8.

290. Ferrand, K., S. Liu, and K. Lemmens, The Interaction Between Nuclear Waste Glass and Ordinary Portland Cement. International Journal of Applied Glass Science, 2013. 4(4): p. 328-340.
291. Snellings, R., Solution-Controlled Dissolution of Supplementary Cementitious Material Glasses at pH 13: The Effect of Solution Composition on Glass Dissolution Rates. Journal of the American Ceramic Society, 2013. 96(8): p. 2467-2475.
292. Ribet, S. and S. Gin, Role of neoformed phases on the mechanisms controlling the resumption of SON68 glass alteration in alkaline media. Journal of Nuclear Materials, 2004. 324(2): p. 152-164.
293. Burger, E., et al., Impact of iron on nuclear glass alteration in geological repository conditions: A multiscale approach. Applied Geochemistry, 2013. 31: p. 159-170.
294. Neeway, J.J., et al., Effect of Callovo-Oxfordian clay rock on the dissolution rate of the SON68 simulated nuclear waste glass. Journal of Nuclear Materials, 2015. 459: p. 291-300.
295. Fournier, M., P. Frugier, and S. Gin, Effect of Zeolite Formation on Borosilicate Glass Dissolution Kinetics. Procedia Earth and Planetary Science, 2013. 7: p. 264–267.
296. Fleury, B., et al., SON68 glass dissolution driven by magnesium silicate precipitation. Journal of Nuclear Materials, 2013. 442(1): p. 17-28.
297. Thien, B.M.J., et al., The dual effect of Mg on the long-term alteration rate of AVM nuclear waste glasses. Journal of Nuclear Materials, 2012. 427(1): p. 297-310.
298. Cassingham, N.J., et al., Alteration layer formation of Ca- and Zn-oxide bearing alkali borosilicate glasses for immobilisation of UK high level waste: A vapour hydration study. Journal of Nuclear Materials, 2016. 479.
299. Fisher, A.J., et al., The dissolution of simulant UK Ca/Zn-modified nuclear waste glass: Insight into Stage III behavior. MRS Advances, 2020. 5(3-4): p. 103-109.
300. Aréna, H., et al., Impact of Fe, Mg and Ca elements on glass alteration: Interconnected processes. Geochimica et Cosmochimica Acta, 2018. 239: p. 420-445.
301. Backhouse, D.J., et al., Investigation of the role of Mg and Ca in the structure and durability of aluminoborosilicate glass. Journal of Non-Crystalline Solids, 2019. 512: p. 41-52.
302. Gin, S., et al., Effect of composition on the short-term and long-term dissolution rates of ten borosilicate glasses of increasing complexity from 3 to 30 oxides. Journal of Non-Crystalline Solids, 2012. 358(18): p. 2559-2570.
303. Inagaki, Y., et al., Initial dissolution rate of the international simple glass as a function of ph and temperature measured using microchannel flow-through test method. International Journal of Applied Glass Science, 2013. 4(4): p. 317-327.
304. Gin, S. and J.P. Mestre, SON 68 nuclear glass alteration kinetics between pH 7 and pH 11.5. Journal of Nuclear Materials, 2001. 295: p. 83-96.
305. Kim, C.-W., J.-K. Park, and T.-W. Hwang, Analysis of Leaching Behavior of Simulated LILW Glasses by Using the MCC-1 Test Method. Journal of Nuclear Science and Technology, 2011. 48(7): p. 1108-1114.
306. Advocat, T., et al., Hydrolysis of R7T7 Nuclear Waste Glass in Dilute Media: Mechanisms and Rate as a function of Ph. MRS Proceedings, 1990. 212: p. 57.
307. Fisher.J.A, C.L.C., Technote - the dissolution of thermally treated Intermediate Level Waste. In Press.
308. Fournier, M., et al., Glass dissolution rate measurement and calculation revisited. Journal of Nuclear Materials, 2016. 476: p. 140-154.
309. THERAMIN, D3.3 SHIVA and In-Can Melting technoligies and demonstration test trials. 2019, CEA.

310. THERAMIN, D3.6 Hot Isostatic Pressing (HIP) demonstration NNL/USFD. 2019.
311. Gardner, L.J., S.A. Walling, and N.C. Hyatt, Hot isostatic pressing: thermal treatment trials of inactive and radioactive simulant UK intermediate level waste. IOP Conference Series: Materials Science and Engineering, 2020. 818: p. 012009.
312. Walling, S., et al., Characterisation and Durability of a Vitrified Wasteform for Simulated Chrompik III Waste. Journal of Nuclear Fuel Cycle and Waste Technology(JNFCWT), 2021. 19: p. 339-352.
313. THERAMIN, VICHR Technology. 2019, VUJE.
314. Harnett, L., et al., Reactive spark plasma sintering of Cs-exchanged chabazite: characterisation and durability assessment for Fukushima Daiichi NPP clean-up. Journal of Nuclear Science and Technology, 2019: p. 1-11.
315. Tan, S., et al., Vitrification of an intermediate level Magnox sludge waste. Journal of Nuclear Materials, 2019. 515: p. 392-400.
316. Heath, P.G., et al., Immobilisation of Prototype Fast Reactor raffinate in a barium borosilicate glass matrix. Journal of Nuclear Materials, 2018. 508: p. 203-211.
317. Clarke.J, Conditioning of Legacy Radioactive Wastes Requiring Additional Treatment. 2018, University of Sheffield.

3 Materials and Methods

3.1 Materials

3.1.1 Industrial Samples

A series of samples from two different industrial sources were analysed as part of this project: four samples from Veolia Nuclear Solutions Federal Services (VNSFS) and two samples from Tetronics.

3.1.1.1 Veolia Nuclear Solutions Federal Services - Geomelt Samples

The initial chapter and focus of the thesis are based on the vitrification of ILW equivalent waste from outside of the UK using AMEC's Bulk In-Container Vitrification (Geomelt) System that is currently operated by Veolia Nuclear Solutions Federal Services (VNSFS) [1]. This technology is described in Section 2.3.1 and uses conductive melting to vitrify waste regularly using local soil as a glass additive. Recently AMEC and Veolia Nuclear Solutions – Federal Services (VNSFS) in collaboration with PNNL have been running industrial and lab scale trials to demonstrate that the technology can treat several waste groups including basin sludges/salts from the Hanford site in the USA and ion-exchange resins Fukushima from in Japan [2-21].

3.1.1.1.1 Hanford Samples

Research and testing was initiated in 2003 to find supplemental technologies to treat Hanford (S)LAW tank waste in order make up for the lack of capacity at the waste treatment facility and meet the Tri-Party agreement of treating all LAW waste by 2028, AMEC's Bulk In-Container Vitrification System now operated by Veolia Nuclear Solutions Federal Services (VNSFS) was a considered technology [1, 4, 5, 7, 14, 20, 22-26]. Historically there has been a large degree of research into the vitrification and glass formulation to deal with the heterogenous Hanford LAW [24].

For this round of research and testing initial crucible, engineering and full scale tests were undertaken beginning in 2004 on two Hanford waste streams, firstly sludge simulant from the KE basin in the 100 K area and secondly, as part of the Demonstration Bulk Vitrification System (DBVS) project, Low Activity Waste (LAW) simulant from the 200 West Area initially based upon an average of 6 single-shell S and U tanks and laterally focusing on a more realistic simulant based upon waste from tank 241-S-109 [2-15, 17-19]. In this project 2 samples of glass were taken from these trails. From the KBasin trials a sample from the larger scaled engineering test has been sampled and labelled as sample KBasin (Figure 3.1). For the test 17.86 kg of KBasin inactive simulant sludge at a waste loading of 39% was vitrified with 27.94 kg of Hanford soil. The simulant was based upon knowledge of the KBasin sludge from various sampling studies that found it to have a particle size upto 0.635 cm, a variable mix of different materials; including sand, organics, concrete, metal oxides, metals, with the major source of radioactivity coming from metallic U fission products (Cs, Sr and daughters) and transuranic elements from neutron capture during irradiation [27-29]. Mischmetal was added to the sludge simulant as the lanthanides (Table 3.1) best represent the U content, consideration of U and U metal oxides is important to the vitrification processing requiring additional operational constraints as they are pyrophoric and due to reduction reactions [2]. Waste soil from the VNSFS Horns Rapids Test Site was chosen as it has a high silica content making it a good precursor for glass formulation (Table 3.2). A starter path composed of 50% soil and 50% graphite flakes helps produce an initial conductive path and initiate melting [2]. The wasteform produced by vitrification was glassy, a brown colour, with some porosity, a small metallic iron rich basal layer and minor iron crystallisation that is confirmed by initial XRD analysis (Figure 3.1) [2], this is seen to be a type 1 (Section 2.1.7) wasteform although this prediction requires further analysis and confirmation. Processing occurred without any technical problems and the pyrophoric material was immobilised through oxidation and incorporation into a silicate matrix to create a non-reactive safe waste-form that meet the requirements of CH-TRU waste and would be suitable for WIPP disposal [2].

Table 3.1 Composition of the radioactive and non-radioactive simulants used in the K Basin Geomelt trials [2].

Component Simulant	Mass Fraction (Radioactive)	Mass Fraction (Non-Radioactive)		
Misch Metal		0.1	Ce	50
			La	22
			Nd	18
			Pr	6
			Rare Earths	4
U Metal	0.04			
U Oxides ($UO_{2.125}$)	0.251			
$Al(OH)_3$	0.142	0.182		
Fe_2O_3	0.423	0.539		
SiO2	0.120	0.154		
Zr	0.020	0.026		

Table 3.2 Compositional analysis of the Horn Rapid Test Site soil. Initial XRD studies of the soil reveal a mix of quartz and aluminosilicates (albite, anorthite, sanidine and muscovite) [2].

Oxide	HRTS Soil
Al_2O_3	0.1303
BaO	0.0007
CaO	0.0407
Cr_2O_3	0.0002
FeO	0.0568
K_2O	0.0218
MgO	0.0198
MnO	0.0010
Na_2O	0.0274
P_2O_5	0.0021
SiO_2	0.6872
SrO	0.0004
TiO_2	0.0117
UO_2	0

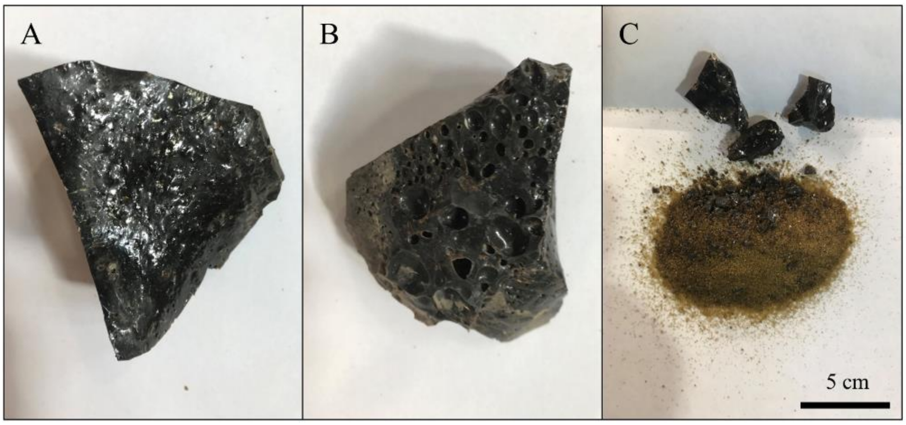

Figure 3.1 A-Brown glass waste from KBasin engineering test, upper uniform surface (KBasin) B- Brown glass waste from KBasin engineering test, lower porous surface (KBasin) C-Crushed glass from the KBasin engineering test (KBasin).

From the Demonstration Bulk Vitrification System (DBVS) project, glass from test 38-C has been analysed and referred to as sample DBVS (Figure 3.2). Test 38-C added Horn Rapids Test Site (HRTS) soil (Table 3.2) and glass additives (predominantly B_2O_3 and ZrO_2) to S-109 simulant (Table 3.6) in specific volumes (Table 3.7) targeting an idealised glass composition developed by initial lab studies (Table 3.5) and specifically for Test 38-C (Table 3.8) to that meets final disposal standards. The simulant was based upon analysis of the sludge ((Table 3.3) and saltcake layer (Table 3.3) found in Tank S-109. The radioactivity in the waste will be dominated by fission products including ^{137}Cs and ^{90}Sr, ^{99}Tc, ^{129}I, ^{93}Zr and ^{79}Se. Longer lived ^{99}Tc is an issue as it will still be present in the LAW at the time of disposal at levels of about 3 parts per million and would need immobilisation in the waste glass. Tc solubility in sodium borosilicate glass is up to 2000 ppm rising to about 2800 ppm under slightly reducing conditions, therefore glass solubility is not a major factor in Tc incorporation into the wasteform and this should not change with Tc oxidation state. Tc (IV) form in the glass is well-dispersed six co-ordinated Tc (IV) with some TcO_2 inclusions. The form of Tc (VII) is equivocal but could be crystalline inclusions of pertechnetate salts and/or isolated dispersed TcO_4^- units [30, 31]. Tc migration via the formation if metallic elements and molten ionic salt (MIS) and volatilisation however is a major issue as it does not allow the Tc the time or the physical opportunity to be dissolved in the glassy wasteforms. Various operational set ups and additions have been used in Test 38-C that built upon previous lab and industry studies [4-15, 18, 19] with the aim of improving processing and glass performance, specifically the use of zircon improved the level of zirconia dissolution in the glass compared to previous trials and the use of a reduced starter path, reduced Fe feed content, reduced temperature, addition of cellulose and reduction in the particle size of the glass feed helped reduce metallic and MIS formation. To reduce volatilisation tests used a cold cap of unmolten feed to cove the melt surface, however the cold cap increased the level of MIS so was managed to reduce its contact with the CRB and other options including lower temperatures and reduced melt times helped reduce vaporisation. To test how effective these measures were Tc or Re (in inactive trials) was added to the melts to analysis glass incorporation. Initial tests from off gas analysis were positive with single-pass retentions of 70.9 wt.% Re and 95% wt.% SO_3 in test 38-C, although further analysis is required to see if the Re was incorporated in the glass (see later).

The full-scale ICV at VNSFS Rapid Horn Test Site, Richland was used to vitrify the simulant waste. The wasteform produced from test 38-C was glassy, dark green colour and had low PCT, VHT and TCLP values including low Tc release rates showing that a good wasteform was produced (Figure 3.2) [5, 6]. No more detailed analysis is present to confirm waste structure or composition, but it is expected like KBasin the wasteform to be type 1 (Section 2.1.7).

Table 3.3 REDOX High-Level Waste Composition from basin sampling [32].

Compound	Concentration
$NaAlO_2$	1.2 M
NaOH	0.69 M
$NaNO_3$	4.83 M
Na_2CrO_7	0.0066 M
$Cr(OH)_3$	0.045 M
Na_2SO_4	0.031 M
$Fe(OH)_3$	0.016 M
U	0.05%
Pu	0.04%

Table 3.4 Salt Cake waste composition from basin sampling dominated by waste from the 242-S Evaporator/Crysalliser.

Compound	Concentration	
	Mother Liquor (M)	Salt (wt%)
H_2O	44-55%	9-13
$NaAlO_2$	1.1-1.2	1-2
$NaNO_2$	1.1-1.8	0-2
$NaNO_3$	2-5	70-90
NaOH	5-5.6	1-4
Na_2CO_3	0.1-0.2	0-7
Na_2SO_4	0-0.05	0-1
Na_3PO_4	0-0.02	0-0.1

Table 3.5 Idealised glass composition for the DBVS vitrification project [5].

Element	Glass Composition Ranges (mass % inclusive)
Na_2O	17-22
B_2O_3	3-5
Al_2O_3	8-12.5
ZrO_2	5.5-8 or 6.4-8 (if $\geq Al_2O_3$)
SiO_2	40-48.5

Table 3.6 S-109 simulant composition [6].

Material	Moles/Mole of Na
Al	0.0088
Ca	0.0002
Cl	0.0014
Cr	0.0028
F	0.0011
Fe	0.0009
K	0.0008
P	0.0109
SO_3	0.0074
NO_3	0.8241
NO_2	0.0123
CO_3	0.0338
OH	0.0666
Organic C	0.0050

Table 3.7 Feed volumes for test 38-C [6].

Material	Mass, kg	Wt%
S-109 Simulant	21,252	38.1
HRTS Soil	25,924	46.5
$ZrSiO_4$	4,613	8.3
B_2O_3	2,200	3.9
SiO_2	1,426	8.3
$Al(OH)_3$	373	0.7
Total	55.787	100

Table 3.8 Idealised glass composition for Test 38-C [6].

Component	Mass Fraction
Al_2O_3	0.0800
B_2O_3	0.0500
BaO	0.0005
CaO	0.0285
Cl	0.0003
Cr_2O_3	0.0013
F	0.0001
Fe_2O_3	0.04
K_2O	0.0186
MgO	0.0137
MnO	0.0006
Na_2O	0.2000
P_2O_5	0.0058
SiO_2	0.4804
SO_3	0.0035
SrO	0.002
TiO_2	0.0064
ZrO_2	0.0700

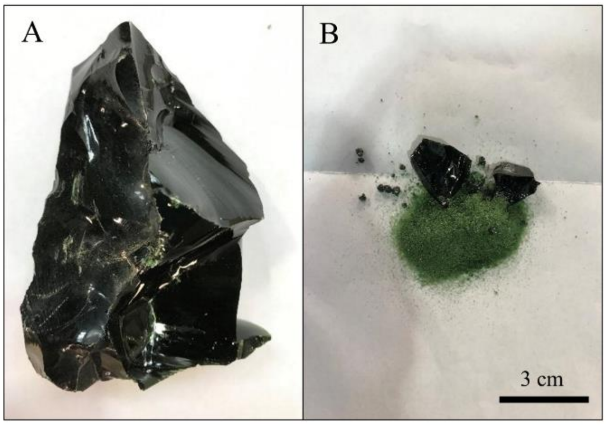

Figure 3.2 A - Dark green from DBVS test 38-C (DBVS) B-Crushed glass from the DBVS test 38-C (DBVS).

3.1.1.1.2 Fukushima Daiichi Samples

As described in Section 2.3.2 water treatment at the Tsunami damaged Fukushima (1F) Daiichi Nuclear Power station produced large volume of solid waste. A series of engineering scale tests have been carried out using different simulant mixtures of the solid secondary waste from the Fukushima (1F) water treatment facilities, French simulant sludge from AREVA and glass additives, with Cs and Sr were added as inactive simulants, tests were carried out at the Horn Test Site, Richland. Material from Melts 4 (MRI4) and 7 (MRI7) were further analysed in this project, Melt 4 produced a grey-black coloured crystalline rich glassy wasteform, while Melt 7 produced a black glassy wasteform (Figure 3.3 and Figure 3.4 and Table 3.9 and 3.10) [16, 21]. Relatively extensive analysis shows in both wasteforms a type 1 (Section 2.1.7) glass wasteforms with homogenous radionuclide distribution and variable crystallisation density of rutile and karelinaite, that requires confirmation [16, 21]. Other analysis showed that both wasteforms had good compressive strength and durability with comparative or higher levels than reference glasses [16], with high Cs and Sr retention levels (Table 3.11) that potentially could be improved further with by recycling of Cs laden particulate-off gas systems. They showed that the Geomelt process can vitrify up to 80% of the Fukushima water treatment waste catalogue with high waste loadings. As part of this study a pre-conceptual design for a GeoMelt ICV at Fukushima Daiichi was created this has a sintered melter filter to recycle Cs particulates and would raise Cs retention to 99+%. Future tests of this prototype will support the Japanese use of ICV melters to deal with water containment from Fukushima [16].

Table 3.9 Details of the different engineering tests carried out to test the Geomelt process as a possible method for treating the waste [16, 21, 33].

Melt	Waste Processed	Radioactive Tracers	Waste Loading
4	KUR-EH (engineered Herschelite (Na-Chabazite - $Na_2,K_2,Ca,Sr,Mg)_2[Al_2Si_4O_{12}]_2 \cdot 12H_2O$) and KUR-TSG (granular titanosilicate)	Cs (CsCl in water and absorbed on KUR-EH) and Sr ($SrCO_3$ dry powder)	77%
7	KUR-EH and simulated barium sulphate/iron ferrocyanide ($M_2NiFe(CN)_6$ sludge (AREVA – early processing sludge)	See above.	64% (reduced - AREVA sludge is rich in S - low solubility in glass).

Table 3.10 Mass of the waste components and additives used in each test [21].

Waste Simulant	Melt 4 (kg)	Melt 7 (kg)
KUR-EH	134	110.79
KUR-TSG	47.20	
AREVA Sludge Simulant		9.80
ALPS Carbonate Slurry		
ALPS Iron Coprecipitation Slurry		
Glass Additives (B_2O_3, $LiCO_3$ etc)	37.80	52.82
Water	20	26.59
CsCl (Average Fukushima (1F) KUR-EH ion exchange vessels mass, based on activity, dissolved in water and rotary mixed to absorb Cs onto the KUR-EH. The mixture solar dried).	150 (g)	127.65 (g)
$SrCO_3$	165 (g)	140.41 (g)
Fukushima (1F) simulant soil (Richland HRTS (Table 3.2) soil blended with additives to match Fukushima soil samples).		

Table 3.11 Details of the wasteform produced in the Geomelt trials with Cs and Sr retention levels [16].

Melt	Waste Description	Retention (Calculated through continuous isostatic stack sampling)	
		Cs	Sr
4	Semi-crystalline mixture of a dark glass and TiO_2. All materials in the melter appear to have been processed.	99.44	99.99
7	Homogenous dark glass. All materials in the melter appear to have been processed.	98.47	100

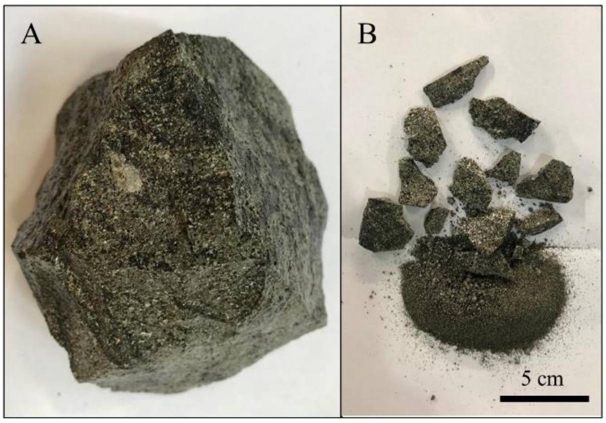

Figure 3.3 A- Grey-black glass ceramic wasteform from Melt 4 (MRI4) B- Crushed glass ceramic from Melt 4 (MRI4).

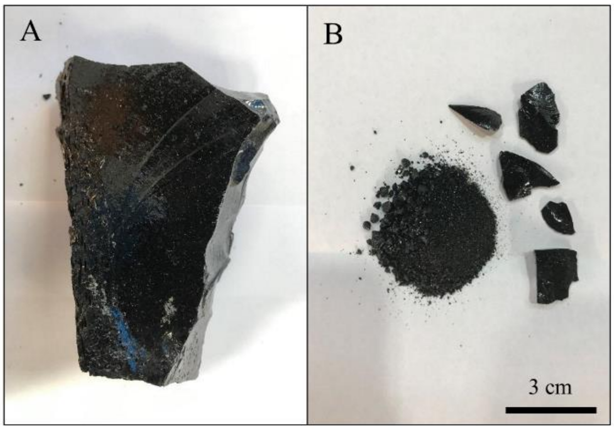

Figure 3.4 A- Black glass wasteform from Melt 7 (MRI7) B- Crushed glass from Melt 7 (MRI7).

3.1.1.2 Tetronics - Plasma Samples

PCM is currently stored and packaged at Sellafield in PVC bags in 200 L mild steel drums, weighing 20 Kg and contain 25-80 kg of PCM waste. Currently the drums are super compacted at waste treatment complex before being grouted and placed in larger 500 L drums awaiting long term storage. This process has several issues including the non-compatible nature of some PCM waste, the concentration of radionuclides and the increase volume of cementation. Plasma vitrification has been suggested as an alternative based on the volume reduction of waste and the ability to immobilise the radiotoxic and mobile Pu in a passively safe glassy material. The high temperature of plasma allows drums to be vitrified as supplied without opening, increasing efficiency and safety but increasing the metallic content of the final waste [34-39]. Information is available from several lab and industry studies that have looked at the vitrification of PCM focusing on the processing conditions, glass additive composition and waste product composition and durability [36, 37, 40-44]. COSTAIN and Tetronics (have carried out industry trials to test the use of plasma technology for the vitrification of PCM [41, 42]. Material from the most recent, 2019, COSTAIN industry trials is supplied for analysis in this project. The trials were carried out at the Tetronics facility in Swindon using a pilot plasma operating facility [41, 42]. 5 simulant 200 L PCM drums were supplied by Sellafield that represent the endmembers of the PCM inventory

Not all the drums have enough material to supply as slag formers therefore a vitrifying glass former was required to create a sufficient melt pool and vitrified waste product. Historically and for HLW a borosilicate glass is used to vitrify nuclear waste, however borosilicate glass frit was hard to source so an alternative was required [45]. $CaO-Al_2O_3-SiO_2$ (CAS) has been shown to incorporate the primary elements of PCM waste with upto ca.40 wt% FeO_x and PuO_2 upto ca.20 wt% , the glass components are cheap, readily available and it has readily used in the plasma industry with Tetronic’s having a lot of experience of it producing stable melts trials with successfully products with high chemical durability [36, 41, 46-48]. The addition of 5 kg pre-charge (29% SiO_2, 33% CaO, 33% Al_2O_3 and 5% Fe_2O_3) and 60 kg of slag makers (52% SiO_2, 32% CaO and 16% Al_2O_3) gave a good modelled final composition in the stable diluting the wasteform and producing compositions for all the final wasteforms in the target region Anorthite/Pseudowallastonite region on the CAS phase diagram (Table 3.13).

The total energy input was modelled to ensure that the target temperature of 1600 °C was reached over the melt time of 10 hrs, with the input of air and water (Trials 4-5) allowing the full oxidation of the organic material [42]. The off gas dust was also measured and had measurable levels (3-10%) of Cl (likely as $CaCl_2$ in the dust) with the Cl from volatilisation of the PVC and controlled by levels of PVC in the waste [42]. This will be looked at later in the project (Chapter 6) as Cl is a corrosive gas and ideally it would be contained in the melt and glass therefore trials were undertaken to investigate the potential of CAS glass for incorporating Cl and preventing it escaping to the off-gas system.

The melts produced a glassy slag product above a basal metal alloy layer, an increased soaking period (pre-charge melt period) and increased levels of pre-charge material helped incorporate the metallic element and reduce the size of the alloy layer. XRF analysis showed the alloy had had variable amounts of Al, Si, Fe, Cu, Ni, Cr and Ca at greater than 1wt.%, with the non-metallic elements from slag contamination. In the different trials there was purple-pinkish and brown colouration of the refractory caused by alumino chrome spinel and iron staining [42].

Table 3.12 Drum compositions (Actual Weight in Kg) for the different trials [41, 42].

Waste Component	Drum T (High Organic Wood) (Trial 5)	Drum V (High Inorganic) (Trial 1)
Drum and Lid	17.4	17.4
PVC Liner	1.52	1.52
Steel Drum Liner	8.84	8.74
Scaffolding Board	29.4	
PVC Suit and/or Double Bags		
Hand Tools and Ancillary Equipment		
Rubber Hose		
Wellingtons		
Paper		
Lab Glassware		
Floor Sweepings		
Vermiculite and Water		
Strippable Coating (Decongelsure)		
Polybottles		
Alumina Furnice Bricks		
Electric Cable (2.5mm)		
Rubber Gloves		
Whitehaven Bricks		18.04
Windscale Spec Concrete		17.14
50mm MS Pipe		
50mm Pipe Flanged		
Galvanised Steel Sheet		
Cast Iron		
50mm SS Pipe		
Steal Scaffolding Poles		
Aluminium Scaffolding Poles		
6mm Steel Plate		
22mm Copper Pipe		
Total	57.16	62.84

Table 3.13 Final predicted wasteform composition for Valingar trials [41].

	Trial 1 (DrumV)	Trial 5 (Drum T)
SiO_2	47.7	51.5
CaO	32.6	32
Al_2O_3	18	16.5
Other	1.6	0.1

Material from vitrification of Drum T and Drum V were further analysed in this project [41, 42, 49], unfortunately the slag material from the other trials had been disposed of at the time of contact. Drum V waste was vitrified in Trial 1. The vitrified waste product was supplied attached to a residual unmolten drum base (Figure 3.5A) The waste was a mix of black glassy material and dull grey crystalline slag that had some zoned grey-white crystalline material (Figure 3.5B-D). Slag and crystalline material were most prevalent adjacent to the metal drum and likely relates to heterogeneous crystallisation against the unmolten drum (Figure 3.5A).

The material from Trail 1 was divided in this project into the crystalline slag material (sample 1 -Figure 3.5D, mixed slag and glass material (sample 1A - Figure 3.5B and C) and glass material separated from sample 1A (sample 1A_glass - Figure 3.5B and C).

Drum T was vitrified in Trial 5. The vitrified waste product was supplied attached to the metallic molten remnants of a drum, showing the greater successful of the melt pool in trial 5. The was a solid vitrified block that had an external white rim of the protective refractory material attached showing that there was a reaction between the melt and refractory (Figure 3.6A). The waste for this project was divided equally into two textures. Furthest from the metallic drum was vuggy material (sample 5_Vu) that had up to 1cm circular evenly distributed vugs through the structure and close to the drum was crystalline material (5_Xc) that had long crystalline growth and no vuggy material (Figure 3.6B). This dual texture is related to heterogenous crystallisation adjacent to the drum and the rising of the less dense gaseous air that was injected into Trial 5 to oxidise the organic material in the waste simulant.

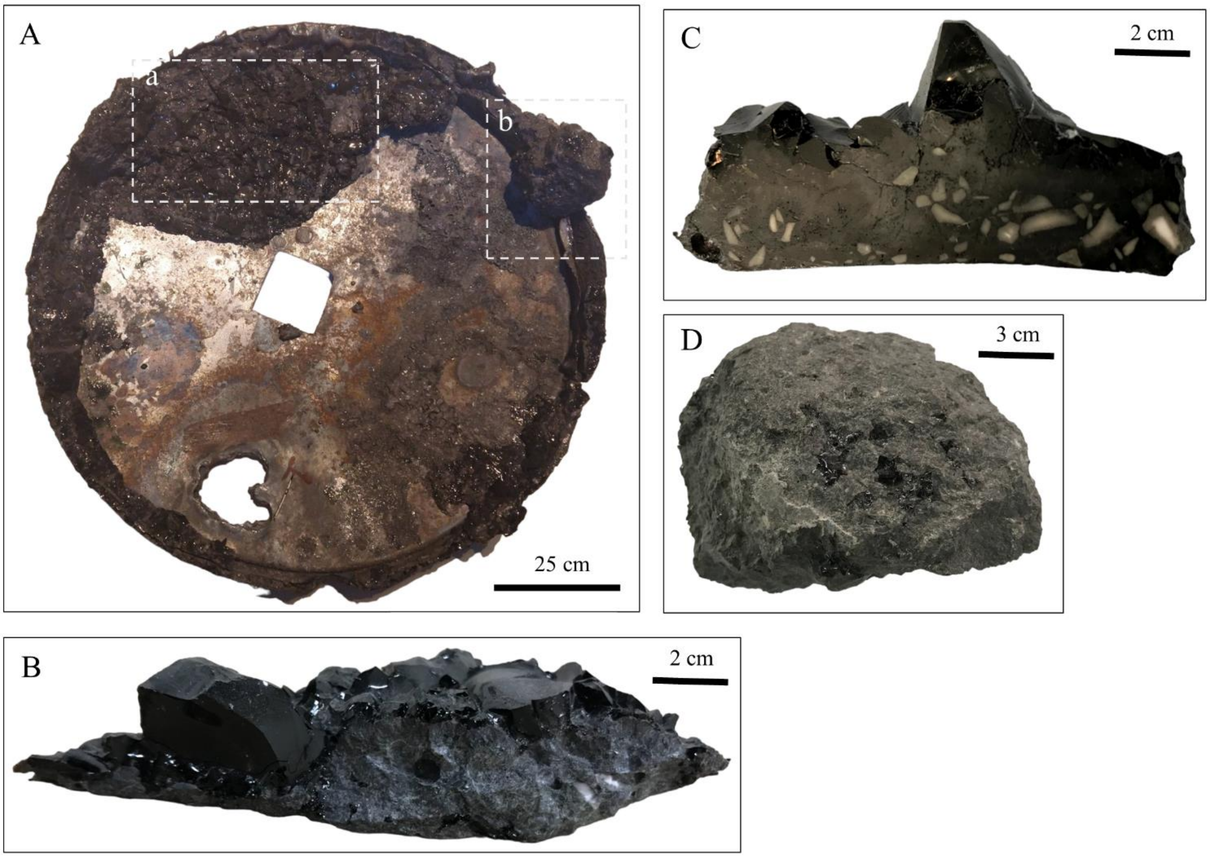

Figure 3.5A - Overview of the Trial 1 waste. Waste for sample 1A (B and C) was taken from area a and waste for sample 1 (D) was taken from area b. B – Mixed glass and crystalline waste mixed material is sample 1A and separated glass material is sample 1A_glass C – Cross Section through the mixed glass and crystalline waste showing the white-grey zoned crysals. D – Crystalline material from area b that makes up sample 1.

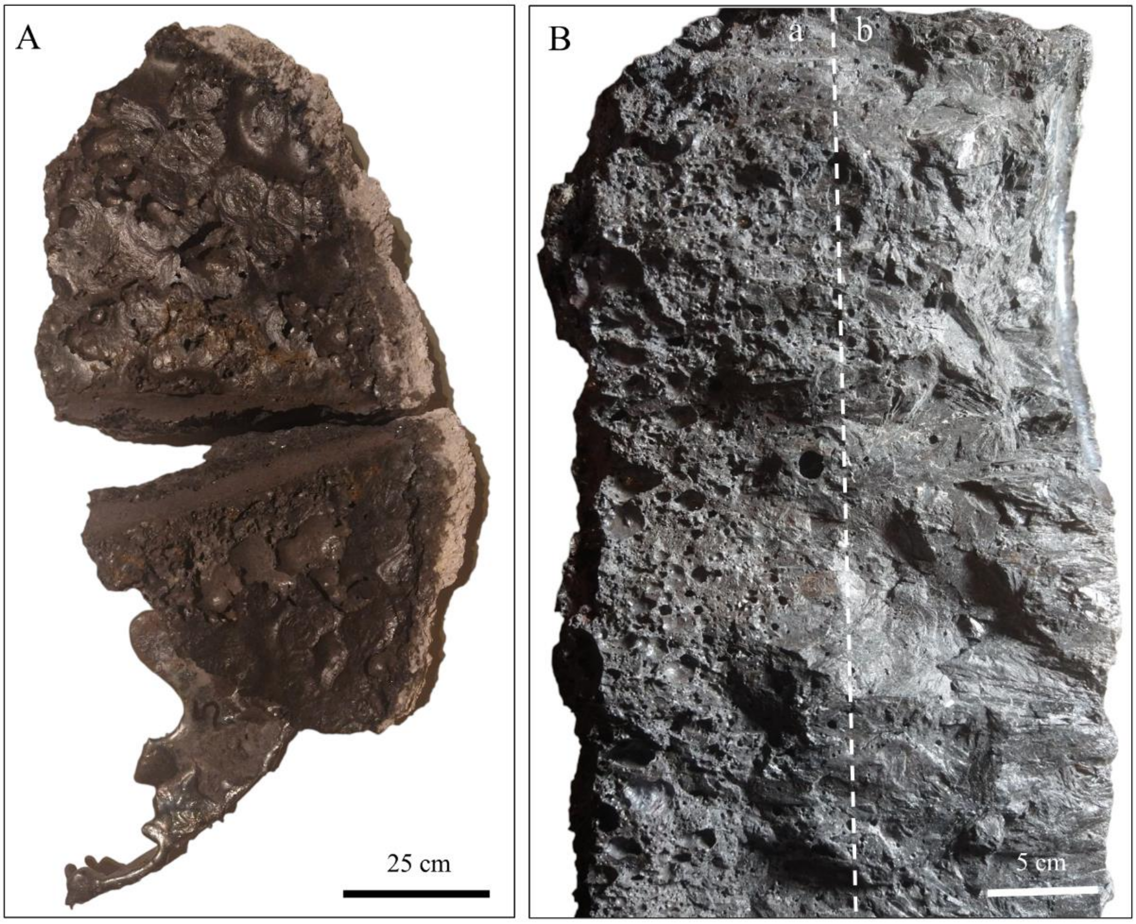

Figure 3.6A - Overview of the Trial 5 waste. B – Profile of Trial 5 waste with the basal drum side on the right side of the of the image. Vuggy (5_Vu) was taken from area a and crystalline (5_Xc) was taken from area b.

There has now been a commitment by Sellafield to build a commercial PCM pilot vitrification rig that can process up to 6,000 200L drums per annum with several 10 furnaces in 24h operation [42]. As part of this aim Cavendish Ltd are now working toward an active pilot rig at Tetronics in Swindon with designs looking at vitrifying whole drums of waste and tests for operating parameters like electrode infringement on the melt, Pu criticality in the final wasteform, drum off gassing, Pu contamination of the wider system, including the crucible and off-gas system. This work is ongoing but is likely to move forward fast in the next few years as demand for a working facility is high [50].

3.1.2 Glass Melting (in-house samples)

A proportion of the glass in this thesis was acquired from industry, however a series of CAS glass were produced to investigate PCM waste loading.

Historic studies of PCM waste vitrification have focused on making simulate PCM wastes and doing small-scale melts using different glass forming additives [36, 37]. This method has produced very useful insights into the waste loading and Pu partitioning of PCM vitrification, but none have focused upon the specific solubility and structural effects of the different PCM waste components in the waste glass. The target base CAS glass composition is based upon the average target glass composition CaO (32 wt%) - Al_2O_3 (17 wt%) - SiO_2 (51 wt%) from the recent Tetronic industrial trials, predicted to produce a stable wasteform [41].

To investigate the effects of the addition of waste components to this base glass a series of glass melts targeted the 3 important potential problem components of the PCM waste – plutonium (Pu), metal and PVC were produced. Considerations for each waste element is required and discussed further below.

Plutonium is a radiotoxic element therefore cannot be used in normal lab situations due to safety and practicality reasons. Two different inactive surrogates will be used, cerium (Ce) and hafnium (Hf), to investigate the effects of plutonium (Pu). Two different surrogates have been chosen because although each surrogate has similarities to Pu non fully represent its properties therefore a multi-surrogate approach allows for the best prediction of Pu behaviour in the glass. When selecting a surrogate, it is important to understand and consider the different chemical and physical properties of the surrogate and how they compare to Pu. Valence, electronic configuration, ionic radii, coordination will control the structural, chemical and solubility behaviour of Pu and the surrogate in the glass, while redox potential, density, oxide melting temperature and particle size distribution will control Pu and surrogate reaction kinetics, dissolution, and distribution in the glass [51].

Ce is a good and widely used surrogate for Pu in glass and ceramic synthesis [36, 37, 51-58] as it mirrors its structure and behaviour in many ways: the ionic radii of Pu and Ce almost identical, both Pu and Ce have both tri and tetravalent oxidation states (a property of no other non-active surrogate), Ce and Pu oxides have similar melting temperatures, in both tri Ce and Pu are more soluble than tetravalent Ce and Pu and Pu(III) and Ce (III) have similar solubilities in borosilicate glass (2-2.5 mol%) at 1400°C, with both have increasing solubility with temperature due to a shift in the oxidation state from tetravalent to trivalent [51, 55, 58-62]. Based on the lack of research the solubility of both Pu and Ce in CAS glass is unknown and the selection of surrogate (both Ce and Hf) is based upon other glass compositions. However, Ce has different density, electronic configuration, and redox potential to Pu. Redox potential variance between Ce and Pu demonstrated by Ce (IV)/Ce (total) ratio of 0 and Pu (IV)/Pu (total) of up to 0.9 in borosilicate glasses is a major issue with surrogate selection because of the different solubilities of tri and tetravalent species [51, 63], therefore although Ce is a very useful surrogate it is important to look at other surrogates especially regarding valency. Hf is a widely used surrogate for Pu (IV) in glassy wasteforms [51, 52, 55, 59, 60] this is important when regarding the redox potential of Ce and Pu as mentioned previously it is predicted under oxidising conditions that all the Ce will be Ce (III) but in the Pu system there may be some Pu (IV) present [51, 56, 57, 64].

Hf exhibits similar melting temperatures to PuO_2, has a similar electronic configuration to Pu (IV) and has a high density and thermal neutron cross Section which is useful for glass settling and neutron poison studies (Table 4.16) [51, 65]. Hf (IV) has been shown to have similar solubilities to Pu (IV) of approximately 0.1-0.5 mol% in borosilicate glass at 1100-1500°C with a slight increase in solubility with increasing temperature, this makes Hf good for analogous studies with Pu and confirms that actinides appear more soluble in trivalent than tetravalent oxidation state [51, 55, 59, 60, 66, 67]. In alumino silicates Hf solubility increases to 3-6.5 mol% at 1250-1400 ° supporting the small increase in solubility with temperature. Glass composition is shown to have major impact on the solubility of Hf^{4+} likely due to the presence of excess network modifiers in the glass matrix with an solubility increase linked to a shift to peralkaline compositions with increasing Na^+ (or equivalent) [60, 62, 68]. The reduced ionic radius of Hf (IV) make it unsuitable for ceramic studies of Pu (IV) [51].

For this study based upon the reasons above a series of Ce doped CAS glass and a series of Hf doped CAS glass were produced to investigate the effects of Pu incorporation on the glass structure. Ce has many properties that are like Pu but significantly has a different redox potential, therefore it is important to include Hf to investigate the incorporation of tetravalent species in the glass.

Metal from the drum and waste and the PVC from packaging form a major component of PCM waste. It is important to understand the metal waste loading in the glass because if the metal is not incorporated into the glass structure it will and has been shown in plasma trials form a separate phase that sinks to the base of the melt pool [42]. This causes a separate waste form that potentially provides a place for radionuclides to partition to and requires separate disposal. Even though studies have found that Pu portioning is minor [36, 37], it would be beneficial if the glass can incorporate larger volumes of the metallic elements as this would reduce metallic volumes increasing waste performance as there would be no mixed waste solubility issues and reducing costs as the metal would not require disposal at the LLW (if the radionuclide partition to the glass) or further treatment if contaminated. The metallic waste was a mix of metals with a ratio based upon the metallic composition of a typical PCM waste drum (Table 3.15) [36, 37] with the stainless steel supplying a mix of metallic elements (Table 3.16).

Table 3.15 PCM drum metallic composition.

Metal Component	Weight %
Stainless Steel	96.4995
Aluminium	1.0004
Copper	0.5002
Lead	1.9998

Table 3.16 Stainless steel composition.

Stainless Steel Components	Weight %
Fe	69
Cr	18
Ni	10
Mo	3

PCM waste is packaged waste PVC [38], low temperature pyrolysis of PVC can release large amount Cl and with no molten waste phase to incorporate then there could be a large release to the off-gas phase. This is problematic as the Cl can form several harmful and toxic gases, organic chemicals such as deoxins and furans are expected to be destroyed by the elevated temperature but metallic chlorides and toxic gases such as HCl and Cl_2 are highly corrosive to refractories and off gas equipment. The formation of oxychlorides is particularly concerning as these can incorporate and facilitate the release of actinides along with the "puffing" pressure releases from the system. HEPA filters can limit release of actinides to the environment to 99.97% (for Ce) with the risk for fine particulate ash and aerosol escape, although zero escape levels were reported in industrial trials, with this and the expense of HEPA filters, the optimisation and improvement of reduced release and volatilisation and increased waste incorporation is preferred [69]. It is important to understand how Cl is potentially incorporated into the glass because if the glass can incorporate more Cl, it will reduce the risk to operators and damage to off-gas systems and apparatus during glass melts. The PVC was sourced from Romar Innovate Limited and has the same composition to PVC used on actual PCM drums at Sellafield.

Table 3.17 Information on oxides, carbonates and metals used to make the CAS glass series.

Oxide/Metal	Purity (%)	Supplier
SiO_2	>99.5	Glasswork Services
$CaCO_3$	>99.3	Glasswork Services
$Al(OH)_3$	Reagent Grade	-
CeO_2	99.9	Acros Organics
HfO_2	99.9	Alfa Aesar
Pb Metal	99.8	Alfa Aesar
Cu Metal	99.5	Alfa Aesar
Al Metal	98	Alfa Aesar
Stainless Steel (AISI 316)	-	Goodfellow

Waste components were added to the base glass at 1, 5 and 10 wt.% (note - a. except HfO_2 which was added as the molar equivalent of CeO_2 and b. metal which was added as close to the wt.% as possible as the metal components allowed only specific additions) and the addition of ~0.207 wt.% for the PuO_2 surrogates. PuO_2 levels in PCM waste are very low (<0.1wt%) with a maximum of 230 g PuO_2 per PCM waste drum, 0.207 wt.% represents the CeO_2 molar equivalent for PuO_2 in an average PCM waste drum with a more representative figure of 50 g of PuO_2 in a 80 kg PCM waste drum, the molar equivalent of HfO_2 is slightly adjusted due to different molecular weights [34, 36, 37, 69].

The CAS glasses were produced from mixed oxides, carbonate, and metal precursors (Table 3.17). The oxides and carbonates were dried overnight at 120°C (CeO_2 and HfO_2 at 800°C) to remove any excess water and then the calculated amounts were weighed out to an accuracy of 0.0001g according to the waste loading, metal component and CAS composition above. Batch materials were homogenised, and size reduced using a planetary mill which aids the melting process and reduces the risk of un-melted precursor in the final glass. The precursor was mixed with IPA to form a slurry and milled in a small zirconia mill pot with zirconia mill media for 4 periods of 5 minutes at 400 rpm reversing the milling motion after each period. Milled precursors were dried overnight at 90 °C before being sieved to recover the sample and break up any agglomerations.

Because of processing issues milling the metal and PVC a slightly different approach was taken for the metal and PVC CAS glasses compared to the Ce and Hf melts. A master batch of base composition oxides was milled using the same conditions as the Ce and Hf glasses. Different amounts of the master batch and PVC/metal were weighed in alumina crucibles to account for the waste loadings described above and then hand mixed to ensure even distribution.

In all the melts the precursors were transferred to top-hat alumina crucibles and placed in an electric muffle furnace. This was ramped to 1430°C over a period of ~5hrs at 3°C per minute and then dwelled at 1430°C for 4hrs. 1430°C was chosen based upon the liquidus temperature of the glass with this composition [41]. Previous industry and lab trials [36, 37, 40, 41, 44, 69] have used a higher operating temperature of 1500-1600 °C to ensure that to ensure the metal (assuming all the metal is steel) in the PCM waste is molten aiding preferential mixing and incorporation in the slag phase [36, 37]. The discrepancy of melt temperatures between this study and previous studies is noted, however the focus in this project was on glass production and there could be operational benefits of lower melt temperatures [37]. Due to the viscosity of the glass no pouring or annealing was possible and the samples were air cooled in the crucibles before being destructively removed from the crucible prior to crushing/mounting. Increased viscosity is not necessarily an issue however as it appears future plans are not to pour PCM melts [69, 70].

The CAS 0 base glass was the closest to being poured and had some mobility out of the crucible suggesting that the addition of the various waste increases the viscosity of the CAS glass (Figure 3.7A). The CAS glass produced was clear in colour and no obvious crystalline material (Figure 3.7B). The Ce-series of CAS glasses were all clear with no evidence of crystalline material. They varied in colour with the increased amount of Ce causing the glass to go from a pale yellow to a dark brown (Figure 3.8). The Hf-series of glass were all clear with no evidence of crystalline material or colour (Figure 3.9). The metal series of glass produced a set of dark green-black coloured glasses with no obvious evidence of crystallisation (Figure 3.10). The PVC series of glass were all clear with no evidence of crystalline material or colour (Figure 3.11).

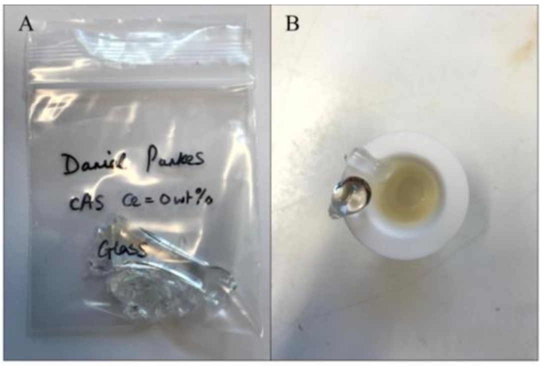

Figure 3.7A - Clear CAS0 glass B - Attempt to pour the CAS showed it had some mobility at elevated temperature.

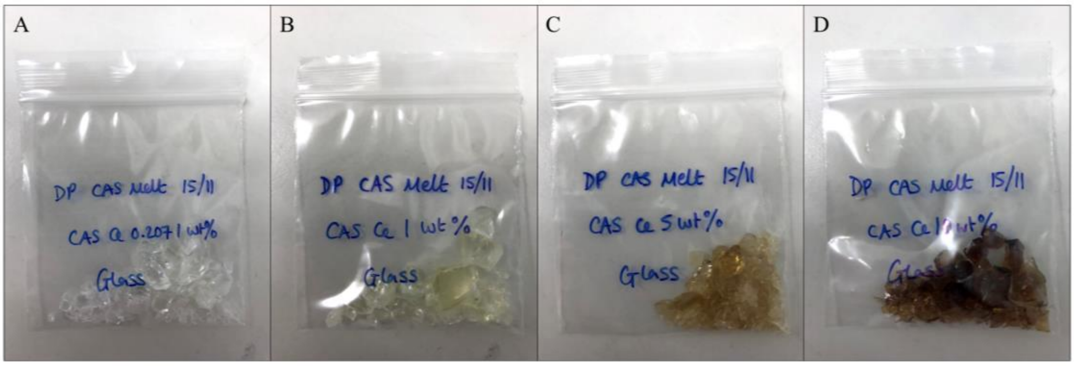

Figure 3.8 Ce - series of CAS glasses A – Ce0207 = CAS + 0.207 wt.% Ce B Ce1 = CAS + 1 wt.% Ce C Ce5 = CAS + 5 wt.% Ce D – Ce10 = CAS + 10 wt.% Ce.

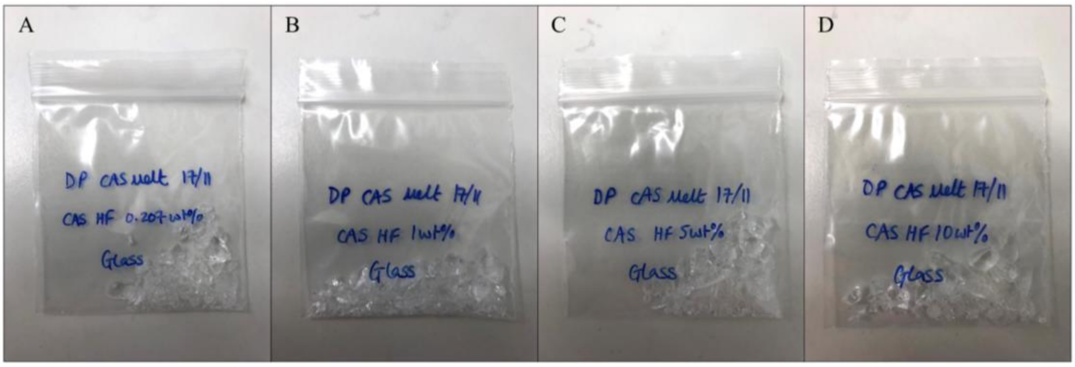

Figure 3.9 Hf - series of CAS glasses A – Hf0207 = CAS + 0.207 wt.% Hf B – Hf1 = CAS + 1 wt.% Hf C -Hf 5 = CAS + 5 wt.% Hf D – Hf10 = CAS + 10 wt.% Hf (note wt.% labelling is for reference only in the Hf series because Hf was added as the molar equivalent of Ce so the values will be slightly adjusted).

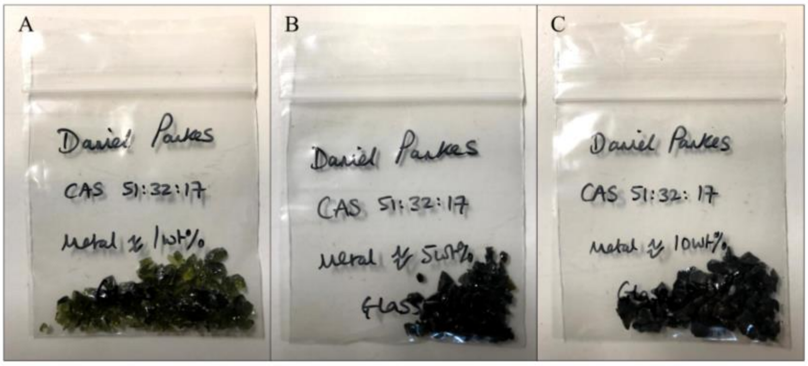

Figure 3.10 Metal(M) - series of CAS glasses A – M1 = CAS + 1 wt.% Metal B – M5 = CAS + 5wt.% Metal C – M10 = CAS + 10wt.% Metal (note wt.% labelling is for reference only as metal components only allowed specific additions so values will be slightly adjusted).

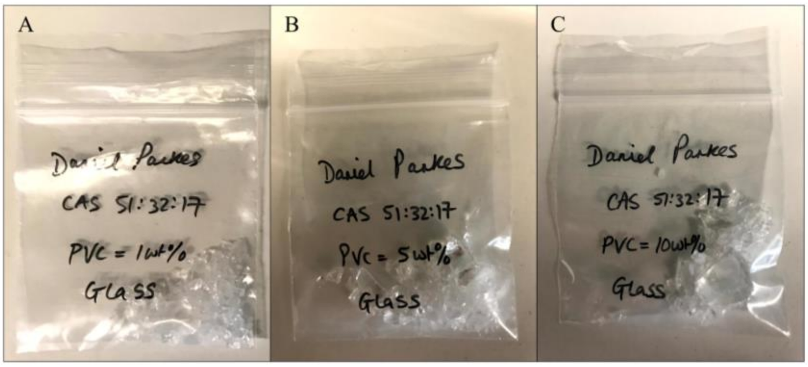

Figure 3.11 PVC - series of CAS glasses A -PVC1 = CAS + 1 wt.% PVC B – PVC5 = CAS + 5wt.% PVC C – PVC10 = CAS + 10wt.% PVC.

3.2 Materials Characterisation

3.2.1 Resin Mounting/Polishing and Glass Crushing

Prior to analysis both produced, and industry glass were processed to allow furthermore complex analysis. Glass pieces were mounted in epoxy resin and allowed to cure overnight. Excess resin was removed on a Buehler auto/ecomet grinder-polisher using SiC p800 and p1200 grit papers and the surface polished using 6, 3 and 1 µm oil based (to prevent any sample reaction with water) diamond paste to create an optical grade surface finish. Small pieces of glass were also crushed using a percussion mortar to size reduce the glass, crushed glass was progressively sieved and re-crushed to produce specific size fractions (75-150 µm and <75 µm) for dissolution and material characterization.

3.2.2 Glass composition

It is important to understand glass composition as it has important implications for waste retention and properties and effects further analytical techniques. Glass was analysed via acid-digest in hydrofluoric acid and then calculated using ICP-OES (Section 3.2.11). Glass samples were heated in a mix of hydrochloric, nitric, and hydrofluoric acid before being diluted and measured using a Ciros Vision ICP-OES and/or Agilent 7500ce ICP-MS. This was carried out for the bulk Tetronics samples in the chemistry department at the University of Sheffield. Unfortunately, the opportunity to get glass analysis via this route stopped as an option halfway through the project due staff retirement, therefore subsequent analysis of glass composition was carried out via Laser Ablation ICP-MS two technique comparison? at the British Geological Survey. Laser ablation uses a laser to remove material from the surface of the sample creating a plume of particles and ions. The process of laser ablation includes heating, evaporation, and ionisation of the surface material. The material is carried to the ICP-MS in a constant stream of argon gas and then analysed (Section 3.2.2) [71]. Laser ablation was carried out on samples that had been resin mounted and polished to 1 μm creating a flat even surface for analysis. Laser ablation was carried out using an elemental scientific imageGEO193 with a 193 nm excimer laser run at 1 to 500 Hz with a argon gas fluence of 0 to 15 j/cm^2. The laser creates craters square or circular craters (Figure 3.12) of between 1-150 micron which allows for fine point analysis and broader sample mapping, for each sample several points (5-15) were analysed and averaged to account for sample heterogeneity. Analysis was done using an Agilent Technologies 8900 series ICP-MS which allows up to 50 elements to measure to ppb levels with a multielement standard used for calibration and quality control.

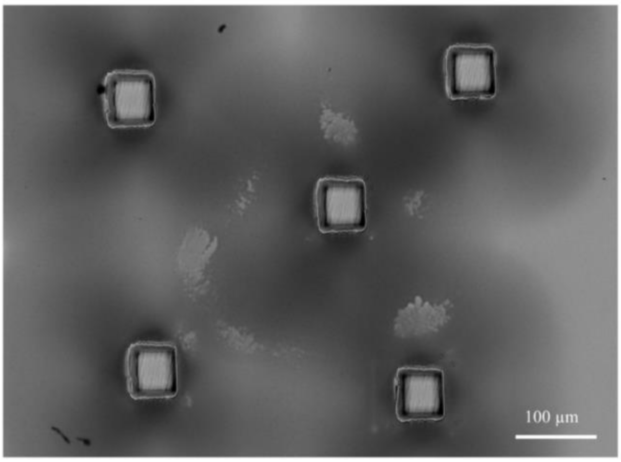

Figure 3.12 SEM image showing the laser ablation sites from analysis of a glass sample. Composition was calculated as an average of the different sites to account for special heterogeneity.

3.2.3 Pycnometery

Pycnometery measures the density of the samples, although of general interest this is most important for use in later dissolution and EXAF's calculations. A constant volume gas pycnometer has 2 known volume chambers one sealed and one containing the sample. To measure density the pressure difference is measured between the two chambers assuming ideal gas behaviour, measured chamber and tank volumes, rigid working parts and static gas equilibrium and used to calculate sample volume. The volume is then used to calculate density from a known sample mass (Figure 3.13) [72]. The density of the glass was measured using the <75 micron glass powder using a Accu PyC II 1345 pycnometer over 10 cycles and with a fill pressure of 19.5 psi.

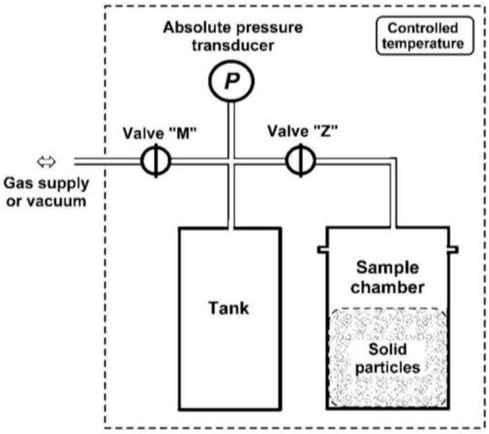

Figure 3.13 Constant-volume pycnometer [72]

3.2.4 Thermal Analysis

Simultaneous Thermal Analysis (STA) combines the measurement of Differential Scanning Calorimetry (DSC) [73] and the Thermogravimetric Analysis (TGA) [74] of a sample during constant or variable heating. TGA measures the changing mass of the sample during heating and allows observation of heat induced chemical reactions e.g., volatilisation. DSC measures the differential heat flow applied to the sample and a reference material to maintain a constant temperature difference during heating. Modulated DSC applies a sinusoidal heating profile allowing more complicated thermal analysis. DSC allows exothermic e.g. crystallisation and endothermic e.g. melting or glass transitions to be observed in the heating profile.

Measurements were made using a TA Instruments Discovery DSC/TGA: SDT 650 using a heating rate of 10 °C per minute from 0-1000 °C under an air atmosphere.

3.2.5 X-ray Diffraction (XRD)

Some of the waste products there purely glassy and others had crystalline phases present. XRD confirms the presence or absence of crystalline phases in support of other techniques such as SEM (Section 3.2.6) and allows for their phase identification and quantitative phase analysis.

XRD uses_X-rays which are a form of electromagnetic radiation that have a frequency of 10^{16}-10^{18} Hz and a corresponding frequency of 10^{-10} cm. In the Bruker D2 a CU source produces K_α monochromatic X-rays with a wavelength of 1.5418 A. Bragg diffraction is a phenomenon that occurs when the incident X-rays reflect off the crystal lattice at a specific angle. This diffraction is defined by the Bragg equation (Equation 3.4) and leads to constructive interface of scattered X-rays as they reflect in phase. X rays that interact the surface at an incident angle of (theta) will either be reflected or partially transmitted depending on the parameters in the Bragg equation (Equation 3.4 and Figure 3.14). Two incident X-rays interact with a sample and scatter off different atoms with in it. The extra length travelled by the lower x-ray is equal to $2dsin\theta$. Constructive interference of the two X-rays occurs when the extra distance is equal to an integer multiple of the x-ray wavelength [75, 76]. In the Bruker D2 the x-ray source remains fixed, but the sample and the detector are rotated in a Bragg-Brentano parafocussing circle geometry. This scans through a series of θ angles with the detector recording the x-ray intensity at each angle creating an x-ray diffraction pattern with defined peaks where the Bragg equation is satisfied, and constructive interface occurs. Peak width, height and position in the diffraction pattern is caused by variations in the microstructural characteristics of the samples. Crystallite size and defects can enhance peak broadening, peak position is largely defined by unit cell parameters as this controls the d spacing and is commonly used to diagnostically identify phases in the sample., while peak height can match phase abundance although caution is required as this can be affected by others factors and requires more thorough analytical analysis. In glass the lack of long-range order means there are no defined peaks instead the signal produced is a large region of diffuse scattering [76]. In samples containing crystallites phase identification was completed by comparison of peak position and intensity to known standards in the COS (Crystallographic Open Database) [77] and/or PDF-4+ (Powder Diffraction File) database [78].

$n\lambda = 2dsin\theta$ Equation 3.1

n is the diffraction order (1-3), λ is the wavelength of the incident X-rays and θ is the glancing angle of the x-ray off the lattice plane [75, 76].

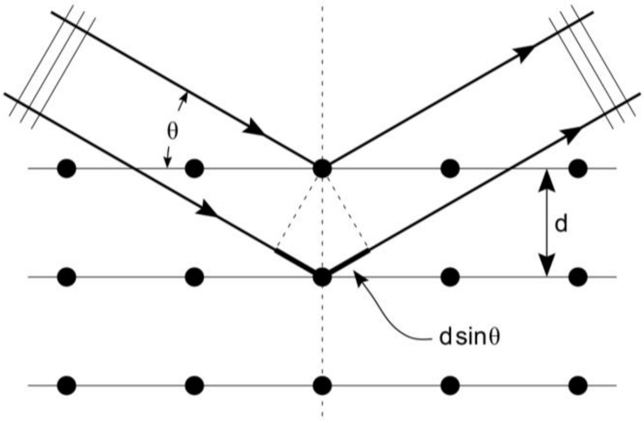

Figure 3.14 Bragg Diffraction diagram [75].

Sample analysis was carried out on powdered samples (<75 µm) which were well mixed and mounted in a zero – background PMMA holder, to ensure a flat surface the sample was pressed down using a glass slide to counteract effects from preferred orientation and surface roughness. Analysis was carried out on a Bruker D2 Phaser machine in a Bragg-Brentano Geometry with a Cu K-alpha source (λ = 1.5418), a 10mA current and 30kV accelerating voltage. A Ni foil removes Kβ-beta incident X-rays and diffracted X-rays are collected using a Lynxeye position sensitive detector. Data was collected between 5 and 80 degrees with a step size of 0.02 and a count time of ~2s per step with 10 degrees of rotation. Fluorescence settings were used in iron containing samples to reduce the elevated signal from fluorescence.

3.2.6 Scanning Electron Microscopy (SEM)

SEM can be used in unison with other techniques such as XRD (Section 3.2.5) to investigate the composition and structure of a sample, it allows for very high-resolution imaging and chemical analysis using (EDS(X)).

In the SEM the electron beam is produced by-passing an electrical current through a tungsten filament. Electrons from the filament are accelerated down the SEM column under vacuum and a series of magnetic lenses focuses the electrons into a thin beam that can be used for analysis, it is important to adjust the voltage and current of the beam to optimise for the required analysis. When the electron beam interacts with the sample several different signals (Figure 3.15) are produced including secondary electrons, backscattered electrons, and X-rays. Secondary (SE) and backscattered (BSE) electrons are used for imaging samples. SE electrons can provide detailed surface information and result from inelastic scattering of the incident electron whereas BSE come from elastic scattering deeper in the sample and can be informative of elemental composition. Inelastic scattering of the incident electron also produces X-rays that can be used for compositional analysis of the sample in EDS(X) – Energy Dispersive Spectroscopy. EDS can routinely measure elements where Z>11 but cannot detect lighter elements (H, He and Li) and most detectors cannot detect Z=4-11 which are often calculated by stoichiometry. EDS can provide semi-qualitative elemental analysis of phases and if the correct stable conditions and standards are used this can be improved to quantitative analysis. Individual spectra can be combined to create a compositional map of a region where each pixel represents an induvial spectrum, this can be useful in looking at compositional zoning in a sample [79].

Resin mounted samples that were polished to a 1-micron finish were prepared for SEM. To create a conductive path and reduce charging on the surface during analysis the samples were coated in a thin layer of carbon using an Agar Auto Carbon Coater and then a conductive path created using Ag DAG or Cu tape.

SEM analysis was carried out using a Hitachi TM3030 with a 15 Kv accelerating voltage and a working distance of 8mm. For EDS analysis the SEM is fit with a Bruker Quantax Energy Dispersive X-ray spectrometer (EDS) with post analysis completed in the Bruker Quantax 70 software.

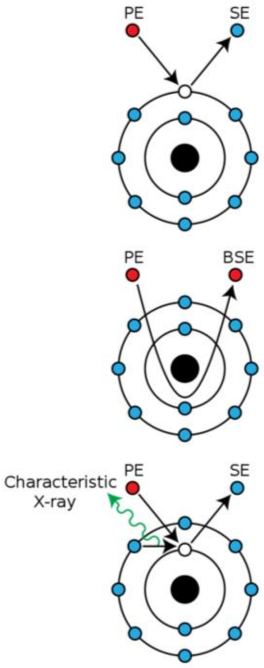

Figure 3.15 Generation of different signals from SEM analysis [80].

3.2.7 Solid State Nuclear Magnetic Resonance (NMR) Spectroscopy

NMR spectroscopy can provide detailed information on the structure of the glass network specifically in this project the coordination and neighbour species of Si and Al.

The details of the science behind the collection of NMR spectroscopy are a very complicated field beyond the scope of this project but in summary is based on nuclear spin and charge creating a magnetic moment in a nucleus. Placed in an external magnetic field (B_0) the magnetic moments become aligned and exists in a specific number of environments (spin states) defined by 2I (spin) +1, each state has a specific energy with the energy gap between the states defined by the Zeeman splitting specific to each different nucleus. The energy gap (absorbance frequency) is proportional to the effective external magnetic field (B_{eff}) that is equal to the induced external magnetic field (B_0) minus any magnetic effects created by the electron density distribution that surrounds the nuclei. Application of a radio pulse at the required radio frequency to match the energy gap promotes nuclei from the lower to the upper energy magnetic state and the individual magnetic nuclei can be resonant in a coherent procession producing shifts in magnetic planes and a detectible electronic signal that can be Fourier Transformed into a frequency signal. Parameters of the signal include the chemical shift that shows the frequency of absorption, peak intensity that shows the proportion of spin environments, line shape that shows population inhomogeneity and finally spin-spin splitting that provides information on neighbouring nuclei. In this project the chemical shift and peak intensity of the different structural components that collectively make up the NMR signal is important. Change in peak intensity are simply proportional to the amount of different individual environments, whereas changes in the chemical shift are caused by changes to the energy gap caused by shifts in electron density around a nucleus affecting B_{eff}. Different nuclear environments can shield or deshield the nuclei creating up/high (reduce ppm) and down/low (increase ppm) shift patterns in the NMR spectrum chemical shift. The chemical shift is normalised on a ppm scale to account for variations in spectrometer frequency and is recorded as the difference to a known standard [81-83].

Peak locations and intensity NMR shifts in ^{29}Si and ^{27}Al NMR have been correlated with a change in the co-ordination or nearest neighbour to the targeted nucleus and are diagnostic of the different Si and Al structural environments in the glass [84-100].

For ^{29}Si NMR co-ordination can have a major effect on the chemical shift with an up field associated with increasing co-ordination, however in silicate based glasses Si is only found in Si[4] so higher co-ordination is not further considered [97]. Major changes in Si chemical shift in aluminosilicates can be attributed to 2 effects, changes in tetrahedral silica with variation in the number and type of non-bridging oxygens creating various Q-species (Section 2.1.7) and the replacement of neighbouring Si with Al. Condensation of the silica tetrahedron by relacing bridging oxygen with non-bridging oxygens (NBO's) (Q_4 is Si with four bridging oxygens, reducing in number with the addition of each NBO to Q_0 that is Si with four NBO's) causes a low field shift as the silica go from Q_4 to Q_0 with Q_4 -100ppm to Q_0 -65 to -70ppm as glass is depolymerised with a shift of ~10ppm per additional NBO with greater shifts with more electronegative modifiers due to greater reduction in the covalency of the bonds [94, 96]. Superimposed on this chemical shift is that the addition of Al (Si(0Al) is defined a Si nucleus bonded with oxygens to four other Si nuclei with each additional Al increasing the number in brackets up to Si(4Al) which is a Si nucleus bonded with oxygens to four other Al nuclei) shields the nucleus and there is a low field shift of ~5ppm from Si(0Al) is -107.4 to -115 ppm to Si(4Al) is -85 to 83 when in Q^4 coordination. Issue with the deconvolution of these two effects is due to geometry of the tetrahedral lattice and cation effects cause the two effects do overlap one another. The trends above are described based on structural lattice effects including the strong correlation with bond angle and a weaker correlation with bond length and structural effects including distortion to SiO_4 interconnected tetrahedra effecting the electron density symmetry around the nucleus causing a low field shift. Other effects such as changes in tetrahedral ring order and ring buckling would also have associated changes in bond angle and length that could cause changes in the ^{29}Si NMR .When structural effects are not influencing the shift then chemical shifts correlate with changes in the mean covalency of the bond effected by the electronegativity of the cation can cause a high field shift in the order of increasing covalency from Si-O….M^+ to Si-O-Al to Si-O-Si, although it is that seen shifts between different M^+ cations is not significant (2-3ppm) [90, 92-96, 99, 100]. As for ^{29}Si NMR co-ordination has a major effect on the chemical shift of ^{27}Al NMR (Al[n] is a co-ordination notation where n is the number of surrounding nuceli) for a drop in 1 Al co-ordination there is a high field shift in the chemical shift value of ~20-30ppm with Al[4] at 60ppm, Al[5] at 40ppm and Al[6] at 10ppm. All of these species have been proven to be present in CAS glass of varying composition with Al [4] a network former and Al[5] and Al[6] network modifiers and charge compensators potentially forming structures like triclusters. As for ^{29}Si NMR the chemical shift in ^{27}Al NMR there is a similar shift in relation to Q species in Al [4] from about 62 to 85 ppm but it is difficult to separate the individual species due to the range of overlap and this is also the case for the Al(mSi) substitution which would require isotropic Al NMR. The patterns can be described again by correlation with mean bond angles in Si-O-Si(Al) and mean covalency of bonds with the associated change in shielding environment although chemical shift values are not available [84-89, 91, 97, 99]. It can be understood that the deconvolution of aluminosilicate NMR is a complex nature with many factors contributing to the nuclei environment and individual trends need to be deconvolved individually using some of the factors above.

NMR spectroscopy for this project was undertaken at the UK High-Field Solid-State NMR Facility at Warwick University under there the Warwick Analytical Science Centre (WASC) Seedcorn funding (EP/V007688/1). ^{29}Si and ^{27}Al NMR was collected under Magic Angle Spinning on the Bruker Neo Avance 500 MHz using a 4 mm ZrO_2 MAS HXY probe and two pairs of DuPont Vespel caps. Spectrum were collected at a spectral range of 50 KHz and a small pulse angle to allow quantitative interpretation. The principal field was defined by a frequency of 500 MHz, a magnetic field strength of 11.74 T with at spinning rotation rate of 12.5 KHz. Spectrum were calibrated against Kaolinite as the Si standard at -92 ppm and $AlNO_3$ as the Al standard at 0ppm.

NMR was carried out for the non-metal bearing CAS glass series, spectra were calibrated and exported using the Bruker Topspin software. The exported spectrum was deconvolved using either adapted Rampy code python developed at the University of Paris by Charles Le Losq [101] for ^{29}Si or the Dmfit programme developed at (CEMhti) Conitions Extreme et Materiaux: Haute Temperature et Irrasiation, Orleans by Dominique Massiot for ^{27}Al [102]. For ^{29}Si the least squared fitting method. Spectral deconvolution was achieved using several Gaussian peaks (^{29}Si – 2-3 centred at -55, -93 and -105 ppm in a fit range of -20 and -180 ppm and ^{27}Al – 3 - 4 at 10, 40, 60 and 80 ppm in a fit range of -75 to 175 ppm).

For ^{29}Si spectra the least squared fitting method was used with spectral deconvolution achieved using several Gaussian peaks (^{29}Si – 2-3 centred at -55, -93 and -105 ppm in a fit range of -20 and -180 ppm. In Dmfit the ^{27}Al spectra were fit using the CZSimple model as ^{27}Al is a quadrupole nucleus as it has a spin of 5/2 therefore has a lower level of symmetry in the nuclei and the distribution cannot be described by simple Gaussian distributions. The CZSimple model is based on the Czjzek distribution of quadrupolar interaction used to initially model Mossbauer spectra [85, 103, 104] that has been adapted to NMR fitting [85, 102, 105, 106]. The model used centres in the region at 10, 40, 60 and 80 ppm in a fit range of -311 to 311 ppm or -187 to 195 ppm depending on experimental run with a fixed em of -150 and d=5.

3.2.8 Mossbauer Spectroscopy

The Mössbauer effect is the recoil-free emission and resonant absorption of gamma rays by specific atomic nuclei. Mossbauer spectroscopy uses this effect to investigate the nuclear structure of specific elements, most commonly iron (Fe^{57}), with thermal broadening or the doppler effect used to overcome nuclear recoil. The velocity required to get complete overlap and peak absorption is called the isomer shift (IS) mm/s. Fe foil is used as a reference as it has an IS of 0 as the transition energy in the source and absorber and it ensures that all velocities are sitting on the same absolute energy scale. Variations in the Fe environment including changes to the co-ordination number and oxidation state will create variation to the transition energy causing changes to the isomer shift value and splitting (quadrupole and hyperfine) of the spectrum into different peaks (Figure 3.16) [107, 108]. Specifically changes in the isomer shift value are a result of a shift of the nuclear energy levels due to interactions between the positive nucleus and a variable surrounding electronic field interactions caused by the addition of ligands (O, S etc) around the nucleus. For Fe an increase in oxidation state from 2+ to 6+ relates to a decrease in 3d electrons reducing shielding so increasing contact density and reducing isomer shift. Changing the co-ordination number and ligand type can also affect the contact density increasing electronegativity or ligand amount will reduce contact density so increase isomer shift. Quadrupole Splitting (QS) is the splitting of the Mossbauer signal into several peaks. An asymmetric local electric field gradient (EFG) created due to lattice effects (asymmetric electronic charge and/or ligand distribution) interacting with the non-spherical nuclear charge distribution exhibits torque on the nucleus, causing the degenerate nuclear energy levels to split. The degree of asymmetry in the EFG effects the size of the quadrupole splitting, generally, an increase in the asymmetry of the EFG causes an increase in the QS with the EFG symmetry sensitive to both oxidation state and site geometry including co-ordination and site distortion. QS is higher for more distorted coordination polyhedra, Fe^{2+} over Fe^{3+} octahedra over tetrahedra. [107, 108].

Mossbauer spectroscopy was carried out on a Wissel Spectrometer using <75 µm powder at room temperature. The spectrometer was set in transmission mode and used a 50 mCi ^{57}Co source embedded in a Rh matrix. An α - Fe foil was used for calibration and a constant acceleration waveform of velocity range +/- 10 mms^{-1} was used to collect the spectrum. Due to the complex nature of the samples, there is often more than one Fe site contributing to the spectrum. The recoil software was used to deconvolve the spectrum using mixed Gaussian-Lorentzian doublets to fit the data. Due to the dependence of the IS and QS on oxidation and co-ordination environment of each Fe site in the sample then QS vs IS plots can be compared to previous samples and standards to compare and determine the elemental environment in the sample (Figure 3.17) [107].

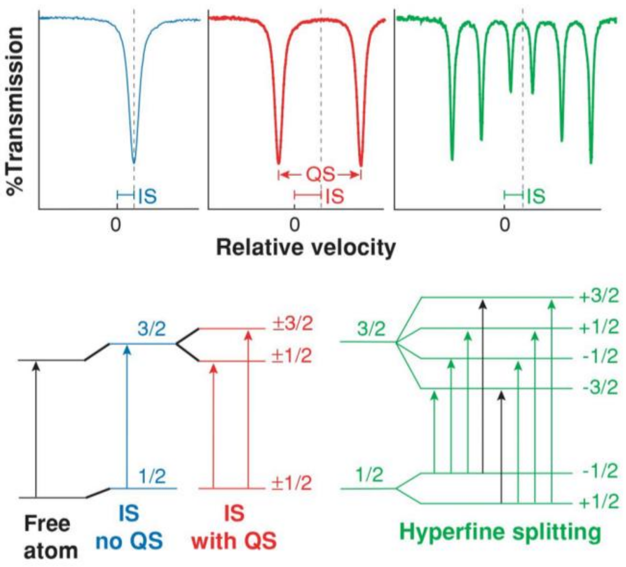

Figure 3.16 Variation in the transition energy created by a change in energy (Isomer Shift) or splitting (quadrupole and hyperfine) of the nuclear energy levels. Figure taken from [107].

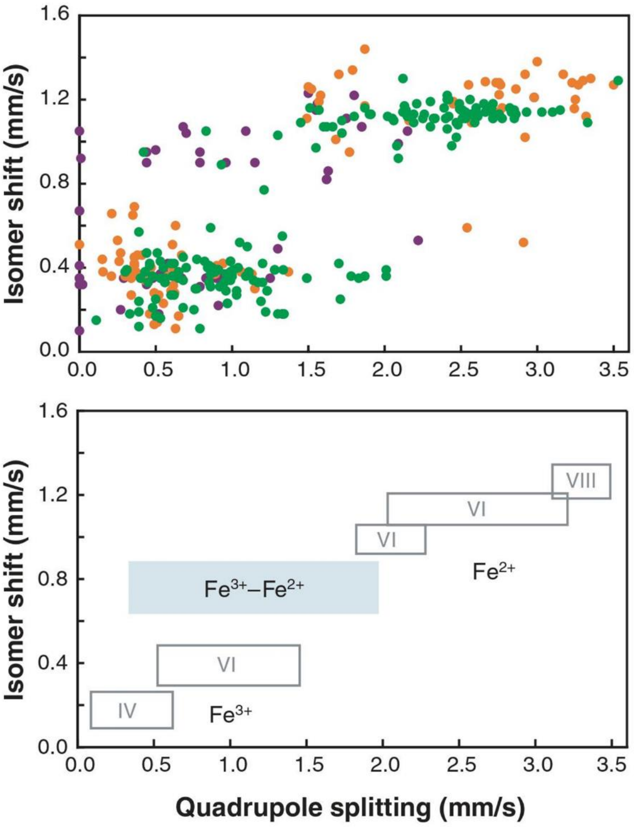

Figure 3.17 Plot of Isomer Shift (IS) vs Quadrupole Splitting (QS) for a range of Iron (Fe) standards. Position of the sample in IS vs QS space is informative of nuclear environment due to reasons discussed in the text with an intermediate $Fe^{2.5+}$ ‘blue region’ with intermediate IS values created by a delocalisation of electrons around adjacent Fe^{3+} and Fe^{2+} sites. The range in QS for specific co-ordination is created by variation in local site distortion. Figure taken from [107].

3.2.9 Raman Spectroscopy

Raman Spectroscopy measures the molecular interaction between an incident beam of light and the chemical bonds in a material and in general gives a measure of bond vibration frequencies. It can provide detailed information about the chemical structure, crystallinity, and degree of polymerisation within a sample as well as on any molecular interactions. When a laser (light source) interacts with a sample the photons are either absorbed, scattered, or transmitted through the sample. Scattered protons interact with either the electron cloud (Rayleigh) or the nucleus (Stokes and anti-Stokes) promoting the molecule to unstable virtual states and transferring energy between the photon and molecule, the virtual decay quickly decays to a new state with either the gain (Stokes), minor change (Rayleigh) or loss (anti-stokes) of energy. Raman spectroscopy detects the energy changes of incident protons and plots this as frequency vs intensity of the amount of scattering [109].

Bond vibrational states that promote a change in the electron cloud polarizability of the molecule promote Raman scattering, these are caused by symmetric vibrational modes. For basic models the vibrational energy for Raman scattering can be predicted using Hooks law, however for more complex systems the best effort can be made to attribute common bands to spectra however sometimes molecular groups have to be applied because a few close vibrational bonds can combine in the spectra to form peaks. Like most optical techniques interpretation for specific peaks is best done by using standard reference material and spectra [109, 110].

Raman Spectroscopy was performed on a Renishaw Invia Raman Spectrometer using a CCD detector and a green line (514.5 nm) laser at a power of 20 mW and a x50 objective lense. Spectra were collected from 20 up to 1900 (variable) cm^{-1} with 10 accumulations per sample each having a 10 s exposure time.

Raman Spectroscopy was carried out on all the samples including the USA Geomelt glasses and the CAS series. Spectra were collected using the Renishaw WiRE software and raw files were exported for further analysis. The spectra were further processed and analysed using adapted Rampy python code developed at the University of Paris by Charles Le Losq [101], background removal was performed using a third order polynomial and deconvolved using the least squared fitting method (Figure 3.18).

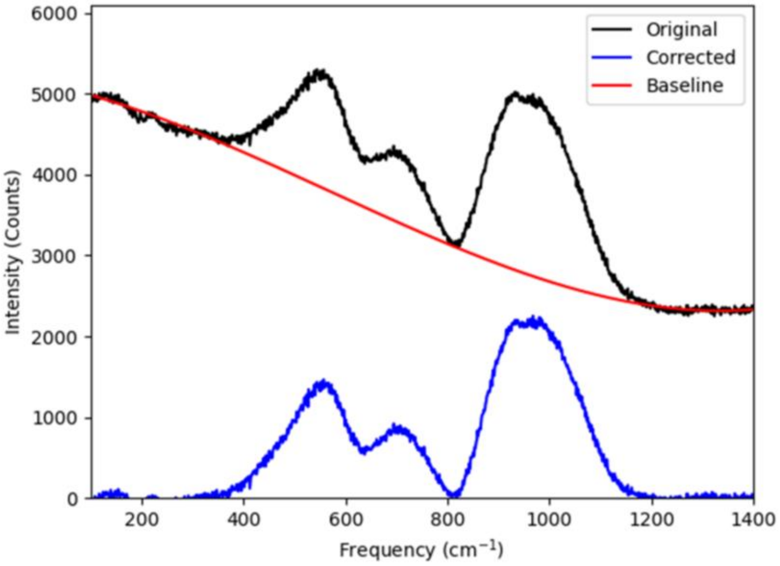

Figure 3.18 Example of background removal of CAS M10 Raman Spectra using the Rampy python code.

Spectral deconvolution was achieved using several Gaussian peaks dependant on the sample. CAS and Tetronics glasses are similar so can be fitted using Gaussians centred at 350, 500, 700, 900 and 1000. The shape of all the USA glasses is very different due to their diverse chemistry therefore require different Gaussian positions. KBasin was fitted with Gaussians centred at 300, 500, 600, 700, 800, 1000, 1200; DBVS at 300, 500, 650, 700, 1000, 1100 and 1400; MRI7 at 300, 400, 500, 850, 1050 and 1400.

For analysis and interpretation of what the different Gaussians may mean the best initial reference glass is pure SiO_2 as the SiO_2 framework forms the major structure in all the glasses in this project with the addition of network modifiers (Ca, Na etc), Al, B and Fe complicating the spectra by altering existing peaks associated with SiO_2 and adding new peaks. In pure SiO_2 and glasses that have additional components the Stokes side of the Raman spectra that be divided into four major regions that lie between 0 and approximately 1400 cm^{-1}. Peaks and features in this region have been attributed to several different vibrational modes that are outlined and referenced in (Table 3.18).

Table 3.18 Attribution of features in the Raman spectroscopy of silicate glasses with additional modification from the addition of network modifiers, Al, Ti, Fe and B.

Region	Attributions	Reference
20-250 cm^{-1} Boson Region	Explanations for this peak have included long range interactions in the glass including the medium range order with vibrations due to rotational motions in rigid silica tetrahedral units with an increase in intensity and frequency with increased distortion. Distortion in silica tetrahedra can be affected by network depolymerisation with possible modification ordering, nature of network modifier and Al-Si substitution.	[97, 111-114]

250-700 cm^{-1} Lower Frequency Region	This region relates to the medium range order in glass. In silicates the reason for peaks and changes are associated to stretching, bending, breathing, and rocking vibrations of Si-O$_{bridging}$-Si (Si-O^{o}) T-O bonds in 3-6 (or higher) membered rings where T is Si but can be Al or Fe with substitution effecting the frequency due to the weaker bond and altered bond angles created with reduced force constant. Early studies found that pure Silica Raman features could be attributed to exclusively stretching motion in 2 six-membered ring structures (one with pucking) with variable bond angles (120° and 160°) and the associated A1-2 and W1-4 vibrational modes. This is supported by recent studies that attribute motion at ~440 cm^{-1} to oxygen motion in 5-6 membered rings with oxygen in Si-O with potentially asymmetric vibrations although the exact nature of the motion is a little ambiguous. This could describe the bonds at ~440 cm^{-1} and higher frequency seen in pure silica, however there are 2 features that require further structural modification, features at ~500 cm^{-1} and ~600 cm^{-1} in pure silica that relate to 'defect' bands D1 and D2 respectively. D1 and D2 relate to additional ring structures in the silicates. D1 is related to the breathing motion (Si-O-Si A1 symmetric stretching) of oxygen in slightly puckered 4 membered rings at a small fraction of about 1%, a long tail (~280-400 cm^{-1}) relates to stretching in 5, 6 or higher membered rings. D2 relates to oxygen breathing in 3 membered rings in SiO$_2$. The R band at ~455cm^{-1} that relates to vibration in 5 but predominantly 6-membered rings. With the addition of network modifiers such as Na and Ca in these peaks evolve into a broader peak centred at ~580 cm^{-1} with reduced intensity as depolymerisation increases and often several minor peaks which is well illustrated in studies of natural samples evolving from ryolite (Si-Rich) to basalt (Si-Poor). The peak at ~580 cm^{-1} relates to Si-O^{o} rocking in fully polymerised Q4 units and a shoulder peak at ~600 cm^{-1} relates to the Si-O-Si bending in depolymerised structural units as does a lower peak at 350 cm^{-1}. In this region ~530-540 cm^{-1} is breathing in T-O-T Q$_3$ units and 635 cm^{-1} is deformation of Q2 units. There is some variability in these values in the literature based upon interpretation and glass composition. Increasing electronegativity value of the modifier and the substitution of Si for Al in aluminosilicates can reduce the values quoted for pure silica above as these will have a lower force constant and reducing bond strength and bond angle. Early studies attributed additional peaks in charge compensated aluminosilicates to the presence of additional interconnected 3D Al$_2$Si$_2$O$_8^{2-}$ and Al$_2$O$_4^{2-}$. The addition of Al to silicate rings is acknowledged as altering the Si peaks mentioned above, but the presence of pure Al-O-Al bonds is more controversial except in the highest abundance Al glasses due to known factors as aluminium avoidance, although other techniques (NMR) have found evidence for structures such as Al triclusters. In Al rich units	[89, 97, 98, 111-136]

	peaks at 550-560 cm^{-1} is attributed to stretching in Al-O-Al bonds. In specific calcium rich glasses then peaks at 340-400 cm^{-1} have been attributed to Ca-O motion with increased frequency with depolymerisation as the Ca site collapses. The addition of boron can further confuse the Raman signal in borosilicates as the borate vibrations are superimposed on the Silicate structure with large levels of overlap especially with the addition of other elements like Al and Fe which add further peaks and cause frequency shifts. Borate peaks that maybe visible in the lower frequency region include symmetric ring breathing vibrations of borate groups including 465-500 cm^{-1} isolated biborate, 535 cm^{-1} diborate, 670 is tetraborate, 600-650 metaborate, 650-660 is penaborate. 630 danburite and 586 is reedmergnerite. (B,Si)-O-B bending and rocking is at ~520 and ~447 respectively with motion in BO$_4$ units at 450-550. 630 can attributed to motion of BO$_4$ bonded in silicate units.	
700-870 cm^{-1} Intermediate Frequency Region	This is a poorly understood region however there has been attempting to identify the peaks in different glass again as above there is some discrepancy of exact values between publications so estimates are quoted. In line with the explanation above the frequency in silica Raman can be attributed to Si-O$_{\text{bridging}}$-Si (Si-O^{o}) stretching motion in two ring structures with variable bond angles and substitution by Al and Fe for Si effecting the frequency due to reduced force constant. Commonly the specific motion at 800 can be attributed to the stretching motion in the Si-O-Si plane or of the Si in its rigid cage which reduces in frequency and broadens with reduced silica. In Al rich glasses and aluminates then can have Al-O^{o} stretching in variable tetrahedral units of AlO$_4$ with variable NBO oxygens attached in Q(Al) units with peaks at 794 cm^{-1} Al Q_4, 780 cm^{-1} Al Q_3, 775 cm^{-1} Al Q_2 and 765 cm^{-1} Al Q_1 with values shifted due increasing force constant when Si replaces Al and electronegativity effects caused by modifier type with high values at 780-850 cm^{-1} related to Al-O stretching in a rigid cage. In calcium (alkali) aluminosilicate glass there is no evidence of these higher aluminate frequencies. The addition of boron can cause a range of new peaks in this region symmetric breathing in boroxal rings with 3 BO$_3$ triangle is at 800-808, symmetric breathing in six membered rings with a single BO$_4^-$ tetrahedra is at 700-735 cm^{-1}, 835-840 cm^{-1} is pyroborate vibration, 740-775 cm^{-1} motion in metaborate chains, 770 cm^{-1} is 4 co-ordinated diborate or symmetric breathing of BO$_4$ tetrahedra in 6 membered rings and finally 760 cm^{-1} is specifically relating to [3]B-O-[4]B bending bridges. Finally, the addition of Ti can cause peaks at Ti-O-Si and Ti-O-Ti at 840 cm^{-1} and 726 cm^{-1} respectively.	[84, 85, 89, 97, 111, 112, 114, 115, 118-121, 124, 126-130, 132, 135]

870-1200 cm^{-1} Higher Frequency Region	In silicates and charge compensated alkali aluminosilicate the two-ring model described in previous regions can describe this upper region with two structures with variable bond angles and changes in frequency relating to Al substitution. This region is represented by a single peak but spectral deconvolution into various Gaussians breaks it down into induvial contributions. In silicates peaks at 1050 and 1170 relate to Si-O^{o} stretching in fully polymerised Q4 structural units with 1050 Q_4, II and 1170 Q_4, I relating to T_2 and Al motion. With the addition of extra modifiers the glass network starts to break down and numerous additional peaks/gaussians associated with the (Si,Al)-O bond stretching in different Q^n tetrahedral units. A1 Si-O$^-$ stretching in Q_0, Q_1, Q_2 and Q_3 units causes peaks at 850, 900, 950 and 1100 respectively. Substitution of Al for Si and increased modifier electronegativity will shift the values of these peaks to lower frequency due to weaking of the bonds created by a reduced force constant and a reduction in covalency. Addition of Boron as in lower frequency regions creates additional bands in Borosilicate glass the region is attributed to B-O bond stretch in BO_4 units including orthoborate at 875-1000 cm^{-1} tetraborate at 1050 cm^{-}1 and 885 cm^{-1}, pyroborate at 900 cm^{-1} and diborate at 1000 cm^{-1}. Boron can also act like Al and alter the Si Q species with Q_4(B) attributed to 970 cm^{-1} and Q_4(B) attributed to 1150 cm^{-1}. In Fe rich glass there is Fe^{3+-}O stretching band at 930-990 which increases with levels of Fe$^{3+.}$	[84, 89, 95, 97, 111-120, 123, 124, 126-130, 132-135, 137, 138]
1200 -1600 (Extra) High Frequency Region – Borate	This region relates to the symmetric stretching of different B-O bonds in BO_3 and chain type metaborate molecular groups where BO_3 units interconnect. This can be represented as a single peak in the 1200-1600 cm^{-1} region that can be deconvolved using gaussians. Peaks (gaussians) in this region have been attributed at 1216 -1260 cm^{-1} to stretching in pyroborate groups, at 1510-1570 cm^{-1} to B-O stretching with a single NBO in [BO_3] triangles and molecular O stretching, B-O$^-$ stretching in chain type metaborate molecular units, at 1490 cm^{-1} to BØ$_2$O$^-$ triangles linked to BO_3 units, at 1385-1397 cm^{-1} to B-O$^-$ triangle stretching vibrations in BO_4 units from different borate groups and at 1400 cm^{-1} to BØ$_2$O$^-$ triangles linked to BØ$_4^-$ units, at 1400 cm^{-1} to ring stretching and at 1250 cm^{-1} to stretching of B-O bons involving oxygens that connect different groups.	[112, 128, 130, 135]

For some glasses including the geomelt glass in Chapter 4 basic devolution is too difficult due to complex composition creating a complicated Raman signal that is an average of the multitude of signals from the glass. In this instance and average Raman Polymerisation Index [90, 139] can be used to interpret the glass structure. The Raman polymerisation index takes a more general approach to connectivity and looks to compare the integrated intensity of the higher frequency region (attributed mainly to depolymerisation) and the intermediate frequency region (attributed mainly to motion in SiO_4 polymerised tetrahedra) as a measure of glass polymerisation. The polymerisation is defined as RPI = (Intensity of Medium Frequency Area/Intensity of Higher Frequency Area) with higher values of RPI indicating more polymerised glass.

3.2.10 X-ray Absorption Spectroscopy (XAFS)

XAFS probe the local environments of material using the absorption patterns of synchrotron generated X-rays. Synchrotrons are beneficial in x-ray absorption spectroscopy as they provide a high flux of X-rays that allow a high signal to noise ratio experiment to be achieved in a short time with a highly stable beam over a range of different energies [140]. X-rays are absorbed by the promotion of photo-electric core at energies that match or are above the binding energy of the electrons in the elements core. The XAS edge is split into two regions the lower energy XANES (X-ray near edge structure) focused on the sharp absorption edge and includes the smaller pre-edge peak and the EXAFS (Extended X-ray absorption fine structure) which the region at a higher energy beyond the binding energy where the core electron can be ionized and released and modelled as a photoelectron interacting with near neighbours. (Figure 3.19 (right)). In this project the focus has been on the XANES region and its position and features. Edge adsorption relates to excitation at the binding energy leading to an increase in absorption created by electric dipole allowed transitions between orbitals XANES edges are labelled in relation to the core shell the electron is expelled from: K-edge from 1s orbital, L-edges from 2s and 2p orbitals and M-edges from 3s, 3p and 3d orbitals with promotion to upper orbitals giving specific edge energies for absorption (Figure 3.19 (left)).

The position and shape of the edge and its features relate to changes in local atomic environment and factors such as electron configuration, co-ordination, ligand type, local site symmetry and spin state, interpretation of these features can relate these factors to changes in properties such as oxidation state, co-ordination, local neighbour type, bond length and therefore deconvolve the local atomic environment of the sample [141-158].

To prepare the samples for a XAF measurement a small amount of powder was dry milled to reduce size and aid mixing. A small amount of the milled powder was mixed with polyethylene glycol (PEG) and pressed into a 13 mm disk to an amount and depth of 1 absorption length [143]. Most of the data was collected at the Beamline 6-BM (National Synchrotron Light Source II, Brookhaven National Laboratory, New York, USA) with additional Ca data collected at Beamline B18 (Diamond Light Source, Harwell Science and Innovation Campus, Oxfordshire, UK) as part of the rapid access scheme. The measurement set up was the same as for data collection at the Beamline 6-BM. Intensities of both Incident (I_0) and Transmitted (I_t) X-rays were measured using separate ion chambers, a reference ion chamber (I_r) allowed reference XANES spectra to be collected for energy calibration and alignment. A channel cut Si (111) monochromator tuned x rays in the beam path allowing different energies and elements to be probed for analysis.

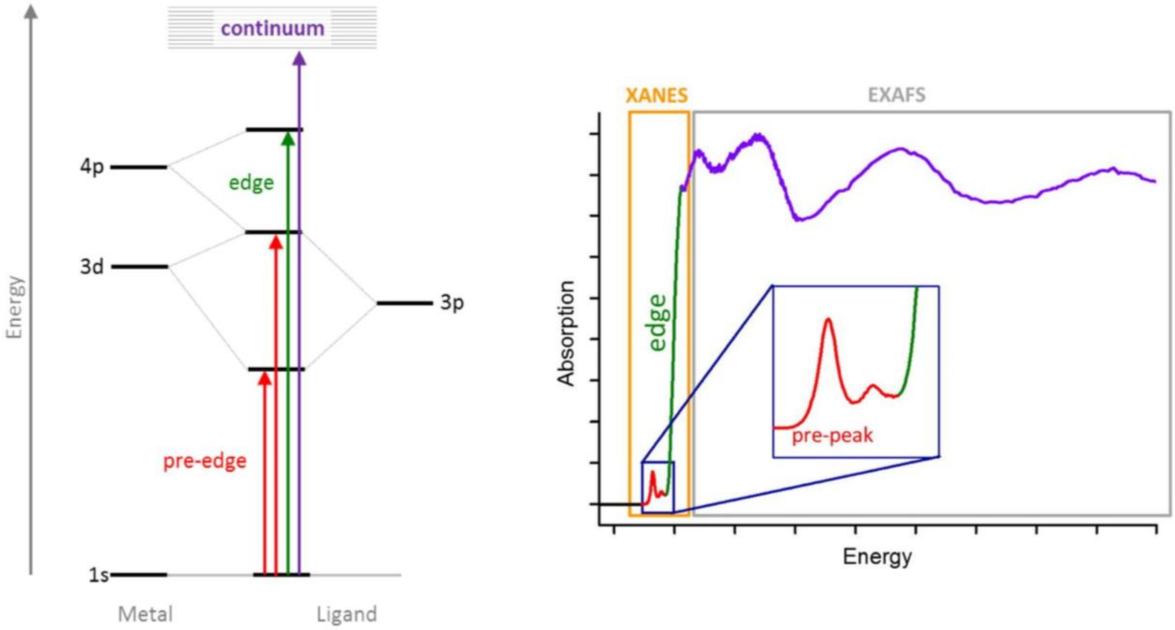

Figure 3.19 Principal energy transitions for the different peaks in a typical XAS spectrum (left) [141] and a typical XAS spectrum showing the different regions used in analysis (right) [141].

Iron (Fe) spectra were acquired between ~6904 and ~8075 eV in transmission mode to analyse the Fe – K edge (7112 eV) XANES. A metal foil Fe reference allowed calibration to the edge position and alignment of samples. A suite of standards: synthetic FePO)$_4$ (Fe(III) or Fe^{3+} oxidation state and tetrahedral (IV) coordination), aegerine (NaFeSi$_2$O$_6$ – (Fe(III) or Fe^{3+} oxidation state and octahedral (VI) coordination), staurolite (Fe$_2$Al$_9$O$_6$(SiO$_4$)$_4$(O,OH)$_2$ – (Fe(II) or Fe^{2+} oxidation state and tetrahedral (IV) coordination) and siderite (FeCO$_3$ – (Fe(II) or Fe^{2+} oxidation state and octahedral (VI) coordination) of known oxidation and co-ordination environment were measured to aid analysis of the samples [145, 147, 148, 151, 152, 156-158]. Cerium (Ce) spectra were acquired between ~5524(63) and ~6141 eV in transmission mode to analyse the Ce – L3-edge (5723.4 eV) XANES. CeO$_2$ was measured as a reference allowing alignment of the samples. 2 standards (CePO$_4$ (Ce(III) or Ce^{3+} oxidation state and nine-fold (IX) coordination) and CeO$_2$ (Ce(IV) or Ce^{4+} oxidation state in eight- fold (IIX) coordination)) of known oxidation and co-ordination were measured to aid analysis of the samples with diagnostic features in each standard identifying the co-ordination environment and oxidation state (Figure 3.20) [153]. Strontium (Sr) spectra were acquired between ~15905 and ~164848 eV in transmission mode to analyse in to analyse Sr – K edge (16104.6 eV). SrTiO$_3$ was measured as a reference channel and standard to aid analysis and alignment of the samples. Zirconium (Zr) spectra were acquired between ~17798 and ~ 18968 eV in transmission mode to analyse to analyse Zr – K edge (17998 eV). A metal foil Zr reference allowed calibration to the edge position and alignment of samples. A suite of standards of known oxidation and co-ordination were measured to aid analysis of the samples these were BaZrO$_3$, CaZrTi$_2$O$_7$, ZrSiO$_4$, M-(monoclinic) ZrO$_2$, wadeite, T-(tetragonal) ZrO$_2$, zektzerite. Hafnium (Hf) spectra were acquired between ~9361 and ~10531 eV in transmission mode to analyse the Hf – L3-edge (9560.7 eV). HfO$_2$ (Hf (IV) in seven-fold (VII) coordination) was measured as a reference channel and standard to aid analysis and alignment of the samples. Vanadium (V) spectra were acquired between ~5257 and ~6199 eV in transmission mode to analyse the V – K edge (5465.1 eV). A metal foil V reference allowed calibration to the edge position and alignment of the samples. A suite of standards: VO_2 (V(IV) or V^{4+} oxidation state and octahedral (VI) coordination), V_2O_3 (V(III) or V^{3+} oxidation state and octahedral (VI) coordination),) V_2O_5 (V(V) or V^{5+} oxidation state in five-fold (V) coordination) and vanadylsulfate (V(IV) or V^{4+} oxidation state in octahedral (VI) coordination) of known oxidation and co-ordination were measured to aid analysis of the samples [142, 150, 154, 155, 159].

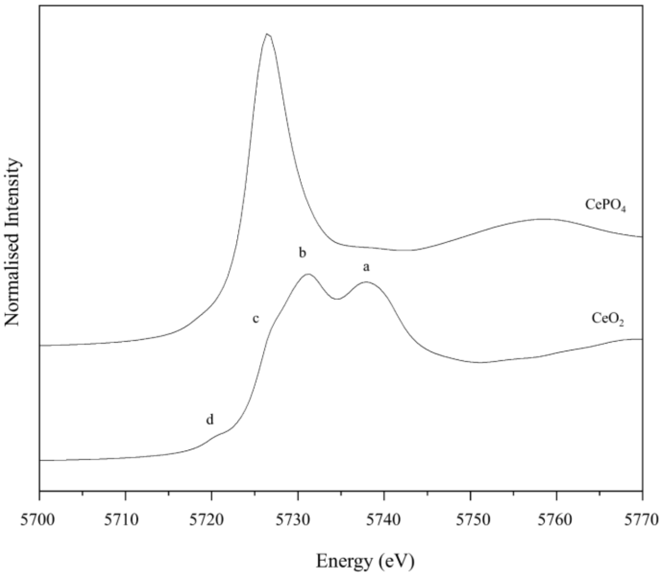

Figure 3.20 Ce L3-edge XNAES spectra for the standards $CePO_4$ and CeO_2 with identification features that are common to Ce in The Ce(III) in nine-fold coordination ($CePO_4$) and CeO_2 (Ce(IV) in eight- fold coordination CeO_2, allowing comparison and identification of the Ce environment in unknown samples in this project. A single intense peak in the $CePO_4$ relates to promotion of an electron from the $2p^6 4f^0 5d^0$ to the $2p^5 4f^0 5d^1$ orbital and is indicative of Ce^{3+}. The more complex peak in the CeO_2 relates to a several different absorptions from the initial $2p^6 4f^0 d^0$ creating 4 distinct features with promotion to a-$2p^5 4f^0 5d^1$ b-$2p^5 4f^1 d^1 L^1$ (L is a ligand hole) c- $2p^5 4f^2 d^1 L^2$ and d- a quadrupole transition and is indicative of Ce^{4+} [153].

Calcium (Ca) spectra were acquired between ~3951 and ~4750 eV in transmission mode to analyse the Ca K-edge (4038.5). Samples were internally aligned to allow comparison. A suite of standards: labradorite $(Ca,Na),(Al,Si)_4O_8$ (distorted polyhedron with seven (VII) oxygens), wollastonite ($CaSiO_3$) (distorted octahedral (VI) coordination) and calcite ($CaCO_3$) (octahedral (VI cordination) of known co-ordination environment were measured to aid analysis of the samples [123, 124, 160].

Analysis and interpretation of the XANES region is the major focus of this project looking at the shape and edge position that has been shown to be diagnostic of the local atomic environment [123, 124, 142-148, 150-158, 160]. All XAFS data was initially analysed using the Athena software [161]. Athena was used to normalise, align and calibrate the spectra and to define E_0 is defined as the threshold energy of the edge and marks the energy of increased absorption associated with the promotion the core electrons. In this study E_0 is defined as the maximum of the first peak in the derivative of the spectrum, this is adjusted accordingly for spectrum with pre-edge features to the maximum in the second peak of the first derivative to be a more consistent measure of the ‘edge’ position and the main 1s-4p transition. If a reference foil is present it was used to calibrate samples to absolute energy scales as the maximum peak of the first derivative defined as E_0 can be attributed to well defined elemental binding energies [142, 143, 145, 147, 148, 150-153, 155-158, 162]. In Fe foils E_0 is calibrated to 7112 eV, V foil is calibrated to 5465 eV and Zr foil to 17998 eV as defined in [162] spectral values can be shifted by a fixed value of +0.92 eV for studies that calibrate the Fe foil to 7110.8 eV [145, 157, 158].

The E_0 or ‘edge’ position is sensitive specifically to the oxidation state of the absorbing element and has been shown to increase with increased oxidation state with a linear relationship for some elements with a potential increase of ~ 1-2 eV per oxidation unit if other factors such as ligand environment are constant [141-148, 151]. As discussed in addition to the E_0 position the shape of the absorption edge can be used in addition to the position to diagnose the atomic environment. A range of techniques including fingerprint analysis, linear combination fitting, principal component analysis and pre-edge fitting use standards to investigate the atomic environment by comparing standard spectra to sample spectra [123, 124, 142-148, 150-158, 160].

For different elements different techniques were implemented based upon the available and complexity of sample and standard data. Hafnium (Hf), strontium (Sr) and zirconium (Zr) were compared to standard data using the fingerprint technique were features in standard data are qualitatively matched to features in sample spectra. For cerium (Ce) the standard data is better resolved and is sensitive to oxidation state [153] therefore using Athena estimates of relative percentages of each standard environment was estimated through the linear combination fitting of the standards giving a quantitative measure to the fingerprint analysis. This is however only an estimate as crystalline standards can only be used to infer the environment in a glass structure and the local environment and structure can affect the shape of the edge.

For elements with a pre-edge feature (iron (Fe), vanadium (V) and calcium (Ca)) a more robust method than crystalline standard linear combination fitting for supporting fingerprint analysis is the fitting of the pre-edge peaks. The pre edge feature occurs in first row transition metals and occurs due dipole forbidden but quadrupole allowed 1s-3d promotions enhanced by 3d-4p hybridisation, as for the main edge variations changes in the atomic environment especially oxidation state and coordination can alter the shape and position of the pre-edge feature allowing it to be a useful tool in determining the local environment of the metal absorber. For Fe there has been many studies that have shown that the pre-edge feature can be deconvolved to investigate the oxidation state and co-ordination environment [145, 147, 148, 151, 152, 156-158].

Pre-edge peaks were fit in Larch [163], initially the background was removed, in other studies a wide range of different functions have been used including spline, pseudovigt, arctangent and polynomial [145, 147, 148, 156-158], in this study a combined linear and lorentzian function was used (Figure 3.21). After background subtraction studies use either gaussian [147, 148, 152, 158] or pseudo-voigt [145, 150, 151, 156, 157] components to fit the pre-edge feature. For Fe, V and Ca the methodology in [145, 157] was followed using pseudo-voigts to devolve the pre-edge features. In iron (Fe) pre-edge analysis, oxidation state has a major control on the pre-edge position and co-ordination strongly controls the intensity with a decreasing trend from co-ordination 4 (tetrahedral) – 6 (octahedral) [141-143, 145-148, 150-152, 154-156, 158] although it has been shown that these relationships are less defined if metallic iron is present

[156]. V pre-edge fitting is not as well developed as a technique as Fe pre-edge fitting however previous fitting of a range of organic and inorganic compounds [142, 150, 155] shows that there is general relationship between the oxidation state/co-ordination environment and the pre-edge parameters. Pre edge fitting for Ca has not been used before this study with previous studies looking at development of the technique [123, 124, 160]. Post fitting the peaks it is common to construct pre-edge centroid position vs integrated area/peak height plots (Figure 3.22) using standard data with known oxidation state/coordination that allow identification of oxidation state/coordination in the samples [145, 147, 150-152, 155-158].

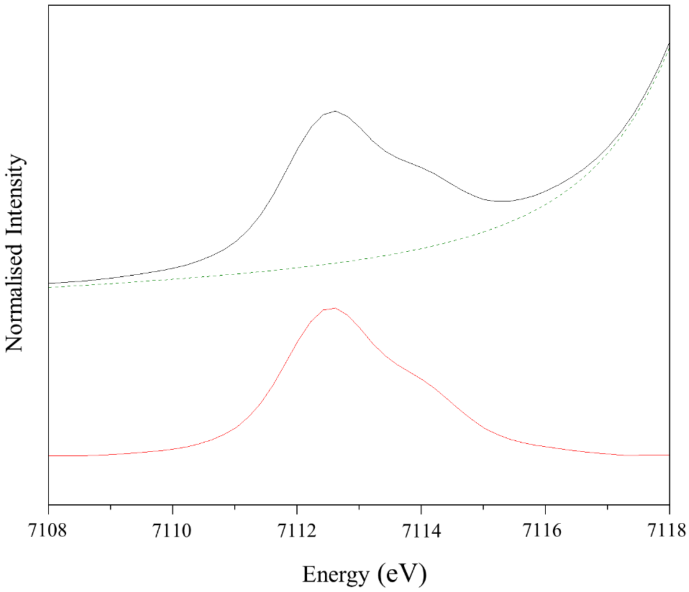

Figure 3.21 Example of background removal of the Staurolite Fe K-edge XANES pre-edge using a combined linear and Lorentzian function.

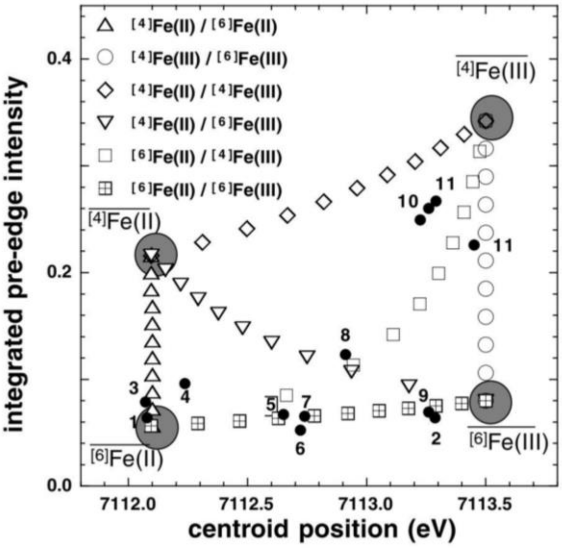

Figure 3.22 Example of pre-edge centroid position vs integrated area plot from [145] used to determine oxidation state and co-ordination of Fe in samples.

3.2.11 Dissolution Tests

3.2.11.1 Overview of Dissolution Tests

A range of tests have been developed analyse sample durability [164], in this project two static tests were chosen from this range, the powdered PCT – Product Consistency Test [165] and the monolith MCC-1 – Materials Characterization Center test [166, 167] . PCT and MCC tests are best used to find residual glass rates (stage IV) but are often and have been used in this study to infer an initial rate (Stage I/II) although caution is required as static tests unlike dynamic tests cannot negate feedback mechanisms like gel formation and solution saturation that create an indistinguishable (from initial rate) rate drop [168].

3.2.11.2 Sample Preparation

All samples were prepared in accordance with the parameters set out in [165, 167, 169] with minor alteration to account for the fragile nature of monoliths and improve the accuracy of SA measurement. For the PCT-B tests crushed glass powder was sieved to isolate the 75-150 µm fraction this gives and average diameter size of 112.5 µm. The glass powder was washed in isopropanol using an ultrasonic bath (2 minutes bursts until the IPA is clear) to remove fine material and dried at 90°C overnight to remove excess isopropanol. For MCC-1 tests blocks of glass were cut into standard 10 x 10 x 5 mm monoliths (estimated measurements were taken using digital callipers) using an ISOMet low speed saw. Tolerance for monolith dimensions were ±2 for the 10 mm dimensions and ± 1.5 for the 5 mm dimension with variance corrected for by adjustments to the leachate volume to get the acquired SA/V ratio of 10 m^{-1}. All monoliths were manually ground and polished using a Buehler Ecomet, this ensures a flat even finish to allow for accurate SA measurements and ensure congruent dissolution. 400 grade SiC paper was used to remove any large edges/knicks, were necessary. 800 and 1200 grade SiC paper was used on each monolith with a standard 2 minutes per side, with monolith rotation ensuring an even finish. 6, 3 and 1 µm diamond suspension was used on each monolith with 2 minutes on top/bottom surfaces and 1 minute on each edge, again, rotation of monolith ensured an even 1 micron finish. Between steps monoliths were rinsed with IPA to remove residual polishing media/grit. Polished monoliths were photographed using a Leica M205A stereo microscope and DMC4500 camera. Image J used the calibrated images to record the accurate (more so than the estimated measurements taken using digital callipers) SA of each monolith. Corrections for pores and breakages were calculated assuming a spherical geometry and any pore/breakage with a SA <0.002 cm was deemed insignificant to the calculation and ignored. Monoliths were rinsed and soaked in IPA for approx. 15 minutes prior to experimental set up, to remove any residual dirt and grease.

3.2.11.3 Vessel Preparation

15 and 40 ml Savillex perfluoralkoxy (PFA) vessels were prepared for PCT-B and MCC-1 dissolution tests in accordance with [165, 167]. New pots were qualified and old pots were cleaned to remove the effects of prior experiments. The qualification process involved rinsing the pots in DI water then filling the vessels with 5% NaOH solution and placing in a 90°C oven for 7+ days**.** The NaOH was removed, and pots were rinsed and filled with UHQ water and placed in a 90°C oven for +16 hrs. After this period if the mass loss was <5 wt%, the UHQ, pH

was 5-7 and the UHQ fluorine content (measured on the ICP-MS) was <0.5 μg/mL) the pot is acceptable to use when dry. To wash used pots, they are soaked in 1% decon solution overnight before being rinsed UHQ water. The pots are then soaked in 1% nitric acid overnight and then rinsed again in UHQ water. Pots are filled with UHQ water and placed in a 90°C oven for +16 hrs, after this period if the mass loss is <5 wt% and the UHQ pH is 5-7 the pot was acceptable to use when dry.

3.2.11.4 PCT and MCC Test Details

PCT-B and MCC-1 dissolution tests were carried out under the conditions stated in [165, 167]. The PCT-B test was conducted in clean 15ml Savillex perfluoralkoxy (PFA) vessels, in duplicate, in UHQ water at 90°C and a SA/V = 1200m^{-1}. Sampling time points were 1, 3, 7, 14, 28 and 35 days with duplicate blanks and sacrificial duplicate dissolution tests for each timepoint. Glass was weighed into each vessel with the target amount calculated using the measured (pycnometry) density, assuming a spherical particle size and a target SA/V of 1200m^{-1}, the actual glass amount added was recorded to allow for an accurate SA ratio to be calculated. 10ml of UHQ was added to each pot, it was then weighed and placed in the oven, pot lids were tightened after 1 day (except 1 day) to reduce solution loss. On sampling pots were removed from the oven and allowed to cool before being weighed to calculate the evaporative loss during the test and allow for an accurate SA/V ratio to be calculated. After weighing the solution was removed from the pots and filtered through 0.22 μm Fisher scientific polyethersulphone (PES) syringe filters into centrifuge tubes ready for ICP-OES/MS chemical analysis, the pH of the solution was recorded using a Mettler Toledo pH meter calibrated between pH 4 and 10. The same set up and sampling methodology was followed for the MCC-1 tests except monoliths were placed in clean 40ml Savillex perfluoralkoxy vessels with PFA baskets and UHQ volume added to target a SA/V = 10 m^{-1} and due to sample availability there was only a 12-month timepoint (Tetronics glass) or 3-, 6- and 12-month timepoints (Geomelt glass).

3.2.11.5 Post Test Analysis

The post sampling concentration of cations in the leachate solutions is analysed using ICP-OES and ICP-MS analysis (as for initial glass composition in Section 3.2.2). These techniques uses a plasma to ionise samples and generate either photons (ICP-OES) or ions (ICP-MS) that can then be accurately analysed in an optical system (ICP-OES) or by a mass spectrometer (ICP-MS) to provide accurate elemental levels in the dissolution liquid [170, 171]. Due to the mass-based analysis technique ICP-OES is less accurate (ppm) than ICP-MS (ppb). ICP-OES analysis was carried out using the Thermo Fisher iCAP 6000 spectrometer using the ITEVA software. ICP-MS was carried out on the Thermo Fisher iCAP RQ spectrometer using the Qtegra ISDS software. Samples and calibration standards were acidified to 2% nitric acid by volume to stabilise elements in solution and all samples and standards were matrix matched to reduce matrix effects on analysis.

The post sampling concentration of cations in the leachate solutions is analysed to calculate comparable elemental loss values using equations outlined in [165, 167] and described below. The solution chemistry and SA/V ratio is used to calculate normalised mass loss of element calculated using (Equation 3.7).

$NL_i = \frac{(C_i - C_{i,b})}{f_i \cdot (SA/V)}$ Equation 3.2

C_i (average concentration of i in solution in mg L^{-1} measured by ICP-OES/MS)
$C_{i,b}$ (average concentration of i in the blank in mg L^{-1} measured by ICP-OES/MS)
f_i is the mass fraction of i in the glass calculated using (Equation 3.8).

$f_i = mass_i\% \cdot \left(\frac{mol_i}{mol_{oxide}}\right) \cdot \left(\frac{MW_i}{MW_{oxide}}\right)$ Equation 3.3

$mass_i\%$ mass % element i oxide in the glass
mol_i molar quantity of element i in the oxide
mol_{oxide} number of moles of oxide
MW_i molecular mass of element i (g mol^{-1})
MW_{oxide} molecular mass of the oxide (g mol^{-1})
f_i was calculated using chemical data from laser ablation ICP-OES (Section 3.2.2). For monoliths and powders the V is measured from the experiment. For monoliths the surface area is measured from the experiment using optical images (see above) and for powders the SA is a geometric surface area calculated assuming a spherical particle geometry and using measured density (pycnometery) (Equation 3.4).

$SA = \frac{3m}{\rho r_0}$ Equation 3.4

m mass of glass sample added to the pot
ρ glass density (gm^{-3}) measured using pycnometry
r_0 average particle radius assuming a geometric surface area and spherical particles giving an average radius of 56.25 µm due to the sieve fraction of 75-150 µm

In this study SA of the particulate material was calculated using a geometrical method assuming a spherical particle geometry as outlined in [165]. However, some studies us a surface area calculated in a BET machine using helium gas absorption can give a measure of SA. Experimental length scales (BET better for shorter and geometrical longer as the facets will be smoothed by dissolution) determine the best measurement technique to use but for this study the importance is the consistency calculation to allow comparison between different tests. NL calculated with SA generated from BET analysis will overestimate the SA due to faceted particles and the He accesses increased pores and microcracks. For comparative analysis a factor of 2.5 can be applied to NL loss values calculating using BET SA to allow comparison to NL calculated assuming spherical particle geometry [172].

Dissolution rate or normalised mass loss per given time is calculated for the different stages of the glass dissolution curve using (Equation 3.5) and allows the different rate regions (see section 2.2.2.2) to be categorised.

$NR_i = dNL_i/dt$ Equation 3.5

In preparation for SEM analysis, after being allowed to air dry powders and monoliths were mounted in epoxy resin and allowed to cure overnight. Excess resin was removed using SiC p800 and p1200 grit papers and the surface polished using 6, 3 and 1 µm oil based diamond paste (to prevent any sample reaction with water) to create an optical grade surface finish. SEM analysis (see Section 3.2.6) of the resin mounted samples was carried out to investigate the effects of dissolution.

3.3 References

1. Veolia, Our GeoMelt Vitrification Technologies to Stabilize Waste.
2. AMEC, Bulk Vitrication Treatment of K Basin Sludge Simulant Final Report. 2003.
3. Witwer.K. Preliminary Demonstration Of Geomelt Treatment Of Hanfords K-Basin Sludge. in ICEM - Internation Conference on Environmental Remediation and Radioactive Waste Managment. 2011. Reims, France.
4. Witwer, S.K., Woolery.W.D, Dysland.J.E. Progress of the Hanford Bulk Vitrification Project ICV Testing Program in WM'06. 2006. Tucson, AZ.
5. Witwer, S.K., Dysland.J.E. Hanford Bulk Vitrification Technology Status. in WM'07 Conference. 2007. Tucson, AZ.
6. Bagaasen, L.M., et al. Method to Reduce Molten Salt Penetration into Bulk Vitrification Refractory Materials. 2008. United States: WM Symposia, Phoenix, AZ, United States(US).
7. Witwer, K.S., et al. Hanford's Supplemental Treatment Project: Full-Scale Integrated Testing of In-Container-Vitrification and a 10,000-Liter Dryer. in 2008 Waste Management Symposium - WM2008/WM'08: HLW, TRU, LLW/ILW, Mixed, Hazardous Wastes and Environmental Management - Phoenix Rising: Moving Forward in Waste Management. 2008. United States.
8. Bagaasen, L.M., et al. Transport of Technetium and Rhenium into Refractory Materials during Bulk Vitrification. 2006. United States.
9. Kim.S.D, V.D.J., Hrma.R.P, Schweiger.J.M, Matyas.J, Crum.V.J, SMith.E.D, Sevigny.J.G, Buchmiller.C.W, Jr.Tixier.S.J, Yeager.D.J, Belew.B.K, Development and Testing of ICV Glasses for Hanford LAW. 2003, PNNL.
10. Hrma.R.P, K.S.D., Vienna.D.J, Matyas.J, Smith.E.D, Schweiger.J.M, Yeager.J.D, Testing of Large Scale ICV Glasses with Hanford LAW Simulant. 2005, PNNL.
11. Group, C.M.H., Technical Assessment of Bulk Vitrification Process/Product for Tank Waste Treatment at the Department of Energy Hanford Site. 2006.
12. L.E. Thompson, L.M., and D. Hamilton., Status and Direction of the Bulk Vitrification Program for the Supplemental Treatment of Low Activity Tank Waste at Hanford. Proceedings of WM’05 Symposia. WM-5138, AMEC Earth and Environmental, Inc., Richland, Washington., 2005.
13. Mahoney.A.L, V.D.J., Feed Variability and Bulk Vitrication Glass Performance Assessment. 2005, PNNL.
14. AMEC, Demonstration and Test Plan in AMEC Proposal to Bulk Vitirifcation RFP #93505 to CH2M Hill Hanford Group, November 2002. 2002.
15. Kim.et.al, Matrix Crucible Testing of Bulk Vitrification Glasses for Hanford Low Activity Waste. 2005, AMEC Earth amnd Environmetal.
16. Finucane, K.G., et al. The Development of GeoMeltR In-Container Vitrification (ICV)TM for Fukushima Daiichi Water Treatment Secondary Wastes - 21347. in WM2021: 47 Annual Waste Management Conference. 2021. United States.
17. Witwer, K. Preliminary Demonstration of GeoMelt Treatment of Hanford’s K-Basin Sludge. in Waste Managment Conference. 2011. USA.
18. Kim, D.S., et al. Glass Formulations for Immobilizing Hanford Low-Activity Wastes. in Waste Management 2006 Symposium - WM'06 - Global Accomplishments in Environmental and Radioactive Waste Management: Education and Opportunity for the Next Generation of Waste Management Professionals. 2006. United States.
19. Rassat.S.D, M.A.L., Russell.L.R, Bryan.A.S, Sell.R.L, Cold Dissolved Saltcake Waste Simulant Development, Preparation, and Anlaysis. 2003, PNNL.

20. Veolia, Support US Departmnet of Energy (DOE) cleanup mission at the Hanford site. 2003.
21. Kurion Japan K.K, V.N.S.I., Project of Decommissioning and Contaminated Water Management (Research and Development of Processing and Disposal of Solid Waste) - The Holistic Evaluation of Applicability of GeoMelt® ICV™ for Treatment of 1F Water Treatment Secondary Waste Fiscal Year 2019-2020. 2021.
22. Raymond, R.E. INITIAL SELECTION OF SUPPLEMENTAL TREATMENT TECHNOLOGIES FOR HANFORDS LOW ACTIVITY TANK WASTE. 2004. United States.
23. Medicine, N.A.S.E., Review of the Continued Analysis of Supplemental Treatment Approaches of Low-Activity Waste at Hanford Nuclear Reservation:Review #2 Consesus Study Report. 2022.
24. Marcial, J., et al., Hanford low-activity waste vitrification: A review. Journal of Hazardous Materials, 2024. 461: p. 132437.
25. Witwer.S.K, D.J.E., Garfiled.S.J, Beck.H.T. Hanfords Supplemental Treatment Project: Full-Scale Integrated Testing of In-Container-Vitrification and 10,000 Liter Dryer. in WM2008 Conference. 2008. Phoenix, AZ.
26. Washington State Department of Ecology, U.S.E.P.A.a.U.S.D.o.E. Amended March 6, 2024.
27. Knollmeyer, P., C. Phillips, and P. Townson, PROGRESS WITH K BASINS SLUDGE RETRIEVAL STABILIZATION & PACKAGING AT THE HANFORD NUCLEAR SITE. 2006.
28. Schmidt, A.J., Hanford Spent Nuclear Fuel Project Databook.
29. Energy, D.o., Hanford K-Basin Sludge Chararcterization Overview. 2005.
30. Soderquist, C.Z., et al., Redox-dependent solubility of technetium in low activity waste glass. Journal of Nuclear Materials, 2014. 449(1): p. 173-180.
31. Soderquist, C.Z., et al., Formation of Technetium Salts in Hanford Low-Activity Waste Glass. Journal of the American Ceramic Society, 2016. 99(12): p. 3924-3931.
32. Tingey.M.J, B.H.G., Deschane.R.J, Dangerous Waste Charaterisitics of Waste from Hanford Tank 241-S-109. 2004, PNNL.
33. Lehto, J., et al., Removal of Radionuclides from Fukushima Daiichi Waste Effluents. Separation & Purification Reviews, 2019. 48(2): p. 122-142.
34. Egan.M, P.A., Towler.G, Treatment of Plutomium Contaminated Material at Sellafield: Best Practical Environmnetal Option Study. 2008, Sellafield.
35. NuSAC, Plutonium Contaminated Material (PCM). 2005.
36. Hyatt, N.C., et al., Thermal treatment of simulant plutonium contaminated materials from the Sellafield site by vitrification in a blast-furnace slag. Journal of Nuclear Materials, 2014. 444(1): p. 186-199.
37. Boast.L, Investigation of the Thermal Treatment of Higher Activity Waste., in Material Science. 2018, Sheffield.
38. NDA, Packaging of Plutonium Contaminated Material at the Waste Treatment Complex. 2013: Nuclear Decommisioning Agency.
39. NDA, An Overview of NDA Higher Activity Waste. 2015, Nuclear Decomissioning Agency.
40. Hyatt, N.C., et al., Characterisation of Plasma Vitrified Simulant Plutonium Contaminated Material Waste. MRS Proceedings, 2006. 985: p. 0985-NN10-06.
41. Tetronics, 1107 COSTAIN Plasma Trials Procedure for Nuclear Demonstration Furnace. 2019.
42. Tetronics, 1107 Plasma PCM Trials Report for Nuclear Demonstration Furnace. 2020.

43. Deegan, D. and C. Scales, The Role of Tetronics Plasma Vitrification Technology in the Management and Conditioning of Nuclear Waste. 2007.
44. Boast, L., M.C. Stennett, and N.C. Hyatt, Thermal treatment of plutonium contaminated material (PCM) waste. MRS Advances, 2017. 2(13): p. 735-740.
45. Harrison, M.T., Vitrification of High Level Waste in the UK. Procedia Materials Science, 2014. 7: p. 10-15.
46. Owen.E.D, F.E.J. 1981, Idaho National Labaratory.
47. Reimann.A.G, K.C.P. 1993, Idaho National Laboratory.
48. Reimann.A.G, G.D.J., Eddy.L.T, Anderson.L.G. 1992, Idaho National Laboratory.
49. Tetronics, Nuclear plasma trials Drum Preparation - R01. 2019.
50. Faulds, D. 2022.
51. Bingham, P.A., et al., The Use of Surrogates in Waste Immobilization Studies: A Case Study of Plutonium. MRS Proceedings, 2008. 1107: p. 421.
52. Harrison, M.T., et al., Survey of Potential Glass Compositions for the Immobilisation of the UK's Separated Plutonium Stocks. MRS Online Proceedings Library, 2007. 985(1): p. 403.
53. Stennett, M.C., et al., An Evaluation of Single Phase Ceramic Formulations for Plutonium Disposition. MRS Online Proceedings Library (OPL), 2006. 985: p. 0985-NN04-02.
54. Stennett, M.C., et al., Processing and Characterisation of Fluorite-Related Ceramic Wasteforms for Immobilisation of Actinides, in Environmental Issues and Waste Management Technologies in the Ceramic and Nuclear Industries XI. 2006. p. 81-90.
55. Deschanels, X., et al., Plutonium solubility and self-irradiation effects in borosilicate glass. Progress in Nuclear Energy, 2007. 49(8): p. 623-634.
56. Darab, J.G., Li, H., Schweiger, M. J., Vienna, J. D., Allen, P. G., Bucher, J. J., Edelstein, N. M. and Shuh, D. K. Proceedings of plutonium futures-the science. . in Topical conference on plutonium and the actinides. 1997. Santa Fe, USA.
57. Schreiber, H.D., An electrochemical series of redox couples in silicate melts: A review and applications to geochemistry. Journal of Geophysical Research: Solid Earth, 1987. 92(B9): p. 9225-9232.
58. Cachia, J.N., et al., Enhancing cerium and plutonium solubility by reduction in borosilicate glass. Journal of Nuclear Materials, 2006. 352(1): p. 182-189.
59. Lopez, C., et al., Solubility of actinide surrogates in nuclear glasses. Journal of Nuclear Materials, 2003. 312(1): p. 76-80.
60. Strachan.D, V.R.E., Shuh.K.D, Ewing.C.R, Distribution & Solubility of Radionuclides & Neutron Absorbers in Waste Forms for Disposition of Plutonium Ash & Scraps, Excess Plutonium, and Miscellaneous Spent Nuclear Fuels. 1998: Environmental Management Science Program.
61. Feng.X, L.H., Davis.LL, Li.L, Darab.G.J, Shuh.K.D, Ewing.C.R, Wang.M.L, Vance.R.E, Allen.G.P, Bucher.J.J, and C.M.I. Edelstein.M.N, Schweiger.J.M, Vienna.D.J, Strachan.M.D , and Bunker.C.B, Distribution & Solubility of Radionuclides & Neutron Absorbers in Waste Forms for Disposition of Plutonium Ash & Scraps, Excess Plutonium, and Miscellaneous Spent Nuclear Fuels. 1998: Environmental Management Science Program.
62. Feng, X., et al. Distribution and Solubility of Radionuclides in Waste Forms for Disposition of Plutonium and Spent Nuclear Fuels: Preliminary Results. 1999. United States.
63. J. G. Darab, H.L., M. J. Schweiger, J. D. Vienna, P. G. Allen, J. J. Bucher, N. M. Edelstein and D. K. Shuh. in Proceedings of plutonium futures-the science. Topical conference on plutonium and the actinides. 1997. Santa Fe, USA.

64. http://www.webelements.com.
65. Bastick.E.R, Determination of Selenium in glass by radioactivation method. Journal of the Society of Glass Technology, 1958. 42: p. 84-88.
66. Feng.X, e.a., Distribution and Solubility of Radionuclides in Waste Forms for Disposition of Plutonium and Spent Nuclear Fuels: Preliminary Results. 1999, PNNL.
67. Harrison.T.M, S.R.C., Bingham.A.P and Hand.J.R, Scientific Basis for Nuclear Waste Management XXX, edited by D. S. Dunn, C. Poinssot and B. Begg, (Mater. Res. Soc.Proc. 985, Warrendale, PA, 2007) in press.
68. Chevreux, P., et al., Hafnium solubility determination in soda-lime aluminosilicate glass. Journal of Non-Crystalline Solids, 2017. 457: p. 13-24.
69. Schwarz.R, B.P.a., Thermal Treatment of Plutonium Contaminated Materials Phase 2: Vitrification Study Final Report. 31st May 2012.
70. Morgan, S., Personal Communication.
71. Dussubieux, L., M. Golitko, and B. Gratuze, Recent Advances in Laser Ablation ICP-MS for Archaeology. 2016.
72. Tamari, S., Optimum design of the constant-volume gas pycnometer for determining the volume of solid particles. Measurement Science and Technology, 2004. 15(3): p. 549.
73. Zheng, Q., et al., Understanding Glass through Differential Scanning Calorimetry. Chemical Reviews, 2019. 119(13): p. 7848-7939.
74. PerkinElmer, A Beginner's Guide to Thermogravimetric Analyis.
75. Bragg, H.W., Bragg, Lawrence W, X Rays and Crystal Structure. 1918: G.Bell and Sons Ltd, London.
76. Dinnebier, E.R.B., L.J.S, Powder Diffraction Theory and Practice. 2008: The Royal Society of Chemistry.
77. Gražulis, S., et al., Crystallography Open Database (COD): an open-access collection of crystal structures and platform for world-wide collaboration. Nucleic Acids Research, 2011. 40(D1): p. D420-D427.
78. Blanton, T. and S. Gates-Rector, The Powder Diffraction File: a quality materials characterization database. Powder Diffraction, 2019. 34(4): p. 352-360.
79. Goldstein.I.J, N.E.D., Micheal.R.J, Ritchie.M.W.N, Scott.J.H.J and Joy,C,D, Scanning Electron Microscopy and X-Ray Microanalysis. 4th ed. 2018: New York: Springer.
80. Hurt, R. 2016.
81. Hornak, J., The Basics of NMR. 1997.
82. Günther, H., NMR spectroscopy : basic principles, concepts, and applications in chemistry. 2013, Wiley-VCH Weinheim: Weinheim.
83. Maciejewski.M, Basics of NMR Spectroscopy 2016, UConn Health, University of Connecticut.
84. Neuville, D., L. Cormier, and D. Massiot, Al Coordination and Speciation in Calcium Aluminosilicate Glasses: Effects of Composition Determined by 27Al MQ-MAS NMR and Raman Spectroscopy. Chemical Geology, 2006. 229: p. 173-185.
85. Neuville, D.R., L. Cormier, and D. Massiot, Al environment in tectosilicate and peraluminous glasses: A 27Al MQ-MAS NMR, Raman, and XANES investigation. Geochimica et Cosmochimica Acta, 2004. 68(24): p. 5071-5079.
86. Neuville, D.R., et al., Local Al site distribution in aluminosilicate glasses by 27Al MQMAS NMR. Journal of Non-Crystalline Solids, 2007. 353(2): p. 180-184.
87. Neuville, D., V. Montouillout, and D. Massiot, Local environment of Al in aluminosilicate glasses: A NMR point of view. Journal of Non-Crystalline Solids, 2007. 353: p. 180-185.

88. Neuville, D., et al., Structure of Mg- and Mg/Ca Aluminosilicate Glasses: 27Al NMR and Raman Spectroscopy Investigations. American Mineralogist - AMER MINERAL, 2008. 93: p. 1721-1731.
89. Chen, Z., et al., Insight into the Relationship Between Viscosity and Structure of CaO-SiO2-MgO-Al2O3 Molten Slags. Metallurgical and Materials Transactions B, 2019. 50.
90. Kilinc, E. and R.J. Hand, Mechanical properties of soda–lime–silica glasses with varying alkaline earth contents. Journal of Non-Crystalline Solids, 2015. 429: p. 190-197.
91. Lippmaa, E., A. Samoson, and M. Magi, High-resolution aluminum-27 NMR of aluminosilicates. Journal of the American Chemical Society, 1986. 108(8): p. 1730-1735.
92. Smith, K.A., et al., High-resolution silicon-29 nuclear magnetic resonance spectroscopic study of rock-forming silicates. American Mineralogist, 1983. 68(11-12): p. 1206-1215.
93. Lippmaa, E., et al., Investigation of the structure of zeolites by solid-state high-resolution silicon-29 NMR spectroscopy. Journal of the American Chemical Society, 1981. 103(17): p. 4992-4996.
94. Magi, M., et al., Solid-state high-resolution silicon-29 chemical shifts in silicates. The Journal of Physical Chemistry, 1984. 88(8): p. 1518-1522.
95. Mysen, B.O., A. Lucier, and G.D. Cody, The structural behavior of Al3+ in peralkaline melts and glasses in the system Na2O-Al2O3-SiO2. 2003. 88(11-12): p. 1668-1678.
96. Merzbacher, C.I., K.J. McGrath, and P.L. Higby, 29Si NMR and infrared reflectance spectroscopy of low-silica calcium aluminosilicate glasses. Journal of Non-Crystalline Solids, 1991. 136(3): p. 249-259.
97. Henderson, G.S. and J.F. Stebbins, The Short-Range Order (SRO) and Structure. Reviews in Mineralogy and Geochemistry, 2022. 87(1): p. 1-53.
98. Cormier, L., Glasses: Aluminosilicates. Encyclopedia of Materials: Technical Ceramics and Glasses, 2021.
99. Oestrike, R., et al., High-resolution 23Na, 27Al and 29Si NMR spectroscopy of framework Aluminosilicate glasses. Geochimica et Cosmochimica Acta, 1987. 51(8): p. 2199-2209.
100. Stebbins, J.F., Identification of multiple structural species in silicate glasses by 29Si NMR. Nature, 1987. 330(6147): p. 465-467.
101. Le Losq, C., Rampy: a Python library for processing spectroscopic (IR, Raman, XAS...) data. , Zenodo, Editor. 2018.
102. Massiot.D, F.F., Capron.M, King.I, Le Calvé.S, Alonso.B, Durand.O.J, Bujoli.B, Gan.Z, Hoatson.G, Modelling one and two-dimensional solid-state NMR spectra. Magnetic Resonance in Chemistry, 2002. 40: p. 70-76.
103. Czjzek, G., et al., Atomic coordination and the distribution of electric field gradients in amorphous solids. Physical Review B, 1981. 23(6): p. 2513-2530.
104. LeCaër, G. and R.A. Brand, General models for the distributions of electric field gradients in disordered solids. Journal of Physics Condensed Matter, 1998. 10: p. 10715-10774.
105. Bureau, B., et al., From crystalline to glassy gallium fluoride materials: an NMR study of 69Ga and 71Ga quadrupolar nuclei. (0926-2040 (Print)).
106. Hoatson, G., et al., ^{93} Nb magic angle spinning NMR study of perovskite relaxor ferroelectrics (1-x) Pb (Mg_ {1/3} Nb_ {2/3}) O_ {3}-xPb (Sc_ {1/2} Nb_ {1/2}) O_ {3}. Phys. Rev. B, 2002. 66.

107. Dyar, M.D., et al., MÖSSBAUER SPECTROSCOPY OF EARTH AND PLANETARY MATERIALS. Annual Review of Earth and Planetary Sciences, 2006. 34(1): p. 83-125.
108. Stennett, M.C., Introduction to Mossbauer Spectroscopy.
109. Smith.E, D.G., Modern Raman Spectroscopy - A Practical Approach. 2004.
110. Ferraro.R.J, N.K., Brown.W.C, Introductory Raman Spectroscopy. 2 ed. 2002: Elsevier.
111. Le Losq, C., et al., The role of Al3+ on rheology and structural changes in sodium silicate and aluminosilicate glasses and melts. Geochimica et Cosmochimica Acta, 2014. 126: p. 495-517.
112. Neuville, D.R., D. de Ligny, and G.S. Henderson, Advances in Raman Spectroscopy Applied to Earth and Material Sciences. Reviews in Mineralogy and Geochemistry, 2014. 78(1): p. 509-541.
113. Merzbacher, C.I. and W.B. White, The structure of alkaline earth aluminosilicate glasses as determined by vibrational spectroscopy. Journal of Non-Crystalline Solids, 1991. 130(1): p. 18-34.
114. Drewitt, J., L. Hennet, and D. Neuville, From Short to Medium Range Order in Glasses and Melts by Diffraction and Raman Spectroscopy. Reviews in Mineralogy and Geochemistry, 2022. 87(1): p. 55-103.
115. Fu, X., A. Wang, and M.J. Krawczynski, Characterizing amorphous silicates in extraterrestrial materials: Polymerization effects on Raman and mid-IR spectral features of alkali and alkali earth silicate glasses. Journal of Geophysical Research: Planets, 2017. 122(5): p. 839-855.
116. Di Genova, D., et al., Approximate chemical analysis of volcanic glasses using Raman spectroscopy. Journal of Raman Spectroscopy, 2015. 46(12): p. 1235-1244.
117. Di Genova, D., et al., Effect of iron and nanolites on Raman spectra of volcanic glasses: A reassessment of existing strategies to estimate the water content. Chemical Geology, 2017. 475: p. 76-86.
118. Haghdani, S., M. Tangstad, and K.E. Einarsrud, A Raman-Structure Model for the Viscosity of SiO2-CaO-Al2O3 System. Metallurgical and Materials Transactions B, 2022. 53(3): p. 1733-1746.
119. McMillan, P., B. Piriou, and A. Navrotsky, A Raman spectroscopic study of glasses along the joins silica-calcium aluminate, silica-sodium aluminate, and silica-potassium aluminate. Geochimica et Cosmochimica Acta, 1982. 46(11): p. 2021-2037.
120. McMillan, P., A Raman spectroscopic study of glasses in the system CaO–MgO–SiO2. American Mineralogist, 1984. 69(7-8): p. 645-659.
121. Neuville, D.R. and B.O. Mysen, Role of aluminium in the silicate network: In situ, high-temperature study of glasses and melts on the join SiO2-NaAlO2. Geochimica et Cosmochimica Acta, 1996. 60: p. 1727-1737.
122. Neuville, D.R., L. Cormier, and D. Massiot, Al coordination and speciation in calcium aluminosilicate glasses: Effects of composition determined by 27Al MQ-MAS NMR and Raman spectroscopy. Chemical Geology, 2006. 229(1): p. 173-185.
123. Neuville, D.R., et al., Al speciation and Ca environment in calcium aluminosilicate glasses and crystals by Al and Ca K-edge X-ray absorption spectroscopy. Chemical Geology, 2004. 213(1): p. 153-163.
124. Neuville, D.R., et al., Environments around Al, Si, and Ca in aluminate and aluminosilicate melts by X-ray absorption spectroscopy at high temperature. American Mineralogist, 2008. 93(1): p. 228-234.

125. Sen, P.N. and M.F. Thorpe, Phonons in $A{X}_{2}$ glasses: From molecular to band-like modes. Physical Review B, 1977. 15(8): p. 4030-4038.
126. Seifert, F.A., B.O. Mysen, and D. Virgo, Three-dimensional network structure of quenched melts (glass) in the systems SiO2–NaAlO2, SiO2–CaAl2O4 and SiO2–MgAl2O4. American Mineralogist, 1982. 67(7-8): p. 696-717.
127. Mysen, B.O. and M.J. Toplis, Structural behavior of Al3+ in peralkaline, metaluminous, and peraluminous silicate melts and glasses at ambient pressure. 2007. 92(5-6): p. 933-946.
128. Jolivet, V., et al., Quantification of boron in aluminoborosilicate glasses using Raman and 11B NMR. Journal of Non-Crystalline Solids, 2019. 511: p. 50-61.
129. Parkinson, B.G., et al., Quantitative measurement of Q3 species in silicate and borosilicate glasses using Raman spectroscopy. Journal of Non-Crystalline Solids, 2008. 354(17): p. 1936-1942.
130. Yadav, A.K. and P. Singh, A Review on Structure of Glasses by Raman Spectroscopy. RSC Advances, 2015. 5: p. 67583-67609.
131. Mysen, B.O., D. Virgo, and F.A. Seifert, The structure of silicate melts: Implications for chemical and physical properties of natural magma. Reviews of Geophysics, 1982. 20(3): p. 353-383.
132. Mysen, B.O., D. Virgo, and I. Kushiro, The structural role of aluminum in silicate melts—a Raman spectroscopic study at 1 atmosphere. American Mineralogist, 1981. 66(7-8): p. 678-701.
133. Galeener, F.L. and J.C. Mikkelsen, The Raman spectra and structure of pure vitreous P2O5. Solid State Communications, 1979. 30(8): p. 505-510.
134. Brawer, S.A. and W.B. White, Raman spectroscopic investigation of the structure of silicate glasses (II). Soda-alkaline earth-alumina ternary and quaternary glasses. Journal of Non-Crystalline Solids, 1977. 23(2): p. 261-278.
135. Cormier, L., et al., In situ evolution of the structure of alkali borate glasses and melts by infrared reflectance and Raman spectroscopies. Physics and Chemistry of Glasses-European Journal of Glass Science and Technology Part B, 2006. 47: p. 430-434.
136. Galeener, F.L., Planar rings in vitreous silica. Journal of Non-Crystalline Solids, 1982. 49(1): p. 53-62.
137. Le Losq, C., et al., Determination of the oxidation state of iron in Mid-Ocean Ridge basalt glasses by Raman spectroscopy. American Mineralogist, 2019. 104.
138. Le Losq, C., et al., Percolation channels: a universal idea to describe the atomic structure and dynamics of glasses and melts. Scientific Reports, 2017. 7(1): p. 16490.
139. Colomban, P., Polymerization degree and Raman identification of ancient glasses used for jewelry, ceramic enamels and mosaics. Journal of Non-Crystalline Solids, 2007. 323: p. 180-187.
140. Brown, E., Gordon Jr., and Waychunas, A, Glenn. X-ray Absorption Spectroscopy: Introduction to Experimental Procedures
141. Kowalska, J. and S. DeBeer, The role of X-ray spectroscopy in understanding the geometric and electronic structure of nitrogenase. Biochimica et biophysica acta, 2015. 1853: p. 1406-1415.
142. Wong, J., et al., K-edge absorption spectra of selected vanadium compounds. Physical Review B, 1984. 30(10): p. 5596-5610.
143. Newville.M, Fundamentals of XAFS. 2004: Consortium of Advanced Radiation Sources, University of Chicago, IL.
144. Bare.R.S, XANES Measurements and Interpretation. 2003, UOP LLC, Des Plaines, IL: EXAF's Data Collection and Analysis Course, NSLS, July 14-17.

145. Wilke, M., et al., Oxidation state and coordination of Fe in minerals: An Fe K-XANES spectroscopic study. American Mineralogist, 2001. 86(5-6): p. 714-730.
146. Sarangi.R, Introduction to X-ray Absorption Near Edge Spectroscopy (XANES). 2010, Stanford University.
147. Mottram, L.M., et al., A feasibility investigation of speciation by Fe K-edge XANES using a laboratory X-ray absorption spectrometer. Journal of Geosciences, 2020. 65(1): p. 27-35.
148. Berry, A.J., et al., XANES calibrations for the oxidation state of iron in a silicate glass. 2003. 88(7): p. 967-977.
149. Morris, D.J. and P. Zhang, In situ X-ray Absorption Spectroscopy of Platinum Electrocatalysts. Chemistry–Methods, 2021. 1(3): p. 162-172.
150. Giuli, G., et al., V oxidation state and coordination number in silicate glasses by XAS. 2004. 89(11-12): p. 1640-1646.
151. Giuli, G., et al., XAS Determination of the Fe Local Environment and Oxidation State in Phonolite Glasses. American Mineralogist, 2011. 96: p. 631-636.
152. Giuli, G., et al., Iron local structure in tektites and impact glasses by extended X-ray absorption fine structure and high-resolution X-ray absorption near-edge structure spectroscopy. Geochimica et Cosmochimica Acta, 2002. 66(24): p. 4347-4353.
153. Bailey, D., et al., Ce and U speciation in wasteforms for thermal treatment of plutonium bearing wastes, probed by L 3 edge XANES. IOP Conference Series: Materials Science and Engineering, 2020. 818: p. 012019.
154. Nomura, K. Solution X-Ray Absorption Spectroscopy (XAS) for Analysis of Catalytically Active Species in Reactions with Ethylene by Homogeneous (Imido)vanadium(V) Complexes—Al Cocatalyst Systems. Catalysts, 2019. 9, DOI: 10.3390/catal9121016.
155. Levina, A., A.I. McLeod, and P.A. Lay, Vanadium Speciation by XANES Spectroscopy: A Three-Dimensional Approach. Chemistry – A European Journal, 2014. 20(38): p. 12056-12060.
156. Simon, H., et al., Fe K-edge x-ray absorption spectroscopy of corrosion phases of archaeological iron: results, limitations, and the need for complementary techniques. Journal of Physics: Condensed Matter, 2021. 33(34): p. 344002.
157. Petit, P., et al., Determination of the iron oxidation state in Earth materials using XANES pre-edge information. Journal of synchrotron radiation, 2001. 8: p. 952-4.
158. Wilke, M., et al., Determination of the iron oxidation state in basaltic glasses using XANES at the K-edge. Chemical Geology, 2005. 220(1): p. 143-161.
159. Lamsal.C, Electronic, thermelctric and optical properties of vanadium oxides: VO2c, V2O3 and V2O5. 2014, New Jersey Institute of Technology.
160. Cormier, L. and D.R. Neuville, Ca and Na environments in Na2O–CaO–Al2O3–SiO2 glasses: influence of cation mixing and cation-network interactions. Chemical Geology, 2004. 213(1): p. 103-113.
161. Ravel, B. and M. Newville, ATHENA, ARTEMIS, HEPHAESTUS: data analysis for X-ray absorption spectroscopy using IFEFFIT. (0909-0495 (Print)).
162. Bearden, J.A. and A.F. Burr, Reevaluation of X-Ray Atomic Energy Levels. Reviews of Modern Physics, 1967. 39(1): p. 125-142.
163. Newville, M., Larch: An Analysis Package for XAFS and Related Spectroscopies. Journal of Physics: Conference Series, 2013. 430(1): p. 012007.
164. Thorpe, C.L., et al., Forty years of durability assessment of nuclear waste glass by standard methods. npj Materials Degradation, 2021. 5(1): p. 61.

165. ASTM, ASTM C1285. Standard Test Methods for Determining Chemical Durability of Nuclear Waste Glasses: The Product Consistency Test (PCT) Standard C1285-21. 2014.
166. Strachan, D.M., R.P. Turcotte, and B.O. Barnes, MCC-1: A Standard Leach Test for Nuclear Waste Forms. Nuclear Technology, 1982. 56(2): p. 306-312.
167. ASTM, ASTM C1220. Standard Test Method for Static Leaching of Monolithic Waste Forms for Disposal of Radioactive Waste. . 2017.
168. Vienna, J.D., et al., Impacts of glass composition, pH, and temperature on glass forward dissolution rate. npj Materials Degradation, 2018. 2(1): p. 22.
169. Fisher.J.A, C.L.C., Materials Characterisation Centre-1 (MCC-1) monoloithic dissolution test - Standard Operating Procedure (SOP) adopted at the University of Sheffield for the project - Experimental studies to investigate the durability of UK HLW glasses using a new base glass formulation and glasses from POCO operations - RWM.01.008-09308. 2020, NucleUS Immobilisation Science Laboratory, University of Sheffield
170. Agilent. An Introduction to the Fundamentals of Inductively Coupled Plasma - Optical Emission Spectroscopy (ICP-OES). Available from: https://www.agilent.com/en/support/atomic-spectroscopy/inductively-coupled-plasma-optical-emission-spectroscopy-icp-oes/icp-oes-faq.
171. Agilent. An Introduction to the Fundamentals of Inductively Coupled Plasma - Mass Spectrromery (ICP-MS). Available from: https://www.agilent.com/en/product/atomic-spectroscopy/inductively-coupled-plasma-mass-spectrometry-icp-ms/what-is-icp-ms-icp-ms-faqs#:~:text=ICP%2DMS%20is%20an%20elemental,a%20mass%20spectrometer%20%E2%80%93%20the%20MS.
172. Fournier, M., et al., Glass dissolution rate measurement and calculation revisited. Journal of Nuclear Materials, 2016. 476: p. 140-154.

4 Geomelt® Samples

The aim of this chapter is to analyse and assess a series of Geomelt® samples that Veolia have produced as part of feasibility studies for both USA and Japanese equivalent ILW waste types (Section 3.1.1.1). Vitrified products are analysed with a variety of techniques with specific focus on the type and quality of the waste product, how well it incorporates the waste elements, including the radionuclides tracers and how this effects the vitrified products performance.

4.1 Compositional Analysis

The average oxide elemental composition of the four Geomelt® glasses, KBasin, DBVS, MRI4 and MRI7 (Table 4.1) was measured using laser ablation ICP-OES.

Table 4.1 Measured composition (mol %) of the four Geomelt® samples laser ablation ICP-OES (standard deviation is in brackets), elements have been split into roles in the glass network.

Component	KBasin	DBVS	MRI4	MRI7
Network Formers				
SiO_2	77.27 (0.23)	55.14 (0.22)	54.47 (0.26)	49.46 (0.17)
B_2O_3	<0.01	4.58 (0.05)	5.47 (0.08)	9.19 (0.12)
P_2O_5	0.02 (<0.01)	0.08 (<0.01)	0.02 (<0.01)	0.03 (<0.01)
Intermediate (Former)				
Al_2O_3	8.16 (0.11)	6.33 (0.05)	6.72 (0.01)	7.94 (0.09)
Network Modifiers/Charge Balancers				
Li_2O	0.01 (<0.01)	0.01 (<0.01)	8.67 (0.26)	8.39 (0.07)
Na_2O	2.07 (0.02)	21.18 (0.14)	11.56 (0.15)	9.05 (0.06)
K_2O	1.05 (0.01)	1.12 (0.01)	0.30 (0.01)	0.39 (<0.01)
Cs_2O	<0.01	<0.01	0.01 (<0.01)	0.01 (<0.01)
MgO	2.55 (0.02)	2.28 (0.02)	1.25 (0.03)	1.52 (0.01)
CaO	3.71 (0.10)	3.40 (0.05)	1.62 (0.08)	7.92 (0.08)
BaO	0.03 (<0.01)	0.03 (<0.01)	0.04 (<0.01)	1.54 (0.01)
SrO	0.02 (<0.01)	0.02 (<0.01)	0.09 (0.01)	0.13 (<0.01)
Transition Metal Oxides				
Y_2O_3	<0.01	<0.01	<0.01	<0.01
TiO_2	0.71 (0.01)	0.66 (0.01)	8.80 (0.15)	0.13 (<0.01)
ZrO_2	0.38 (0.01)	3.57 (0.02)	0.01 (<0.01)	1.52 (0.01)
HfO_2	<0.01	0.04 (<0.01)	0	0.02 (<0.01)
V_2O_5	0.01 (<0.01)	0.01 (<0.01)	<0.01	1.39 (0.08)
Cr_2O_3	<0.01	<0.01	0.01 (<0.01)	<0.01
MnO	0.07 (<0.01)	0.06 (<0.01)	0.02 (<0.01)	0.02 (<0.01)
Fe_2O_3	1.47 (0.01)	3.26 (0.04)	1.28 (0.01)	0.93 (0.03)
NiO	<0.01	<0.01	<0.01	0.06 (0.05)
Lanthanides				
La_2O_3	0.17 (<0.01)	<0.01	<0.01	<0.01
Ce_2O_3	0.35 (<0.01)	<0.01	<0.01	<0.01
Pr_2O_3	0.03 (<0.01)	<0.01	<0.01	<0.01
Nd_2O_3	0.10 (0.01)	<0.01	<0.01	<0.01
	99.97	99.97	99.99	99.99

KBasin has high contents of SiO_2 and Al_2O_3 which will form the framework of the glass structure and are sourced from the Hanford soil added as a glass former [1]. The soil also significantly contributes to the CaO, Fe_2O_3, Na_2O, K_2O, TiO_2 and MgO levels in the glass [1]. In the KBasin glass other significant elements come from the waste simulants added to the melt including, Fe_2O_3, ZrO_2, Al_2O_3 and SiO_2. Lanthanides (Ce_2O_3, Nd_2O_3, Pr_2O_3 and La_2O_3) and rare earths are surrogates and represent waste uranium, actinides and fission products. The ratio of lanthanides is analogous to the additions although measured as oxides not metallic elements showing that there has been minimal loss and the glass has incorporated most of the radioactive simulants, other rare earths were individually <0.01 % (Table 4.2) [1].

Table 4.2 Lanthanide and rare earth ratios in batch and measured glass compositions (standard deviation is in brackets).

Lanthanide	Fraction batched as elemental ratio to total lanthanides and RE [1]	Fraction measured as elemental ratio to total lanthanides and RE.
Ce	0.50	0.53 (<0.01)
La	0.22	0.25 (<0.01)
Nd	0.18	0.16 (<0.01)
Pr	0.06	0.05 (<0.01)
Rare Earths	0.04	0.002 (excludes Sc and Pm) (<0.01)
	1	0.99

DBVS composition matches closely to the batch composition and lies within the idealised glass composition aimed for in the DBVS project (Table 4.3) [2, 3]. Elevated levels of Na_2O are due to the high levels in the salt waste [4] diluting the glass formers like SiO_2 and Al_2O_3. Elevated levels of ZrO_2 and B_2O_3 are due to the addition of these elements to improve glass properties [2, 3, 5-9] There was virtually no (0.0001 wt.%) Re_2O_7 (TcO_2) detected in the DBVS sample suggesting it was volatised during the vitrification and not encapsulated in the glass.

For MRI4 and MRI7 it is less clear what the feed was. No soil was used in vitrification with the waste and individual glass additives (B_2O_3, Li_2CO_3, ZrO_2…etc) contributing to the final waste composition [10]. Herschelite ($(Na_2,K_2,Ca,Sr,Mg)_2[Al_2Si_4O_{12}]_2\ 12H_2O$) [11-14] forms the basis of the ion exchangers the glass was designed to immobilise and predominantly supplies the majority of the glass formers in the wasteform. Variation o*f* these elements, and levels of elements like B_2O_3, Li_2CO_3 and, ZrO_2 are from additions of glass additives added to optimise the glass properties [10, 12]. Elevated levels of TiO_2 in MRI 4 and BaO, NiO and V_2O_5 in MRI7 are due to high levels of these elements in the simulant waste stream, for NiO, V_2O_5 and TiO_2 there is some variation in the analysis values due to the presence/absence of crystalline phases during spot analysis. MRI4 contains KUR-TSG, a granular tintanosilicate used to remove Sr as part of the KURION mobile system [11, 12, 14]. The MRI7 contains waste from the AREVA system that was an early Sr and Cs removal system that arrived from Europe but was quickly taken out of service due to the inefficient removal of Cs and highvolumes of waste generated. It used co-precipitation to remove radionuclides using barium chloride to precipitate strontium as strontium sulphate, barium sulphate ($BaSO_4$) to remove Sr and nickel ferrocyanides ($M_2NiFe(CN)_6$) to remove Cs, where M is an transition metal. Although not confirmed the high vandium content of MRI7 is assumed to be from vanadium substituting for nickel in the ferrocyanide as vanadium has been proven to be an effective absorber of Cs using cyanoferrate [10, 11, 14-16]. Cs and Sr levels in the two waste glasses are similar showing that the waste compositions have similar retention capability for the surrogates

Table 4.3 Batched and measured compositon of the DBVS glass (wt.%), elements have been split into groups based upon there varying roles in the glass network.

Component	Mass Fraction (Batched) [3]	Mass Fraction (Measured)
	Network Formers	
SiO_2	0.4804	0.4912
B_2O_3	0.0500	0.0473
P_2O_5	0.0058	0.0017
	Intermediate (Former)	
Al_2O_3	0.0800	0.097
	Network Modifiers/Charge Balancers	
Na_2O	0.2000	0.1946
K_2O	0.0186	0.0157
MgO	0.0137	0.0136
CaO	0.0285	0.0283
BaO	0.0005	0.0006
SrO	0.002	0.0003
	Transition Metal Oxides	
TiO_2	0.0064	0.0078
ZrO_2	0.0700	0.0652
Cr_2O_3	0.0013	0.0002
MnO	0.0006	0.0008
Fe_2O_3	0.04	0.0349
	Anions	
Cl	0.0003	-
SO_3	0.0035	-
F	0.0001	-
	1.0017	0.9992

of the radioactive components. Estimates of expected Cs levels calculated from input batch values match the measured levels suggesting that the glass has high retention levels for Cs and that the Cs is well and evenly distributed in the glass (Table 4.4) [12]. Estimates of expected Sr levels calculated from input batch values are below the measured levels for both MRI4 and MRI7 suggesting that the glass has high retention levels for Sr and either there is some uneven distribution of Sr in the glass and/or there are also other Sr sources in the waste (see Herschelite above) (Table 4.4) [12]. Interestingly KBasin and DBVS also both have measurable Sr likely sourced from the soil.

Table 4.4 Estimated from (from batched input values [12]) and measured (Laser ablation ICP-MS) levels of Cs and Sr in the MRI4 and MRI7 wasteforms.

Sample	Cs (estimated Batched) wt.% [12]	Cs (Measured) wt.%	Sr (estimated Batched) wt.%)[12]	Sr (Measured) wt.%
MRI4	0.04	0.05	0.05	0.15
MRI7	0.04	0.05	0.05	0.21

Potentially elevated values of the Ti in the MRI4, V in MRI7 and Fe in KBasin, DBVS and MRI4 are possible as it was impossible not to include some crystalline materials in the analysis although corroboration with EDS analysis suggests that this is a minor effect, and the compositions can be used as glass compositions.

4.2 XRD

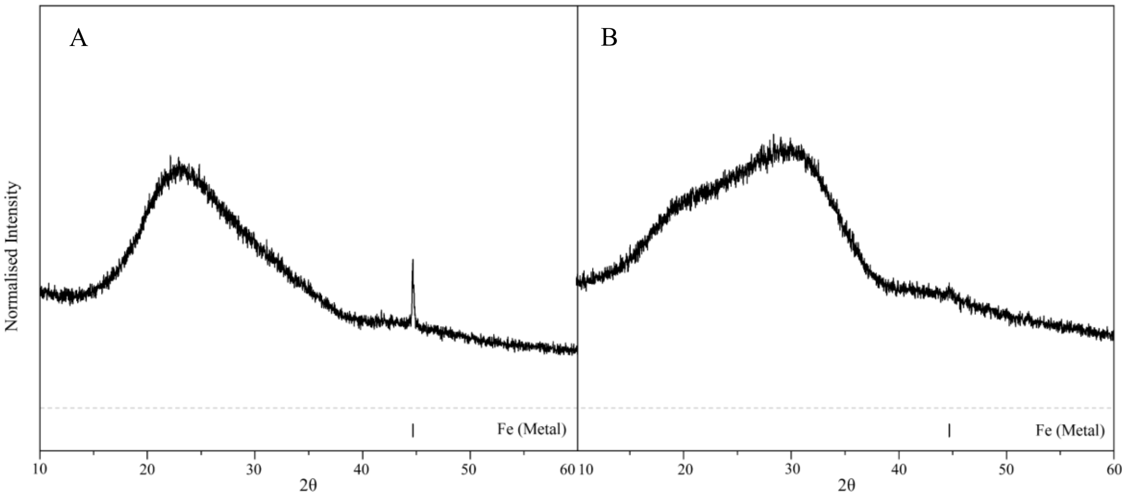

Figure 4.1 XRD pattern for the A-KBasin and B-DBVS samples

All four XRD spectra for the USA Geomelt® wasteforms have a contribution of amorphous scattering from a glass phase (Figure 4.1 and 4.2). In addition, each sample has some well-defined sharp diffraction peaks created by crystallisation phases. KBasin, DBVS and MRI4 have metallic Fe in the final wasteform (Figure 4.1 and 4.2) The MRI4 wasteform also has rutile in the sample in line with the high Ti concentration in the compositional analysis of the wasteform and the original waste (Figure 4.2). The MRI7 samples wasteform has karelianite (V_2O_3) and a spinel phase suggesting that the glass phase cannot accommodate the extra V, Fe and Ni in the wasteform (Figure 4.2). These observations are mostly in line with industrialanalysis of these samples , differing slightly in MRI4 and MRI7 with the absence ofthe extra titanium oxide and cerium oxide phases and the exact karelianite composition [1, 12].

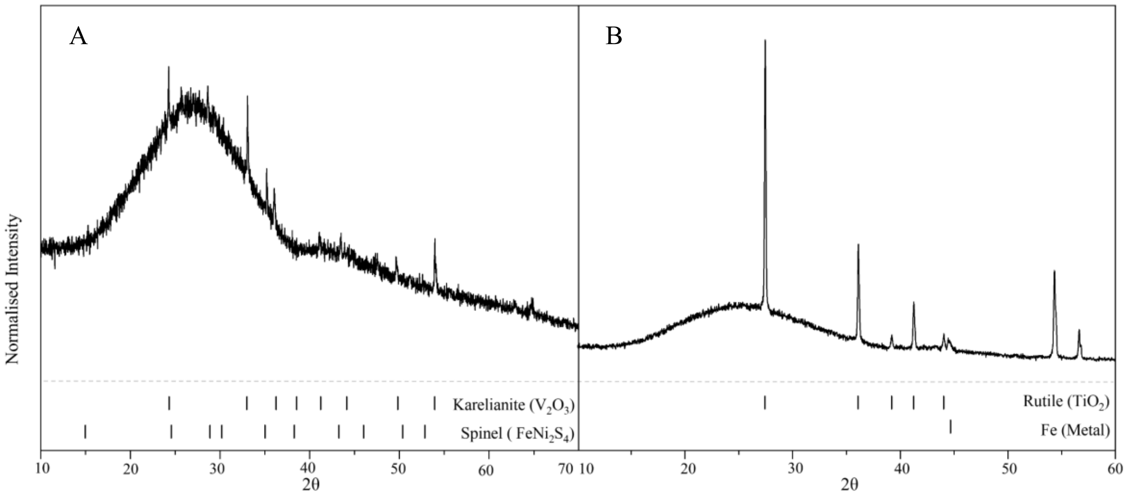

Figure 4.2 XRD pattern for the A-MRI4 and B-MRI7 samples.

4.3 SEM

SEM analysis of elemental distribution in the USA Geomelt® wasteforms is shown in Figure 4.3-4.6. Observations support the measured compositional analysis from this study, the XRD analysis agrees with previous studies [1, 12]. The K Basin glass shows small-medium (<1 to 60 μm) relatively uncommon circular metallic Fe inclusions in a glass matrix, these may include some Ca and Ce although the lower concentration of these elements may cause distribution to be influenced by SEM detection limits. The glass matrix appears to incorporate the other elements and shows an even distribution across the sample (Figure 4.3).

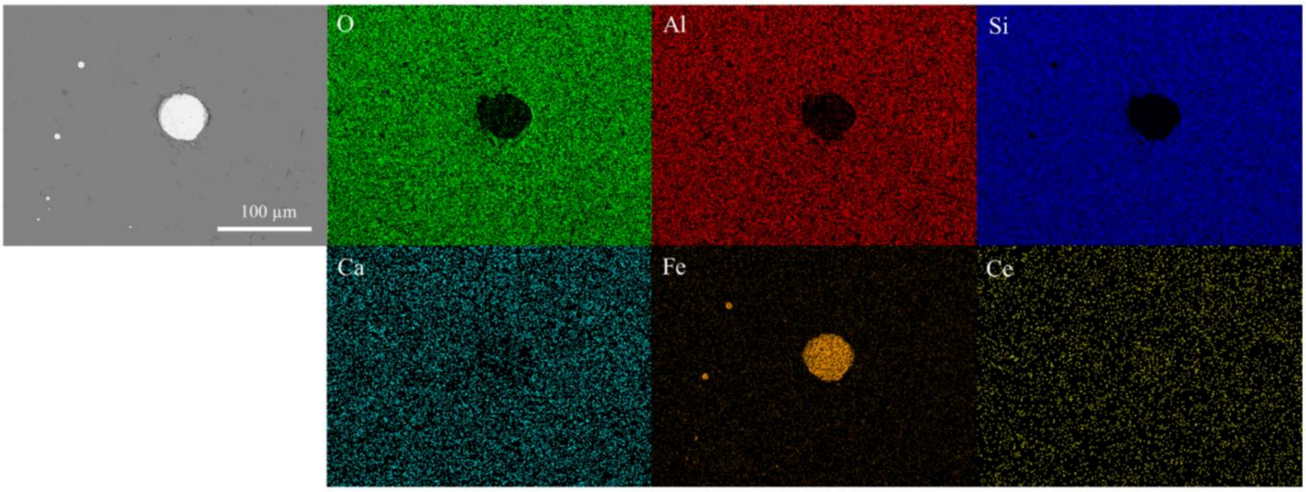

Figure 4.3 SEM image and EDS maps of major elements for the KBasin sample.

The DBVS glass shows small (<1 to 5 µm) relatively uncommon cubic metallic Fe inclusions, the glass phase again incorporates the other elements with even elemental distribution at varying concentration, Re was below detection limits and is not included in this analysis (Figure 4.4).

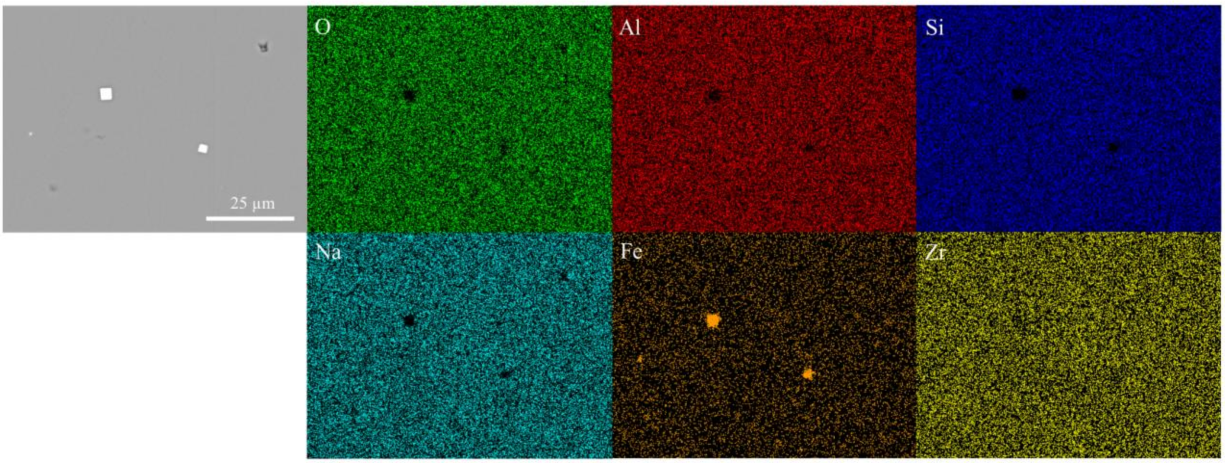

Figure 4.4 SEM image and EDS maps of major elements for the DBVS sample.

The main bulk of the MRI4 sample has common Ti rich thin (1 to 5 µm) long (up to 1 mm) needles of Rutile's in a glassy matrix with no visible incorporation of any other elements that are incorporated in the glassy matrix including Sr. The Cs concentration was too low for meaningful analysis. MRI4 also has common large (0.5-1 mm) rounded inclusion, the content of these appears heterogeneous, but it was not possible to investigate this further in this project (Figure 4.5).

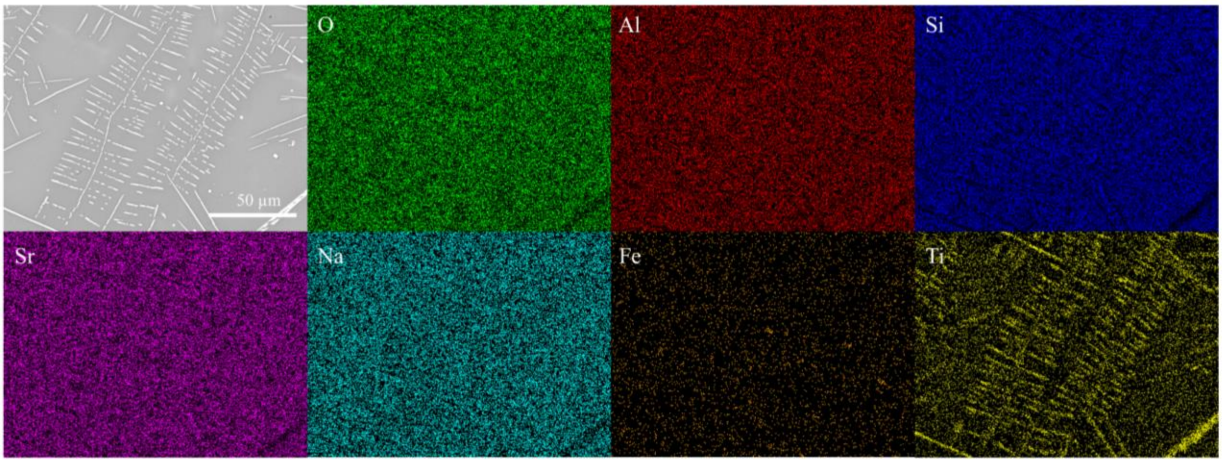

Figure 4.5 SEM image and EDS maps of major elements for the MRI4 sample.

MRI7 shows long (0.1 to 0.6 mm) thin (0.1 µm) needles and cubic crystallites (50 to100 µm) of karelianite which potentially shows elemental V substitution/inclusion for Fe, Ni, S and Zr and Ba (not shown) which has been observed in previous industrial analysis [12]. MRI7 also has rare small (<1 to 5 µm) spherical Fe-Ni-(Zr-Ba) sulphides. In MRI7 the glassy matrix incorporates the other elements at varying concentration and shows even distribution of elements including Sr, but the Cs concentration was too low for meaningful analysis. V appears to be concentrated in the crystalline phase (Figure 4.6).

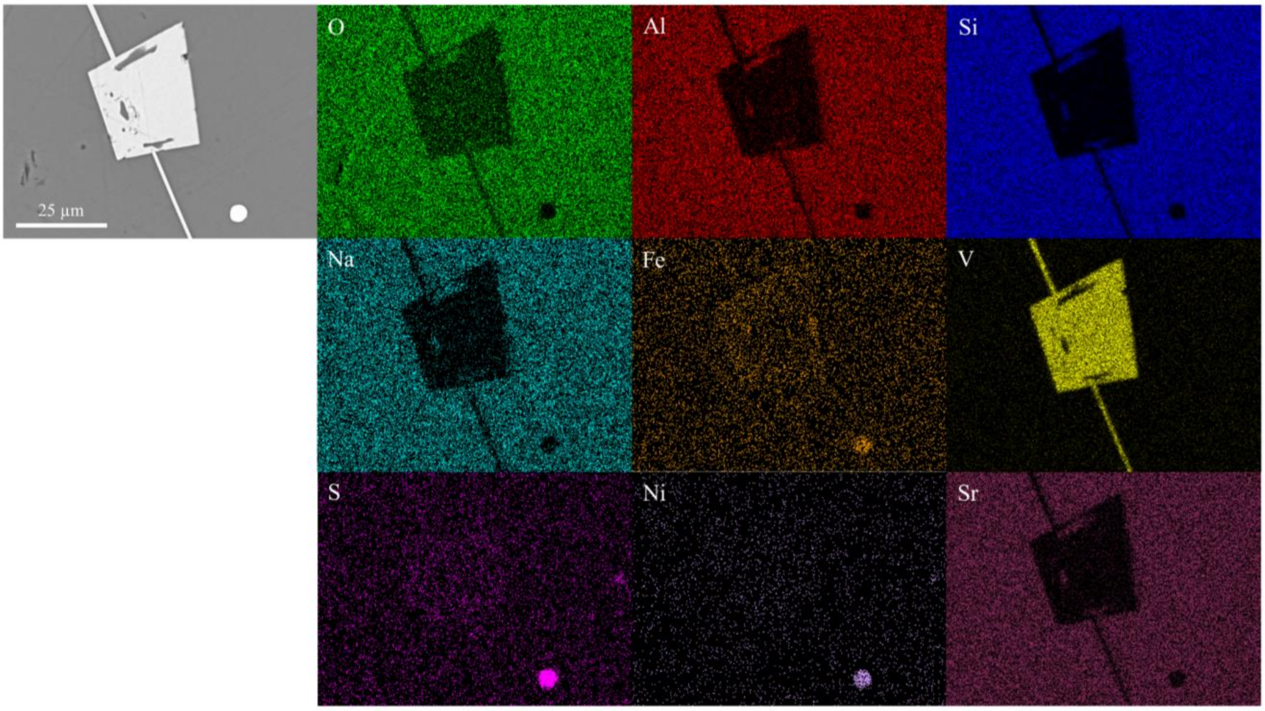

Figure 4.6 SEM image and EDS maps of major elements for the MRI7 sample.

4.4 Density

The density (Table 4.5) for all the USA Geomelt® glasses is similar with MRI7 having the highest density followed by DBVS. These denser glasses have increased levels of high atomic elements like Zr and Ba (Table 4.1) attributing to the slightly elevated glass densities.

Table 4.5 Density values for the four USA Geomelt® samples.

Sample	Density (g/cm^3)
KBasin	2.5388 +/- 0.0083
DBVS	2.6508 +/- 0.0125
MRI4	2.5953 +/- 0.0075
MRI7	2.6555 +/- 0.0081

4.5 Thermal Analysis

The temperature vs heat flow curve (Figure 4.7) shows thermal events that occur during the heating of the sample in a DSC. Exothermic events (crystallisation (T_x)) appear as positive peaks in the curve whereas endothermic events (glass transition (T_g) and melting (T_m)) appear as negative peaks. T_g is defined as the onset of the glass transition/behaviour defined as the intercept of the extrapolated tangents at the endotherm onset [17]. Background issues introduces a caveat to temperature interpretation for the glass transition (T_g) and crystallisation events (T_x) (Figure 4.7 and Table 4.6). MRI 4 is excluded completely from interpretative analysis as there are no major events seen in background profile and it is likely that thermal behaviour is controlled by the behaviour of rutile that is inert at these lower temperatures. A tentative T_g is reported for KBasin, DBVS and MRI7 (Table 4.6) falling in the region for silicate and borosilicate glasses [18, 19] and aligning with predicted values based upon composition, although these values must be treated with caution as the identification of T_g in (Figure 4.7) is hampered by the background signal. The tentatively elevated values in unison with the compositional data would suggest quite high viscosity although this is not thought to be a processing issue due to in container disposal but could pose a risk with volatilisation due to the requirement for higher processing temperatures. These are both areas that require further analysis and testing. Exothermic crystallisation events (Figure 4.7 and Table 4.6) occurs in all the samples (excluding MRI4) at higher temperatures which relates to unidentified crystallisation (T_x) in the sample.

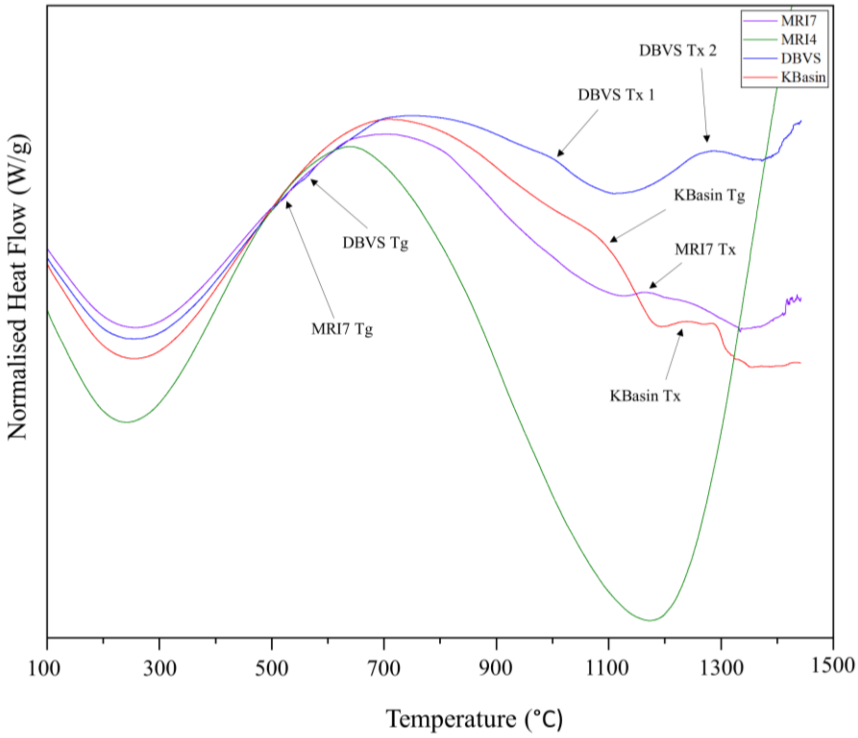

Figure 4.7 Figure showing DSC normalised heat flow data for USA Geomelt® samples versus increasing temperature.

Table 4.6 Estimated En1 (T_g) and Ex1 (T_x) values for the USA Geomelt® samples.

Sample	T_g (°C)	T_m(°C)
KBasin	1095	1240
DBVS	545	995 (1) and 1275 (2)
MRI7	550	1165

4.6 X-ray Absorption Spectroscopy (XAS)

The features of X-ray absorption spectra can be used to investigate the structural environment of different cations in the glass.

Transition metals Fe and V can be present in variable oxidation states and co-ordination environments, allowing elements like Fe to undertake different roles in the glass network, depending on the redox conditions [20]. X-ray absorption spectroscopy (XAS) techniques using comparisons to standard material are used to investigate the local environment.

Visual comparisons of data taken from the X-ray absorption near edge spectroscopy (XANES) region, or the fingerprint technique, and linear combination fitting of standard profiles allow comparison to the local environment in standard material [21]. Confidence in the standard material for both V and Fe is seen by replication of the shape of previous measurements [22-28]. The complicated nature, multiple peaks and the presence of metallic Fe which has been shown to effect the energy position [29] of the absorption edge make this technique hard for Fe and also V. XANES spectra plotted in Figure 4.8A and B show subtle differences between glasses. All spectra suggest that Fe environment in aegirine ($NaFe^{3+}Si_2O_6$) is the closest matching standard for the local environment of Fe in glass, however EXAFS fitting would be required to determine whether this represented a similar structure regarding nearest neighbour oxygen atoms. The V environment is unclear with several of the standards resembling the sample. The inaccurate and ambiguous nature of these techniques for complicated edges like Fe and V means that it is not used further for these elements in this study but can be useful for elements with simpler edges and lack of other options like Ce (see below).

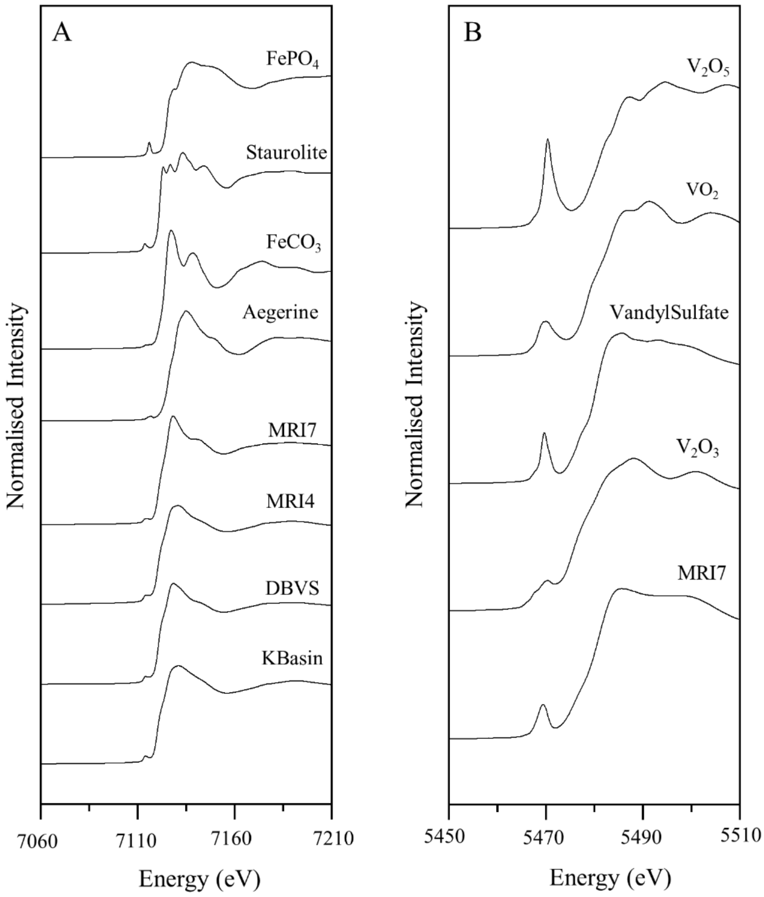

Figure 4.8A Fe K-Edge XANES spectra for the USA Geomelt® samples and 4 standards staurolite, aegirine, $FeCO_3$ and $FePO_4$. B V K-Edge XANES spectra for the USA Geomelt® sample MRI7 and 4 standards: V_2O_5, VO_2, vandylsulfate and V_2O_3.

Table 4.7 E0 positions for Fe K-Edge XANES spectra for USA Geomelt® samples and 4 standards staurolite, aegirine, $FeCO_3$ and $FePO_4$.

Sample	E_0 Energy (keV)
Aegerine	7115.80
Staurolite	7111.59
$FeCO_3$	7114.61
$FePO_4$	7115.40
KBasin	7110.60
DBVS	7109.81
MRI4	7110.21
MRI7	7115.64

Table 4.8 E_0 positions for V K-Edge XANES spectra for USA Geomelt® sample MRI7 and 4 standards VO_2, V_2O_3, V_2O_5 and VanadylSulfate.

Sample	E_0 Energy (keV)
VO_2	5469.6
V_2O_3	5466.2
V_2O_5	5472.4
VanadylSulfate	5471
MRI7	5472

Another aspect of the XANES fingerprint technique is to compare the E_0 position. The definitions and values of E_0 in this study for both Fe and V are generally in line with other studies [23, 25, 26, 29-33]. The position of E_0 should increase with increased oxidation state due to an increase in binding energy [21], however for Fe (and V see later) the complicated nature of the edge makes using the E_0 position hard and genuine shifts can be hidden by ambiguous E_0 definition. However, for this study as consistent approach as possible for defining E_0 was followed and this can be seen in (Table 4.7) where, in general, the E_0 for the standards is shifted to higher energies with higher oxidation state in line with an increase in the electron binding energy. This is mirrored in the samples with lower E_0 energies indication Fe in mainly an Fe^{2+} environment except MRI7 which has a higher energy of an Fe^{3+}environment which disagrees with other techniques (see below) and illustrates the potential ambiguity in E_0 definition relating to the complex structure and angle of the main edge with several peaks in the second derivative making it difficult to definitively identify E_0. As for Fe the E_0 position for the V spectrum is defined in this study as the maximum in the second peak of the first derivative of the XANES spectrum and is calibrated with a vanadium foil to 5465 eV [34]. The E_0 position for V, as for Fe, increases with increased oxidation state in the standards, however the value for the MRI7 sample implies an oxidation state that is higher than the predicted value from other more robust technique (see below) (Table 4.8), this suggests that as for Fe the ambiguous positioning of E_0 and the complex nature of the samples edge make this an unreliable technique for identifying the oxidation state.

In comparison to the shape of the XANES spectra and E_0 position the deconvolution of the pre-edge feature is a more robust method for investing elemental environment in transition metals such as Fe and V. For Fe there have been many studies that have shown that the pre-edge feature can be deconvolved to investigate the oxidation state and co-ordination environment [23, 25, 26, 29-33]. Studies use either Gaussian [23, 26, 31, 33] or pseudo-voigt [24, 25, 29, 30, 32] components to fit the pre-edge feature. For Fe the methodology in [25, 32] was followed using pseudo-voigts to devolve the pre-edge features (see Section 3.2.10) with successful fits of standards in (Figure 4.9A and B). Confidence in the fits is confirmed by the replication of the standard fits for staurolite (Fe^{2+}(IV)), $FeCO_3$ (Fe^{2+}(VI)), $FePO_4$ (Fe^{3+}(IV)) and aegirine (Fe^{3+}(VI) seen in [25, 32]. The position of the pre-edge peak centroid is sensitive to oxidation state and the integrated intensity to co-ordination environment [23, 25, 26, 30-33]. Fitting of the standards allows a comparative figure of oxidation and co-ordination to be created (Figure 4.10), the separation of the average Fe^{2+} and Fe^{3+} is ~1.4 eV which is consistent with other studies [23, 25, 26, 30-33] and allows the investigation of the Fe environment in the samples. The average value for Fe^{2+} may be a little high as $FeCO_3$ as a standard appears erroneously high, however it is used in other studies so, as stated above, reproduces the consistent and comparable plot. Each sample from the Geomelt® trials was fitted each with 2 variable pseudo-voigts with peak centroids close to 7105 eV (Figure 4.9A and B) indicating that the Fe in all USA Geomelt® glass is Fe^{2+}. Variable peak intensities indicate variable co-ordination environment for Fe in the Geomelt® glasses with all glasses having variable tetrahedral/octahedral contribution and sitting in the mixed '5-fold' co-ordination either being a mix of 4- and 6-fold sites or co-existence of 4, 5 and 6 coordinated sites [20]. The Fe^{2+} in these sites will undertake a network modifier role depolymerising the network by creating non-bridging oxygens whilst forming two ionic bonds that can nevertheless increase network strength when compared to monovalent network modifiers [20].

V pre-edge fitting is not as well developed as a technique as Fe pre-edge fitting however previous fitting of a range of organic and inorganic compounds [22, 24, 27] shows that there is general relationship between the oxidation state/co-ordination environment and the pre-edge parameters. For V the same technique as for Fe was employed using pseudo-voigts to deconvolve the pre-edge feature for sample MRI7 (the only sample to have measurable amounts of V) and comparison of this fit to that of standards in (Figure 4.11). Successful fits (Figure 4.11) for reagent grade V_2O_5 (V^{5+} (distorted square pyramidal)), V_2O_3 (V^{3+}(distorted VI)), VO_2 in (V^{4+}(distorted VI)) and (V^{3+}(distorted VI)), Vanadyl Sulfate ($VOSO_4.H_2O$) (V is present as V^{4+} (distorted VI) in the vanadyl cation surrounded by 5 H_2O molecules in a $[VO(H_2O)_5]^{2+}$ cation) match any previous studies [22, 24, 27, 35-38]. Fitting of standards allows the construction of comparison plots (Figure 4.12 and 4.13), pre-edge centroid position is sensitive to oxidation state, there is some ambiguity if peak height or integrated intensity is better correlated to co-ordination environment [22, 24, 27], both are plotted here to allow comparison to the MRI7 sample. MRI7 can be fitted with two pseudo-voigts with a peak centroid at 5460.2 eV, indicating that the V in this case is V^{3+}. Both peak height and integrated intensity showing that the V is in a distorted octahedral site geometry. MRI7 contains a large amount of karelianite (V_2O_3) crystallisation which will impact the XANES spectral position and will confuse the signal from the vanadium in the glass, meaning attributing the above interpretation to purely the V environment in the glass needs to be treated with caution.

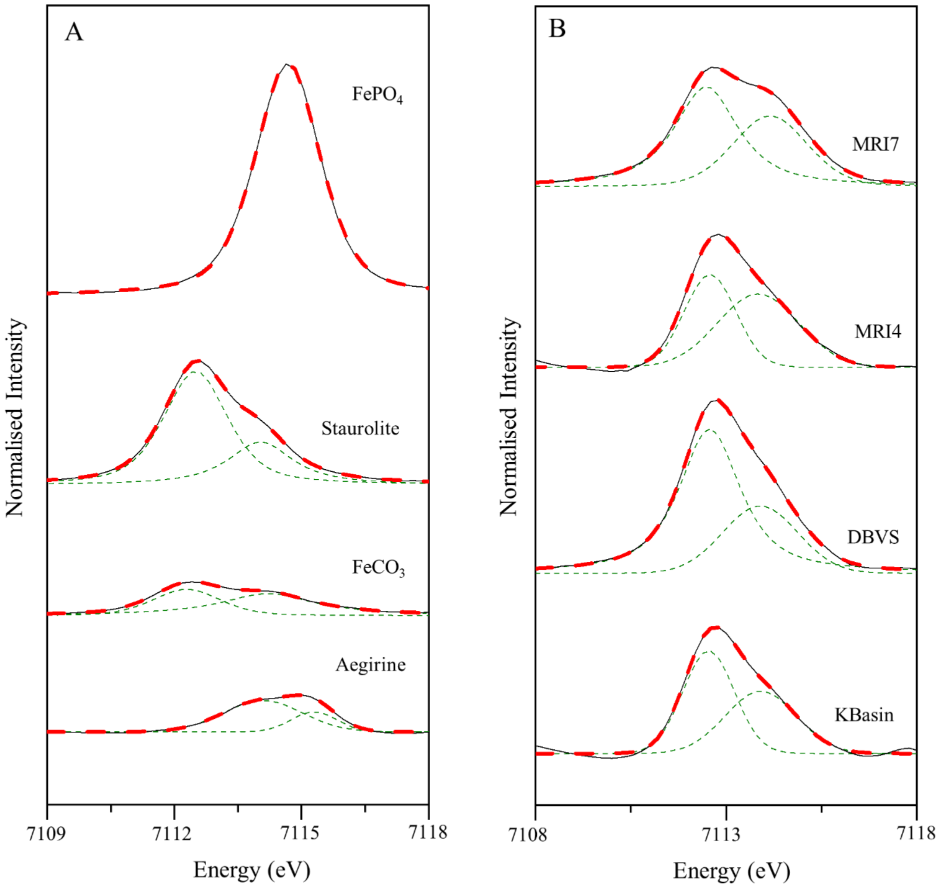

Figure 4.9A - Fitted pre-Fe K Edge XANES spectra for 4 standards staurolite, aegirine, $FeCO_3$ and $FePO_4$. B- Fitted pre-Fe K-Edge XANES spectra for USA Geomelt® samples.

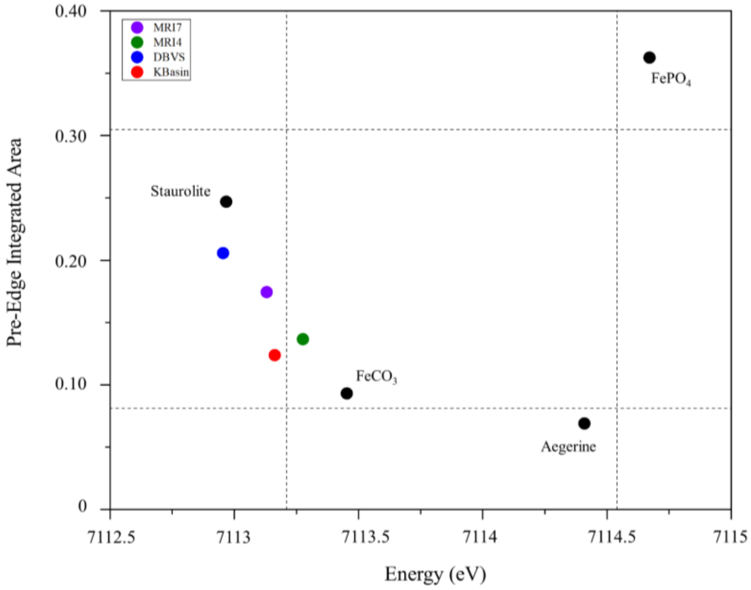

Figure 4.10 Pre-edge integrated intensities and centroid position for 4 standards and USA Geomelt® samples.

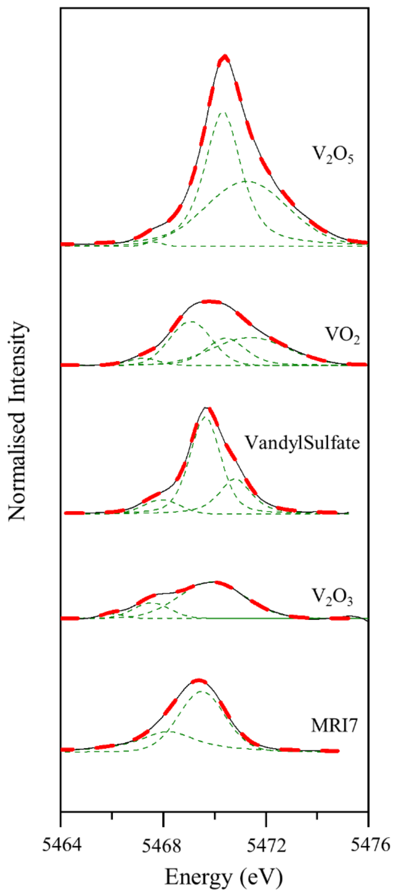

Figure 4.11 Fitted pre-V K-Edge XANES spectra for MRI7 and 4 standards V_2O_5, VO_2, VandylSulfate and V_2O_3.

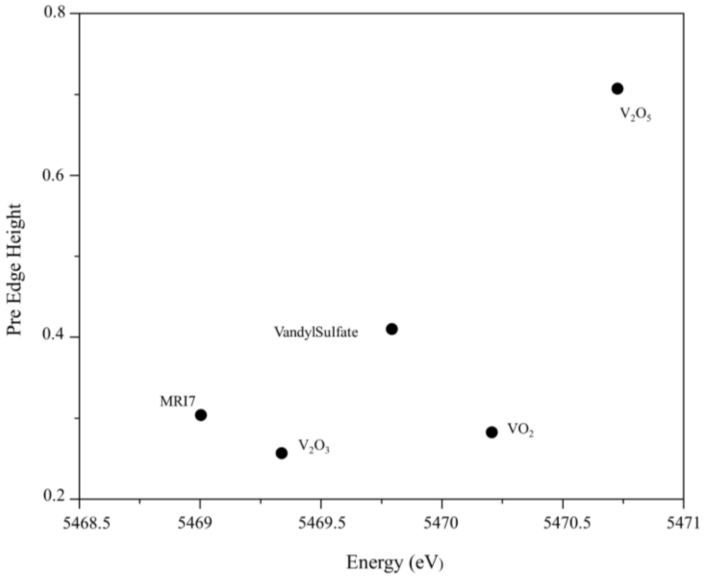

Figure 4.12 Pre-edge integrated area and centroid position for 4 standards and MRI7.

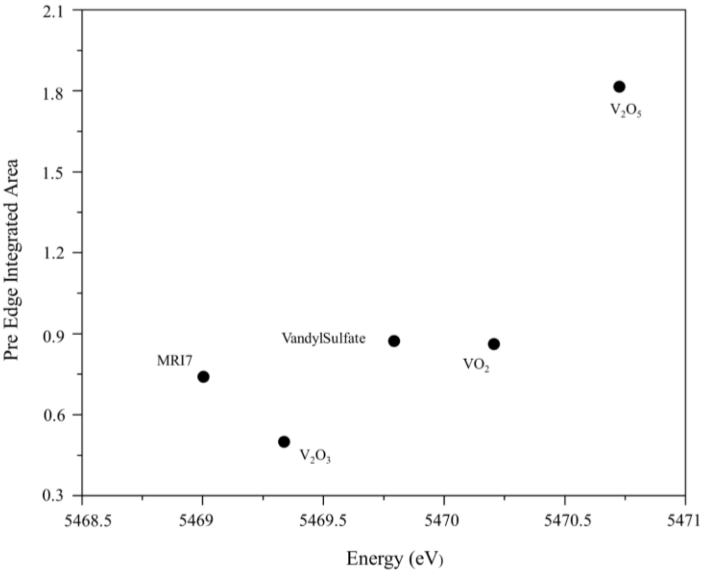

Figure 4.13 Pre-edge height and centroid position for 4 standards and MRI7.

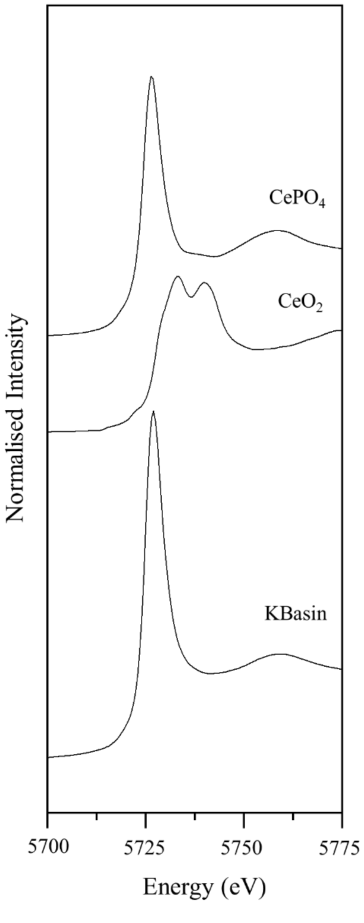

Figure 4.14 Ce L3-Edge XANES spectra for the USA KBasin sample and 2 standards CeO_2 and $CePO_4$.

Ce is the major element in the KBasin simulant representing radioactive actinide species Pu and U. Unlike Fe and V as a non-transition metal Ce has no pre-edge therefore this technique for determining oxidation and co-ordination is not available, however shape of the Ce XANES spectra is simpler and has been shown to very sensitive to oxidation state and is more independent of co-ordination and ligand species [39, 40]. The Ce L3-Edge is very sensitive to Ce oxidation state and fingerprint analysis and linear combination fitting of standards allows the determination of the Ce oxidation state in the CASCe series based upon the features in 2 standards CeO_2 (Ce^{4+}) and $CePO_4$ (Ce^{3+}) (Section 3.2). Fingerprint analysis of the Ce XANES spectra from the KBasin (Figure 4.14) strongly resembles the Ce^{3+} standard which is confirmed with linear combination fitting of the two standards showing zero significant contribution from the Ce^{4+} standard (Section 3.2). As an aluminosilicate, Ce in this glass is likely to be distributed in the modifier network [41] and may mimic Pu due to similar Ce and Pu solubility values [42, 43], although this requires further active work and glass production.

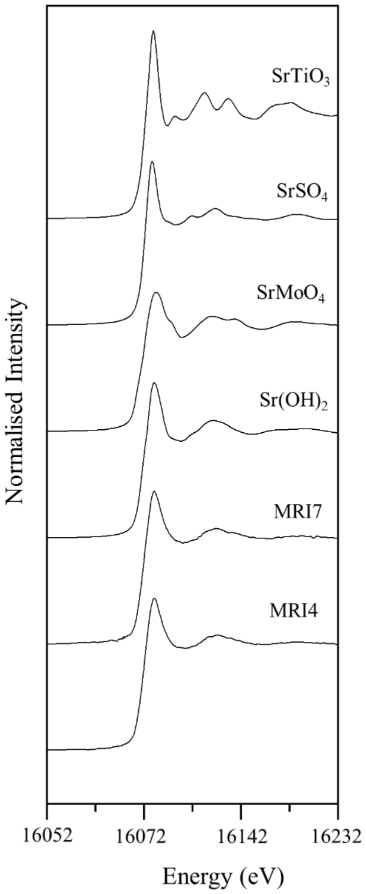

Figure 4.15 Sr K Edge XANES spectra for the USA MRI 4 and 7 sample and 4 standards $SrTiO_3$, $SrSO_4$, $SrMoO_4$ and $Sr(OH)_2$.

Sr is one of the two important radionuclides in the MRI 4 and 7 simulants. Fingerprint analysis of the MRI 4 and 7 spectra (Figure 4.*15*) strongly resembles $Sr(OH)_2$. Consistent 2^+ oxidation state across the standards suggests that the variance in XANES spectra is controlled by co-ordination and local environment. Sr in $Sr(OH)_2$ is in 7-cordinated square face capped trigonal prisms [35] as a 2+ ion the Sr is likely to be distributed throughout the glass as a network modifier.

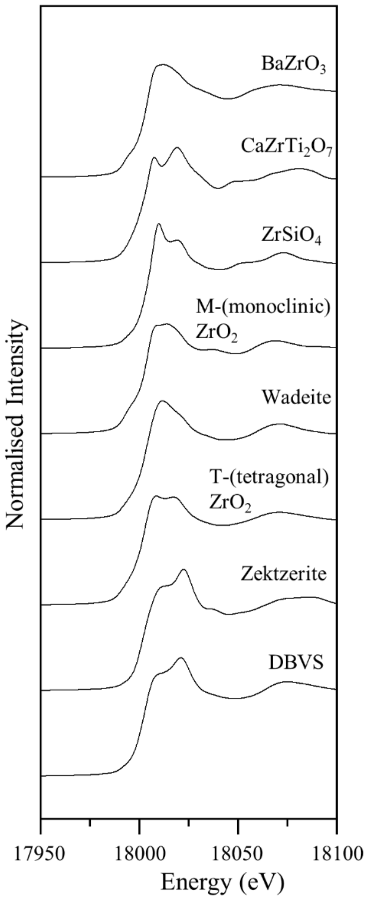

Figure 4.16 Zr K Edge XANES spectra for the USA DBVS sample and 7 standards BaZrO$_3$, CaZrTi$_2$O$_7$, ZrSiO$_4$, MZrO$_2$, Wadeite, TZrO$_2$ and Zektzerite.

Zr is a major element in the DBVS samples. Fingerprint analysis shows that the Zr in DBVS (Figure 4.16) closely resembles a sodium lithium zirconium silicate. The Zr oxidation state is consistent across standards and the sample at 4+ so the shape and position of the XANES spectra is controlled by the co-ordination and local environment suggesting that the Zr is in octahedral co-ordination as found in Zektzerite [44] and in common with other aluminosilicate glasses [45].

4.7 Mossbauer Spectroscopy

Mossbauer spectroscopy was also used to investigate the Fe environment and is a supplemental method to X-ray absorption spectroscopy. Spectra can be fitted with numerous peaks (Figure 4.17) with the position and peak splitting diagnostic of different Fe environments (see Section 3.2.8). Spectra from all the USA glasses are dominated (0.69-0.95) by one doublet centred at an isomer shift of 1-1.1 mm/s with a quadrupole splitting value of 2-2.2 mm/s, this is indicative of Fe^{2+} in either a four (IV) fold tetrahedral coordination for MRI4, MRI7 and DBVS or six (VI) fold octahedral co-ordination for K Basin (Figure 4.18). DBVS, MRI4 and MRI7 glasses have secondary (Table 4.*9*) contributions from isolated Fe^{3+} in a variety of different co-ordination environments. Doublets for MRI4 and DBVS centred at an isomer shift of 0.1 and 0.6 mm/s with a respective quadrupole splitting of 0.6 and 0.5 mm/s indicate four (IV) fold tetrahedral coordination, a doublet at an isomer shift of 0.3 mm/s and a quadrupole splitting of 0.4 mm/s MRI7 indicates six (VI) fold octahedral coordination. The other contribution from KBasin accounts a fraction (0.31) of the signal and has a doublet at an isomer shift of 0.9 mm/s and a quadrupole splitting of 1.4 mm/s this represents a mixed region with Fe in an average Fe$^{2.5+}$ with intermediate IS values created by a delocalisation of electrons around adjacent Fe^{3+} and Fe^{2+} sites (Figure 4.*18*) [46]. QS values generally increase with the distortion of regular shaped cation sites and there may be some evidence for both Fe^{2+} and Fe^{3+} for this with the Geomelt® samples plotting in the middle of the co-ordination ranges (Figure 4.18) [46].

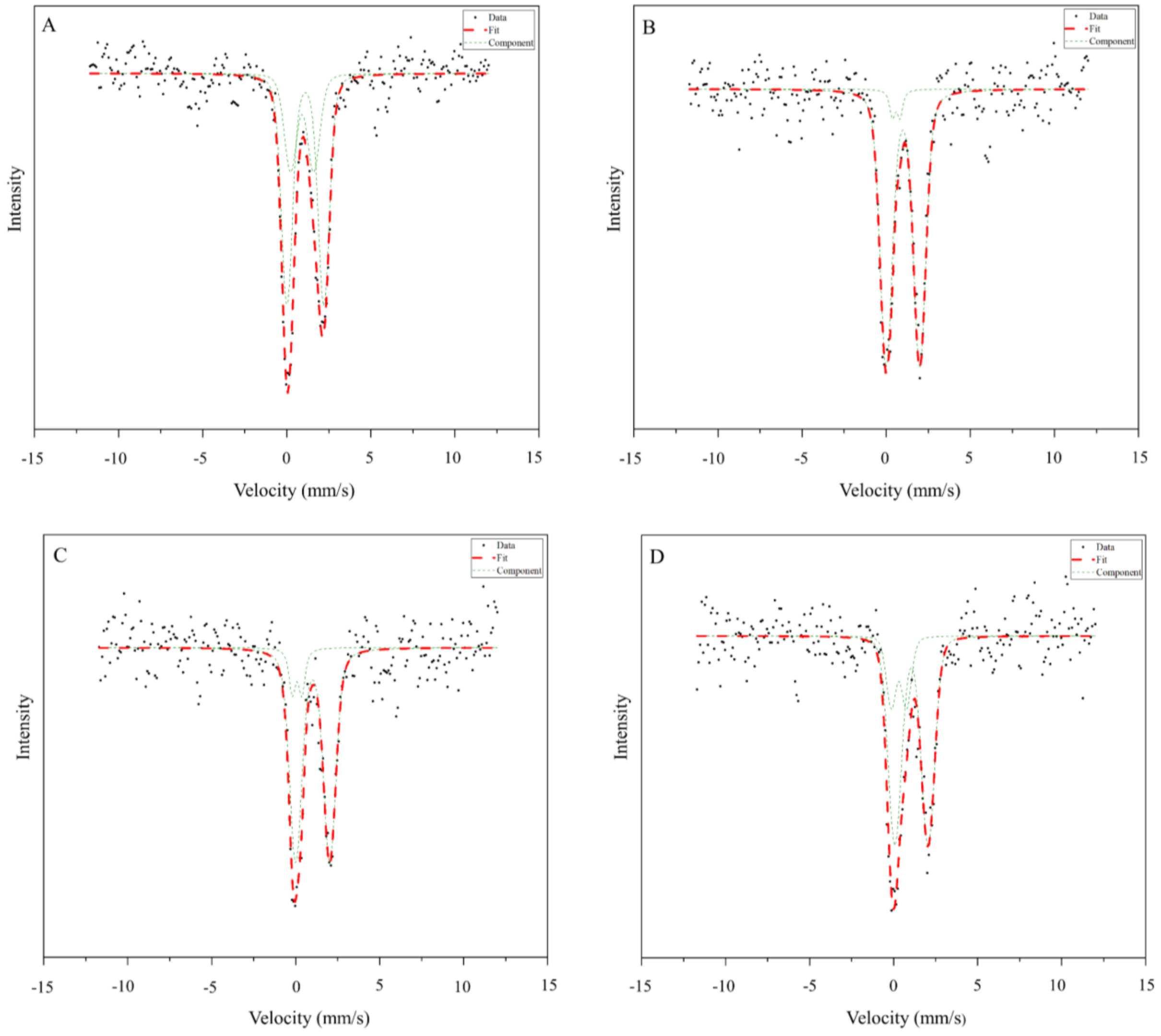

Figure 4.17 Fitted Mossbauer spectra for A-K Basin B-DBVS C-MRI4 D-MRI 7

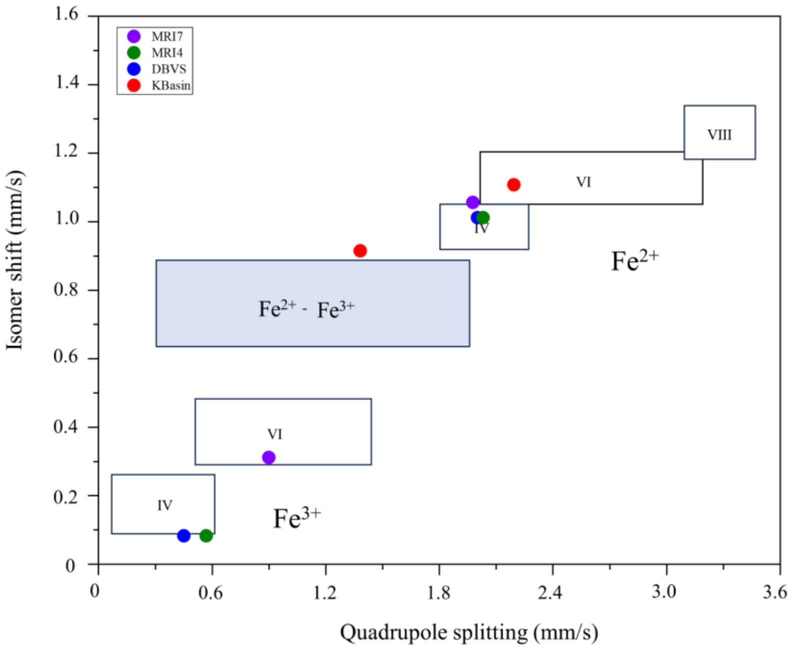

Figure 4.18 IS (Isomer shift) and QS (Quadrupole splitting) diagram from [46] with the values from each fit in (Figure 4.18) plotted.

Table 4.9 Fraction of Fe^{3+} in each sample as a fraction of the total Fe content.

Sample	$Fe^{3+}/\Sigma Fe$
KBasin	0 (note mixed site is not included)
DBVS	0.05
MRI 4	0.11
MRI 7	0.21

It is a common method to compare Fe data from Mossbauer Data and XANES data as complementary techniques for investigating the Fe cation environment. In the USA Geomelt® data there is a mixed agreement between the two techniques. Both show that in all the Geomelt® glasses there is a major contribution from Fe^{2+}, which dominates. The Mossbauer helps deconvolve this signal into Fe^{2+} in Fe (IV) character for DBVS, MRI4 and MRI7 and Fe (VI) co-ordination for KBasin (Figure 4.18). This is supported in the XANES data as although diluted by other Fe sites the KBasin sample has the strongest Fe (VI) signal (Figure 4.10). There is evidence in the Mossbauer of varying different amounts of Fe^{3+} in a variety of different co-ordination environments (Figure 4.18 and Table 4.9), it is hard to deconvolve an estimate of Fe^{3+} from the averaged XANES data, there is a small shift energy shift toward the Fe^{3+} environment in all samples with minor variation between samples (Figure 4.10). The $Fe^{3+}/\Sigma Fe$ (Table 4.9 Fraction of Fe3+ in each sample as a fraction of the total Fe content. has a weak linear trend with the XANES pre-edge centroid position as expected from the literature [33] excluding KBasin and MRI4. It is known that this relationship is unreliable with the presence of metallic Fe that may affect the KBasin sample and to a lesser extent DBVS [29], this may potentially explain the underreported energy value in the KBasin sample despite the significant Fe^{3+} contribution. The higher centroid position value of MRI4 in the XANES data is harder to explain but may relate it to having the lowest Fe content (Table 4.1) and the hardest Mossbauer signal to resolve and interpret.

4.8 Raman Spectroscopy

Raman spectroscopy has been collected for all four USA Geomelt® samples. KBasin, DBVS and MRI7 all represent a typical glass spectrum with a Boson frequency (50-100 cm^{-1}), low frequency (350-550 cm^{-1}), mid frequency (670-850 cm^{-1}) and high frequency (800-1300 cm^{-1}) region (Figure 4.19 and Table 3.20). The shape of DBVS and MRI7 spectra are quite different to the shape of the KBasin due to the varying ratio of the different regions with the KBasin having a more intense low frequency region and a reduced high frequency region with the reverse for DBVS and MRI7. This is analogous with geological igneous rocks on the trend from silica rich ryolite with intense low frequency regions to silica poor basalt with reduced frequency regions. The ryolite graphs also show an increased mid region analogous to the KBasin glass This indicates, as expected from the measured compsoitions, that the synthetic KBasin glass is most representative of a silica rich igneous glass and DBVS and MRI7 are most representative of silica poor igneous glasses [47, 48]. MRI4 has a high level of rutile crystallisation in the sample which made isolation of the glass near impossible therefore the signal is a mix of glass and crystallisation rutile making it impossible to deconvolve and interpret the glass portion of the glass spectrum (Figure 4.19 Raman spectra for the USA Geomelt® samples.. Spectral deconvolution was performed (see Section 3.2.9) on the KBasin, DBVS and MRI7 using variable numbers of Gaussian peaks (Figure 4.20) that allow further interpretation and identification of structural features responsible for the Raman signal. The lower frequency region may show features such as defect bands for the silica rich K Basin and potential Q3 and Q2 vibrations in the more depolymerised DBVS and MRI7 (Table 3.20) however the complicated nature of the glasses makes specific identification in this region an arbitrary exercise. The enhanced mid region in the KBasin glass is likely evidence of increased Si motion either in the Si-O-Si plane or in a rigid cage within a polymerised silicate framework, bands in this region in the other glasses again could have a range of possible sources (Table 3.20). In the higher frequency region, the broader shape in DBVS in comparison to MRI7 could show a shift in Q speciation with an increase in the Gaussian band at ~ 985 cm^{-1} in DBVS broadening the peak and potentially being indicative of an increase in the Q3 species over the Q2 species increasing polymerisation. In the K Basin spectra, it appears that the high frequency region is dominated by higher polymerised structural Q3 and Q4 units. Although care must be taken with this tentative interpretation as other elements could be strongly affecting the Raman shifts. All the glasses except KBasin also show a weak higher frequency peak at ~ 1440 cm^{-1} for DBVS and ~1405 cm^{-1} for MRI 4 and 7 attributed to $BØ_2O^-$ triangles linked to BO_3 units and $BØ_2O^-$ triangles linked to $BØ_4^-$ units respectively suggesting a change in the boron behaviour (Figure 4.18 and Table 3.20).

Although the Raman spectra have been deconvolved using Gaussians and some tentative interpretation has been offered for the different signals, the complicated multi element nature of the glass make individual identification difficult and potentially unreliable due to the overlaps and frequency shifts discussed in (Table 3.20). A more robust technique is to use the Raman Polymerisation Index (RPI) [49, 50] for complex elements to compare to compare the polymerisation and framework connectivity in the different USA Geomelt® samples and quantify the variance see in the areas of the different frequency regions. The RPI looks at the ratio of the low frequency to high frequency region and offers a way of averaging the different signals and comparing the different regions, larger RPI values show an increased lower frequency in comparison to the high frequency region which is indicative of an increase in signals relating to motions in (Si-O°) ring structures in the low frequency region and a reduction in the Si-O$^-$ stretching in depolymerised units in the high frequency region (Table 3.20). The K Basin glass has the largest RPI value followed by DBVS and MRI7 (Table 4.10), these values support the analysis from the deconvolution (Figure 4.20) and the observations seen in geological igneous rocks. This is useful as it allows some predications to be made for the Geomelt® glasses based upon observations of synthetic and natural glasses with higher silica content and RPI predicting higher viscosity, high melt temperature and high chemical durability.

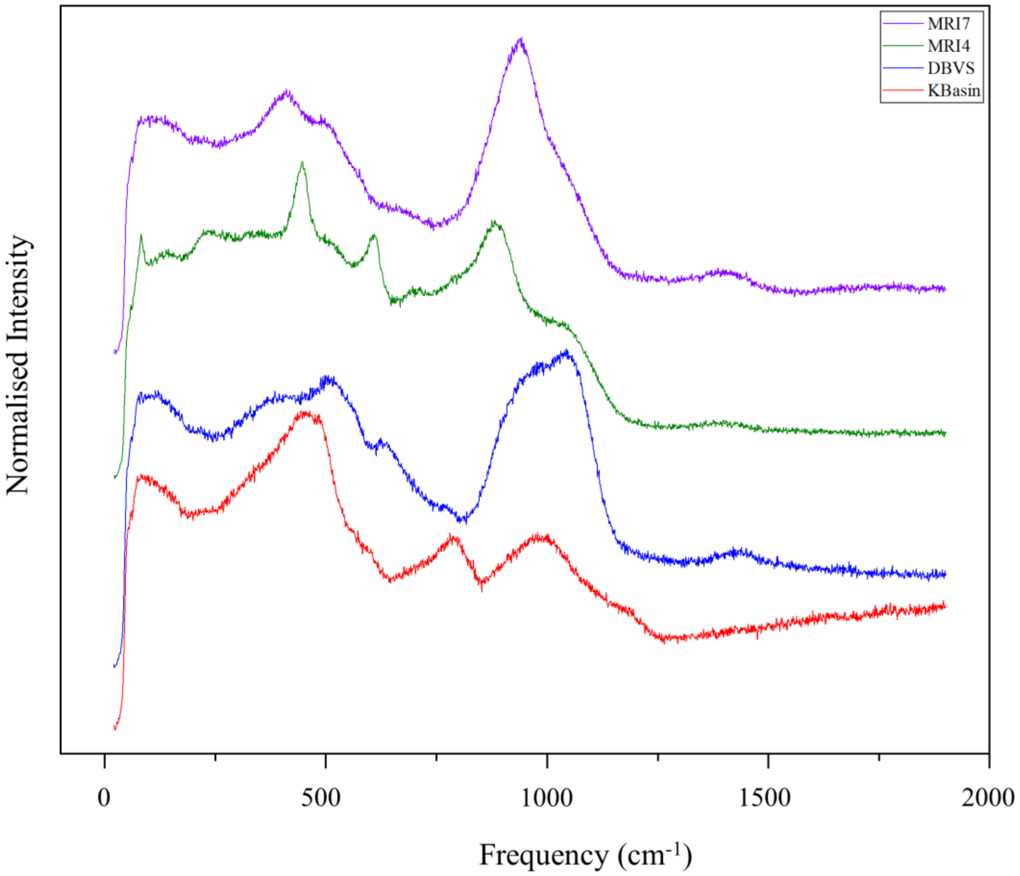

Figure 4.19 Raman spectra for the USA Geomelt® samples.

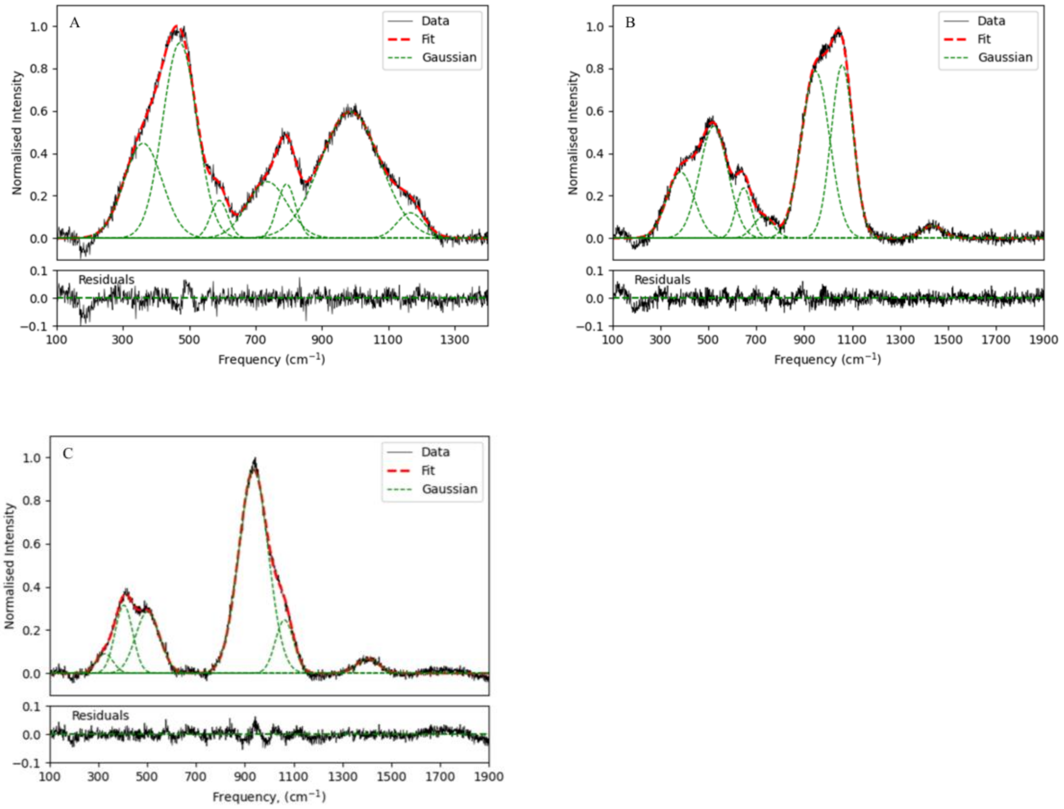

Figure 4.20 Fitted spectra for A- KBasin B- DBVS C- MRI7

Table 4.10 Raman Polymerisation Index (RPI) for the USA Geomelt® samples.

Sample	Raman Polymerisation Index (RPI)
KBasin	1.34
DBVS	0.72
MRI7	0.43

4.9 Glass Durability

To investigate the effects of the structural variation of the different glasses on product durability 2 different durability tests were undertaken both at 90°C in UHQ water: a short-term PCT-B-B test conducted for 35 days, and a long-term MCC-1 monolith test conducted for 12 months. The PCT-B-B uses powdered material to calculate and compare elemental release rates from the waste products and the MCC-1 uses monolith samples to observe the growth and morphology of dissolution layers overtime (see Section 3.2.11).

4.9.1 PCT-B powder Tests

Na, B and Li can be used as tracer elements to calculate glass dissolution rates as these are not expected to interact with the silica gel layer or be included in any secondary alteration phases that could impact on the calculated rates. The only tracer that is common to all four Geomelt® glasses is Na and so this element has been focused on to compare dissolution rates (Figure 4.21 and Table 4.11) for all glasses. KBasin, DBVS and MRI4 show a typical dissolution trend (a fast initial release followed by a rate drop) whereas MRI7 shows an unusual exponential release rate. KBasin, DBVS and MRI4 show an initial rate (NR_0) over the first day then a rate reduction followed by a linear residual rate (NRt) that lasts for the rest of the test. KBasin has the lowest NR_0, NRt and the lowest overall Na release after 35 days which is expected considering the compositional and structural data that shows that KBasin has the highest Si content and polymerisation (see above). SEM images of the KBasin sample after dissolution for 35 days show clear Fe precipitation in between glass grains (Figure 4.22). This is likely $Fe(OH)_3$ which is insoluble under the experimental conditions; the lack of Fe in solution during the PCT-B test supports its precipitation as a secondary phase. Fe-hydroxide precipitation will also lower the pH (Figure 4.24) due to the absorption of OH^- ions from the solution and the maintenance of near neutral pH could also be a contributing factor to the low dissolution rate in the KBasin samples.

DBVS has the lowest (or certainly lower than KBasin) durability related to the high concentration of network modifiers particularly Na. After 35 days, the solution containing the DBVS glass, had a high pH (Figure 4.24) buffered by the elemental release that increase the OH^- concentration in solution and increasing network hydrolysis. MRI4 and MRI7 are harder to compare to KBasin and DBVS in relation to relative durability, this is because both have extensive crystallisation of either rutile (TiO_2) in MRI4 or karelianite (V_2O_3) in MRI7. For MRI4 the rutile appears very insoluble, so it is not directly affecting the solution data, however, because it is incorporated into the compositional data (Table 4.1) it does impact on the dissolution and normalised mass loss calculation by overestimating the Ti levels in the glass. This will impact on the relative position and value of the Na loss and, therefore, resultant calculated rate. The presence of crystalline phases is important when comparing across different glasses and assessing waste form suitability. Although MRI4 has a similar behaviour to DBVS in relation to dissolution and pH (Figure 4.21 and Figure 4.24) the dissolution rate value would be adjusted if a more accurate glass composition could be measured. Ideally, as the radionuclide simulant is isolated in the glass, methods to isolate this glass from the rutile for both compositional, structural (raman) and dissolution tests may give a better understanding of glass structure and behaviour and provide a better measure of radionuclide inclusion and release rate. Possible options for this include use of a higher resolution technique for compositional analysis, for example microprobe analysis. Alternatively, using a different dissolution test like the ASTM 1926-23 Standard Test Method for Measurement of Glass Dissolution Rate Using Stirred Dilute Reactor Conditions on Monolithic Samples [51, 52] that determines the mass loss of material from a sample under dilute conditions by measuring the change in step height between a masked and unmasked area of sample with micron scale precision using a technique such as VSI (Section 6.2).

In MRI7 the crystalline material is more dispersed (Figure 4.6) and like KBasin and DBVS an accurate compositional analysis of the glass was obtained (Table 4.1), however unlike the other wasteforms, MRI7 SEM analysis shows that the karelianite is preferentially dissolving over the glass releasing proportionally more vanadium into the solution. The vanadium speciates dissociates into $H_2VO_4^-$ which has a weak pKa value of 8.8 [53] and is reducing the pH in the MRI7 samples that is having a major effect on the dissolution of the glass (Figure 4.24).

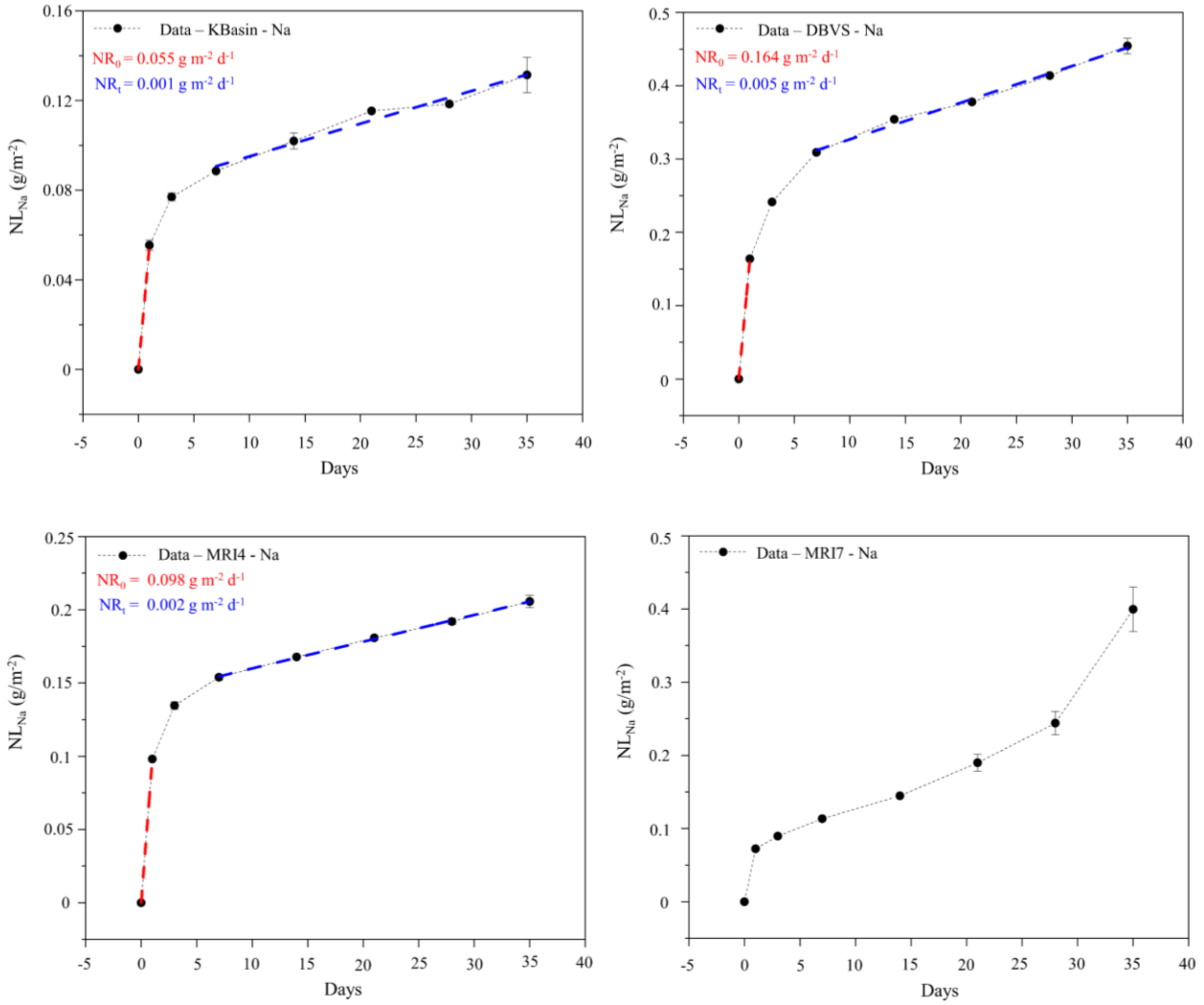

Figure 4.21 Normalised Mass Loss of tracer element Na in PCT-B-B test for K Basin, DBVS, MRI4 and MRI7 with dissolution rates calcualted and shown for initial (red) and residual (blue) time periods.

Table 4.11 Dissolution rates for different elements Na for the different stages: Stage I (initial – NR_0) and Stage II (residual – NR_t).

Sample	NR_0	NR_t
KBasin	0.055	0.001
DBVS	0.164	0.005
MRI4	0.098	0.002

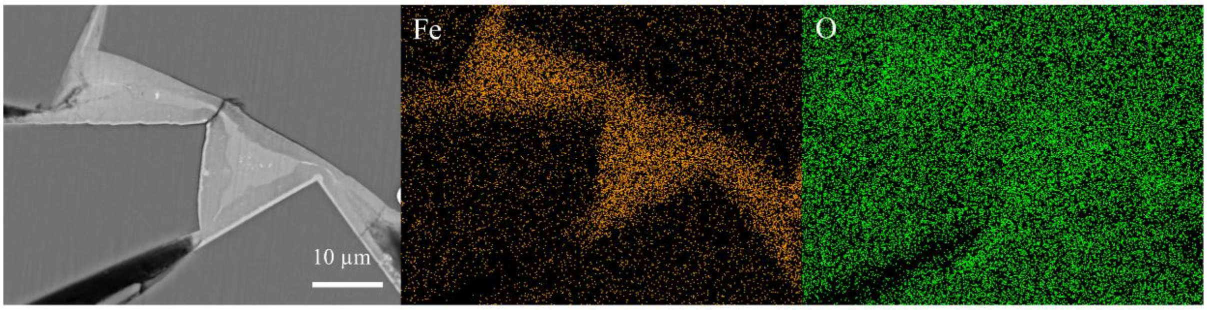

Figure 4.22 SEM image and Fe and O EDS map showing zoned Fe rich precipitates in the 35-day K Basin sample from PCT-B-B dissolution test.

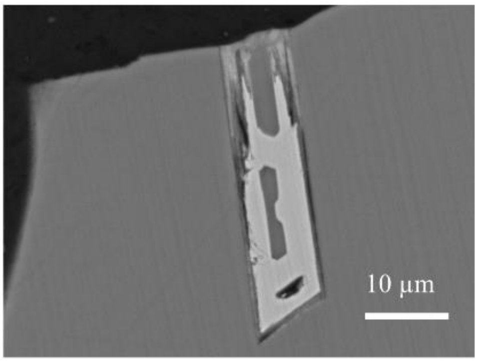

Figure 2.23 SEM image showing the enhanced dissolution of the crystalline karelianite (V_2O_3) in the 35-day MRI7 sample from the PCT-B-B dissolution test.

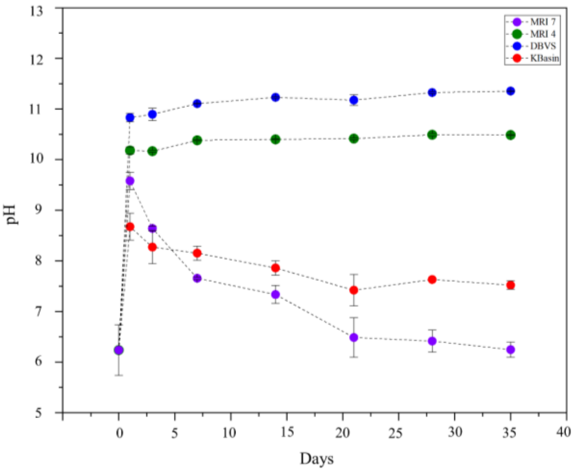

Figure 4.24 pH of the USA Geomelt® samples during the PCT-B-B dissolution test.

The release rates of other elements have been analysed for include Si, Al, Ca, Fe, Mg, Ti and V and the relevant simulant radionuclides for each sample, Ce for KBasin and Sr and Cs for MRI4 and MRI7. The level of Re in solution following 35 PCT tests with DBVS was too low for accountable measurement. Rates traditionally are not calculated from these elements as they are often associated with the precipitation of alteration layers and secondary minerals therefore their concentrations in solution are not always a representation of the rate of glass dissolution. There are clear NL patterns for KBasin, DBVS and MRI4 for groups of elements. The first trend is a classical rate increase drop and residual rate like seen in the Na NL profile and demonstrated by the NL of Si in (Figure 4.25). In addition to Si this trend is also seen in Mg, Ca, Al and potentially Ce (Figure 4.27) in KBasin, Si, Al and Fe in DBVS and Si, Al, Fe, Ti and Cs (Figure 4.28) in MRI 4. This trend is explained by classical dissolution behaviour that is controlling the rate of Na dissolution explained above.

A second trend for some elements shows an initial rate increase then a rate drop before an increasing residual rate and is demonstrated by K in (Figure 4.29) this is seen for Fe in KBasin, K and Mg in DBVS and Sr, K and Mg in MRI4. This pattern is determined as being controlled by precipitation of secondary minerals such as clays or elemental incorporation into a silicate gel layer that is controlling the rate reduction seen in other elements and causes a drop in the rate as elements are removed from solution. The low residual rate that follows is controlled by diffusion through the gel layer and incorporation into secondary phases. The variation in elements between KBasin, DBVS and MRI4 potentially relate to the different pH environments that would control the stability of different phases within or external of the gel layer. SEM analysis of the PCT-B powder didn't show any evidence of alteration or mineral phases except for $Fe(OH)_2$ in KBasin (Figure 4.22) but at this timescale and scale this is not unexpected with potentially gel or very thin alteration layers not visible, however MCC-1 testing (Section 4.9.2) shows evidence of alteration layer formation. In MRI7 the behaviour of the other elements like the tracers is very different, the main additional elements in MRI7 are V, Ca, Mg, Fe, Al, K, Si and Cs and Sr all these elements show an increasing non-linear rate of release and again shows that the reducing pH is having a major effect on the release of elements from the glass and again relates to dissolution of the mineral phase karelianite buffering the reducing pH.

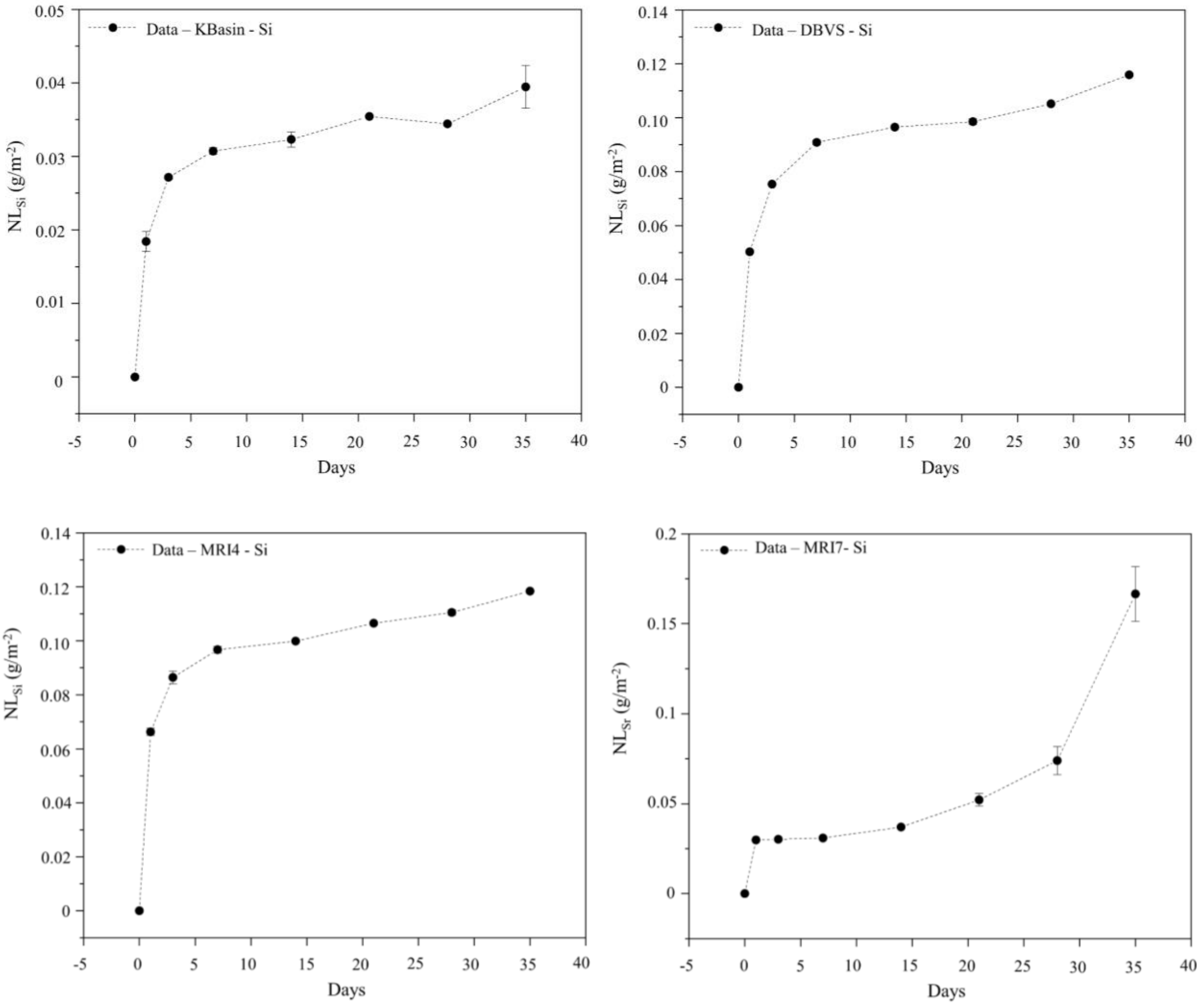

Figure 4.25 Normalised Mass Loss of Si in PCT-B-B tests for KBasin, DBVS, MRI4 and MRI7.

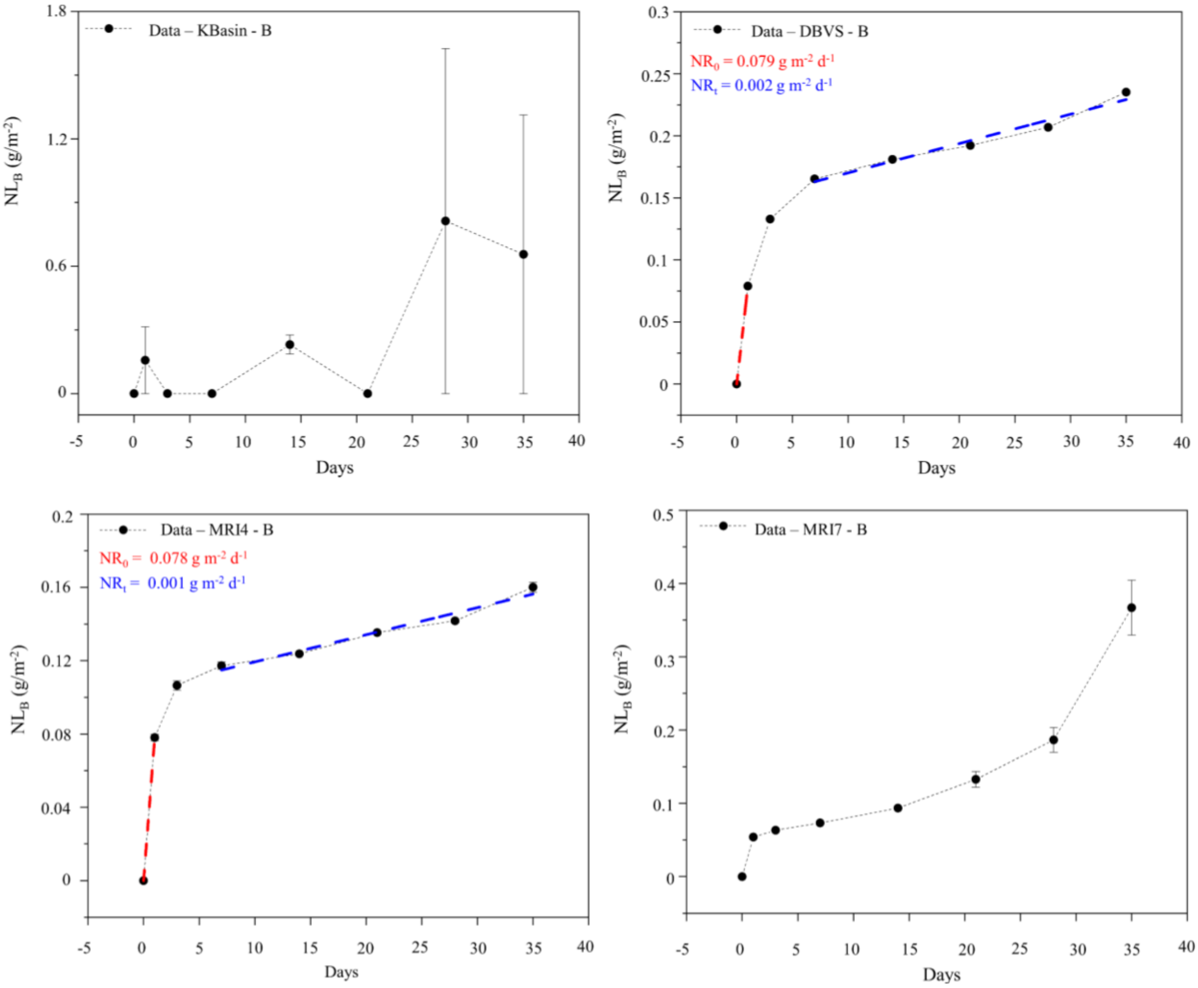

Figure 4.26 PCT-B-B data for the NL mass loss of B for DBVS, MRI4 and MRI7. Levels were too low in KBasin to plot a significant trend.

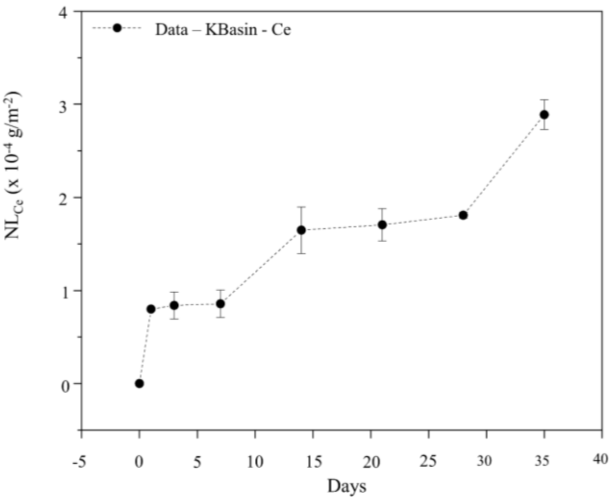

Figure 4.27 Normalised Mass Loss of key radionuclide in PCT-B-B for Ce in KBasin.

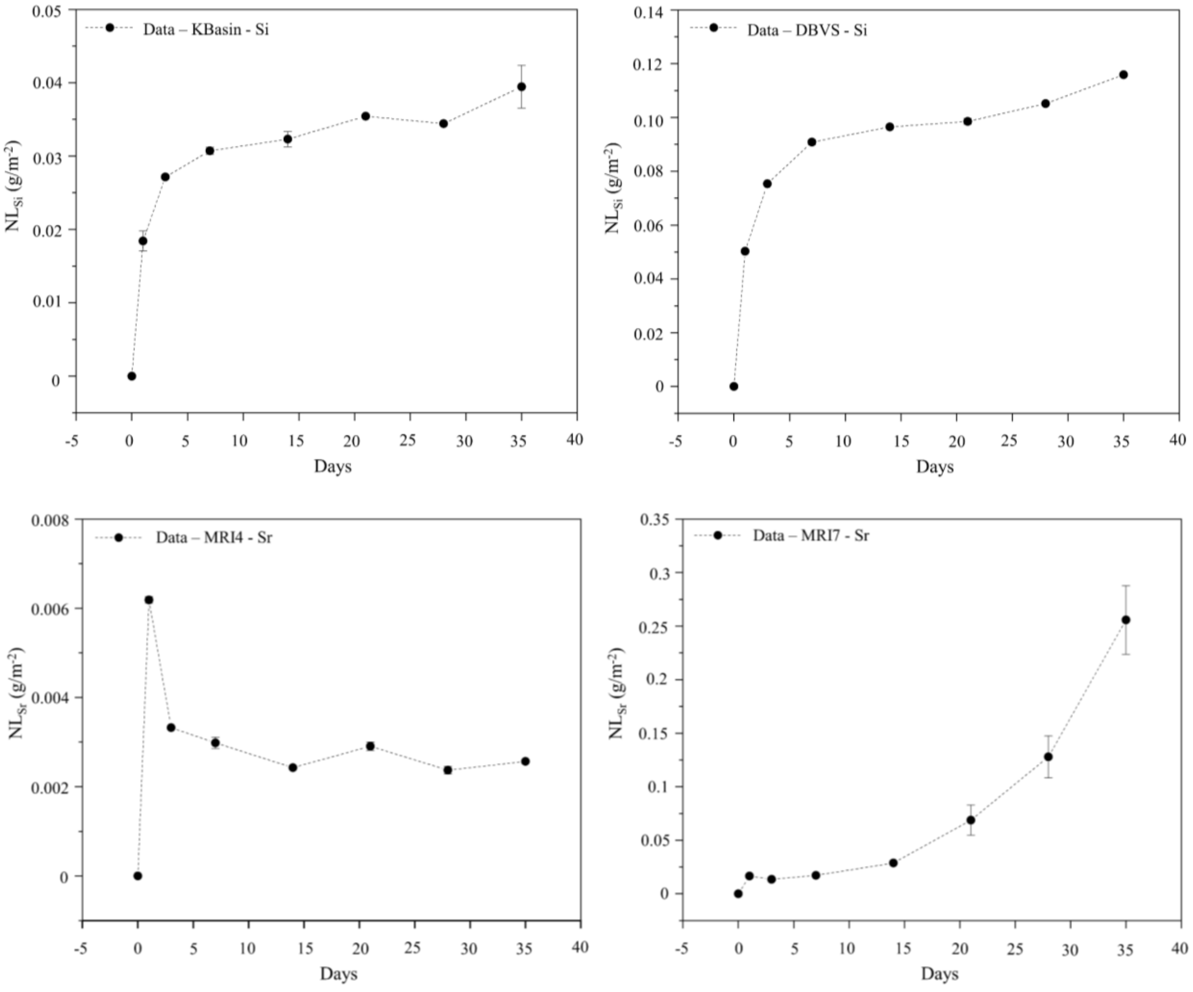

Figure 4.28 Normalised Mass Loss of key radionucildes Cs and Sr in PCT-B-B tests for MRI4 and MRI7.

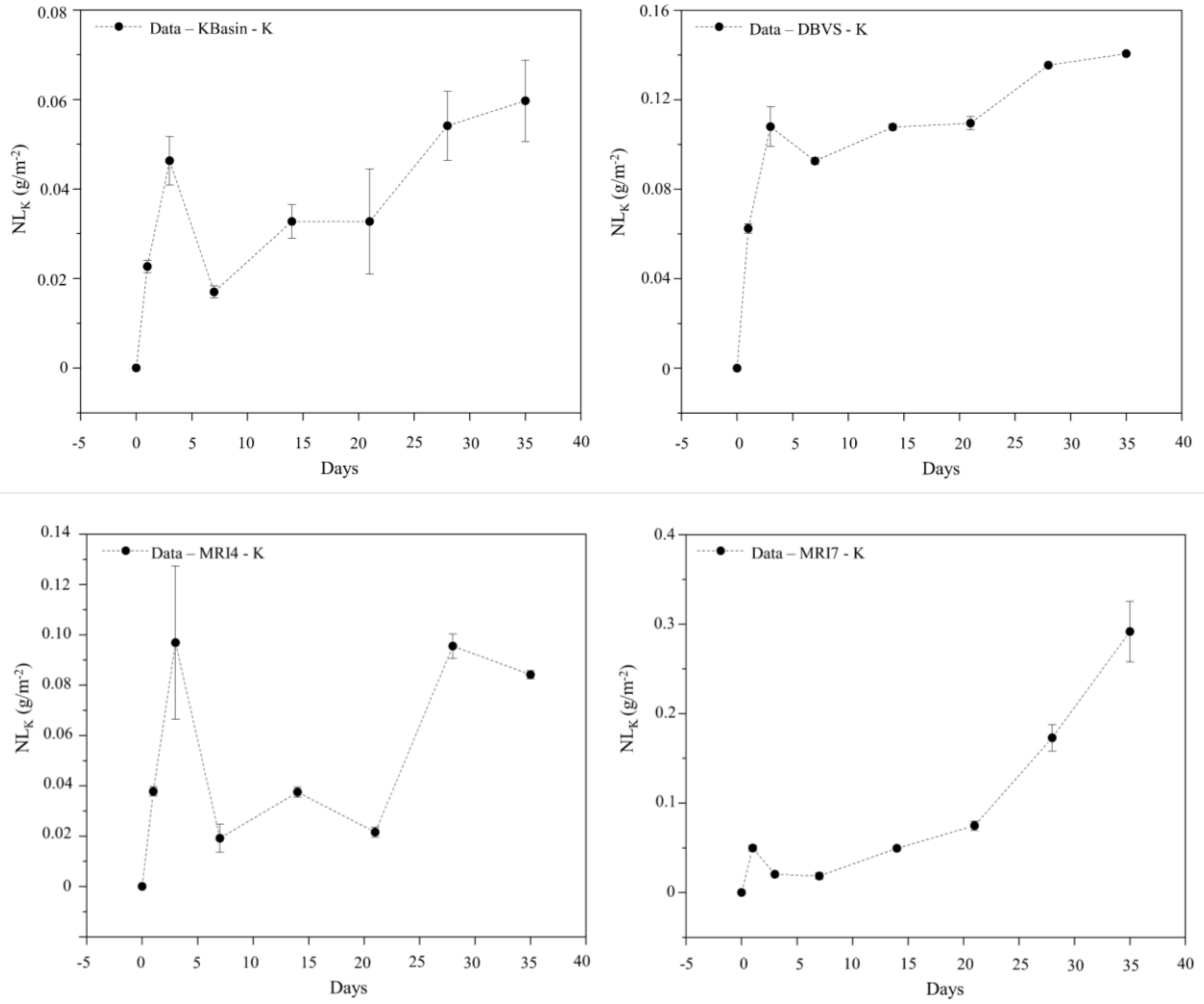

Figure 4.29 Normalised Mass Loss of K in PCT-B-B tests for KBasin, DBVS, MRI4 and MRI7.

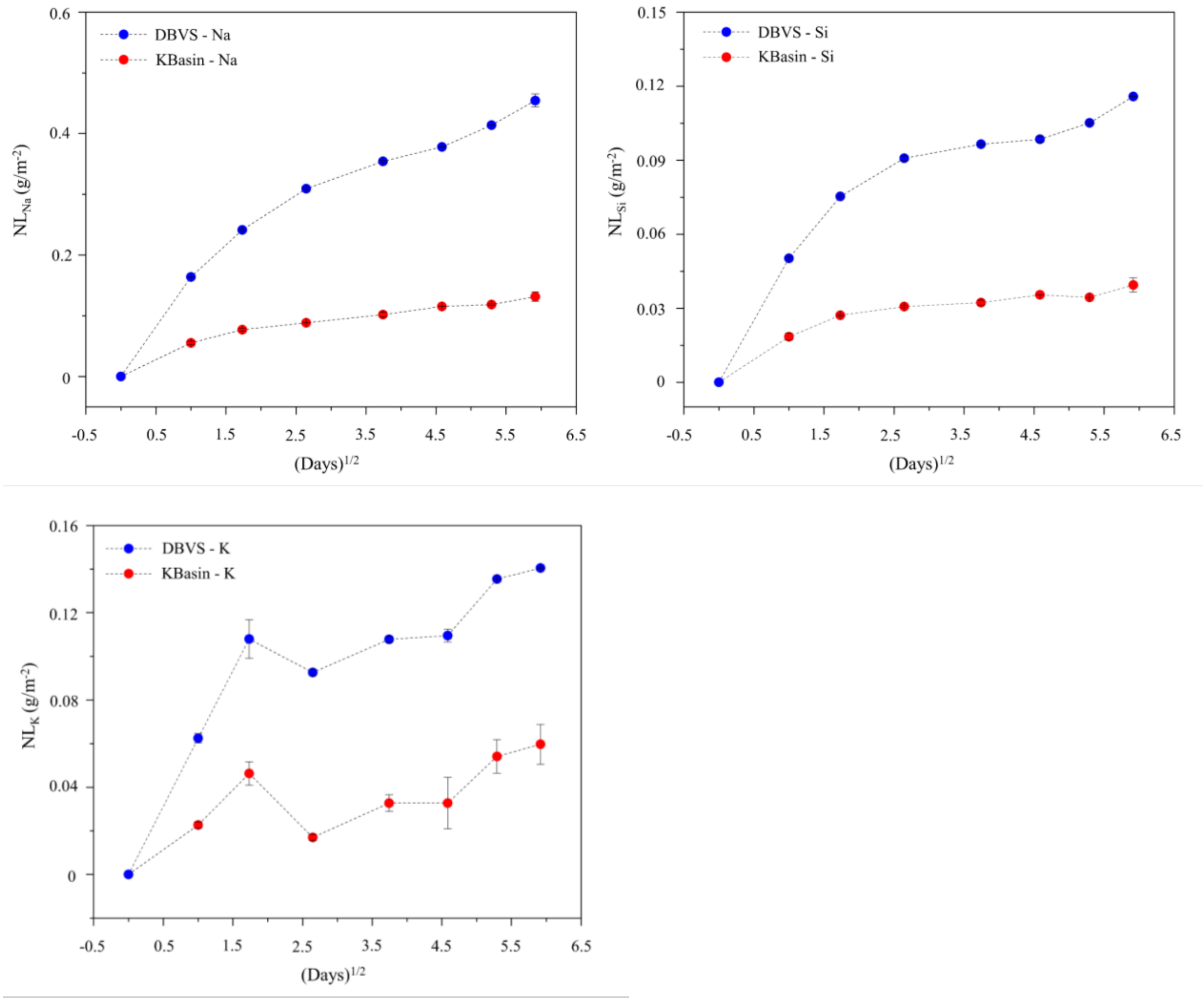

Figure 4.30 $t^{1/2}$ vs NL mass loss graphs for DBVS and KBasin for Na, Si and K.

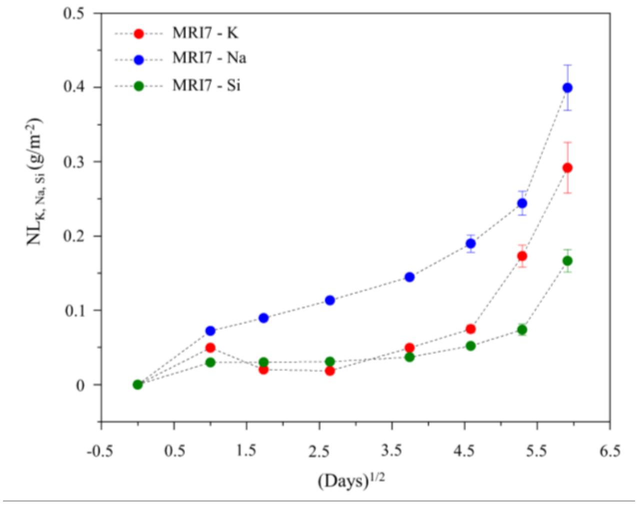

Figure 4.31 $t^{1/2}$ vs NL mass loss graphs for MRI7 for Na, Si and K.

The dissolution literature shows that there is a strong dependence of dissolution rate on pH with accelerated dissolution at both high and low pH and a minimum near neutral pH levels. Recently developed rate equations showed that the rate of glass dissolution is controlled by the concentration of hydronium (H_3O^+), OH^- and H_2O with different processes controlling the dissolution rate under alkaline and acicidic conditions [54-56]. (Figure 4.24) shows that the four glasses experienced very different pH conditions over the course of the 35 day experiment. The DBVS and MRI4 buffered the pH to alkaline conditions (> pH 9), the KBasin reduced the pH to circumneutral and the MRI7 reduced the pH still further to mildly acidic conditions (pH ~6).

At high pH the dissolution the dissolution rate is controlled by the activity of water and the breaking of O-H bonds and is a function of the reaction of water with the orthosilic acid as described in Section 3.2.11. This leads to a profile seen in Section 3.2.11 where orthosilicic acid reaches saturation in solution causing the rate to slow as a pseudo-equilibrium is reached. The reduced rate becomes controlled by diffusion across an alteration layer, which is shown by the linear nature of the graph in (Figure 4.30) after a few days of dissolution. This profile matches those of Na and Si in KBasin, DBVS and MRI4, although KBasin has a reducing pH the drop is potentially not low enough to fall into another regime and the near neutral conditions, combined with the high silica content/high connectivity in glass, attribute to the very low dissolution rate.

Under acidic conditions it is predicted that the activity of the hydronium ion has a major control on the dissolution rate this leads to a different profile. A diffusion controlled rate would expect to be linear on a $t^{1/2}$ plot. The profiles of NL for Na, Si and K in MRI7 (Figure 4.31) appear to show a steady increasing rate which suggests that the release of sodium is not primarily controlled by diffusion. Instead it is hypothesised that the gradually decreasing pH, as more karelinaite dissolves over the course of the 35 day experiment, increases the activity of the hydronium H_3O^+ ion reducing the pH and accelerating dissolution [55].

Previous studies have started to compare PCT-B test data from a range of ILW glass types, HLW glass types and reference glasses to look at their relative durability and allow ranking of different wasteforms (see Section 2.4.3 and [57]). Boron provides the most reliable comparative NL element as it is not commonly incorporated into alteration layers but is often absent from ILW glasses so often requires addition in comparative studies. In this case there is no boron in the KBasin sample so comparative plots (see Section 2.2.2.2), and comparative analysis has focused upon the NL mass loss of Na. In relation to other ILW glasses all the Geomelt® glasses show lower levels of elemental release (Table 4.12) than the majority of other example ILW wasteforms, comparative HLW and reference glass (see Section 2.2.2.2) showing that, relatively, all the Geomelt® glasses are very durable. Ideally more comparative studies with more wasteforms and with other elements that better represent the true breakdown of the network, and are not influenced by ion exchange processes, such as boron would help to confirm this analysis.

Table 4.12 NL_{Na} of USA Geomelt® glasses after 35 days.

Sample	NL_{Na} (35 days)
KBasin	0.131
DBVS	0.454
MRI4	0.206
MRI7	0.399

4.9.2 MCC-1 Monolith Tests

MCC-1 tests support the conclusions from the PCT-B tests but also show some different features that again highlights the difficulty in drawing exclusive findings from a single laboratory dissolution test as each test method has characteristics that impact on the results.

The MCC-1 tests for all four glassy products show that during the tests there has been some development of alteration layers and there has been some significant dissolution of both glassy and crystalline material (Figure 4.32 and 4.33).

KBasin shows that there is extensive $Fe(OH)_2$ growth on the surface of the monolith after 12 months that is not present in the 3 and 6 month monoliths (Figure 4.32, 4.33 and 4.34). As observed in the PCT-B test, the pH drops but to a lesser extent which is expected given the reduced overall dissolution in MCC tests due to a reduced glass surface area (Table 4.13). The NL_{Na} shows that, at 12 months, there may be depletion of Na in the altered glass layer and potentially some incorporation of Na in the $Fe(OH)_2$ precipitate or an unidentified alteration product (Table 4.14). The drop in NL_{Na} data at 12 months correlates with an increase in the release of the key radionuclide surrogate Ce that represents U behaviour in the glass and K, this suggest that there may be some preferential ion exchange. When the Na is depleted then ion exchange processes start to favour the release of other network modifiers including Ce and K this could have impacts on the key radionuclide losses to the surrounding environment (Table 4.14). The morphology of the $Fe(OH)_2$ formation is different to that observed in the PCT-B test where there is more minor precipitation is concentric and is found between the grains. In MCC-1 tests the precipitate covers the surface this shows another variation in tests and effects on dissolution rate and may relate to the more static set up of the MCC-1 tests. Overall, the dissolution data agrees well with the PCT-B tests and shows that the KBasin sample is very durable with minimal elemental release. The increasing NL of key elements such as Si shows that, unlike PCT-B tests, no rate reduction has occurred, and the solution is still undersaturated and that Fe rich precipitates on the surface are having no passivating affect.

In the MCC-1 tests with DBVS there is evidence of a small alteration layer from 3-12 months (Figure 4.32 and 4.33), NL solution data (Table 4.13) suggests that this may have incorporated elements such as Fe, Ca and Mg as these show a drop in solution whilst other elements show a steady increase in NL (Table 4.14). The pH (Table 4.13) follows a similar trend to PCT-B test suggesting continued elemental loss via diffusion across the alteration layer. The supposed loss of Re is not trusted in this study due to the very low levels retained in the original glass, but it suggests that if any is retained it will likely easily leach out of the product over the timescales involved.

The MCC-1 test with MRI 4 follows a similar trend to DBVS in elemental loss, with a reduction in K, Mg in solution observed at 12 months (Table 4.14), and an increase in pH (Table 4.13). This supports the conclusion from PCT-B data that MRI4 and DBVS are dissolving in a similar way, but due to rutile contaminated compositional data for MRI4 relative durability cannot be discerned. No major rutile dissolution was seen (Figure 4.32 andFigure 4.*33*) suggesting other than effecting compositional analysis it is a very durable phase that is not involved in dissolution. Cs appears in the MCC-1 test to be leaching at an increasing NL following other major elements such as Si, but Sr mirrors the K, Mg and Ca with a NL drop potentially showing it is being incorporated into the alteration layer which is beneficial as it reduces its release to the environment (Table 4.14). In the MRI4 MCC-1 tests there are rare, unusual unfilled vermiform features that have cut across both the glass and crystalline textures these have in the past been attributed to residual features from monolith formation creating localised accelerated dissolution and are not expected to have a major impact on glass dissolution values (Figure 4.32) [58].

In the MRI7 MCC-1 test there is obvious dissolution of the mineral phase karelianite, as seen in the PCT-B tests (Figure 4.32Figure 4.33). Karelianite dissolution appears to influence the dissolution conditions, but this is not as pronounced as in the PCT tests as the pH drop is not so extreme. Values of NL excluding V are at similar levels to DBVS and MRI4 suggesting that the dissolution conditions are more analogous in the MCC tests compared to the PCT-B tests likely due to the reduced surface area and the reduced availability of crystalline V-rich phases on the surfaces of the monoliths (Table 4.13). This effect again highlights the importance of the correct selection of tests for glasses that have significant degrees of crystallisation and how selecting variable tests can lead to different conclusions regarding durability. In the MRI7 there is a drop in NL values for Fe, Al and Mg which is a different set of elements to the MRI4 but again potentially shows elemental incorporation into an alteration layer. The radionuclides (Cs and Sr) in the MRI7 MCC-1 test also show increase with time to suggest they are just being released from the glass and not being incorporated into any alteration layers in contrast to MRI4 (Table 4.14).

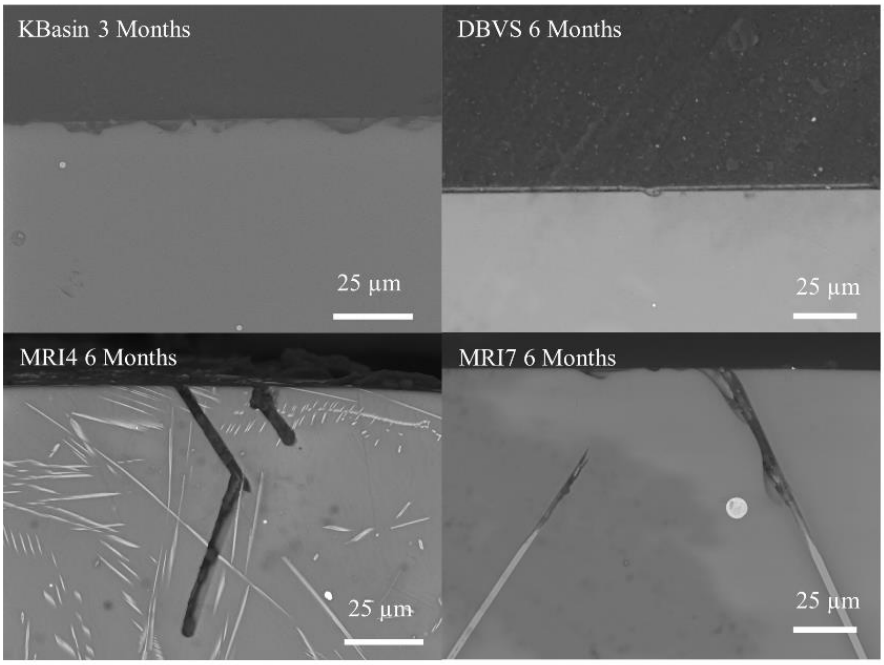

Figure 4.32 Upper surface of 3 month KBasin MCC-1 monolith showing minor pitting and a weak alteration layer. Upper surface of the 6 month DBVS MCC-1 monolith showing minor pitting and a weak alteration layer. Upper surface of the 6 month MRI4 MCC-1 monolith showing a weak alteration layer and tubular dissolution features. Upper surface of the 6 month MRI7 MMC-1 monolith showing a very weak alteration layer and dissolution of karelianite (V_2O_3) crystals.

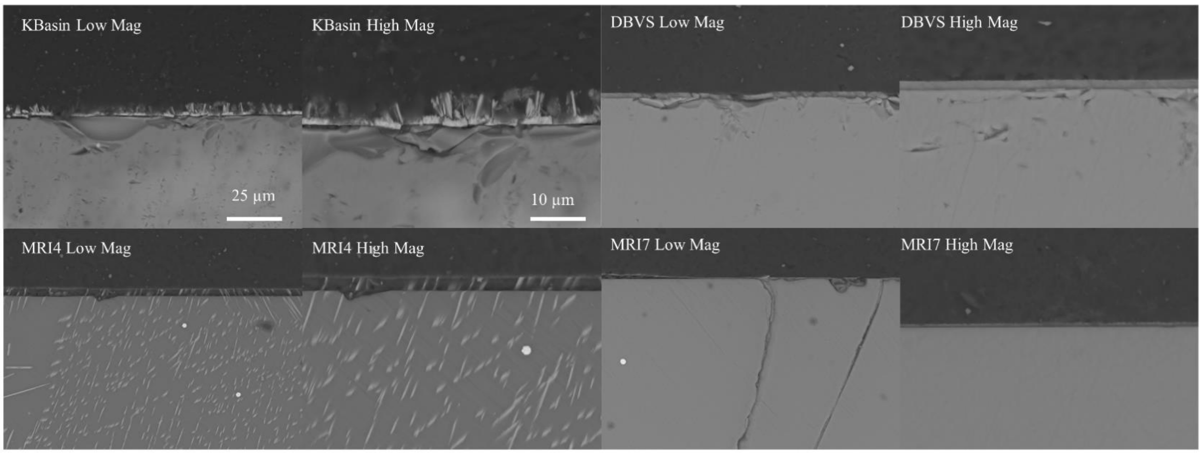

Figure 4.33 Low and high magnification SEM images of the upper surface of 12 month MCC-1 monoliths for USA Geomelt® samples.

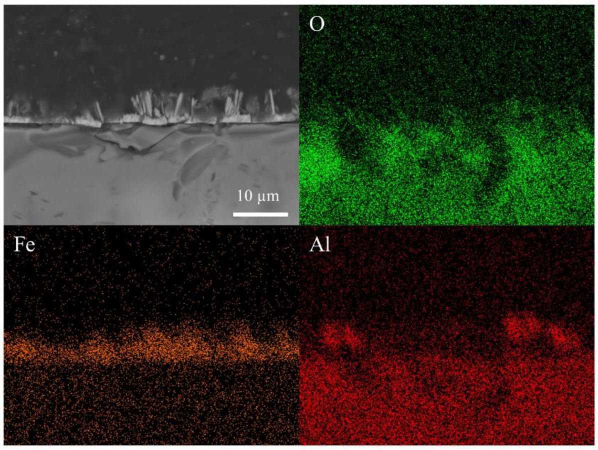

Figure 4.34 High magnification image of 12 month KBasin MCC-1 monolith and EDS maps for O, Fe and Al showing the Fe and Al enrichment in alteration layer crystalline features.

Table 4.13 pH data date from the MCC-1 dissolution test.

Month	KBasin	DBVS	MRI4	MRI7
0	6.25 +/- 0.50	6.25 +/- 0.50	6.25 +/- 0.50	6.25 +/- 0.50
3	7.76 +/- 0.11	8.75 +/- 0.01	8.47+/- 0.28	8.20 +/- 0.03
6	7.20 +/- 0.06	9.06 +/- 0.04	8.47 +/- 0.02	8.08 +/- 0.04
12	7.04 +/- 0.23	9.06 +/- 0.05	8.40 +/- 0.53	7.82 +/- 0.05

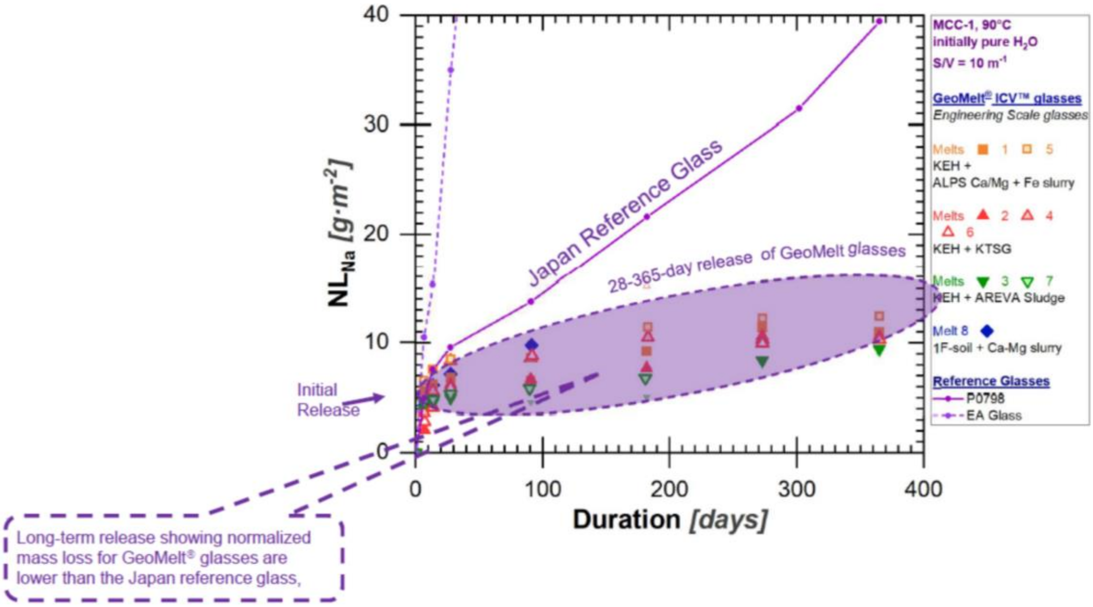

Figure 4.35 Historical MCC-1 tests for MRI4 and MRI7 and reference glasses [10].

Table 4.14 Normalised Mass loss date for key elements from the MCC-1 dissolution test (error in brackets)

Element	Month	KBasin	DBVS	MRI 4		MRI 7	
Na	3	1.47 (0.13)	10.16 (0.29)	5.39 (1.42)		4.98 (0.14)	
	6	3.00 (1.56)	12.96 (0.16)	6.70 (0.31)		5.74 (2.91)	
	12	0.79 (0.30)	16.92 (0.49)	9.08 (0.06)		6.70 (0.56)	
B	3	0	5.84 (0.12)	5.29 (1.49)		5.07 (0.10)	
	6	0	7.38 (0.10)	6.54 (0.32)		5.85 (2.74)	
	12	0	9.40 (0.30)	9.03 (0.16)		7.09 (0.43)	
Li	3	0	0	4.28 (1.24)		4.37 (0.10)	
	6	18.07 (4.66)	0.13 (0.13)	6.04 (0.29)		5.63 (2.62)	
	12	0	0	8.33 (0.15)		6.64 (0.35)	
Ce (KBasin) Re (DBVS) Cs, Sr (MRI4/7)	3	0	10.12 (1.06)	0.49 (0.14)	3.40 (0.93)	0.44 (0.00)	4.06 (0.04)
	6	0	13.54 (0.74)	6.14 (0.22)	4.44 (0.02)	5.50 (2.66)	4.06 (2.07)
	12	0.49 (0.35)	0	8.89 (0.11)	3.74 (0.15)	6.43 (0.27)	5.16 (0.08)
Si	3	1.71 (0.13)	2.71 (0.05)	4.99 (1.42)		4.24 (0.08)	
	6	2.44 (0.16)	3.29 (0.03)	6.13 (0.26)		4.63 (2.07)	
	12	3.63 (0.23)	4.06 (0.13)	8.24 (0.09)		5.16 (0.08)	
K	3	2.70 (0.57)	11.03 (0.77)	6.43 (1.71)		5.35 (0.10)	
	6	2.67 (0.29)	12.51 (0.27)	7.18 (0.28)		5.58 (2.93)	
	12	4.38 (0.25)	15.53 (0.43)	5.61 (0.29)		7.39 (0.79)	
Al	3	0.44 (0.01)	4.88 (0.09)	4.34 (1.98)		4.25 (0.13)	
	6	1.02 (0.11)	5.95 (0.02)	5.20 (0.35)		4.38 (1.96)	
	12	1.11 (0.71)	6.66 (0.17)	6.94 (1.06)		3.18 (0.19)	
Fe	3	0	0.10 (0.00)	0.04 (0.03)		0.21 (0.03)	
	6	0	0.15 (0.14)	0.01 (0.00)		0.25 (0.11)	
	12	0	0.04 (0.01)	0.01 (0.01)		0.06 (0.02)	
Mg	3	1.59 (0.08)	3.53 (0.02)	2.80 (0.15)		4.36 (0.14)	
	6	2.17 (0.17)	1.57 (0.20)	3.26 (0.22)		4.27 (2.39)	
	12	2.39 (0.33)	0.13 (0.01)	0.98 (0.62)		3.93 (0.30)	
Ca	3	1.56 (0.04)	3.56 (0.32)	4.78 (0.87)		4.16 (0.11)	
	6	2.33 (0.15)	3.45 (0.10)	5.23 (0.25)		4.41 (2.20)	
	12	1.68 (0.35)	2.25 (0.25)	3.65 (0.06)		4.44 (0.13)	
Ti (MRI4) V (MRI7)	3	-	-	0		23.29 (1.13)	
	6	-	-	2.42×10^{-4} (7.26×10^{-5})		68.665 (0.00)	
	12	-	-	0		75.66 (4.35)	

In relation to previous studies the MCC-1 tests support previous analysis by PNNL on the glasses showing the reproducibility of the studies and confirming the textural observations and NL values for the MRI 4 and 7 glasses [10, 12] including the dissolution and non-dissolution of key mineral phases and the NL value after 365 days.

No previous dissolution work has been carried out on the USA glasses (KBasin and DBVS) so there are no comparisons but there has been some previous MCC-1 tests carried out on MRI4 and MRI7 by PNNL [10]. These tests support the results from this study by showing that NL_{Na} from the MRI4 and MRI7 (Table 4.11) lie within the envelope of previous analogous dissolution trials and well below the release rate of the key HLW references glasses in the US

(EA Glass) and Japan (PO798) (Figure 4.35). This shows that glasses although showing variable dissolution behaviour are still relatively durable in comparison to other reference glasses supporting the conclusion from comparative PCT-B analysis. In general, the MCC-1 tests support the conclusions from the PCT-B tests but also show different features that again highlights the difficulty in drawing exclusive findings from variable dissolution tests as they each have varying characteristics that impact on the results.

4.10 Conclusions

A series of Geomelt® glasses have been extensively analysed with the aim of investigating the answers to the questions posed in Section 2.2.

In relation to the first two aims in 2.2.1.1, what is the structure of the waste including the distribution and abundance of crystalline phase and the composition of the crystalline and glass components, overall, the Geomelt® process has produced 4 glassy wasteforms that have managed to incorporate the range of elements from the wasteform with compositional analysis being consistent with waste additions. There is variable crystalline abundance and composition in the different Geomelt® glasses with very limited Fe metal precipitation in KBasin and DBVS and more extensive karelinaite (V_2O_3) and rutile (TiO_2) crystallisation in MRI7 and MRI4 respectively. The glass composition is complex with a wide range of different elements accommodated in the glass component of each waste from. The glass compositions strongly follow the input waste and soil/glass frit compositions with minor changes due to volatilisation or crystallisation with important highlights being the high Si content of the KBasin glass, the high Na content of the DBVS mirrors the salt content of the waste and a more variable range of elements in the MRI4 and 7 with interest in elevated levels of exotic elements such as Li_2O, B_2O_3, TiO_2 and V_2O_5 coming from the waste and additives added to optimise the glass properties. Answering question 3 in 2.2.1.1 the radionuclide retention is reported as being good with measured levels close to batched levels for all the wasteforms except the DBVS, where it appears that the majority of the Re has been volatilised or has been partitioned to another part of the wasteform such as a metal phase or the refractory wall via salt migration and has not been incorporated in the glass. This is in contradiction to previous analysis of Trial 38-C that found single flow retention of Re to be ~70% with higher expected results for Tc from engineering results. This is an area that requires further study to further understand this discrepancy and study samples from Test-D that was designed to improve radionuclide retention [2, 3, 5, 9, 59-61]. Radionuclide simulant distribution was difficult to ascertain due to the low concentration in the wasteforms causing doubt in SEM analysis, potentially measurable levels of Ce in KBasin show even distribution including possible incorporation into metallic iron nodules and more certain levels of Sr in MRI4 and MRI7 show even glass distribution and exclusion from crystalline phases. The absence of non-specific radionuclide simulant phases suggests no saturation of these elements in the wasteforms, with some potential minor crystalline incorporation in some wasteforms, but mostly retention in the glass component of the wasteforms. Different structural analysis techniques have shown how a range of elements have been incorporated into the glasses, which is important for understanding glass structure and how this could potentially effect dissolution. EXAF's has shown Zr as a glass former, Sr and Ce to be glass modifiers as well as V although this is likely complicated by crystallisation. Fe is shown by both EXAF's and Mossbauer to be mainly a modifier in a 2+ state but, in all glasses, there is minor Fe^{3+} that can act as a network former. Fe^{3+} was present with between 0-21 % in all glasses with the highest Fe^{3+} in MRI7 and the lowest levels in KBasin, although this could be shifted by the presence of metallic Fe and poor signal strength in the Mossbauer spectrum. Raman analysis gives an overall interpretation of glass polymerisation excluding MRI4 which is too crystalline and shows that the order of polymerisation is MRI7<DBVS<KBasin.

In relation to the questions in Section 2.2.2.1 the density and thermal analysis have reported important physical properties of the wasteforms that will be useful in future thermal and processing tests and disposal scenarios. The values of these physical properties align with composition and compares well to other similar glasses. It is predicted that the tentative high thermal values may cause issues with viscosity during processing although the in-can disposal method would negate this but issues with volatilisation during processing could require some consideration. These are both areas that require further studies and could be areas of interest for future project work.

The dissolution tests (PCT-B and MCC-1) help answer the questions in Section 2.2.2.2 and in general show a few key findings, but care is required as they are complicated by the complex nature of the samples. For the Hanford samples, the KBasin is a very durable glass due to its composition with lower than expected pH controlled by the behaviour of iron precipitates contributing to low elemental release but not directly effecting other elements. At low elemental release in the MCC-1 tests there is potentially some preferential ion exchange in the KBasin sample that could affect the release of Ce. DBVS has a reduced durability which is expected from the structural and compositional analysis which indicates a lower silicon content and lower network connectivity due to high sodium. The glass follows a more traditional pattern and rate of dissolution controlled at high pH by the formation of an alteration layer and/or silica saturation. There is preferential elemental incorporation into the alteration layer seen in the MCC-1 data.

For the Japanese sample's, comparative analysis is complicated by the presence of large amounts of secondary crystallisation. In MRI4, where there is little to no dissolution of the rutile, the glass appears to dissolve in comparative way to DBVS at a buffered high pH with control by the saturation of silica and/or the diffusion across and elemental specific alteration layer. The formation of the alteration layer also directly effects the concentration of some elements in solution including Sr as it appears to incorporate them into its structure. Due to the inexact measure of glass composition as the laser ablation analysis included the non-dissolving rutile there are issues with comparative NL values so relative durability of the MRI4 glass is not discernible.

In MRI7 where there is a large amount of vanadium containing karelinaite, that unlike MRI4 appears to preferentially be dissolving over the glass. The crystalline component is more dispersed than in MRI4 so the glass composition can be isolated but the preferential dissolution of karelianite appears to be reducing the pH to an unusually low value which is controlling the dissolution kinetics. This process has a greater effect in PCT-B tests data than in MCC-1 tests due to increased surface area and glass crushing process that exposes more vanadium rich crystals for dissolution. The reduced pH to acidic conditions causes a diffusion controlled mechanism that has a more linear rate of elemental release, with the production of minor alteration layers appearing to affect some elements but unlike in MRI4 excluding either of the radionuclide tracers.

These results show that the PCT-B and MCC-1 dissolution tests although very useful in looking at wasteform performance have raised several issues regarding their use in looking at individual and comparative dissolution performance of ILW wasteforms. The main issues being the mixed crystalline nature of the wasteforms that affects the test results both if the crystalline phases are much more durable than the glass and if the phase is much less durable. This observation highlights the limitations of standardised tests that rely on measuring the release of elements into solution and comparing them to mass fraction measured in the bulk material and a known surface area. The effect seems to be greatest if the crystalline fraction is more soluble than the wasteform, as in the case of MRI 7 and in the PCT-B tests where there is a greater wastefrom SA. In relation to these effects moving forward, other tests such as ASTM 1926-23 Standard Test Method for Measurement of Glass Dissolution Rate Using Stirred Dilute Reactor Conditions on Monolithic Samples [51, 52] that relies on measuring surface retreat maybe more appropriate for removing the composition measurement issues isolating and discerning glass dissolution rates and behaviour for ILW wasteforms. Regardless of the test method it is important to be aware of the effects of crystalline dissolution as it has in some wasteforms a strong control on the glass dissolution environment that effects the mechanism of glass dissolution. Although complicated and potentially not the correct set of tests, the results with a caveat especially in the Japanese glasses can be compared to previous studies to show that, although caveated by effects of crystallisation, all the tests show a) repeatability to previous studies and b) that the Geomelt® system has produced a series of glasses and wasteforms that are very durable in relation to other vitrified ILW glasses and reference glasses.

4.11 References

1. AMEC, Bulk Vitrication Treatment of K Basin Sludge Simulant Final Report. 2003.
2. Witwer, K.S., et al. Hanford bulk vitrification technology status. in WM'07: 2007 Waste Management Symposium - Global Accomplishments in Environmental and Radioactive Waste Management: Education and Opportunity for the Next Generation of Waste Management Professionals. 2007. United States.
3. Bagaasen, L.M., et al. Method to Reduce Molten Salt Penetration into Bulk Vitrification Refractory Materials. 2008. United States: WM Symposia, Phoenix, AZ, United States(US).
4. Tingey.M.J, B.H.G., Deschane.R.J, Dangerous Waste Charaterisitics of Waste from Hanford Tank 241-S-109. 2004, PNNL.
5. Kim.S.D, V.D.J., Hrma.R.P, Schweiger.J.M, Matyas.J, Crum.V.J, SMith.E.D, Sevigny.J.G, Buchmiller.C.W, Jr.Tixier.S.J, Yeager.D.J, Belew.B.K, Development and Testing of ICV Glasses for Hanford LAW. 2003, PNNL.
6. Kim.et.al, Matrix Crucible Testing of Bulk Vitrification Glasses for Hanford Low Activity Waste. 2005, AMEC Earth amnd Environmetal.
7. Hrma.R.P, K.S.D., Vienna.D.J, Matyas.J, Smith.E.D, Schweiger.J.M, Yeager.J.D, Testing of Large Scale ICV Glasses with Hanford LAW Simulant. 2005, PNNL.
8. Mahoney.A.L, V.D.J., Feed Variability and Bulk Vitrication Glass Performance Assessment. 2005, PNNL.
9. Witwer, S.K., Woolery.W.D, Dysland.J.E. Progress of the Hanford Bulk Vitrification Project ICV Testing Program in WM'06. 2006. Tucson, AZ.
10. Finucane, K.G., et al. The Development of Geomelt®R In-Container Vitrification (ICV)TM for Fukushima Daiichi Water Treatment Secondary Wastes - 21347. in WM2021: 47 Annual Waste Management Conference. 2021. United States.
11. Lehto, J., et al., Removal of Radionuclides from Fukushima Daiichi Waste Effluents. Separation & Purification Reviews, 2019. 48(2): p. 122-142.
12. Kurion Japan K.K, V.N.S.I., Project of Decommissioning and Contaminated Water Management (Research and Development of Processing and Disposal of Solid Waste) - The Holistic Evaluation of Applicability of Geomelt®® ICV™ for Treatment of 1F Water Treatment Secondary Waste Fiscal Year 2019-2020. 2021.
13. Mertz, J., et al., Development of a Reactive Transport Model for the Optimization of Ion Specific Media Used at the Fukushima Dai-ichi Nuclear Power Plant – 14579. 2014.
14. Triplett.M, Cesium Removal and Storage Update on Fukushima Daiichi Status. 2015, PNNL.
15. Krtil, J. and J. Mencl, ISOLATION OF RADIOCAESIUM FROM A FISSION PRODUCT MIXTURE BY MEANS OF SORPTION ON VANADIUM(IV) HEXACYANOFERRATE. 1969: Czech Republic.
16. Prevost, T., et al., Areva's Actiflo (TM)-Rad Water Treatment System for the Fukushima Nuclear Power Plant. Kernkraftwerke in Deutschland: Betriebsergebnisse .. 2012. 57: p. 308-+.
17. Zheng, Q., et al., Understanding Glass through Differential Scanning Calorimetry. Chemical Reviews, 2019. 119(13): p. 7848-7939.
18. Avramov, I., T. Vassilev, and I. Penkov, The glass transition temperature of silicate and borate glasses. Journal of Non-Crystalline Solids, 2005. 351(6): p. 472-476.

19. Fokin, V.M., M.L.F. Nascimento, and E.D. Zanotto, Correlation between maximum crystal growth rate and glass transition temperature of silicate glasses. Journal of Non-Crystalline Solids, 2005. 351(10): p. 789-794.
20. Le Losq, C., M. Cicconi, Rita, and D. Neuville, R, Iron in Silicate Glasses and Melts: Implications for Volcanological Processes, in Magma Redox Geochemistry, M. Roberto and R.N. Daniel, Editors. 2021, Wiley. p. 233 - 253.
21. Newville.M, Fundamentals of XAFS. 2004: Consortium of Advanced Radiation Sources, University of Chicago, IL.
22. Wong, J., et al., K-edge absorption spectra of selected vanadium compounds. Physical Review B, 1984. 30(10): p. 5596-5610.
23. Giuli, G., et al., Iron local structure in tektites and impact glasses by extended X-ray absorption fine structure and high-resolution X-ray absorption near-edge structure spectroscopy. Geochimica et Cosmochimica Acta, 2002. 66(24): p. 4347-4353.
24. Giuli, G., et al., V oxidation state and coordination number in silicate glasses by XAS. 2004. 89(11-12): p. 1640-1646.
25. Wilke, M., et al., Oxidation state and coordination of Fe in minerals: An Fe K-XANES spectroscopic study. American Mineralogist, 2001. 86(5-6): p. 714-730.
26. Mottram, L.M., et al., A feasibility investigation of speciation by Fe K-edge XANES using a laboratory X-ray absorption spectrometer. Journal of Geosciences, 2020. 65(1): p. 27-35.
27. Levina, A., A.I. McLeod, and P.A. Lay, Vanadium Speciation by XANES Spectroscopy: A Three-Dimensional Approach. Chemistry – A European Journal, 2014. 20(38): p. 12056-12060.
28. Nomura, K. Solution X-ray Absorption Spectroscopy (XAS) for Analysis of Catalytically Active Species in Reactions with Ethylene by Homogeneous (Imido)vanadium(V) Complexes—Al Cocatalyst Systems. Catalysts, 2019. 9, DOI: 10.3390/catal9121016.
29. Simon, H., et al., Fe K-edge X-ray absorption spectroscopy of corrosion phases of archaeological iron: results, limitations, and the need for complementary techniques. Journal of Physics: Condensed Matter, 2021. 33(34): p. 344002.
30. Giuli, G., et al., XAS Determination of the Fe Local Environment and Oxidation State in Phonolite Glasses. American Mineralogist, 2011. 96: p. 631-636.
31. Berry, A.J., et al., XANES calibrations for the oxidation state of iron in a silicate glass. 2003. 88(7): p. 967-977.
32. Petit, P., et al., Determination of the iron oxidation state in Earth materials using XANES pre-edge information. Journal of synchrotron radiation, 2001. 8: p. 952-4.
33. Wilke, M., et al., Determination of the iron oxidation state in basaltic glasses using XANES at the K-edge. Chemical Geology, 2005. 220(1): p. 143-161.
34. Bearden, J.A. and A.F. Burr, Reevaluation of X-ray Atomic Energy Levels. Reviews of Modern Physics, 1967. 39(1): p. 125-142.
35. Jain, A., et al., Commentary: The Materials Project: A materials genome approach to accelerating materials innovation. APL Materials, 2013. 1(1): p. 011002.
36. Tachez, M. and F. Theobald, Structure du sulfate de vanadyle pentahydraté VO(H2O)5SO4β (variété orthorhombique). Acta Crystallographica Section B Structural Crystallography and Crystal Chemistry, 1980. 36: p. 1757-1761.
37. Meskinfam Langroudi, M., et al., Interaction of vanadium species with a functionalized graphite electrode: A combined theoretical and experimental study for flow battery applications. Journal of Power Sources, 2019. 420: p. 134-142.

38. Rao Popuri, S., et al., VO2 (A): Reinvestigation of crystal structure, phase transition and crystal growth mechanisms. Journal of Solid State Chemistry, 2014. 213: p. 79-86.
39. Bailey, D., et al., Ce and U speciation in wasteforms for thermal treatment of plutonium bearing wastes, probed by L 3 edge XANES. IOP Conference Series: Materials Science and Engineering, 2020. 818: p. 012019.
40. el Damrawi, G. and A. Behairy, Structural Role of Cerium Oxide in Lead Silicate Glasses and Glass Ceramics. Journal of Minerals and Materials Characterization and Engineering, 2018. 06: p. 438-447.
41. Aboelwafa, M.A., et al., Influence of Cerium oxide on the structural aspects of soda-lime aluminosilicate glasses synthesized by sol-gel route. Materials Chemistry and Physics, 2023. 305: p. 127930.
42. Lopez, C., et al., Solubility of actinide surrogates in nuclear glasses. Journal of Nuclear Materials, 2003. 312(1): p. 76-80.
43. Bingham, P.A., et al., The Use of Surrogates in Waste Immobilization Studies: A Case Study of Plutonium. MRS Proceedings, 2008. 1107: p. 421.
44. Shaikh, A.M. and S. Ghose, A first-order phase transition in zektzerite, NaLiZrSi₆O₁₅: high-temperature single-crystal X-ray diffraction study. Physics and Chemistry of Minerals, 2015. 42: p. 747-759.
45. Ficheux, M., et al., Structural evolution of high zirconia aluminosilicate glasses. Journal of Non-Crystalline Solids, 2020. 539: p. 120050.
46. Dyar, M.D., et al., MÖSSBAUER SPECTROSCOPY OF EARTH AND PLANETARY MATERIALS. Annual Review of Earth and Planetary Sciences, 2006. 34(1): p. 83-125.
47. Di Genova, D., et al., Approximate chemical analysis of volcanic glasses using Raman spectroscopy. Journal of Raman Spectroscopy, 2015. 46(12): p. 1235-1244.
48. Di Genova, D., et al., Effect of iron and nanolites on Raman spectra of volcanic glasses: A reassessment of existing strategies to estimate the water content. Chemical Geology, 2017. 475: p. 76-86.
49. Colomban, P., Polymerization degree and Raman identification of ancient glasses used for jewelry, ceramic enamels and mosaics. Journal of Non-Crystalline Solids, 2007. 323: p. 180-187.
50. Kilinc, E. and R.J. Hand, Mechanical properties of soda–lime–silica glasses with varying alkaline earth contents. Journal of Non-Crystalline Solids, 2015. 429: p. 190-197.
51. ASTM, ASTM C1926 - 23 Standard Test Method for Measurement of Glass Dissolution Rate Using Stirred Dilute Reactor Conditions on Monolithic Samples 2023.
52. Thorpe, C.L., et al., Forty years of durability assessment of nuclear waste glass by standard methods. npj Materials Degradation, 2021. 5(1): p. 61.
53. Crans, D.C., et al., The Chemistry and Biochemistry of Vanadium and the Biological Activities Exerted by Vanadium Compounds. Chemical Reviews, 2004. 104(2): p. 849-902.
54. Inagaki, Y., et al., Initial dissolution rate of the international simple glass as a function of ph and temperature measured using microchannel flow-through test method. International Journal of Applied Glass Science, 2013. 4(4): p. 317-327.
55. Strachan, D., Glass dissolution asa function of pH and its implications for understanding mechanisms and future experiments. Geochimica et Cosmochimica Acta, 2017. 219: p. 111-123.

56. Ojovan, M.I. and W.E. Lee, Glassy Wasteforms for Nuclear Waste Immobilization. Metallurgical and Materials Transactions A, 2011. 42(4): p. 837-851.
57. Fisher.J.A, C.L.C., Technote - the dissolution of thermally treated Intermediate Level Waste. In Press.
58. Mansfield, J.T., et al., Localised extended (“vermiform”) features formed during glass dissolution. Journal of Non-Crystalline Solids, 2023. 608: p. 122230.
59. Witwer, K.S., et al. Hanford's Supplemental Treatment Project: Full-Scale Integrated Testing of In-Container-Vitrification and a 10,000-Liter Dryer. in 2008 Waste Management Symposium - WM2008/WM'08: HLW, TRU, LLW/ILW, Mixed, Hazardous Wastes and Environmental Management - Phoenix Rising: Moving Forward in Waste Management. 2008. United States.
60. Bagaasen, L.M., et al. Transport of Technetium and Rhenium into Refractory Materials during Bulk Vitrification. 2006. United States.
61. Group, C.M.H., Technical Assessment of Bulk Vitrification Process/Product for Tank Waste Treatment at the Department of Energy Hanford Site. 2006.

5 Plutonium Contaminated Material (PCM) Vitrification

The aim of this chapter is to analyse a set of samples from 2 of the 5 non-active PCM Plasma trials carried out by Tetronics (Section 3.1.1.2). Material from Trial 1 and Trial 5 represent inorganic (bricks and concrete) and organic endmembers of the PCM waste. Both Trial 1 and 5 produced a crystalline-glass component attached to a partially/unmolten metallic drum component. This project focused on the crystalline-glass component and did not analyse the partially/unmolten metallic drum component. The vitrified crystalline-glass components were analysed with a variety of techniques with the focus on type and quality of the waste product. Analysis includes investigating the texture of the samples, how and where the waste product incorporates different waste elements and how the waste performs in a series of durability trials. These early trials did not include radionuclide tracers for the primary radionuclide in these waste products, plutonium, so there is no information on how this key element would be incorporated or distributed. Glass frit compositions were used to make comparative glasses in (Chapter 6) to investigate how waste components are incorporated into the glass phase, due to preferential surrogate partitioning [1, 2] and wasteform optimisation. Comparison to glass analysis in this chapter allows optimisation of lab trials to best reproduce and interpret industrial trials.

5.1 Volume Reduction

The trials experienced major volume reductions which is beneficial for disposal. A narrow range irrespective of composition shows that the drum and the vitrification additives have a significant contribution to final waste and waste volumes (Table 5.1)

Table 5.1 Volume reductions for the different Tetronics Trials [3].

Source	Volume Reduction (inclusive of charge)
Trial 1	61.30
Trial 2	74.33
Trial 3	71.54
Trial 4	75.10
Trial 5	75.74

5.2 Composition

Compositional analysis of the glassy-crystalline material from different areas of Trial 1 and 5 is outlined in (Table 5.2 and 5.3). Analysis has been carried out historically by Tetronics using XRF measurements and in this project using both acid digestion, EDS and LA ICP-OES. There is generally good agreement between the different measurement techniques with differences attributed to sample heterogeneity. Various elemental additions mostly from the waste drum make comparisons to batched measurements (Section 3.1.1.2 and Table 3.13) difficult but elemental ratios appear broadly analogous to measured values. Consistency of measurements within each trial shows that textural differences and anorthite crystallisation is not significantly affecting composition (Table 5.2 and 5.3), In general, the plasma trials have produced a series of CAS dominated wasteforms which is expected from the composition of the glass former that forms a major part of the waste feed. There are minor additions of other elements such as Fe_2O_3 and K_2O that come from melting of the waste inside the drums and the metallic drum and liner themselves (Table 5.2 and 5.3) [4]. Trial 5 consistently shows elevated Fe_2O_3 potentially related increased measures to ensure drum melting and the addition of oxidants allowing incorporation of metallic Fe as oxides into the glass structure, although SEM (Section 5.4) shows some of this has re-precipitated as metallic iron within the glass [3]. EDS analysis of glass from sample 5_Xc taken near anorthite crystalline phases with major depletion in Al_2O_3 and minor depletion in CaO in the glass supporting SEM analysis and conclusions (Section 5.4) that is depletion is caused by the crystallisation of the anorthite phase. Local substitution of Fe^{3+} for depleted Al^{3+} in the glass would explain the elevated Fe values but requires further confirmation as later analysis (Section 5.7 and 5.8) identifies the majority of Fe as Fe^{2+} and compositional analysis assumes Fe is speciated as Fe_2O_3.

Table 5.2 Compositional analysis of the different textural regions of Trial 1. Analysis is from acid digest ICP-OES of separated textural regions at the University of Sheffield (A), LAS ICP-OES at the British Geological Survey (B), EDS at the University of Sheffield (C) and XRF as part of the original Tetronics trial (D) [3]. Elements have been split into groups based upon there varying roles in the glass network. Standard deviations for measurements in shown in brackets, acid digest ICP-OES and XRF [3] analysis were single measurements.

Component	1A mol% (A)	1 mol% (A)	1A Glass mol% (A)	1A Glass mol% (B)	1A Glass mol% (C)	Average 1 mol% (D) [3]
				Network Formers		
SiO_2	60.56	61.50	61.56	57.66 (2.40)	54.11 (0.49)	43.61
B_2O_3	0.12	0.12	0.29	0.01 (<0.01)	0	0
P_2O_5	0.17	0.19	0.16	0.04 (<0.01)	0.03 (0.03)	0.03
				Intermediate (Former)		
Al_2O_3	9.62	9.10	8.73	11.51 (0.73)	19.24 (0.08)	9.09
				Network Modifiers/Charge Balancers		
Li_2O	0	0	0	0.02 (<0.01)	0	0
Na_2O	0.19	0.19	0.20	0.25 (0.01)	0	0.39
K_2O	0.79	0.70	0.77	0.85 (0.04)	0.94 (0.06)	1.31
MgO	0.71	0.65	0.69	0.84 (0.02)	0.57 (0.04)	0.96
CaO	22.87	22.29	22.46	23.27 (2.07)	17.77 (0.46)	33.93
BaO	0.02	0.02	0.02	0.01 (<0.01)	0.01 (0.02)	0.08
SrO	0.01	0.01	0.01	0.01 (<0.01)	0	0
				Transition Metal Oxides		
TiO_2	0.20	0.20	0.21	0.20 (0.01)	0.14 (0.03)	0.38
ZrO_2	0	0	0	0.01 (<0.01)	0.04 (0.03)	0.03
Cr_2O_3	0.03	0.05	0.03	0.02 (<0.01)	0.04 (0.02)	0.05
MnO	0.06	0.06	0.06	0.06 (<0.01)	0	0.10
Fe_2O_3	4.60	4.90	4.78	5.22 (0.30)	7.01 (0.20)	9.72
ZnO	0.04	0.04	0.04	0.01 (<0.01)	0.08 (0.02)	0.02
			Anions		0	
Cl	-	-	-	-	0.02 (0.02)	0.25
	100	100	100	99.98	100	99.95

Table 5.3 Compositional analysis of the different textural regions of Trial 5. Analysis is from acid digest ICP-OES of separated textural regions at the University of Sheffield (A), Energy Dispersive Spectroscopy at the University of Sheffield (B) and XRF as part of the original Tetronics study (C) [3]. Elements have been split into groups based upon there varying roles in the glass network. Standard deviations for measurements in shown in brackets, acid digest ICP-OES and XRF [3] analysis were single measurements.

Component	5_Vu mol% (A)	5_Xc mol% (A)	%_Xc Glass mol% (B)	Average 5 mol% (C) [3]
Network Formers				
SiO_2	54.96	56.96	52.31 (1.71)	39.93
B_2O_3	0.19	0.25	0	0
P_2O_5	0.18	0.17	0.10 (0.11)	0.03
Intermediate (Former)				
Al_2O_3	13.87	13.21	8.45 (0.03)	13.17
Network Modifiers/Charge Balancers				
Na_2O	0.08	0.08	0	0.41
K_2O	0.76	0.70	0.10 (0.07)	1.16
MgO	0.23	0.22	0.66 (0.10)	0.27
CaO	21.83	20.53	18.65 (1.29)	29.77
BaO	0.02	0.01	0.05 (0.03)	0.06
SrO	0.01	0.01	0	0
Transition Metal Oxides				
TiO_2	0.42	0.42	0.91 (0.27)	0.68
ZrO_2	0.01	0.01	0.09 (0.05)	-
Cr_2O_3	0.05	0.05	0.34 (0.08)	0.07
MnO	0.08	0.08	0.04 (0.05)	0.12
Fe_2O_3	7.29	7.26	18.20 (0.42)	13.97
ZnO	0.03	0.03	0.09 (0.08)	0
Anions				
Cl	-	-	0.02 (0.03)	0.25
	100	100		99.89

A major issue with vitrification of PCM is the degradation/pyrolysis of PVC that can form dioxins and metal chlorides, are toxic organics, but the plasma high temperature will destroy these; the metal chlorides, however, will supply chlorides that that can attack the refractory and off gas equipment. PCM drums can contain high levels of PVC (upto 20 wt.%) with these having high levels of Cl^- (upto 20 wt.%). Potential incorporation of the chlorine into the CAS glass will prevent the release of corrosive gases such as metallic chlorides and toxic gases such as HCl and Cl_2 and radionuclides through the formation of oxychlorides [2].

Extensive analysis of Cl incorporation in CAS glass (Section 2.3.4 and [5-10]) shows that the glass composition can have a major effect on the incorporation of Cl. Cl incorporation in CAS is postulated to be linked to the amount of available network modifier, in this case Ca, in the glass with Cl partitioning into network spaces associated with network modifiers. At elevated Al levels the Ca is required to charge balance the excess charge associated with the Al sites. Very high retention in calcium aluminosilicates [9, 11] complicates this theory and suggests that another mechanism effects the incorporation although CAS with high Cl^- retention (>10 wt.%) [5-7] would challenge this.

Laser ablation ICP-OES cannot measure Cl^- as it is an anion, but XRF and Energy Dispersive Spectroscopy (EDS) attached to an SEM provide a measure of Cl^- in the wasteform for the 1A_glass sample (Table 5.*2*) this allows comparison for lab glasses in Section 6.1.2 and analysis of actual and expected Cl^- retention in CAS glass during PCM plasma trials (Table 5.2) [2]. Cl^- mol% from EDS measurements is calculated assuming that the PVC is composed of 100% PVC resin with no additives and that 57% of PVC resin is Cl^- based on the monomer formula C_2H_3Cl [2]. This is likely an overestimate as Romar Workwear suggests that 35 wt.% of PVC is Cl^- by weight indicating some additives are present in the PVC, as the composition of the additives is unknown then only a maximum estimate for atomic Cl mol% can be calculated.

Historical XRF measurements (Table 5.2) are higher than the EDS measurements suggesting some heterogeneity and difference between bulk and focused glass specific analysis. In both cases and other historical lab trials [1, 2], however, the Cl values are very low and well below the maximum incorporation level of CAS glass meaning that this is not a restricting factor. Based on XRF analysis additional oxidation additives to aid degradation/pyrolysis [3, 4] have not affected incorporation of the Cl^- as the levels in Trial 1 and 5 are similar (Table 5.2). To make conclusions regarding retention it is important to compare measured values to batched values, for Trial 1 and 5 PVC levels are low due to only having PVC liners with batched levels of Cl^- being approximately 0.01-0.02 mol % (Section 3.1.1.2 and Table 3.12), along way below the maximum estimates of 20 wt % from other studies [1, 2, 12]. Due to the low Cl levels in wasteforms it is hard to discern if the wasteforms have successfully retained most of the Cl^- into the glassy wasteforms, elevated values in XRF possibly pointing toward some local concentrating or if there is poor retention due to factors such as low temperature pyrolysis/thermal degradation and CAS composition. This also makes it difficult to conclude the mechanisms controlling the Cl retention in the CAS. Concluding that there is complete retention in the CAS supports the theory that high levels of Ca at a ratio of ~1:2 provide ample Al charge compensation with enough residual Ca sites for Cl accommodation. Localised elevated Ca levels in the XRF sample provide an alternative explanation for increased Cl incorporation in this sample. Alternatively poor Cl retention in previous trials [1, 2, 8, 10] with retention as low as <0.01 wt% [1, 2], supporting that the low levels relate incomplete poor retention. This could be related to two major factors Significant Al in the CAS glass could be reducing the retention via an unknown mechanism and there could the low temperature thermal degradation/pyrolysis of PVC that is removing most of the PVC while the CAS elements are still unmolten and cannot incorporate the Cl, although still low, elevated Cl values in experimental trails were Cl was added as alkaline earth salts [8, 10] rather than PVC would support this theory. This is clearly an area that requires further work including systematic waste loading studies to illustrate the CAS compositional effect on Cl retention and thermal degradation/pyrolysis analysis/optimisation to investigate how much Cl is present during higher temperature glass melting and how this can be maximised.

5.3 XRD

Crystallisation is expected in these samples as they represent material that was adjacent to unmelted drum remnants causing heterogenous nucleation and growth. Heterogeneous nucleation is not expected to form a major part of the wasteforms, but it is unconfirmed how representative the mix of glass and crystalline material is of the full wasteforms. In future this is something that will be important to understand when producing and scaling up lab tests and results and helps when understanding how representative and important results in this project are. Regions with crystalline material from Trial 1 and Trial 5 are dominated by anorthite ($CaAl_2Si_2O_8$) which is expected given the batch material (Figure 5.1A and Figure 5.3A and B). The crystalline material in the crystalline/mixed (1/1A) regions of the Trial 1 are predominantly anorthite (Figure 5.1A and B) with only additional minor corundum (Al_2O_3) is present in Trial 1A (Figure 5.1B). The XRD pattern from the glass region in Trial 1 shows amorphous diffuse confirming the lack of crystallinity in this glass region (Figure 5.2).

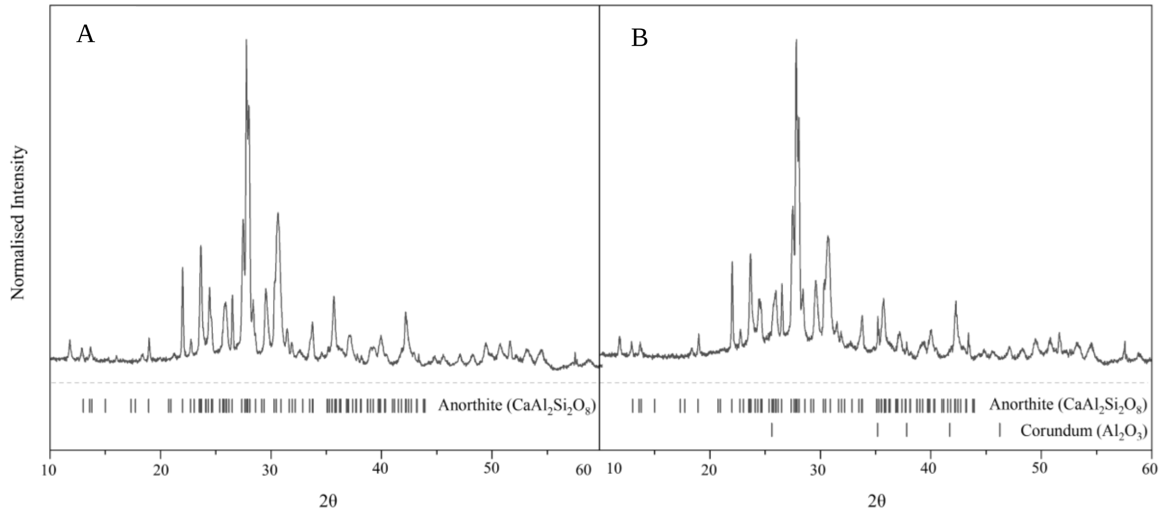

Figure 5.1 XRD pattern for A-1, B-1A

In addition to the major anorthite phase, XRD of Trial 5 samples (Xc and Vu) indicate additional minor crystalline phases (Figure 5.3A and B). Analysis is complicated by complex diffraction of anorthite but tentative analysis of 5_Vu shows both metallic Fe and a phase with the leucite, a potassium-silicate, structure (Figure 5.3A), 5_Xc has metallic Fe but no leucite which is either absent or below detective limits (Figure 5.3B). The presence of metallic iron in Trial 5 agrees with previous studies [1, 2, 12, 13] and is different to the unmolten drum fraction, however, instead of reprecipitating in a separate phase the metallic Fe is incorporated in the waste form. SEM analysis (Section 5.4) shows the metallic Fe is in the form of dendritic regrowth. The growth of metallic Fe is potentially linked to the incomplete oxidation of the metallic Fe due to a shortage of oxidants despite their addition in the Trial 5 melt [3, 4]. It means that a fraction of it cannot be incorporated into the glass likely due to the increased level of drum melting and higher Fe content in Trial 5. This shows variable Fe behaviour linked to oxidation and poses optimisation questions regarding either incorporation of this metallic element or decontamination and separation allowing LLW disposal [1, 2, 12, 13]. These findings emphasise the variable degrees of oxidation that appear to be present in different trials including in (Chapter 6) that control the Fe behaviour and require further thought in relation to the reproducibility of tests, this is discussed more in further Sections. K is a minor element in all samples and appears to be incorporated into the glass phase except in 5_Vu where there is evidence of K in a leucite structured phase that appears to be associated with the Fe precipitation (Section 5.4). It is not clear to why this is not present in Trial 1 or absent/very low levels in 5_Xc but it is likely due to increased drum melting and metallic Fe precipitation in Trial 5_Vu.

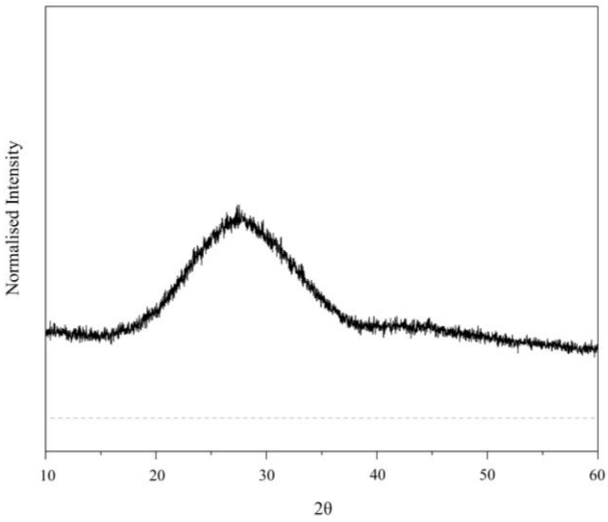

Figure 5.2 XRD pattern for 1A_Glass samples

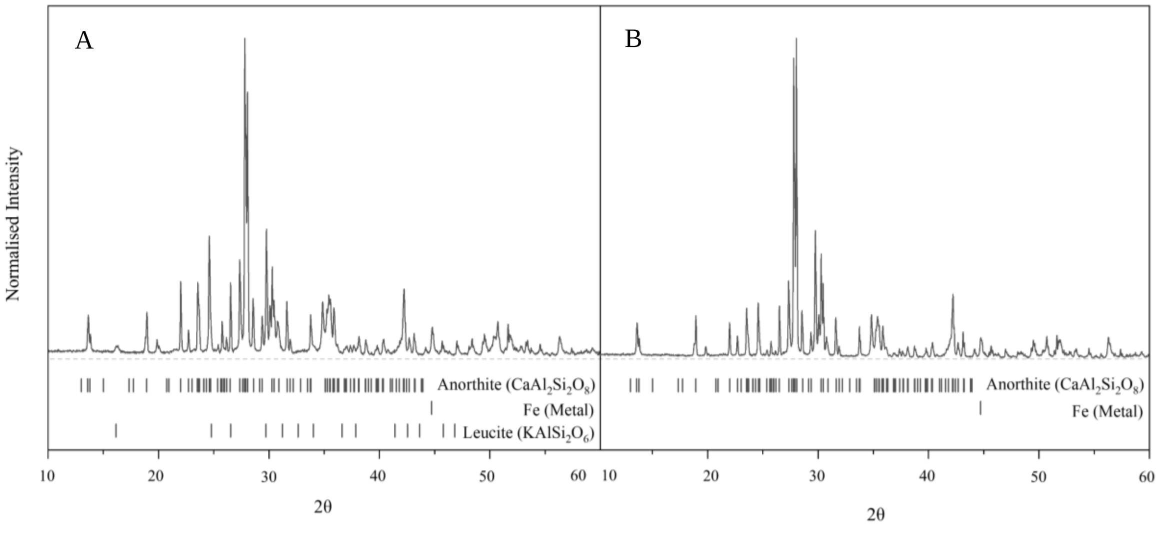

Figure 5.3 XRD pattern for A-5_Vu and B-5_Xc samples

In both Trials 1 and 5 the crystalline assemblage differs greatly from previous lab trials (Section 2.3.4) and current lab trials (Section 6.2) where crystalline material is rarely present It is important to discern what the actual representative crystalline phases in the samples are and how much changes in processing technique, conditions and waste composition is affecting composition. This is important as it has the potential to affect the distribution of the radionuclides in the wasteform and this can have a major impact on the wasteform performance. The next stage of trials (Section 7.2) it is important to categorise and understand the envelope of mineral phases present and study how their abundance and distribution varies in relation to different factors including drum composition, trial set up and processing conditions.

5.4 SEM

Analysis of the crystalline region in the Trial 1 samples represented by sample 1 supports XRD analysis with large (0.5 mm) needles of anorthite in a glassy matrix, the anorthite needles form elaborate radiating patterns (Figure 5.4A). The anorthite needles grade into the glassy matrix forming a transitional boundary to the glass region (Figure 5.4B). The glass region shows no crystallisation (Figure 5.4C) and compositionally uniform distribution of the 3 major batch elements Ca, Si and Al (Figure 5.5). The glass appears to be depleted in Al and Ca in comparison to the crystalline anorthite phase although this is not seen in the bulk compositional data (Table 5.2 and Figure 5.6). The large white grains seen toward the base of the Trial 1 waste (Figure 3.5B and C) are confirmed as being corundum grains (Al_2O_3) identified by XRD analysis (Figure 5.7 and Figure 5.1B) and there is evidence of minor K and Fe speciation into the glass phase (Figure 5.5 and 5.6).

The crystalline textures of the samples in Trial 5 (5_Vu and 5_Xc) are similar and dominated with large (0.5-5mm) broad (50-250 µm) needles of anorthite and appears to be more densely crystallised with less glass than in the Trial 1 samples (Figure 5.8A and B). The two samples differ in that 5_Vu also has abundant large (0.25-5mm) rounded porous that crosscut the crystalline texture suggesting late-stage development (Figure 5.8B). Pore presence in the upper part of the sample are expected with the upward migration of gaseous phases injected to oxidise the organic material in Trial 5 [3, 4] and point toward a vigorous melt. In both Trial 5 samples minor amounts of glassy matrix form the interstitial matrix between the anorthite (Figure 5.8C and Figure 5.9). In the glass phase there is minor growth of small (1-25 µm) tabular and dendritic metallic iron dendritic growth and evidence of a very minor K rich phase that is associated with the metallic iron growth (Figure 5.3A and Figure 5.9) and identified as a leucite structure by XRD (Section 5.3). In line with the detection in the XRD there is increased coverage of metallic Fe and K precipitation in sample 5_Vu that could explain the lack of detection in the 5_Xc and can only be described as increased metallic elements due to increased drum melting away from the unmolten drum and an undescribed K association with the metallic Fe.

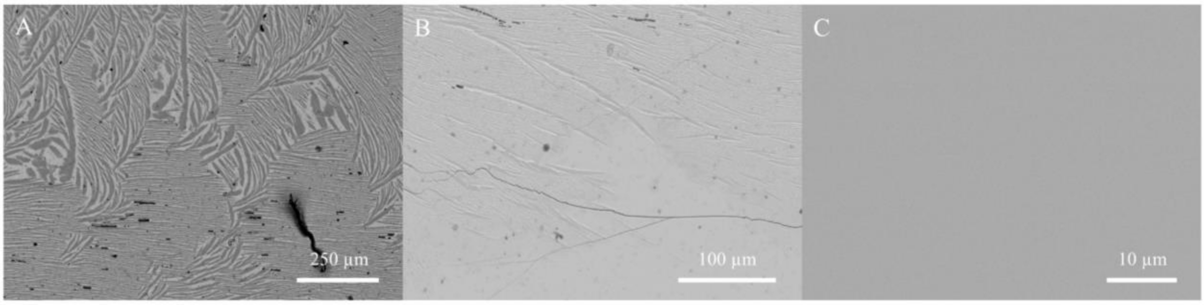

Figure 5.4 SEM images showing the textures present in A- Crystalline regions of Trial 1 region B – Mixed crystalline-glass regions of Trial 1 and C- glass regions of Trial 1

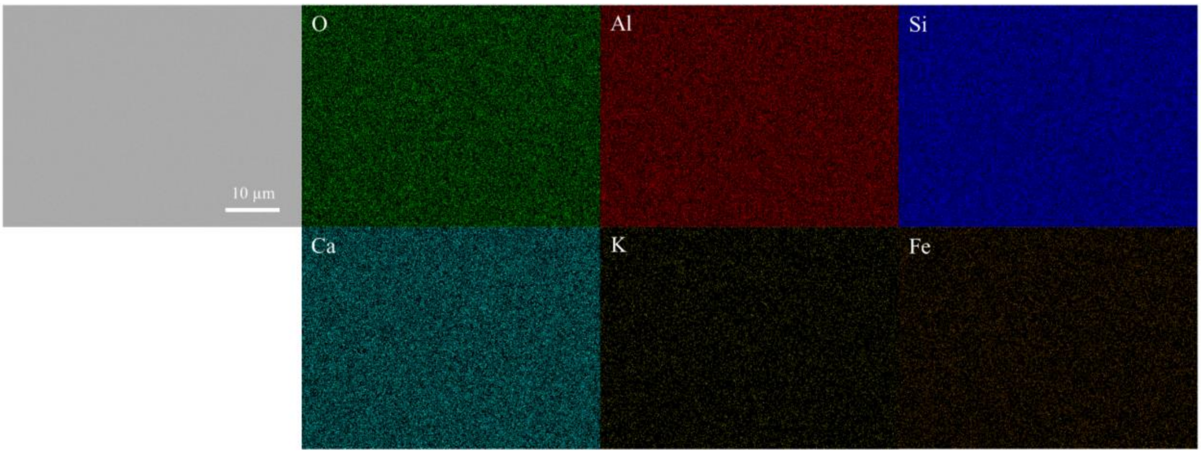

Figure 5.5 SEM and EDS maps of the glass region in Trial 1

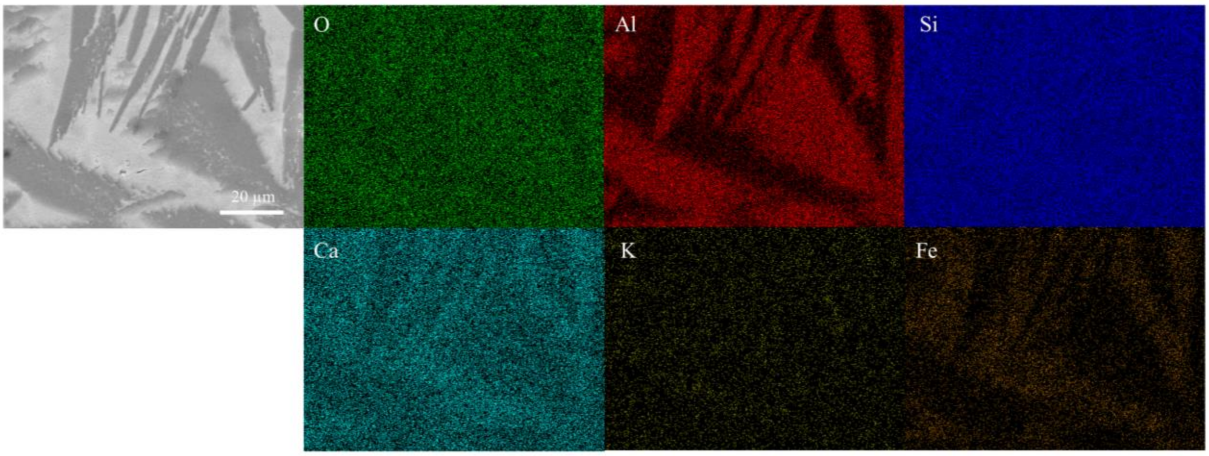

Figure 5.6 SEM and EDS maps of the crystalline region in Trial 1

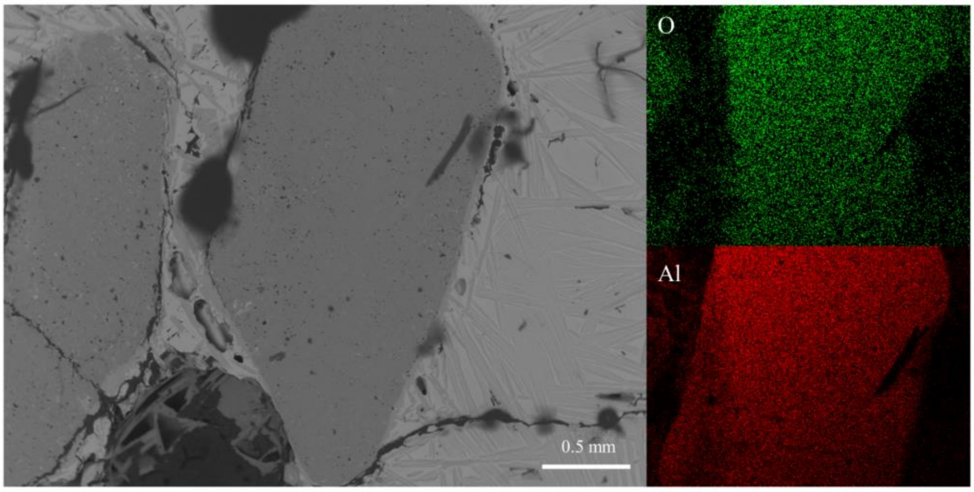

Figure 5.7 SEM and EDS maps of the Corundum (Al_2O_3) in Trial 1A.

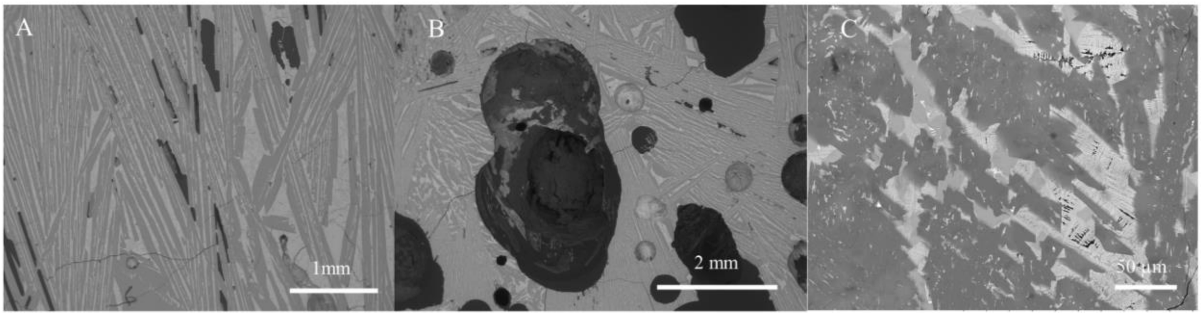

Figure 5.8 SEM images of A 5_Xc overview B 5_Vu overview C 5_Vu more detailed view.

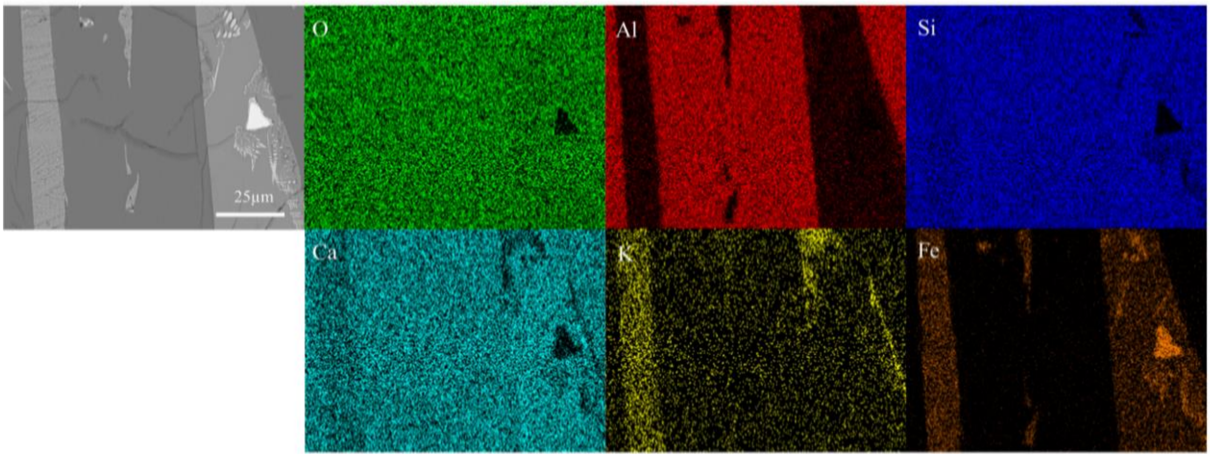

Figure 5.9 SEM and EDS maps for Sample 5_Xc

As discussed in Section 5.3 SEM analysis supports the observation that the mineralogical assemblage is different to previous and current lab trials studies and further work is required to fully understand what representants a standard mineralogical assemblage and what the controls on this are. If anorthite is a major phase in this representative assemblage, then surrogate trials are required to investigate the partitioning of relevant radionuclides between glass and anorthite.

5.5 Density

The density for all the waste is like the metallic CAS glass produced in Chapter 6 (Table 6.7) confirming the values expected from the waste composition (Table 5.4). The densities of the Trial 1 samples are all similar and slightly lower than the Trial 5 samples which can be explained by the slightly lower Fe_2O_3 content of the Trial 1 samples (Table 5.2, 5.3 and 5.4) 5_Vu has a lower density than 5_Xc due to the porous open texture of the sample (Table 5.4 and Figure 5.8B).

Table 5.4 Density measurements for the samples from Trial 1 and 5.

Sample	Density (g/cm^3)
1	2.8097 +/- 0.0094
1A	2.8826 +/- 0.0140
1A_Glass	2.7940 +/- 0.0083
5_Vu	2.9123 +/- 0.0055
5_Xc	3.0367 +/- 0.0074

5.6 Thermal Analysis

Analogous to analysis in Section 4.5 the interpretation of the thermal analysis needs to be treated with a large caveat due to the inability to successfully remove the background. There does however appear to be a few clearly defined thermal events which have been tentatively attributed to the glass transition (T_g), crystallisation events (T_x) and/or a melting (T_m) events (Figure 5.10 and Table 5.5) Estimated T_g, T_x and T_m values the Valingar samples. T_g can only be clearly defined in 1A_glass with the value of 870 °C analogous to previous studies [14, 15] and lab samples in Section 6.5, the lower levels of glass in the other samples and background likely dilute the signal in the other samples. A higher temperature crystallisation event is seen in 1A_glass and 1A at 970-980 °C but is less obvious/absent from the more crystalline samples as the phase may already be present but attribution cannot be assigned without further study, a melting event at 1130-1150 °C is common to all samples and likely is related to the crystalline event seen in 1A and 1A_glass.

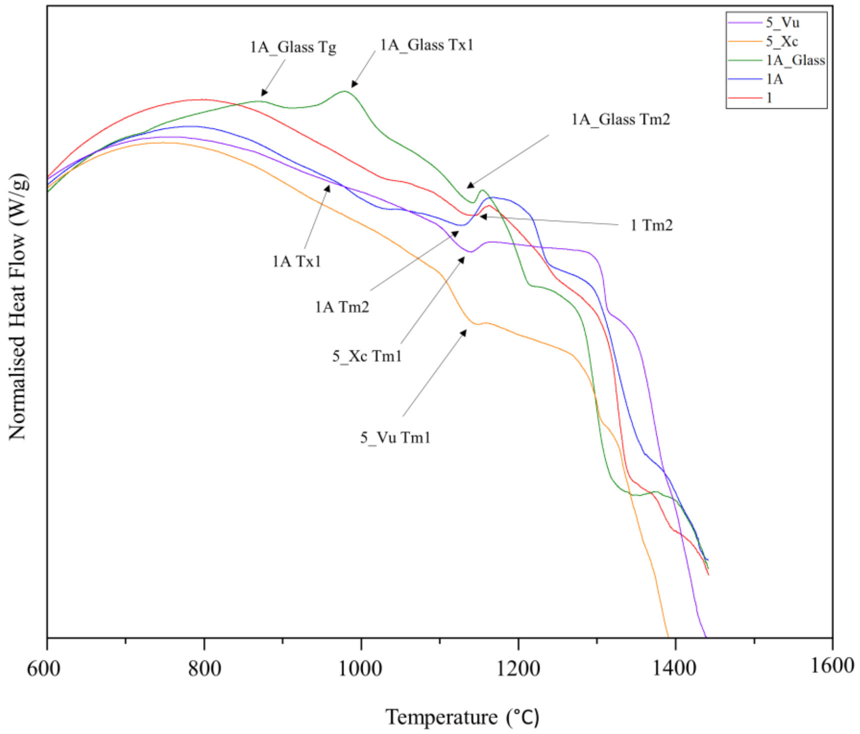

Figure 5.10 Figure showing the normalised heat flow of the USA geomelt samples with increasing temperature.

Table 5.5 Estimated T_g, T_x and T_m values the Valingar samples.

Sample	Tg (°C)	Tx (°C)	Tm (°C)
1	-	-	1140
1A	-	970	1130
1A_glass	870	980	1140
5_Vu	-	-	1140
5_Xc	-	-	1150

5.7 X-Ray Absorption Spectroscopy (XAS)

X-Ray absorption spectroscopy (XAS) and Mossbauer spectroscopy (Section 5.8) were used as complementary techniques to investigate the Fe environment in the Valingar samples. Analogous to analysis in Section 4.6 of USA geomelt samples, the Fe coordination environment was investigated using X-ray absorption. The same standardisation and fitting parameters were used as described in (Section 4.6) with the same considerations. For the Valingar samples, the E_0 position (Table 5.6) indicates that for all the samples excluding 1A_glass, the Fe is Fe^{3+}. This is contradictory to other major analysis techniques (see below) which indicate most of the samples are dominated by Fe^{2+}.

Table 5.6 E_0 positions for Fe K-Edge XANES spectra for the Valingar samples and 4 standards staurolite, aegirine, $FeCO_3$ and $FePO_4$.

Sample	E_0 Energy (keV)
Aegerine	7115.80
Staurolite	7111.59
$FeCO_3$	7114.61
$FePO_4$	7115.40
1	7115.83
1A	7115.84
1A_Glass	7110.20
5_Vu	7115.40
5_Xc	7115.40

The complex shape of the Fe K-edge (Figure 5.11) and the numerous changes in angle make this form of analysis complicated as stated in Section 4.6 for sample MRI7 and may also be complicated in some of these samples by the presence of metallic iron [16] it also makes further investigation of the local environment by linear combinations of the standards difficult. A more robust technique is to fit the pre-edge peak with pseudo-Voigt functions (Figure 5.12A and B) and compare the pre-edge position and integrated area (Figure 5.13) as for Section 4.6. Comparisons of the Valingar samples show that they are dominated by Fe^{2+}, with some minor contribution from Fe^{3+}. The samples are in a range of different coordination environments, Trial 5 samples are in six (VI) fold octahedral co-ordination, Trial 1A_glass almost exclusively four (IV) fold tetrahedral coordinated Fe in the pure glass and the sample 1 and 1A samples in a mixed ‘5-fold’ co-ordination either being a mix of 4- and 6-fold sites or co-existence of 4, 5 and 6 coordinated sites [17]. SEM analysis (Section 5.4) confirms that excluding some minor metallic Fe in Trial 5, all the Fe in the Valingar samples is partitioned into glass part of the wasteforms. The Fe^{2+} oxidation state that is found in the Valingar samples supports a weak oxidising environment as most of the input Fe will be metallic iron (Fe^0) from drum melting. Elevated levels of Fe_2O_3 in Trial 5 could relate to the measures implemented to increase drum melting and the addition of oxidants converting this metal into oxide form, although the presence metallic iron in XRD and SEM shows some incomplete oxidation.

The Fe environment is different to the environment seen in the pre-edge fitting of lab produced metallic CAS glass (Section 6.6) where an oxidation state of Fe^{3+} produced by a stronger oxidising environment. The variable levels of oxidation in the lab and industrial trials is potentially caused by variety of factors such as presence of organic material, graphite electrodes, metallic drum or the size of melt and reduced accessibility and mixing of oxidants. This is critical as it shows that the vitrification environment can have a major impact on the Fe environment that can impact the overall glass framework and wasteforms properties due to Fe^{2+} acting a glass modifier and Fe^{3+} acting as a network former (Section 2.3.3). The coordination in the pure glass sample (1A_glass) in the industrial trials is tetrahedral four (IV) fold - coordinated Fe, which is common for Fe^{2+} in natural glasses (Section 2.3.3 and [17]) and matches samples in Chapter 6 suggesting that Fe in glass irrespective of oxidation state in accommodated in tetrahedral four (IV) fold sites. It appears that crystallisation of anorthite in the samples increases the co-ordination toward octahedral six (VI) fold octahedral coordinated with Trial 1 having a lesser shift than the samples in Trial 5 which correlates with the increased anorthite crystallisation and reduced in glass percentage from Trial 1 to Trial 5 (Figure 5.4 and 5.8). Fe^{2+} has been found in six (VI) fold octahedral coordination in natural glasses (Section 2.3.3 and [17]) and its percentage in the Valingar trials correlates and is controlled by the amount of anorthite crystallisation this is attributed to a shift in its role in the glass to compensate for the depletion Al and to a lesser extent, Ca caused by the anorthite crystallisation.

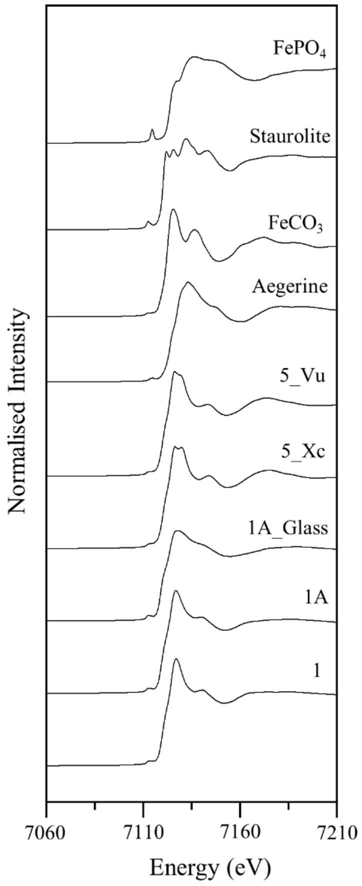

Figure 5.11 Fe K-Edge XANES spectra for the Valingar samples and 4 standards staurolite, aegirine, $FeCO_3$ and $FePO_4$.

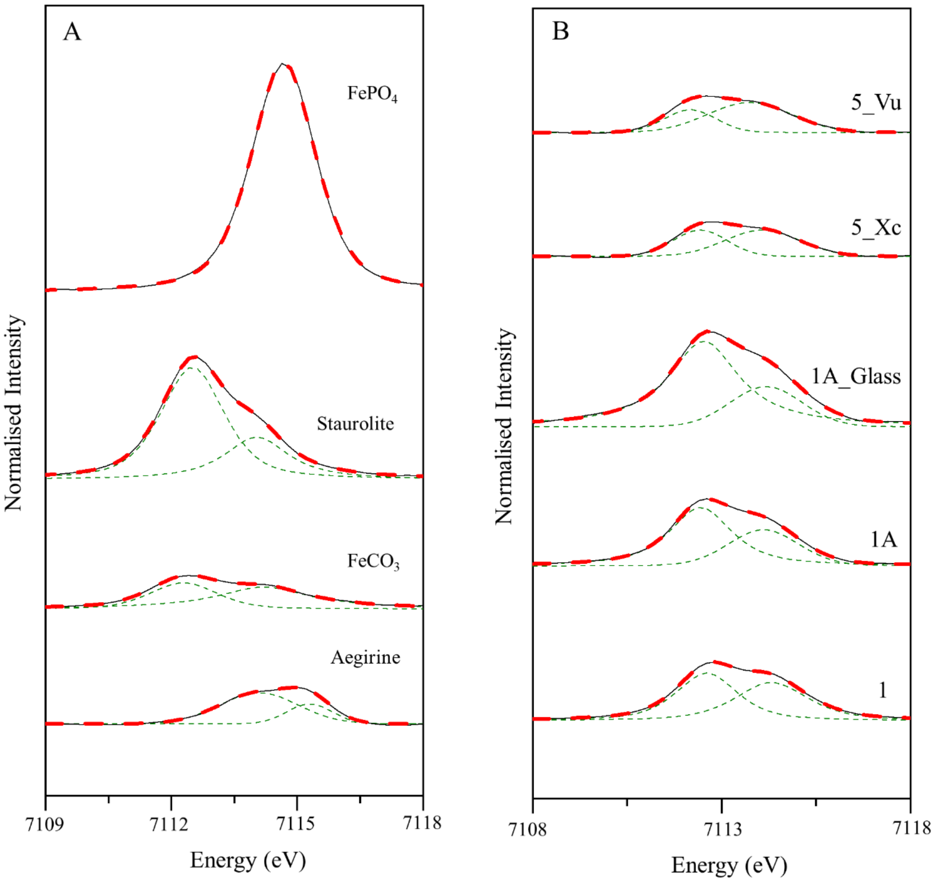

Figure 5.12 Fitted pre-Fe K-Edge XANES spectra for the A 4 standards staurolite, aegirine, $FeCO_3$ and B Fitted pre-Fe K-Edge XANES spectra for Valingar samples.

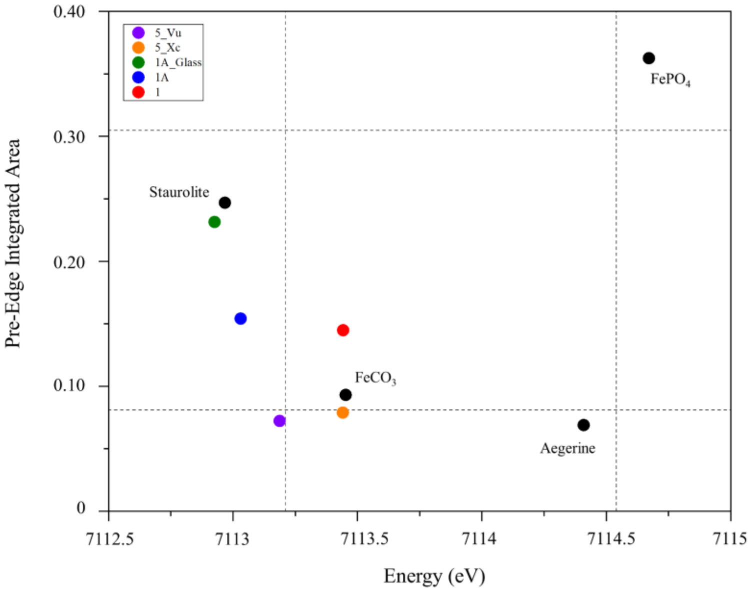

Figure 5.13 Pre-edge integrated intensities and centroid position for 4 standards and Valingar samples.

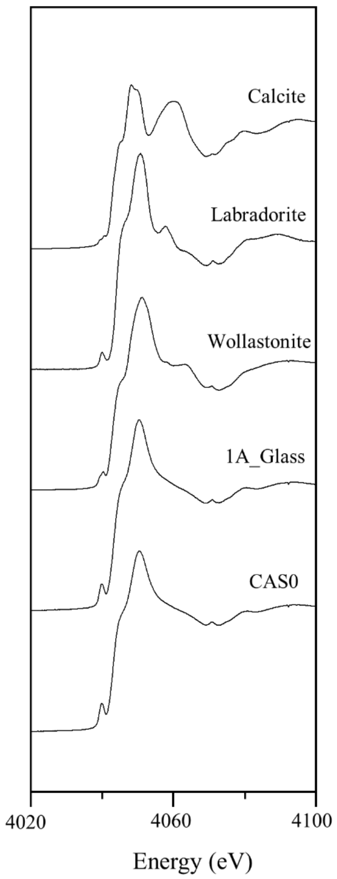

Figure 5.14 Ca K-Edge XANES spectra for the Valingar sample: 1A_Glass, 3 standards calcite, labradorite and wollastonite and CAS0 from Chapter 6 for reference.

A major component of the CAS glass is Ca that acts as a network modifier element and charge compensates the Al in the network structure. Understanding the atomic environment of the Ca is important to understand the structure and behaviour of the CAS glass and allows for comparisons to lab based samples (Section 6.6). Following on from the examples used in the study of Fe and V (see above and Section 4.6) a set of standards have been analysed along with the Valingar 1A_glass sample, the sample area for all CAS glasses from Section 6.6 has also been included in this analysis for comparison (Figure 5.16). As discussed previously (Section 3.2.10) the standards represent a series of co-ordination environments for the consistent Ca^{2+} cation with an apparent increasing pre edge integrated area with co-ordination/distortion, the energy seems consistent except for the outlier labradorite. The oxidation state is constant in Ca^{2+} so it is not as clear as to the effect of the co-ordination on the energy value if any, to work this out a wider standard study is required. What can be concluded from this initial and minor study is that the CAS Ca^{2+} environment is most representative of the minerally equivalent labradorite in a distorted polyhedron with seven oxygens with a possibly high co-ordination shown by the elevated pre edge integrated area. The environment in the Valingar glass is analogous to the CAS glass in Section 6.6 supporting the comparison between the industry and lab samples.

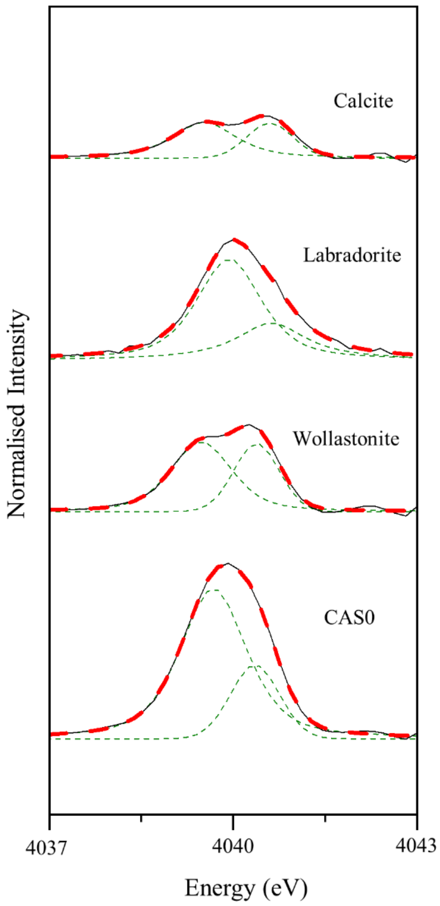

Figure 5.15 Fitted pre-Ca K-Edge XANES spectra for the 3 standards calcite, labradorite and wollastonite and the Valingar sample: 1A_Glass.

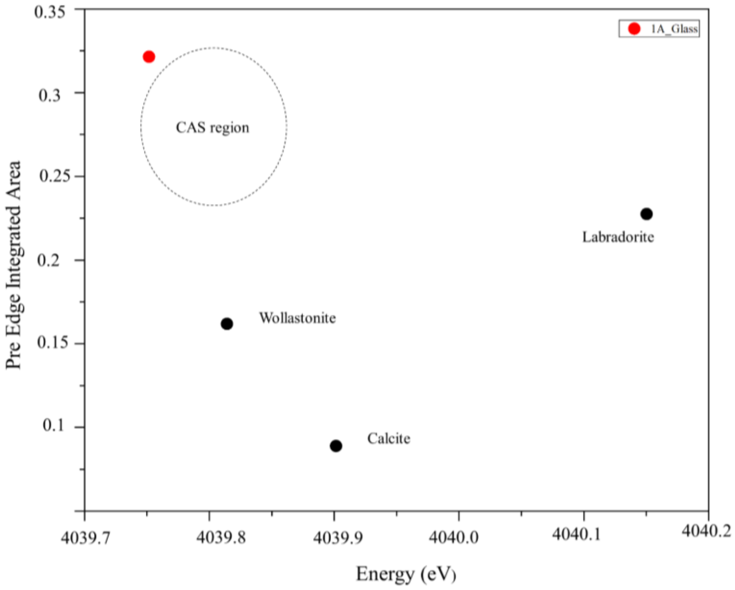

Figure 5.16 Pre-edge integrated area and centroid position for 3 standards calcite, labradorite and wollastonite plotted against the Valingar sample: 1A_Glass. The CAS region from the fitted pre-edge Ca K-edge XANES spectra for samples from Section 6.6 is plotted for comparison.

5.8 Mossbauer Spectroscopy

Mossbauer spectra as for Section 4.7 can be used for a comparison to X-ray absorption analysis to investigate Fe environment. Spectra from the different samples for each trial have been fitted with several Lorentzian peaks (Figure 5.17 and 5.19) with the position and splitting diagnostic of the Fe environments.

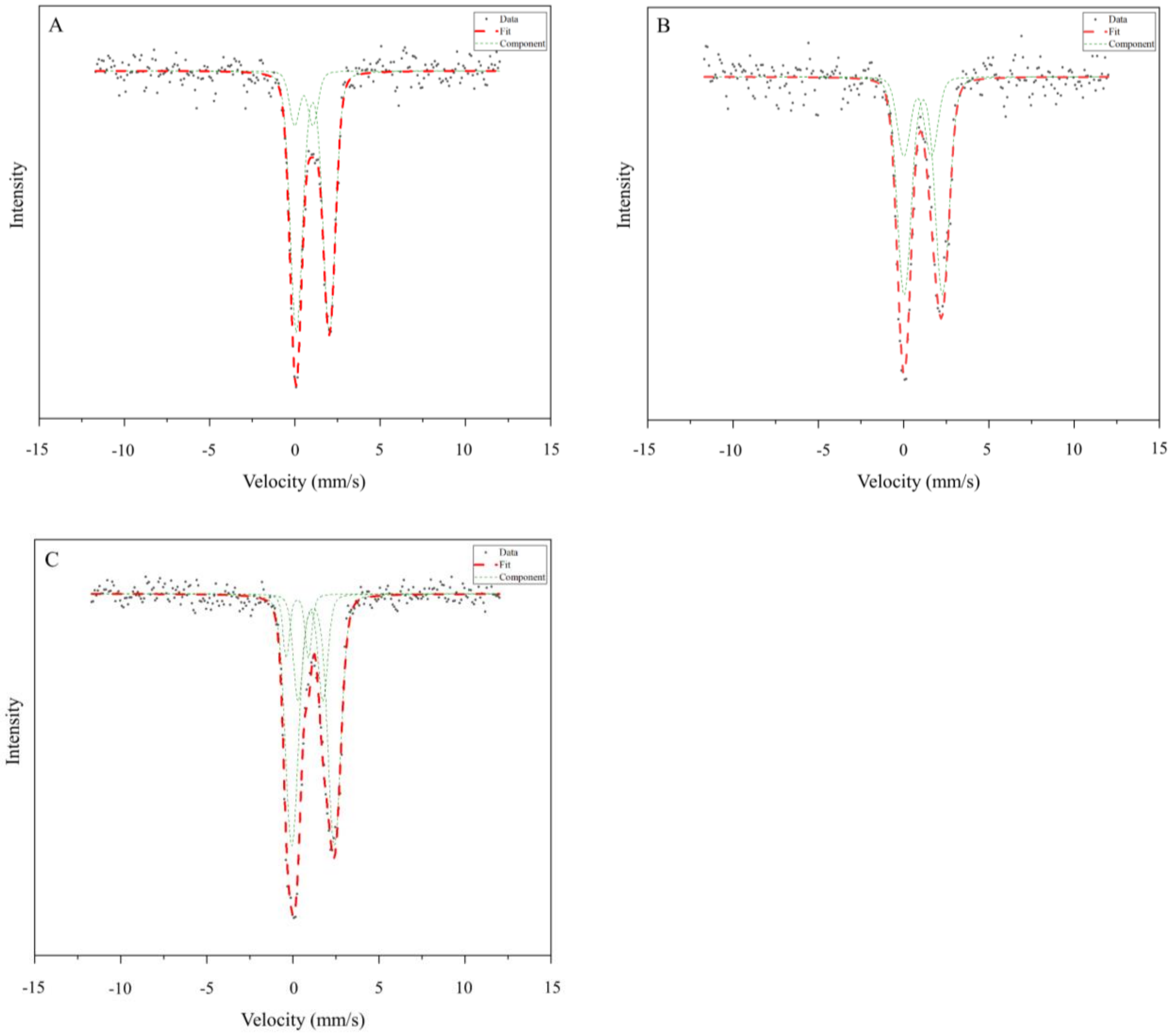

Figure 5.17 Fitted Mossbauer spectra for A-1A_Glass B- 1A C- 1

Samples 1, 1A and 1A_Glass are dominated (0.68-0.85) by a doublet that has an isomer shift of 1.05-1.2 mm/s and a quadrupole splitting of 1.9-2.5 mm/s this is indicative of Fe^{2+} but with different co-ordination environments and some distortion. The samples with some anorthite crystallisation (1 and 1A) have higher quadrupole splitting values (2.2-2.5 mm/s) indicative of six (VI) fold octahedral coordination with greater crystallisation increasing the quadrupole value showing increased distortion of the Fe^{2+} site. The glass sample has a lower isomer shift value of 1.05 mm/s and a lower quadrupole value of 1.9 mm/s indicative of a lower four (IV) fold tetrahedral coordination tetrahedral environment (Figure 5.17 and 5.18) Sample 1 and Sample 1A_Glass have secondary (Table 5.7) contributions from isolated Fe^{3+} in distorted six (VI) fold octahedral coordination. Doublets at isomer shift values of 0.3 and 0.5 mm/s with quadrupole values of 1.3 and 1.1 mm/s respectively are closest to Fe^{3+} in a distorted six (VI) fold octahedral coordination. Sample 1 and Sample 1A also show a contribution (0.22-0.25) from a site that is indicative of a mixed site where adjacent Fe^{2+} and Fe^{3+} caused a delocalisation of electrons creating an average $Fe^{2.5+}$ environment [18]. Doublets at isomer shift values of 0.8 and 1.0 mm/s with quadrupole values of 1.6 and 1.4 mm/s are indicative of the mixed site (Figure 5.17 and 5.18).

Samples 5_Vu and 5_Xc sample are dominated (0.63 and 0.65) by a doublet with an isomer shift of 1.16 mm/s and quadrupole splitting of 2.39-2.50 mm/s, this is indicative of Fe^{2+} in an six (VI) fold octahedral environment, potentially with some distortion due to the elevated quadrupole value (Figure 5.18 and 5.19).

5_Vu has a contribution (0.07) (Table 5.7) from isolated Fe^{3+} in six (VI) fold octahedral environment with a doublet at an isomer shift of 0.50 mm/s and a quadrupole splitting of 0.38mm/s. Both 5_Vu and 5_Xc have contributions (0.28 and 0.37) from a mixed site created by delocalisation of electrons around adjacent Fe^{2+} and Fe^{3+} sites [18] with isomer shift values of 0.81-1.27 mm/s and quadrupole splitting of 0.82-1.23 mm/s (Figure 5.19Figure 5.20).

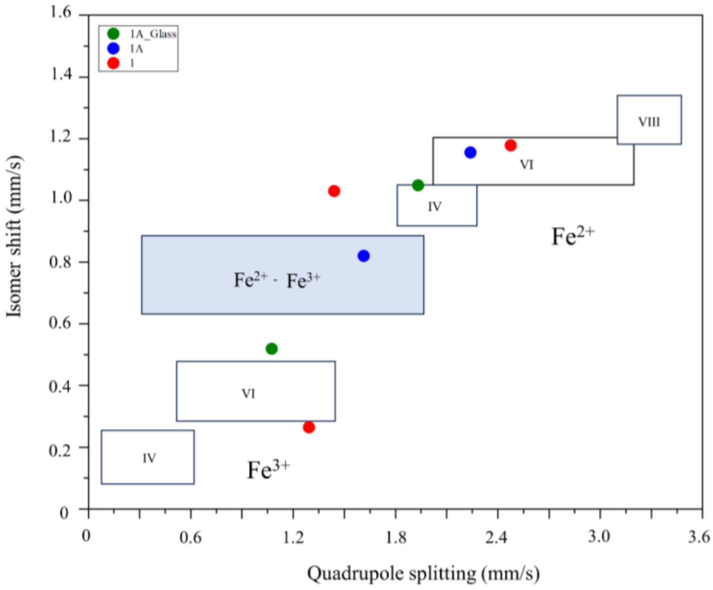

Figure 5.18 IS (Isomer shift) and QS (Quadrupole splitting) diagram from [18] with the values from each fit in (Figure 5.17) plotted.

The Mossbauer data mostly supports the X-ray absorption (Section 5.7) analysis with confirmation of predominantly Fe^{2+} in the independent Fe environments, excluding mixed environments (Table 5.7) The Mossbauer data does identify that there is some significant (upto 0.37) contribution from mixed environment sites where neighbouring Fe^{3+} and Fe^{2+} create a delocalisation of electrons creating an average $Fe^{2.5+}$ environment. This fits with the X-ray absorption data that are slightly shifted to higher value that weakly correlates with the minor level of Fe^{3+} but does not seem to be modified by the more significant levels of the mixed site. This contrasts with metal CAS samples in Section 6.7 where there are significant isolated Fe^{3+} sites that are clearly dominating the X-ray absorption signal.

This supports the reduced oxidation in the industrial samples with oxidation from metallic iron mostly forming Fe^{2+} with only minor isolated Fe^{3+} in comparison to major isolated Fe^{3+} sites in the metal CAS lab glasses.

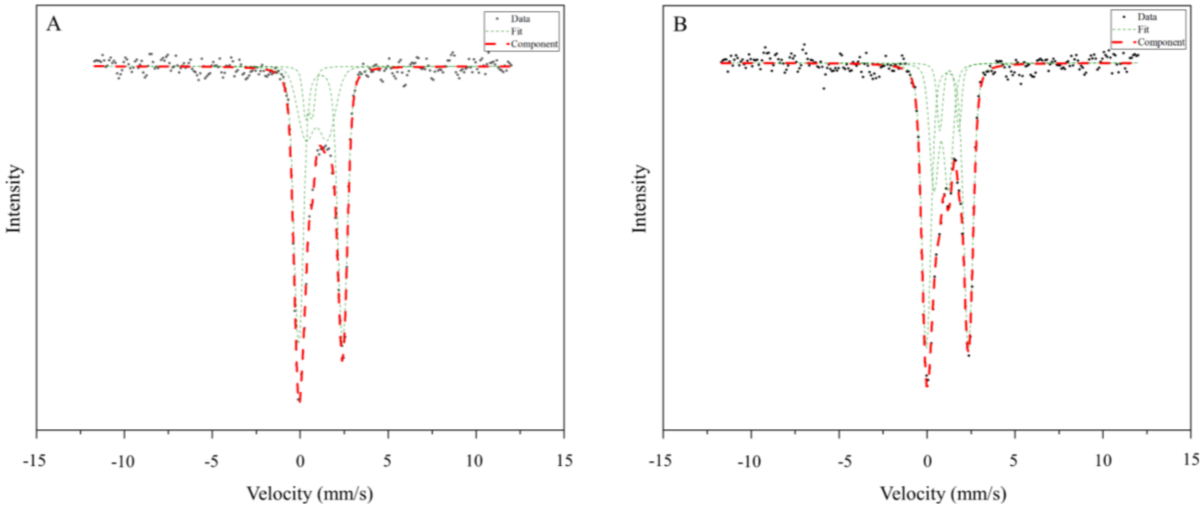

Figure 5.19 Fitted Mossbauer spectra for A-5_Vu B- 5_Xc

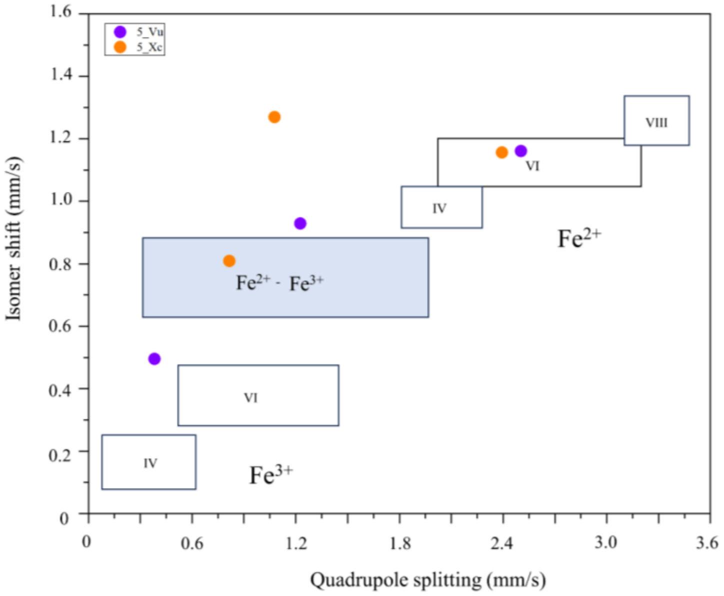

Figure 5.20 IS (Isomer shift) and QS (Quadrupole splitting) diagram from [18] with the values from each fit in (Figure 5.19) plotted .

Table 5.7 Fraction of independent Fe^{3+} in each sample as a fraction of the total Fe content.

Sample	$Fe^{3+}/\Sigma Fe$
5_Vu	0.07
5_Xc	0 (note mixed site is not included)
1A_Glass	0.15
1A	0 (note mixed site is not included)
1	0.10

All the Valingar samples excluding 1A_glass have elevated values of mixed sites with only low amounts of isolated Fe^{3+} in the 1A_glass, 5_Vu and 1 samples. Along with the change in co-ordination environment for the Fe^{2+} sites this supports the conclusion from X-ray absorption data that the crystallisation of anorthite is creating a shift in the Fe behaviour with addition of small amounts of Fe^{3+} that form delocalised $Fe^{2.5+}$ environments, with rare isolated Fe^{3+} in glassier regions. Crystallisation also appears to shift the co-ordination of the Fe^{2+} sites to higher Fe (VI), with 1A_glass dominated by Fe^{2+} in Fe(IV), supporting x-ray absorption data. It is not totally clear as to the reason for the change in co-ordination, but it is likely related to a change in role/position of in Fe^{2+} to accommodate it in a CAS glass structure altered by the local depletion Al and to a lesser extent Ca caused by the anorthite crystallisation.

5.9 Raman Spectroscopy

Raman spectroscopy was carried out to investigate the glass structure from sample 1A_Glass (Figure 5.21), anorthite crystallisation prevented collecting spectra from the glass regions of the other samples. The spectra resemble the general pattern of Raman spectra from various CAS series seen in Section 6.8, supporting the comparison between the industrial and laboratory trial glass. As for the different CAS glasses in Section 6.8 a medium and high frequency region is present, and which can be deconvolved into 3 (medium region) and 2 (high region) gaussian peaks (Table 5.8) attribution of these peaks is ambiguous with various attributions given for different frequency values (see Table 3.20 in Section 3.2.9). The two bands at ~910 and 990 cm^{-1} relate to the stretching in Q species of Q1-2 and Q3 structural units in the silicate network with reduces values caused by the proximity to neighbour aluminium atoms and is indicative of some depolymerisation of the network. The low value at ~415 cm^{-1} relates to Si-O-Si (A1) asymmetric motion in 5-6 membered silicate rings showing that there is still a polymerized structure in the glass supported by high durability in Section 5.10, but the band at 530 cm^{-1} although slightly shifted in frequency could relate to merging of the D1 and D2 band and Si-O^{o} rocking in Q4 unitsor Q3 T-O-T breathing that is seen glasses with increased modifiers and is an indication of increased depolymerisation, which is consistent with the composition and Fe speciation. The peak at ~695 cm^{-1} is poorly defined but likely relates to Si-O^{o} stretching motion but can also relate to bond vibration in the aluminate network. Substitution of Si^{4+} by Al^{3+} and minor Fe^{3+} maybe influencing the position of the peaks, particularly the ones associated with Si-O-X motion, due to changes in the force constant of the bonds.

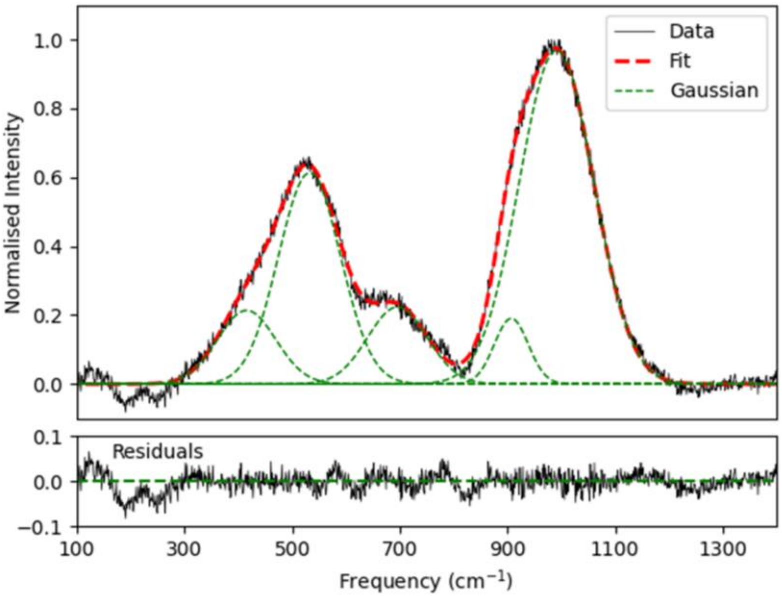

Figure 5.21 Fitted Raman spectra for 1A_Glass sample.

The ratio of the high to medium peak gives the Raman Polymerisation Index (RPI) which is a measure of the polymerisation of the glass, the RPI for the 1A_glass sample is 0.81 which is most analogous and a bit lower than the CAS0 glasses in Section 6.8, suggesting that the Fe addition in the Valingar samples is not greatly changing the structure with Fe^{2+} replacing Ca^{2+} in the glass structure as a network modifier and the minor Fe^{3+} likely replacing Si^{4+} and Al^{3+}in the glass structure as glass formers. The slightly lower RPI in comparison to high silica glasses such as the KBasin (1.34) in Section 4.8 supports the depolymerisation signals seen in the gaussian deconvolution. There is a subtle difference in the Valingar to CAS0 possibly linked factors such as reduced co-ordination of the Fe site in the glass and variable force constant of the Fe. Interestingly Raman spectrum, gaussians and RPI is different to the CAS metal series in Chapter 6, specifically CAS M5 which compositionally is the most analogous to the 1A_glass sample. This supports the prediction that the Fe speciation is different in the CAS metal glasses with the incorporation and structural alteration different for larger concentrations of Fe^{3+} cations with more detail found in Section 6.8. This reinforces the conclusion that the oxidation environment is a very important consideration when recreating synthetic industrial glasses in the lab environment.

Table 5.8 Fitting parameters for 1A_Glass Raman spectra.

Position	Fraction of region
415.262	0.195
532.949	0.596
695.163	0.208
907.163	0.082
990.964	0.918

5.10 Glass Durability

Valingar have carried out some initial dissolution tests on Trial 3 (Drum S) material, presumably from a similar location as the XRF samples in Section 5.2, using the BS EN 12457 test, that found the leaching of the product was minor and within the WAC acceptance levels [19]. To build upon this initial basic study and investigate how differences in the Valingar waste's composition and structure affect durability, two different durability (PCT-B and MCC-1 tests (Section 3.4.11)) were completed on the samples from Trial 1 and Trial 5.

5.10.1 PCT-B Powder Tests

Powder samples for PCT represented the sample identities from the previous above analysis and as described in (Section 3.1.1.2 and Figure 5.22) SEM images to show the successful splitting and sorting of the Trial 1 sample to represent the A – 1 which is dominated by crystalline anorthite, B – 1A which is a mix of anorthite and glass and C – 1A_glass which is just glass material.). SEM analysis of pre-PCT powders shows the successful separation of textures (Figure 5.22) that improves confidence in analysis from the dissolution tests and for other above analysis techniques. MCC tests were also split based upon textures in (Section 3.1.1.2) with an additional intermediate additional texture included for Trial 5 as the transition from the crystalline to porous texture was interpreted as a more gradational change.

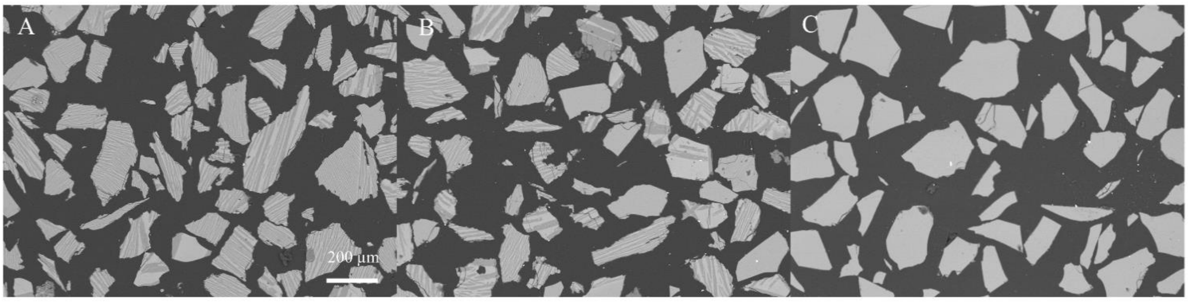

Figure 5.22 SEM images to show the successful splitting and sorting of the Trial 1 sample to represent the A – 1 which is dominated by crystalline anorthite, B – 1A which is a mix of anorthite and glass and C – 1A_glass which is just glass material.

During the PCT-B tests there are very low levels of elemental loss over the test duration showing that the samples are very durable. Significant elements in the glass are the majors Si, Al, Ca, and Fe along with minor amounts of Na and K.

All elements show an initial rise in the NL mass loss that is thought not to relate to the initial rate as seen in Section 4.9.1 as the NL is very low and there is no evidence of the later stages of dissolution. Instead, it relates to the artificial day zero time point with an initial instantaneous release of elements due to the dissolution of fines causing an elevated value, this is normally hidden by the larger elemental release related to glass dissolution (Section 4.9.1) but is highlighted here by the very low elemental release from very durable glasses. The value of this initial release is low for all elements except in K where there is a higher NL (Figure 5.23). Post the initial release there is no more significant release in any of the major or minor elements excluding K with all other elements following a similar pattern to Si (Figure 5.23 and 5.24), this again highlights the very durable nature of the samples. The increased NL and pattern of linear increase in NL with increased test duration shows there is some significant release of K from the glass, with a more significant increase for the samples from Trial 5 than Trial 1, indicating a subtle difference in durability, with Trial 1 being more durable. The release of K, ahead of other network modifiers such as Na and Ca is due to the preferential ion exchange of K due to its low ionic strength, reduced charge, and weaker bonding than other network modifiers in the glass, the analogous behaviour between samples within each Trial shows that the release is not affected by textures or glass concentration. An alternative explanation is that the K release could relate to preferential dissolution of the K rich phase identified as leucite in the Trial 5_Xc. However, this is not thought to be the case as the phase is not seen in Trial 1 or Trial 5_Vu, but the K dissolution behaviour is and there is no supporting evidence of this in SEM analysis of post PCT powders (not shown here) or MCC-1 samples (see later).

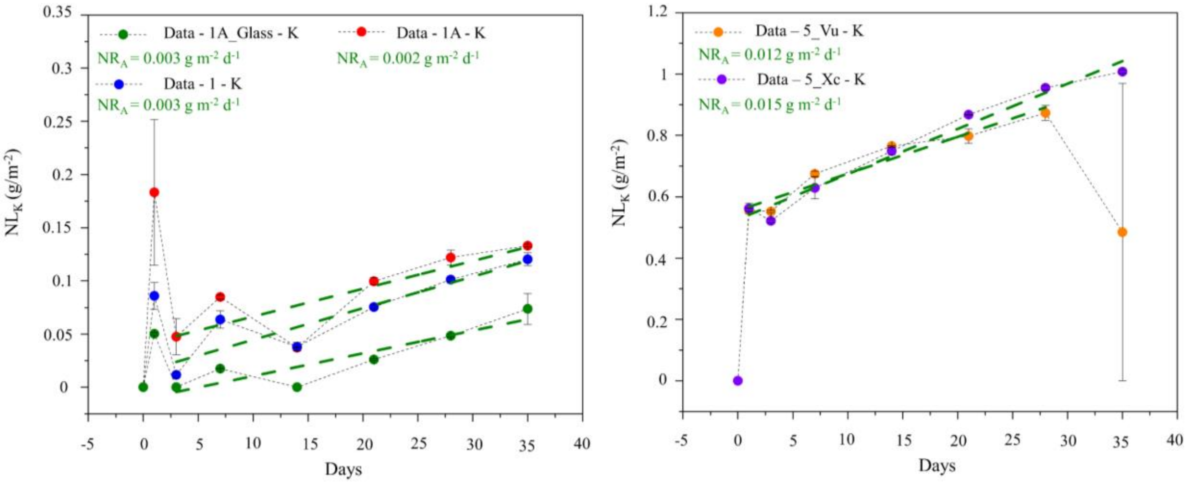

Figure 5.23 Normalised Mass Loss of element K, 1A_Glass, 1A and 1 (left) and 5_Vu and 5_Xc (right) with dissolution rates calculated for is presumed as the early stages of dissolution and labelled as NR$_A$.

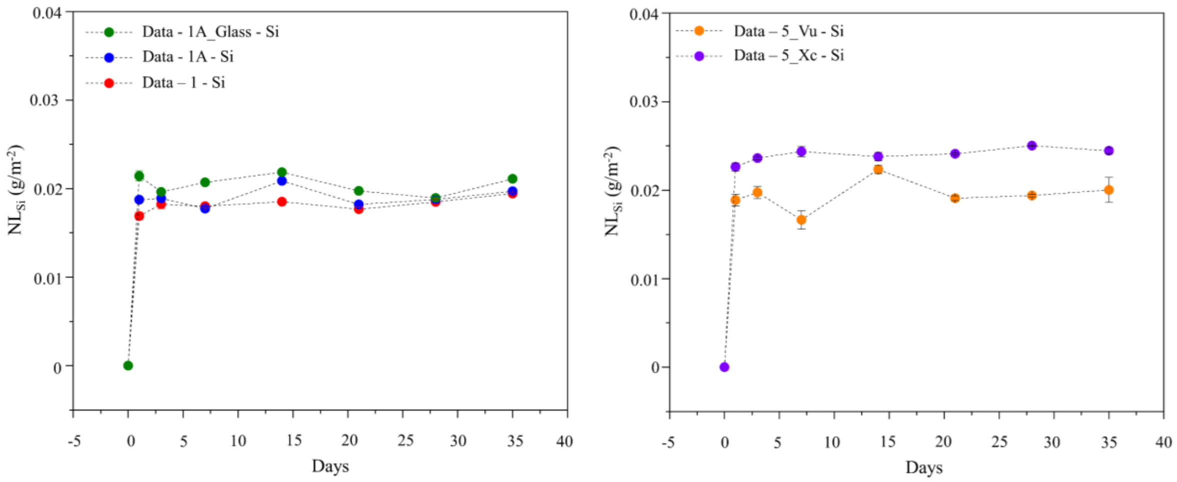

Figure 5.24 Normalised Mass Loss of element Si 1A_Glass, 1A and 1 (left) and 5_Vu and 5_Xc (right).

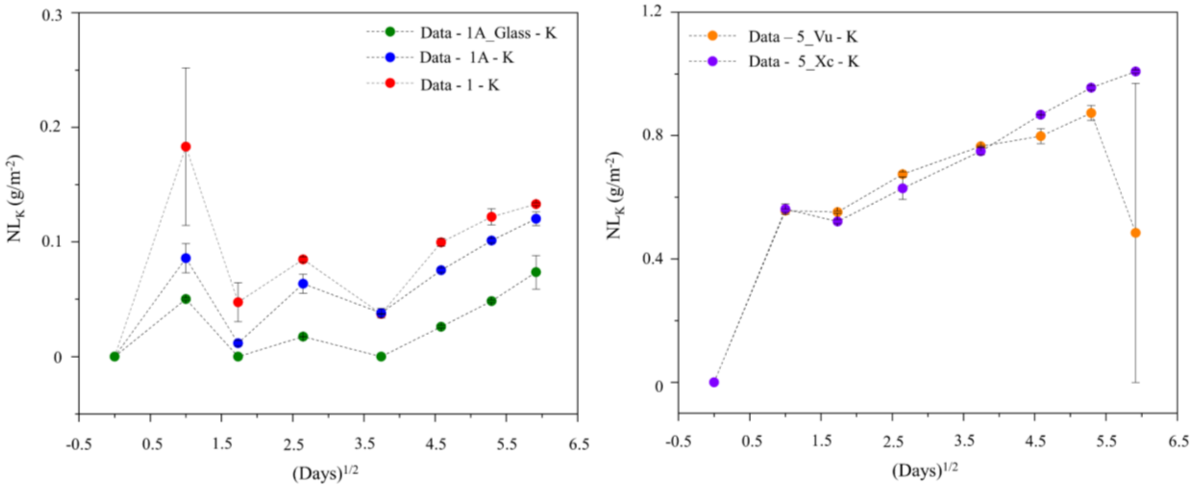

Figure 5.25 $t^{1/2}$ vs NL mass loss graphs for K for 1A_Glass, 1A and 1 (left) and 5_Vu and 5_Xc (right).

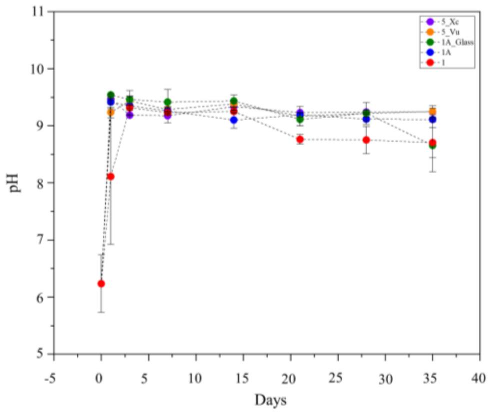

Figure 5.26 pH data for Trial 1 and 5 PCT tests.

In the absence of any significant release of Na, the only reliable tracer in the samples, K has been used as a tracer, but rates are treated with caution due to the higher capacity of K to be incorporated in secondary phases such as clays. The dissolution rate (NL_A) has been calculated for each sample in the two trials but not attributed to a kinetic regime (stage I/II) There is a difference between trials with the rate (NL_A) and overall 35 day release of K a factor of ten higher for the Trial 5 samples than the Trial 1 samples (Figure 5.23), showing as stated above that Trial 1 is slightly more durable than Trial 5. The difference can be potentially attributed to several factors. Firstly as already mentioned, the 5_Xc sample has a clear crystalline K phase tentatively identified as leucite (Figure 5.3 and 5.8) that could be controlling the different K behaviour, however K release appeared analogous to dissolution behaviour in samples where leucite has not been identified indicating this is likely not the primary mechanism for K release in the PCT-B tests and its presence in 5_Xc is not having a major effect. Although K is present in relatively lower amounts (Figure 5.5, 5.6 and 5.9) in the glass, the analogous behaviour of K dissolution behaviour between Trial 1 and 5 points towards the K loss in the PCT-B being controlled by glass dissolution with the difference between Trial 1 and 5 relating to difference in the composition. Trial 5 has subtly lower Si attributed to sample heterogeneity (Table 5.2 and 5.3) and the Fe present in the glass has been identified as Fe^{2+} performing a network modifier role and there is more Fe in Trial 5, although levels in the glass vs metallic Fe needs calculating (Section 5.7 and 5.8). These two factors could act together to structurally depolymerise the glass network and account for the slight reduction in durability. There is no major difference in the K loss and dissolution rates between the samples within the different trials which suggest that the textural and crystalline changes are not having a major impact on the rate of dissolution. The K behaviour, as mentioned above, is linked to ion exchange behaviour and the ionic strength of the ionic species. K has the lowest ionic strength out of the network formers (Ca, Na and K) and is single bonded in comparison to Ca being double bonded, hence its preferential release and dissolution behaviour. The linear nature of K $t^{1/2}$ graph shows the diffusive rate control of the K release and dissolution rate in the PCT-B tests (Figure 5.25).

The weak alkali pH (Figure 5.26) is buffered by the low elemental release rate with no significant variance between samples across the trials supporting the durable nature of the samples and showing that the small variation in K is not having an impact on the pH of solution.

5.10.2 MCC-1 Monolith Tests

Due to the small amount of material available only a single time point MCC-1 could be performed, which limits the conclusions that can be drawn from these tests. In contrast to the PCT-B tests, the increased test duration of 320 days may be used to explain the increased levels in the NL values (Table 5.9), as the difference in the SA/V ratio is accounted for in the NL calculation. There is also the possibility that as in Chapter 4 with the MRI7 tests, except with a reverse in solubility of the phases, the increase SA in the PCT-tests means that the low solubility crystalline phases are having a bigger impact on the wasteforms dissolution and there is more dominant glass dissolution in the MCC-1 tests proportionally increasing the NL. These predictions are supported by the clear visible evidence for preferential glass dissolution over all crystalline phases including the anorthite, leucite and Fe oxide (Figure 5.27 A-I and Figure 28 C-E) supporting the conclusion from the PCT-B tests that the glass, and not the mineral phases, are controlling the elemental dissolution behaviour. Finally, the difference in NL values could relate to the difference stages of dissolution each test has reached with PCT-B progressing faster so spending a longer time in the lower residual rate, whereas the MCC-1 is diluter so remains in the higher initial rate, although the observations from PCT-B tests, a minor alteration layer seen in the most glass rich wasteform (Figure 5.28A) and the MCC-1 solution chemistry would not support this theory. Another issue is as for MRI4 in Chapter 4 the NL calculation will be affected by the crystallisation as a non-dissolving part of the wasteform will contribute to the composition and analysis of the NL. These observations raise the question of how appropriate the tests are for the analysis of the wasteform durability and how comparable they are to one another and other durability tests.

Elemental observations from the MCC-1 tests show some similarities to PCT-B tests but there are obvious differences that show that although the mechanism of dissolution is similar due to the reasons discussed above there are clear differences that question the comparability of the results. As in PCT-B tests, the equitable NL levels between samples in each trial shows that slight variations in glass concentration and the textural differences in the samples within each Trial doesn't have a major impact on the dissolution (Table 5.9). Some of the elemental trends in the MCC-1 tests are comparable to PCT-B tests including lower and analogous levels of dissolution for key elements Si, Ca and Al across all samples in both Trials and higher levels of K dissolution with a factor of ten increased release rate between Trial 1 and 5 samples supporting the conclusion of increased durability of the Trial 5 over the Trial 1 (Table 5.9). In contrast to the PCT-B tests in both Trial 1 and 5 there are also increased dissolution of Na and Sr, with Na at levels of K but lower levels of Sr. As observed for K, there was a factor of 10 difference between Trial 1 and 5 for the NL_{Na} and NL_{Sr} release values (Table 5.9). As stated above, with only a single time point it is hard to draw conclusions about these trends as it is not clear on what is happening either side of the time point, however, likely due to some of the reasons discussed above there is clearly a reduction in the selective ion exchange creating more equitable levels of K and Na in solution. The preferential dissolution on the glass over K and Fe phases (Figure 5.27 F-I) supports that the preferential dissolution of glass and variation in its structure/dissolution behaviour is controlling the solution chemistry not the dissolution of separate mineral phases. In PCT-B tests the lower levels of Si, Al, Ca, and Sr were explained by lower initial release at the early stages of dissolution although for MCC-1 this doesn't completely fit with other observations discussed above therefore it is thought that the major network formers Al and Si and possibly associated Ca, are observed at reduced levels due to their inclusion in gel or secondary alteration phases and the MCC-1 is entering a further stage, possibly stage II, of residual dissolution. Gel layers would preferentially sequester Ca and Sr for charge balancing due to their higher cationic strength. Further work is required to confirm this type of behaviour, as the only evidence seen is a very minor alteration layer in the 1A_glass sample (Figure 5.28A). Finally in Trial 1 there is some minor vermiform features (Figure 5.28 B and F) that were no present in Trial 5, it is thought that these features represent residual damage from monolith preparation in the glass rich regions [20] which may not be present in Trial 1 or crystalline regions of Trial 5 due to the increased strength of the crystalline features.

The pH in the MCC-1 tests is like those in the PCT-B tests: buffered to a weak alkali (Table 5.10). However, in contrast to the PCT-B tests, there are slightly higher pH values in the Trial 5 samples than the Trial 1 samples suggesting that the variable release of the K, Sr and Na are having greater impact in MCC-1 tests over PCT-B tests.

Table 5.9 Normalised elemental release for MCC-1 12 monolith test for samples from Trial 1 and 5 (error in brackets).

Element	5_Xc	5_Intermediate	5_Vu	1	1A	1A_Glass
Al	2.99 (0.30)	3.48 (0.09)	3.77 (0.05)	3.39 (0.06)	4.54 (0.19)	3.07 (0.17)
B	21.00 (8.59)	35.01 (3.06)	18.34 (1.51)	0	0	0
Ca	7.92 (1.33)	6.17 (0.39)	9.62 (0.77)	6.47 (0.13)	5.58 (0.33)	5.52 (0.28)
Fe	1.14×10^{-3} (1.06×10^{-3})	1.58×10^{-3} (4.98×10^{-4})	1.86×10^{-3} (1.62×10^{-4})	7.22×10^{-4} (7.22×10^{-4})	1.60×10^{-4} (1.60×10^{-4})	4.03×10^{-4} (4.03×10^{-4})
K	311.40 (3.15)	505.83 (39.22)	434.21 (28.31)	20.99 (0.23)	15.74 (0.26)	15.38 (2.45)
Mg	0.91 (0.13)	0.63 (0.04)	0.92 (0.06)	0.95 (0.28)	0.76 (0.20)	2.41 (0.14)
Mn	0	0.03 (0.02)	2.72×10^{-4} (2.72×10^{-4})	0.02 (0.02)	0.01 (0.01)	0
Na	346.57 (77.02)	543.23 (25.27)	418.82 (31.82)	13.89 (0.76)	10.27 (0.68)	15.38 (4.25)
P	0	1.19 (0.48)	1.24 (0.87)	0.36 (0.11)	0	0.30 (0.22)
Si	2.59 (0.30)	2.54 (0.01)	2.56 (0.03)	2.90 (0.05)	2.52 (0.14)	2.45 (0.15)
Sr	21.04 (6.16)	34.90 (1.93)	22.27 (2.91)	7.29 (0.21)	6.13 (0.40)	4.94 (0.47)
Ti	1.17 (0.34)	1.95 (0.11)	1.21 (0.16)	0.79 (0.02)	0.64 (0.04)	0.54 (0.05)

Table 5.10 Final pH values for MCC-1 12 monolith test for samples from Trial 1 and 5 initial pH values at Day 0 were 6.25 (0.50) (error in brackets)

Month	5_Xc	5_Intermediate	5_Vu	1	1A	1A_glass
12	9.38 (0.01)	9.38 (0.04)	9.18 (0.17)	8.51 (0.18)	8.87 (0.15)	9.04 (0.02)

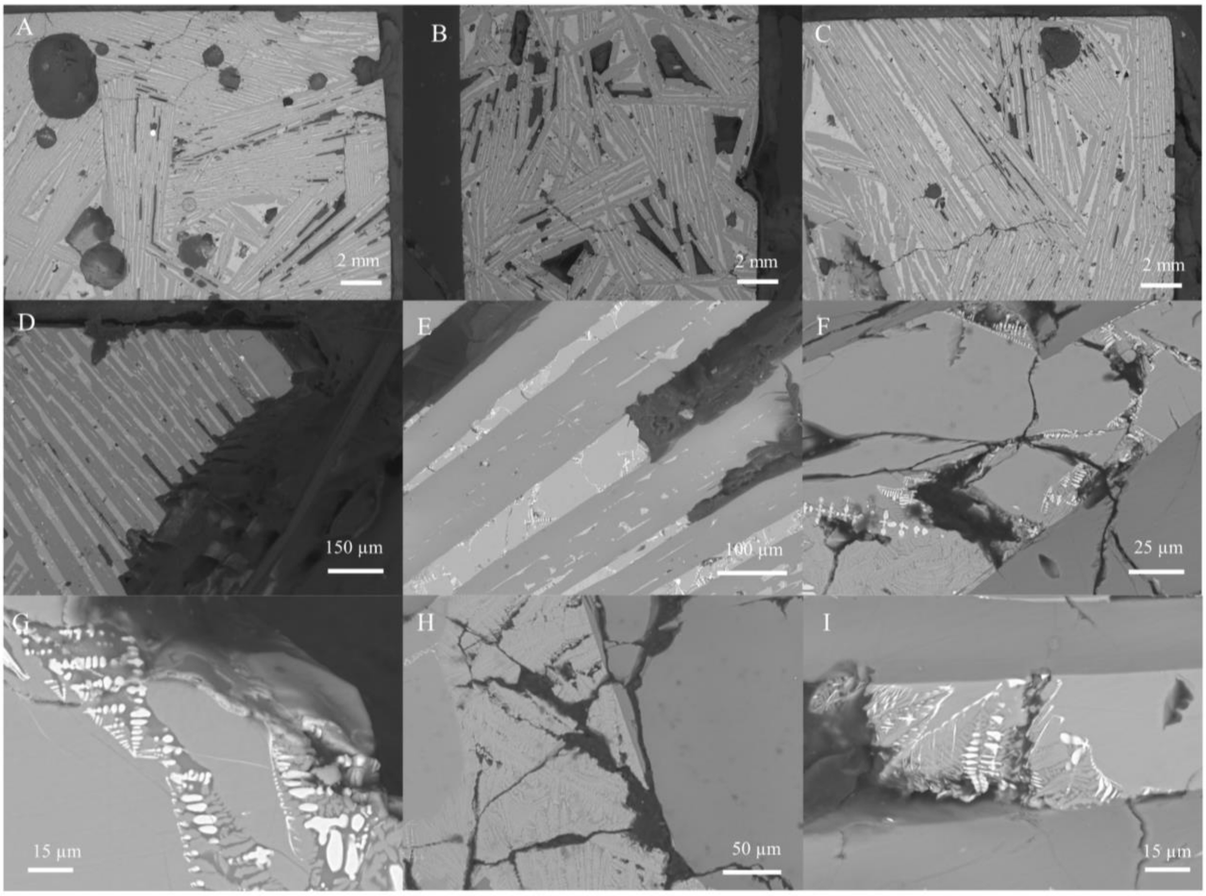

Figure 5.27 SEM images of dissolution textures from the monoliths in Trial 5 A-Overview low magnification of 5_Vu monolith showing large pores and potential enhanced glass dissolution. B-Overview low magnification of 5_Xc monolith showing the potential enhanced glass dissolution. C-Overview low magnification of the 5_intermediate monolith showing enhanced glass dissolution. D-Medium magnification image of the 5_Vu showing the enhanced dissolution along the intermediate glass bands between the anorthite crystals with large porous texture increasing the surface area and enhancing dissolution area. E-Medium magnification of 5_Vu showing the detail of glass dissolution in between the anorthite crystallisation. F-High magnification of 5_Vu showing the dissolution along crack features and avoiding other K and Fe phases. G-High magnification image from 5_intermediate monolith showing glass dissolution around Fe oxide phase. H-High magnification image from the 5_Xc monolith showing the reduced dissolution of the K phase. I-High magnification image from 5_Vu showing the glass dissolution around Fe oxide phase.

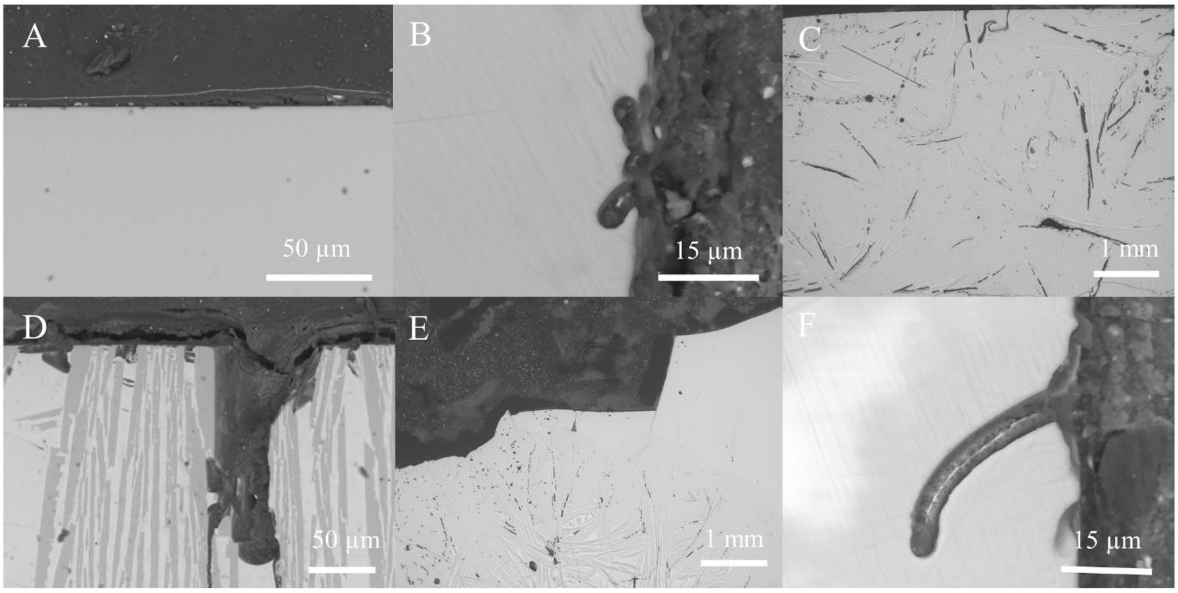

Figure 5.28 SEM images of dissolution textures from the monoliths in Trial 1. A – Potential weak dissolution layer in sample 1A_Glass. B- Minor dissolution feature from sample 1A_Glass. C- Preferential glass dissolution seen in sample 1.D - Prefential glass dissolution seen at the monolith edge in sample 1. E – Overview of mixed sample 1A showing preferential glass dissolution in the crystalline region. F- Veriform dissolution feature from the glass region of mixed sample 1A.

5.11 Conclusions

In relation to the initial (1 and 2) questions in Section 2.2.1.2, Valingar have produced a series of wasteforms using plasma technology to vitrify 5 waste drums that represent the different end member compositions of PCM waste. This project was supplied with 2 of these wasteforms representing the inorganic (bricks and concrete) and organic endmembers of PCM waste. Both Trial 1 and 5 produced a mixed waste form with a glassy-crystalline component attached to a major partially/unmolten drum component in both trials. The metallic drum element was not studied further in this project with focus on the glassy-crystalline component. Anorthite is the dominant crystalline phase and is extensively in the majority of the wasteforms excluding areas of Trial 1 where pure glass phase is present. The proximity of the samples taken from the metallic drum remnants means that crystallisation is heterogenous crystallisation.

Question 3 concentrates on the key waste elements of PCM, the metal and Cl. Fe is the only visible component of the melting and incorporation of the waste stainless steel drum (the source of metal in Trials 1 and 5) with higher levels in Trial 5 samples due to the measures implemented to increase drum melting. There is minor crystallisation of metallic iron in Trial 5 (visible dendritic growth) samples and in 5_Vu a K rich phase identified as leucite the same assemblage is identified but at lower levels in 5_Xc. Concentrations of these phases are linked to the increased drum melting in Trial 5 and away from the unmolten drum itself in 5_Vu. Increased drum melting has created higher levels of Fe that cannot be oxidised and incorporated in the glass so is precipitated (visible dendritic growth) as metallic Fe, comparison is required to lab metals (Chapter 6) to better understand and attribute solubility limits of CAS glass.

Measurable levels of Cl in the glass point toward good retention levels in the glass, supported by previous higher levels of Cl seen in CAS glass previously (up to 10 wt%) [5-7]. However, due to the very low level it is hard to determine the exact cause for this. The Ca:Al ratio would suggest that there are ample Ca sites to accommodate the Cl but the elevated levels of Al in this study and low incorporation levels in previous studies with similar CAS ratios [1, 2] would suggest that Al effects the incorporation via an unknown mechanism. This and variable incorporation levels of Cl in different trials shows this area requires further study.

It is unclear how representative the mix of glass and crystalline phases studied in this chapter is of the total wasteforms, but results show that understanding crystalline phase distribution is important due to the preferential dissolution of the glass phase. Sample heterogeneity, including crystalline distribution, is an area to investigate and understand in future lab and industrial trials.

The structural role of the different elements in the glassy-crystalline has been investigated by a variety of techniques to answer question 4 from Section 2.2.1.2. Fe speciation analysis shows that the Fe is dominated by Fe^{2+} and textural differences within trials are shown not to cause major compositional variances. This shows that all the wasteforms were produced in a weakly oxidising environment with anorthite crystallisation appearing to create some additional sites in the average $Fe^{2.5+}$ or low quadrupole Fe^{2+} environment as well as influencing the Fe^{2+} coordination increasing the coordination from (IV) to (VI) with increased crystallisation. Some minor Fe^{3+} appeared to be associated with the glassier regions of samples including the 1A_glass. These observations contrast with the behaviour in Chapter 6 where Fe was mostly present as Fe^{3+} which further illustrates how different scale, and conditions can have a major impact on speciation in the CAS melts and raises questions about the relevance of lab scale melts. Conclusions from compositional analysis are supported by Raman analysis that shows that despite all the samples containing significant amounts of Fe, Raman spectrum better matches CAS0 than CAS + metal samples in Chapter 6 (see later). This shows the important role Fe speciation has in the glass structure. In the Valingar glass the major Fe^{2+} is incorporated as a network modifier, replacing Ca^{2+} in the CAS structure without causing any major structural changes. Raman analysis shows that the Valingar 1A_glass and CAS type glasses in Section 6.8 in comparison to high silicate glasses such as KBasin in Section 4.8 are more depolymerised, but this doesn't appear to overly influencing durability (see below).

The compositional and structural of the wasteform control its physical properties including density, thermal and dissolution behaviour. It is important to understand these properties in relation to other glasses, waste production and waste disposal as they can have a major influence on all these processes and understanding them helps to answer the questions in Section 2.2.2. Density and Tg of the wasteform closely matches other CAS glasses including the synthetic ones in Chapter 6. For density the compositional trend of increasing Fe and metal incorporation matching the increase in density. With Tg the elevated value of 870 °C for the 1A_glass is important as the higher temperature could have a major impact on properties including increasing viscosity and elemental volatilisation, in particular Cl, that could have implications for the waste processing procedure, this is a major area for future analysis. In relation to processing conditions the variable behaviour of Fe speciation and its effect on the structural properties of the wasteform and glass is strongly influenced by the redox conditions. These can be varied to control factors such as the oxidation of the organic components, but it is vital that this doesn't have a negative impact on the waste properties. Optimisation of the processing properties in relation to waste properties is a critical future direction for the thermal processing of PCM waste.

The most critical disposal property is the durability of the PCM wasteform, a series of different durability tests were carried out to answer questions in Section 2.2.2.2. PCT-B tests show that an initial release due to the dissolution of fine is followed by very minor elemental release for all elements except K. This shows the wasteforms is in the very initial stages of dissolution with the preferential release of K due to its low ionic strength. Trial 1 has lower release than Trial 5 showing it is more durable which can be linked to its higher Si and Fe which acts as a network modifier. Texture has no effect on the dissolution of the different samples and the elemental release is so low that there is no obvious variation in the pH being buffered to a low alkali value. In the MCC-1 tests were limited by the amount of sample material with only one long term time point completed. The MCC-1 shows in comparison to PCT-B elevated NL values which could potentially be described by increased test duration, crystallisation effects or a different glass dissolution phases causing possible increased glass dissolution. Although these are not confirmed and in addition to the changes in compositional elements due to crystallisation it raises questions in the same way as in chapter 4 to the suitability and comparability of these dissolution tests. Independent MCC-1 observations show very low release of majors and higher release of K, Na and Sr in all the tests with little difference in textural variation but the same increased release for Trial 5. These observations support and contradict some of the theories above and suggest that the MCC-1 tests have increased glass dissolution and are potentially entering a later stage, possibly stage II, of dissolution due to the appearance of a weak dissolution layer in the 1A glass sample and the reduction in gel layer forming elements.

These observations as in chapter 4 show that the dissolution of these complex mixed wastes is very complicated, and more work is required to fully understand them. It also raises the question of the appropriateness of these dissolution tests in the determination of the durability of the mixed glass-crystalline wasteforms in this chapter and chapter 4. Further work is potentially required looking at different test such as the ASTM 1926-23 Standard Test Method for Measurement of Glass Dissolution Rate Using Stirred Dilute Reactor Conditions on Monolithic Samples [21, 22] that relies on measuring surface retreat maybe more appropriate, removing the composition measurement issues. It would also allow the isolation of the glass, which appears to be controlling the wasteform dissolution, allowing the calculation of accurate dissolution rates and observation behaviour for these ILW wasteforms without the caveats of the PCT-B and MCC-1 tests. Despite these concerns the apparent lack of release of Na in the samples would suggest that in comparison to other ILW wasteforms (Section 2.2.2.2) the Valingar samples are very durable.

Pu is expected to partition in the glass fraction and the important wasteform properties particularly the durability, appears to be strongly controlled by the glass component. It is therefore critical to further understand sample and melt condition heterogeneity to define glass distribution, composition, structure, and behaviour. This chapter has made a start in illustrating that despite the difference in drum composition there are many of similarities between the wasteform supporting the plan for a uniform treatment method for all waste drums without pre inspection. There are subtle differences between the samples, especially regarding the glass fraction that is predicted to be key to waste immobilisation and performance. It is, therefore, important to build upon the work done in this project and further investigate how these difference effect the final wasteform structure and performance. The next chapter has begun to do this and has used the average baseline glass composition from the Valingar trials as a starting point to create some simulant CAS glasses to investigate the different behaviours of the waste elements. Comparison of the glasses to the 1A_glass sample discussed above and in Chapter 6 have shown that further work is required to address key differences between lab and industry trials most importantly the redox conditions and its effects on Fe speciation.

5.12 References

1. Hyatt, N.C., et al., Thermal treatment of simulant plutonium contaminated materials from the Sellafield site by vitrification in a blast-furnace slag. Journal of Nuclear Materials, 2014. 444(1): p. 186-199.
2. Schwarz.R, B.P.a., Thermal Treatment of Plutonium Contaminated Materials Phase 2: Vitrification Study Final Report. 31st May 2012.
3. Tetronics, 1107 Plasma PCM Trials Report for Nuclear Demonstration Furnace. 2020.
4. Tetronics, 1107 COSTAIN Plasma Trials Procedure for Nuclear Demonstration Furnace. 2019.
5. Siwadamrongpong, S., M. Koide, and K. Matusita, Prediction of Chloride Solubility in CaO-Al2O3-SiO2 Glass Systems. Journal of Non-crystalline Solids - J NON-CRYST SOLIDS, 2004. 347: p. 114-120.
6. Schofield, J.M., P.A. Bingham, and R.J. Hand, The Immobilisation of a Chloride Containing Actinide Waste Surrogate in Calcium Aluminosilicate Glasses, in Environmental Issues and Waste Management Technologies in the Materials and Nuclear Industries XII. 2009. p. 69-80.
7. Schofield, J.M., Vitrification of a chloride containing actinide waste surrogate. 2011, University of Sheffield: Dpeartment of Materials and Science and Engineering.
8. Thornber, S.M., et al., Solubility, speciation and local environment of chlorine in zirconolite glass–ceramics for the immobilisation of plutonium residues. RSC Advances, 2020. 10(54): p. 32497-32510.
9. Chen, X., et al., High chloride content calcium silicate glasses. Physical Chemistry Chemical Physics, 2017. 19(10): p. 7078-7085.
10. Tan, S. and R.J. Hand, Incorporation and phase separation of Cl in alkaline earth aluminosilicate glasses. Journal of Nuclear Materials, 2018. 507: p. 135-144.
11. Zimova, M., The effect of chlorine on the viscosity of Na2O-Fe2O3Al2O3SiO2 melts. American Mineralogist - AMER MINERAL, 2006. 91: p. 344-352.
12. Boast.L, Investigation of the Thermal Treatment of Higher Activity Waste., in Material Science. 2018, Sheffield.
13. Hyatt, N.C., et al., Characterisation of Plasma Vitrified Simulant Plutonium Contaminated Material Waste. MRS Proceedings, 2006. 985: p. 0985-NN10-06.
14. Fokin, V.M., M.L.F. Nascimento, and E.D. Zanotto, Correlation between maximum crystal growth rate and glass transition temperature of silicate glasses. Journal of Non-Crystalline Solids, 2005. 351(10): p. 789-794.
15. Cormier, L., D.R. Neuville, and G. Calas, Relationship Between Structure and Glass Transition Temperature in Low-silica Calcium Aluminosilicate Glasses: the Origin of the Anomaly at Low Silica Content. Journal of the American Ceramic Society, 2005. 88(8): p. 2292-2299.
16. Simon, H., et al., Fe K-edge x-ray absorption spectroscopy of corrosion phases of archaeological iron: results, limitations, and the need for complementary techniques. Journal of Physics: Condensed Matter, 2021. 33(34): p. 344002.
17. Le Losq, C., M. Cicconi, Rita, and D. Neuville, R, Iron in Silicate Glasses and Melts: Implications for Volcanological Processes, in Magma Redox Geochemistry, M. Roberto and R.N. Daniel, Editors. 2021, Wiley. p. 233 - 253.
18. Dyar, M.D., et al., MÖSSBAUER SPECTROSCOPY OF EARTH AND PLANETARY MATERIALS. Annual Review of Earth and Planetary Sciences, 2006. 34(1): p. 83-125.
19. WRC, L/S 10 leaching test data for a vitrified slag sample. 2020.

20. Mansfield, J.T., et al., Localised extended ("vermiform") features formed during glass dissolution. Journal of Non-Crystalline Solids, 2023. 608: p. 122230.
21. ASTM, ASTM C1926 - 23 Standard Test Method for Measurement of Glass Dissolution Rate Using Stirred Dilute Reactor Conditions on Monolithic Samples 2023.
22. Thorpe, C.L., et al., Forty years of durability assessment of nuclear waste glass by standard methods. npj Materials Degradation, 2021. 5(1): p. 61.

6 Calcium Aluminosilicate Series

To build upon the work in Chapter 5 and better understand the behaviour and waste loading in calcium aluminosilicate (CAS) glasses a series of glasses were produced (Section 3.1.2) based upon the average composition of the target Valingar composition [1]. The main waste components in the PCM – (metal, PVC, and Ce and Hf as surrogates for Pu) were added in varying amounts including the maximum expected level of each waste type expected in the PCM waste [2-4] and increased values to allow the investigation of behaviour at increased loading. All the CAS glasses failed to pour and had to be destructively removed from the crucibles. CAS0 with no waste simulants had the lowest viscosity and it was partially mobile whereas the addition of waste simulants increased melt viscosity (Section 3.1.2).

6.1 Compositional Data

6.1.1 Bulk Composition

Glass compositions were analysed by laser ablation ICP-OES at the British Geological Survey (BGS) (Section 3.2.2). Measured mole % compositions are presented against target values (in red brackets) in (Tables 6.1-6.5). Melts have reproduced the target composition to within <5% in all samples. Al_2O_3 is slightly elevated in all samples in relation to batched values due to the degradation of the alumina crucible, except for the samples with HfO_2 addition where unusually the Al_2O_3 is lower and in contrast there is elevated levels of Si.

Table 6.1 Target (in red brackets) and measured mol.% composition for the base CAS (CAS0) glass (standard deviation is in black brackets).

Component	
CaO	35.46 (0.15) (35.98)
Al_2O_3	10.52 (0.07) (10.51)
SiO_2	53.70 (0.17) (53.51)
Na_2O	0.05 (<0.01)
MgO	0.18 (<0.01)
P_2O_5	0.02 (<0.01)
K_2O	0.01 (<0.01)
TiO_2	0.01 (<0.01)
MnO_2	0.01 (<0.01)
Fe_2O_3	0.01 (<0.01)
SrO	0.01 (<0.01)
ZrO_2	0.02 (<0.01)
Total	99.99

It is not clear what is causing this variation but may relate to the substitution of Hf onto the Al site altering the glass structure and relative composition. ZrO_2 in the Hf samples is from impurities in the addition of HfO_2 with MgO and Na_2O and other minor elements largely from impurities in the sand source of SiO_2, except for the phosphorous in the PVC melts which comes from additives in the PVC and increases with increased waste loading. The additions of waste components are in good agreement with the measured levels, except in the higher metal glasses where Cr_2O_3 and NiO are lower which can be explained by eskoliate crystallisation (Section 6.2 and 6.3). Chlorine, the major waste component in PVC, cannot be measured by laser ablation ICP-OES but is investigated in the next Section via Energy Dispersive Spectroscopy (EDS). In the PVC CAS glasses, the measured composition matches the batched composition showing that PVC addition is not affecting the composition due to volatilisation during melting. In comparison to the Tetronics samples in Section 5.2, compositionally the CASM5 appears to be the best representative of the inactive waste simulants, but the Fe speciation and melt redox environment has been shown to affect the structure showing CAS0 may structurally be a better representative, this is discussed further below (Sections 5.8-9 and 6.6-8).

Table 6.2 Target (in red brackets) and LA ICP-OES measured oxide mol.% composition for CAS glasses with Ce addition (standard deviation is in black brackets).

Component	Ce0.207	Ce1	Ce5	Ce10
CaO	35.17 (0.23) (35.95)	34.13 (0.14) (35.84)	33.57 (0.25) (35.50)	33.01 (0.10) (34.57)
Al_2O_3	10.33 (0.16) (10.50)	10.48 (0.12) (10.47)	10.68 (0.12) (10.31)	10.87 (0.24) (10.10)
SiO_2	54.13 (0.18) (53.47)	54.71 (0.17) (53.32)	53.68 (0.16) (52.50)	52.16 (0.23) (51.42)
Na_2O	0.04 (<0.01)	0.06 (<0.01)	0.06 (<0.01)	0.06 (<0.01)
MgO	0.17 (<0.01)	0.17 (<0.01)	0.16 (<0.01)	0.15 (<0.01)
P_2O_5	0.02 (<0.01)	0.02 (<0.01)	0.02 (<0.01)	0.02 (<0.01)
K_2O	0.01 (<0.01)	0.01 (<0.01)	0.01 (<0.01)	0.01 (<0.01)
TiO_2	0.01 (<0.01)	0.01 (<0.01)	0.01 (<0.01)	0.01 (<0.01)
MnO_2	0.00 (<0.01)	0.00	0.00	0.00
Fe_2O_3	0.01 (<0.01)	0.01 (<0.01)	0.01 (<0.01)	0.01 (<0.01)
SrO	0.01 (<0.01)	0.01 (<0.01)	0.01 (<0.01)	0.01 (<0.01)
ZrO_2	0.02 (<0.01)	0.02 (<0.01)	0.01 (<0.01)	0.01 (<0.01)
BaO	0.00 (<0.01)	0.00	0.01 (<0.01)	0.02 (<0.01)
Ce_2O	0.07 (<0.01) (0.08)	0.37 (<0.01) (0.37)	1.77 (0.01) (1.89)	3.66 (0.04) (3.91)
Total	99.99	99.99	99.98	99.97

Table 6.3 Target (in red brackets) and LA ICP-OES measured oxide mol.% composition for CAS glasses with Hf addition (standard deviation is in black brackets).

Component	Hf0.207	Hf1	Hf5	Hf10
CaO	33.22 (0.06) (35.95)	33.96 (0.20) (35.84)	34.71 (0.37) (35.50)	32.24 (0.27) (34.57)
Al_2O_3	8.78 (0.08) (10.50)	9.22 (0.17) (10.47)	9.57 (0.03) (10.31)	8.55 (0.43) (10.10)
SiO_2	57.66 (0.08) (53.47)	56.20 (0.32) (53.32)	53.66 (0.40) (52.20)	55.37 (0.68) (51.42)
Na_2O	0.06 (<0.01)	0.06 (<0.01)	0.04 (<0.01)	0.05 (<0.01)
MgO	0.15 (<0.01)	0.15 (<0.01)	0.15 (<0.01)	0.14 (<0.01)
P_2O_5	0.02 (<0.01)	0.02 (<0.01)	0.02 (<0.01)	0.02 (<0.01)
K_2O	0.01 (<0.01)	0.01 (<0.01)	0.01 (<0.01)	0.01 (<0.01)
TiO_2	0.01 (<0.01)	0.01 (<0.01)	0.01 (<0.01)	0.01 (<0.01)
MnO_2	0.00	0.00	0.00	0.00
Fe_2O_3	0.01 (<0.01)	0.01 (<0.01)	0.01 (<0.01)	0.01 (<0.01)
SrO	0.01 (<0.01)	0.01 (<0.01)	0.01 (<0.01)	0.01 (<0.01)
ZrO_2	0.01 (<0.01)	0.02 (<0.01)	0.02 (<0.01)	0.04 (<0.01)
Hf_2O	0.07 (<0.01) (0.08)	0.33 (0.01) (0.37)	1.79 (0.03) (1.89)	3.55 (0.05) (3.91)
Total	99.99	100	99.99	99.99

Table 6.4 Target (in red brackets) and LA ICP-OES measured oxide mol.% composition for CAS glasses with metal addition (standard deviation is in black brackets).

Component	M1	M5	M10
CaO	34.73 (0.12) (35.71)	34.17 (0.21) (34.81)	31.10 (0.33) (33.62)
Al_2O_3	10.85 (0.08) (10.45)	10.69 (0.09) (10.17)	14.77 (0.66) ((9.95)
SiO_2	53.24 (0.18) (53.12)	51.47 (0.16) (51.78)	48.60 (0.36) (50.02)
Na_2O	0.06 (<0.01)	0.04 (<0.01)	0.04 (<0.01)
MgO	0.18 (<0.01)	0.17 (<0.01)	0.15 (<0.01)
P_2O_5	0.03 (<0.01)	0.02 (<0.01)	0.02 (<0.01)
K_2O	0.01 (<0.01)	0.01 (<0.01)	0.01 (<0.01)
TiO_2	0.01 (<0.01)	0.01 (<0.01)	0.01 (<0.01)
Cr_2O_3	0.10 (<0.01) (0.11)	0.41 (0.01) (0.54)	0.29 (0.01) (1.09)
MnO_2	0.01	0.01 (<0.01)	0.02 (<0.01)
Fe_2O_3	0.41 (0.01) (0.38)	1.94 (0.01) (1.91)	3.42 (0.04) (3.42)
NiO	0.15 (<0.01) (0.10)	0.72 (0.01) (0.53)	1.25 (0.02) (1.08)
CuO	0.08 (<0.01) (0.08)	0.10 (<0.01) (0.08)	0.04 (<0.01) (0.08)
SrO	0.01 (<0.01)	0.01 (<0.01)	0.01 (<0.01)
ZrO_2	0.09 (<0.01)	0.09 (<0.01)	0.08 (<0.01)
MoO_2	0.01 (<0.01)	0.07 (<0.01)	0.14 (<0.01)
PbO_2	0.02 (<0.01) (0.04)	0.05 (<0.01) (0.08)	0.05 (<0.01) (0.06)
Total	99.99	99.99	99.99

Table 6.5 Target (red brackets) and LA ICP-OES measured oxide mol.% composition for CAS glasses with PVC addition (standard deviation is in black brackets). Note: The PVC was added as a wt% of the total mass and cannot be measured using this technique so is included in the batch calculations assuming that it volatilised on melting and is not included in the measured mol% calculations.

Component	PVC1	PVC5	PVC10
CaO	34.32 (0.22) (35.98)	34.42 (0.18) ((35.98)	33.81 (0.15) (35.98)
Al_2O_3	10.81 (0.36) (10.51)	10.37 (0.06) (10.51)	11.21 (0.17) (10.51)
SiO_2	54.36 (0.30) (53.51)	54.79 (0.15) (53.51)	54.50 (0.17) (53.51)
Li_2O	0.02 (0.01)	0	0
B_2O_3	0.06 (0.05)	0	0
Na_2O	0.06 (0.01)	0.02 (<0.01)	0.03 (<0.01)
MgO	0.20 (0.02)	0.18 (<0.01)	0.20 (<0.01)
P_2O_5	0.03 (<0.01)	0.09 (0.02)	0.13 (0.02)
TiO_2	0.01 (<0.01)	0.01 (<0.01)	0.01 (<0.01)
Fe_2O_3	0.02 (<0.01)	0.01 (<0.01)	0.01 (<0.01)
SrO	0.01 (<0.01)	0.01 (<0.01)	0.01 (<0.01)
ZrO_2	0.09 (<0.01)	0.09 (<0.01)	0.09 (<0.01)
Total	99.97	99.99	99.99

6.1.2 Measured Cl amount in the PVC

Chlorine (Cl) is the major component of PVC; it can be a problem for waste processing because the thermal degradation/pyrolysis of PVC produces harmful dioxins and both metallic and gaseous chlorides [4]. The dioxins are toxic organics but are not expected to be a major issue as the high plasma temperature is expected to destroy most of them, however the chloride from the metallic and gaseous chlorides is corrosive and can attack and damage refractory walls and rig equipment. CAS glass was chosen as a glass frit as it has been found to accommodate high levels (>10 wt%) of Cl^- removing it from the off-gas where it can damage refractory walls and rig equipment [5]. Estimates of Cl^- mol% in the final glass were calculated (Table 6.6) assuming that the PVC is composed of 100% PVC resin with no additives and that 57% of PVC resin is Cl^- based on the monomer formula C_2H_3Cl [4]. This is likely an overestimate as Romar Workwear suggests that 35 wt% of PVC is Cl^- by weight indicating some additives are present in the PVC, as the composition of the additives is unknown then only a maximum estimate for atomic Cl- mol% can be calculated, discounting the additives. A more detailed analysis of PVC composition would allow for a more accurate estimate of Cl^- mol% in the future.

As described in Section 2.3.4 and 5.2 the incorporation of Cl in CAS glass depends on composition of the CAS glass with controlling mechanisms linked to the concentration of Ca and or the Al. As in Section 5.2 Energy Dispersive Spectroscopy (EDS) attached to an SEM provides a semi-quantitative measure of Cl^- that allows the level of retention to be investigated. Measured Cl^- Mol% levels are much lower than the estimated atomic concentration even if these are elevated by assumptions of the actual PVC content in the 'PVC' material. CAS glasses in these experiments have poor Cl^- incorporation and retention levels possibly related to the low temperature thermal degradation/pyrolysis of PVC or the CAS glass composition , this is line with previous lab trials [3, 4] and suggests that the low levels in the Tetronic glass are due to poor retention rather than low batch levels (Section 5.2).

As discussed in Section 5.2 to be incorporated into the CAS glass then there needs to be a molten phase to incorporate waste elements, this along with the low temperature thermal degradation/pyrolysis of PVC could be causing the volatilisation of large fractions of the Cl to the off-gas system reducing incorporation. This could also be influencing comparison to previous trials as in these [5-9] the Cl was added as alkaline earth salts that will not experience the same low temperature breakdown increasing incorporation. Although still low, elevated Cl values in experimental trails where Cl was added as alkaline earth salts [8, 9] rather than PVC would support this theory. A way of reducing low temperature thermal degradation/pyrolysis of PVC could provide a major optimisation for future trials and potentially increase Cl retention.

Despite apparent PVC breakdown there is clearly some incorporation of PVC elements into the CAS glasses as both the P_2O_5 and the Cl$^-$ increase with waste loading (Table 6.6). The P_2O_5 increase for each step of PVC addition as expected but the Cl$^-$ is not with analogous amounts in PVC5 and PVC10. This is likely related to the CAS composition effecting the Cl$^-$ incorporation. It could be expected that as the Ca levels are significantly above the level required level to charge compensate the Al then there would be good retention of Cl that would increase with waste loading due to the adequate availability of modifier sites that the Cl associates. The pattern for PVC5 and PVC10 does not support this but supports the idea that there is another mechanism influencing the incorporation of Cl into CAS glasses linked to the higher levels of Al in the CAS glasses and PVC10 that supress the incorporation of Cl via an unknown mechanism that requires further investigation. This is clearly an important area of interest that still has questions to be answered through future systematic trials.

Table 6.6 Target (red brackets) and measured oxide mol% composition for CAS glasses with PVC addition measured by Energy Dispersive Spectroscopy (EDS) (standard deviation is in black brackets).

Oxide	PVC1	PVC5	PVC10
CaO	34.92 (0.42) (35.61)	34.21 (0.96) (34.16)	32.82 (0.12) (32.35)
Al_2O_3	17.59 (0.09) (10.41)	17.62 (0.17) (9.98)	20.12 (0.04) (9.45)
SiO_2	47.24 (0.32) (52.97)	47.53 (0.72) (34.16)	46.28 (0.06) (48.12)
B_2O_3	0	0	0
Na_2O	0	0	0
MgO	0.01 (0.02)	0.11 (0.02)	0.07 (0.04)
P_2O_5	0.12 (0.03)	0.28 (0.05)	0.54 (0.02)
TiO_2	0.05 (0.03)	0.04 (0.02)	0.01 (0.02)
Fe_2O_3	0.02 (0.02)	0.07 (0.02)	0.02 (0.02)
SrO	0	0	0
ZrO_2	0.03 (0.01)	0.04 (0.02)	0.01 (0.01)
Cl$^-$	0.02 (0.01) (0.57)	0.09 (0.04) (2.86)	0.09 (0.01) (5.72)
Total	100	99.99	99.97

6.2 XRD

CAS0 is x-ray amorphous and is shown for comparison for each simulant series (Figure 6.1 - Figure 6.4). The series of CAS + Hf, CAS + Ce, CAS + PVC and CAS + Metal glasses all show an amorphous scattering response indicative of a glass except for Ce5 and M10 that have minor crystalline peaks.

The incorporation of Ce and Hf in CAS glass without any crystallisation suggests that the solubility limits for both in CAS glass at ~1400-1450°C is >3.55-6.6 mol%. This is higher than the maximum quoted values for Pu(III) and Ce (III) in borosilicate glass of (2-2.5 mol%) at 1400°C and Hf (IV) and Pu(IV) of 0.5 mol% in borosilicate glass at 1400-1500°C [10-14], but in line with previous studies of Hf solubility in aluminosilicates that measured a high solubility at 3-6.5 mol% at 1250-1400°C likely due to the presence of excess network modifiers in the glass matrix with an solubility increase linked to a shift to peralkaline compositions with increasing Na^+ [15, 16]. The solubility limits for Ce in aluminosilicates is not yet clear, however, results here (Section 6.6) point toward the same pattern of increased solubility for trivalent over tetravelant as seen in borosilicate glass [10, 11, 13, 16-19], but for lower levels of Ce^{3+} (72-76%) the incorporation is higher than in borosilicate glass (88% Ce^{3+} at 1400°C [10]) showing that aluminosilicates can accommodate more Ce^{4+}in oxidising melts. Ce in different oxidation states has been shown to act as a network modifier in aluminosilicates [20], this acceptance allows the glass composition to be more flexible opening the opportunity to accommodate more varied waste at a higher waste loading. This area needs further study to fully calculate and understand solubility limits and controls on solubility. Previous trials [3, 4, 21, 22] using GGBS or SLS and simulant additives found Ce preferentially (>97%) partitioned into the slag phase with <0.02 wt% Ce in any metallic phase present. CeO_2 levels in the slag phase varied (0.33-1.53 wt%) around the batched value of 1.043 wt% likely due to variable Fe addition from drum melting, crystalline partioning (see below) and natural melt/sample heterogeneity. In samples with crystalline material Ce was preferentially partitioned into the glass phase elevating its concentration in comparison to pure glass samples reaching a maximum of 4 wt% (~1.2 mol%). These levels illustrate the importance of investigating higher waste loading as crystallisation can clearly increase CeO_2 levels in the glass. Although harder to define exact solubility limits in the previous trials, the lack of any CeO_2 phases shows that the as for the lab glasses in this study the batched levels of Ce are below saturation and are predominantly entering the glass phase of the wasteform. Elevated Ce levels potentially caused by crystallisation should easily be accommodated as saturation levels in the similar glass composition in these trials are well above the maximum seen in previous trials and the higher (>86%) Ce^{3+} concentration in the reducing environment should further increase solubility in industry/previous trials if the same pattern as in borosilicates occurs in CAS glass. Comparison of lab and previous trials and the results from the Ce and Hf melts shows that the CAS glass should easily be able to accommodate the expected levels of Pu in PCM melts and there is additional capacity to deal with increased levels due to crystallisation or potentially drum stacking during melting.

There is eskolaite crystallisation in M10 showing that the glass has reached Cr saturation and minor anorthite crystallisation in sample Ce5 (Figure 6.1-6.4). SEM images show that Cr is

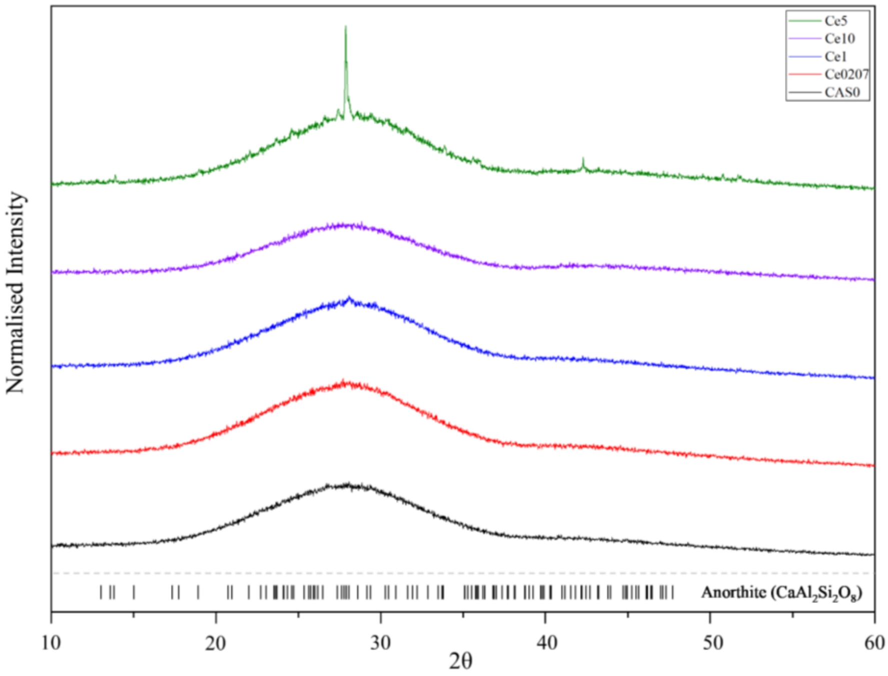

Figure 6.1 XRD patterns for the Ce series.

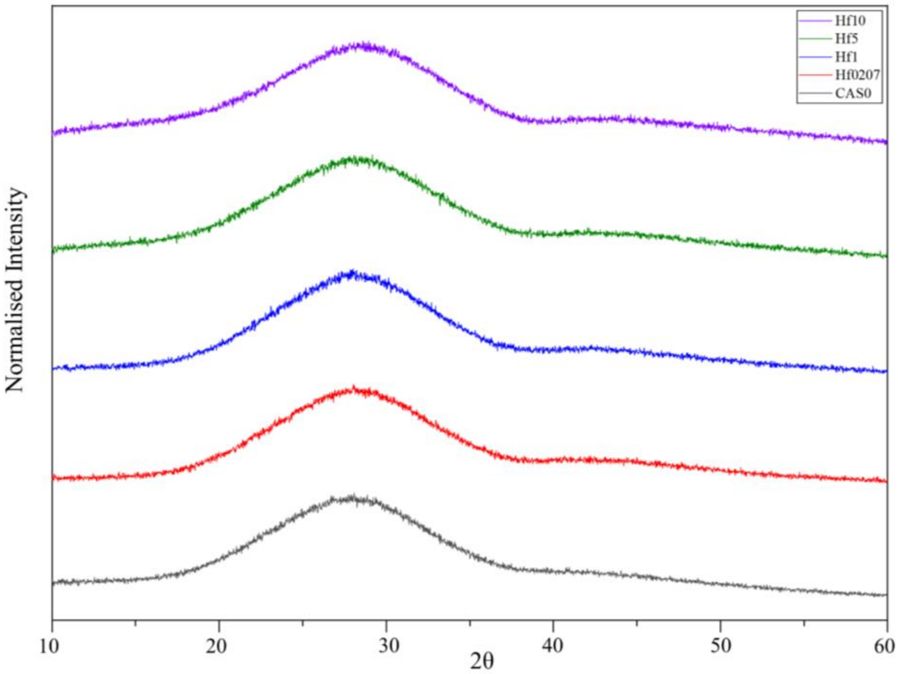

Figure 6.2 XRD patterns for Hf series.

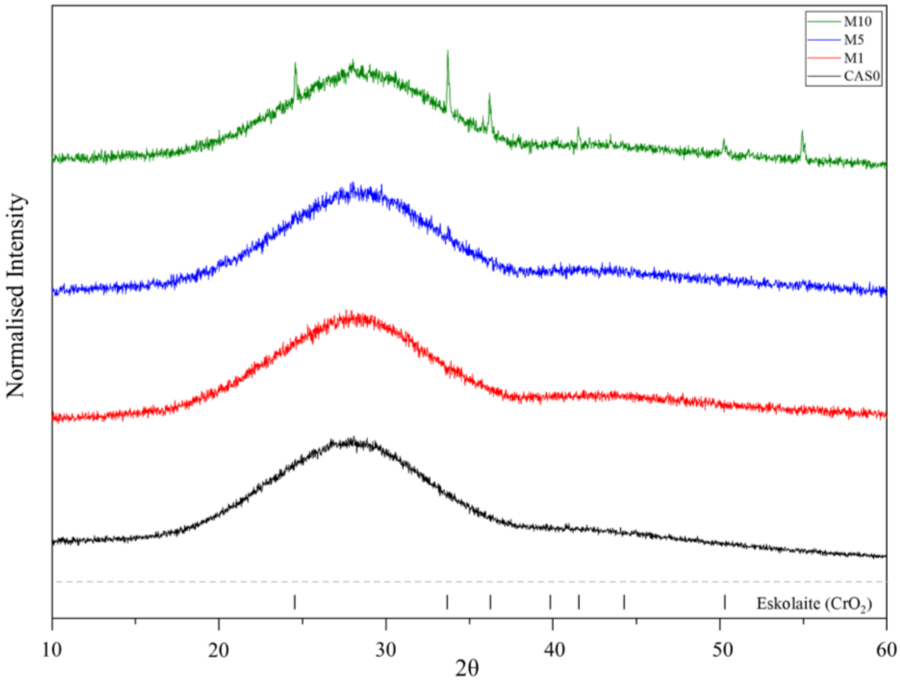

Figure 6.3 XRD patterns for Metal series.

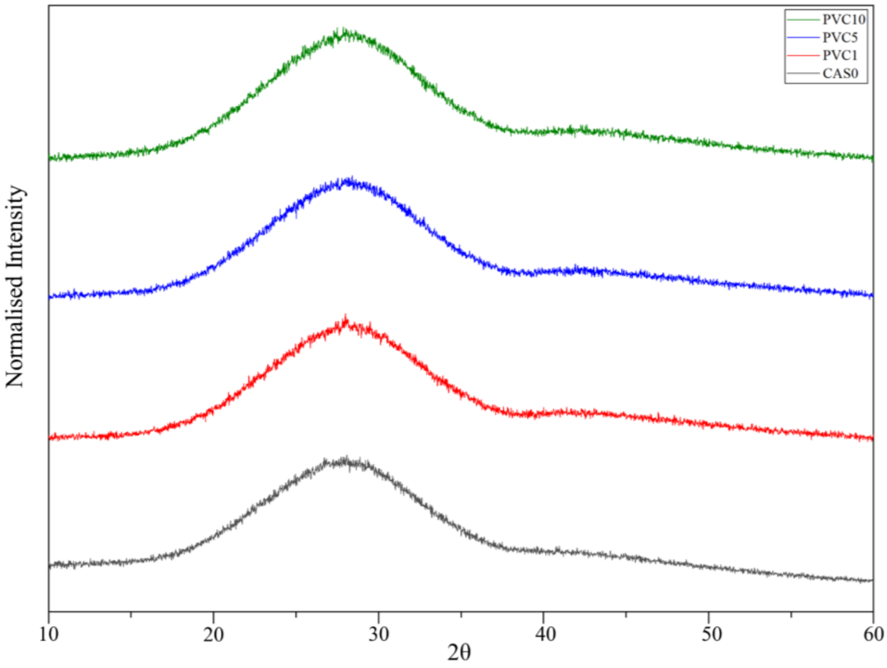

Figure 6.4 XRD pattern PVC series.

also saturated in M5 with eskolaite crystallisation, but the concentration is too low for XRD detection (Figure 6.8). Unlike in previous industrial and lab trials [1-4, 22, 23] there is no additional metallic phase in the metallic waste melts showing that all metallic elements weresuccessfully incorporated into the glass ('slag') phase. This raises questions regarding the need for elevated temperatures to ensure metallic melting, mixing and slag incorporation. It is possible that other factors such as the REDOX environment are controlling metal oxidation and incorporation. Lab melts in this study show that the glasses have the capacity to incorporate the waste elements and question if the high temperatures are required, instead, an effort to increase oxidation and adapt melt set up to reduce slag insulation of the drum base could increase metallic incorporation. Some efforts to improve these factors are already being implemented [21, 24]. The high viscosity at lower temperatures is not thought to be a problem as the plan is to not pour the PCM waste stream [4, 25].

The lack of crystallisation only mirrors the 1A_glass sample from Chapter 5 and from previous lab and industry trials were there is a range of crystalline species present in all samples (Section 3.1.2) [1-4, 22, 23]. This shows that there may be a range of different crystallisation species present related to a range of factors including heterogenous growth against the colder unmolten drum, waste composition, input waste condition i.e. milled or unmilled and melt conditions. This shows, as discussed, that further work is required to understand how representative the glasses and wasteforms in Chapter 5 are and what part of the melt they might best represent. This will allow the research conclusions to be implemented to the processing of the PCM waste and the design of the final wasteform.

6.3 SEM

The glasses from CAS0, CAS + Ce, CAS + Hf and CAS + PVC all show an amorphous glass with no evident crystallisation and even distribution of the main batch and waste materials with no contractions or 'hot spots' which is an important factor in radionuclide disposal because this could lead to criticality concentration issues. There is no evidence of anorthite crystallisation in Ce5 suggesting it is rare and localised glass (Figure 6.5-7 and 6.10). Ce and Hf glasses show no crystallisation supporting XRD analysis and showing that solubility limits in these glasses for these surrogates is >3.5 mol%. CASM1-10 series shows increasing crystallisation with increasing metal content (Figure 6.8). Crystallisation in M10 and M5 is an oxide is rich in Cr, with some Fe incorporation (Figure 6.9), supporting the XRD analysis (Figure 6.3). Crystallisation is present in M5, although it is below the detectable limits if the XRD (Figure 6.4). The glass matrix in the CAS + Metal series is amorphous and shows even elemental distribution including of Cr and Fe (Figure 6.9).

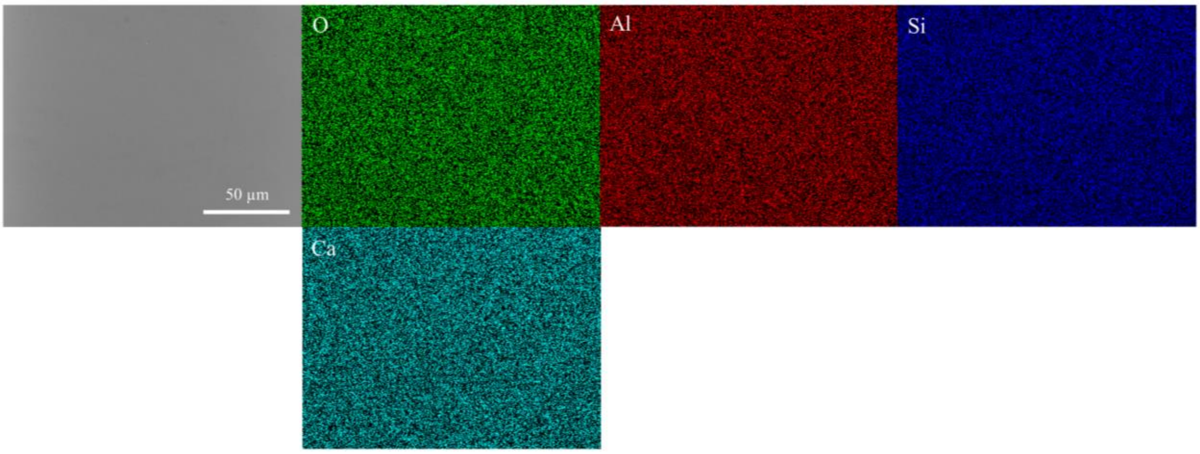

Figure 6.5 SEM image and EDS map for the CAS0 glass.

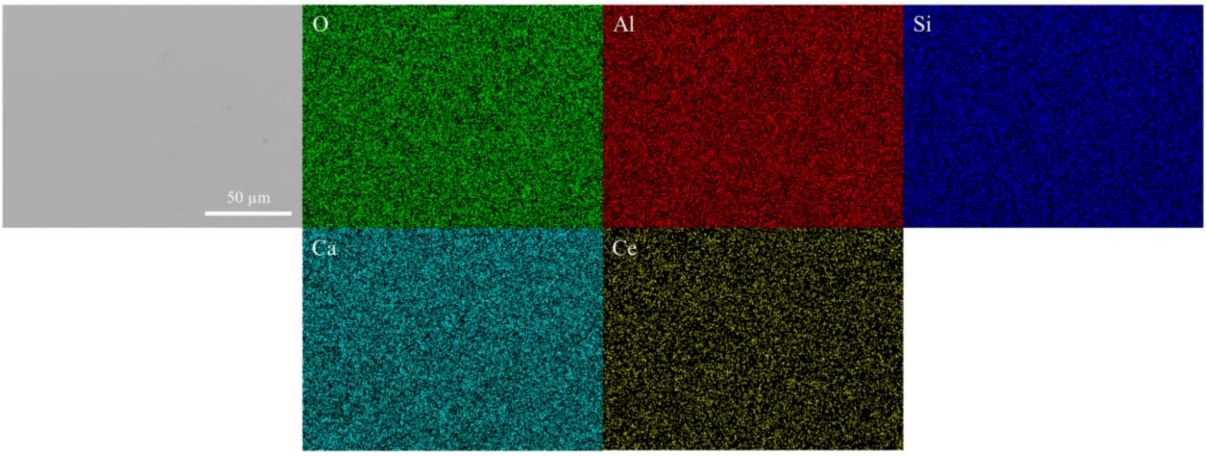

Figure 6.6 SEM image and EDS map for the Ce10 glass.

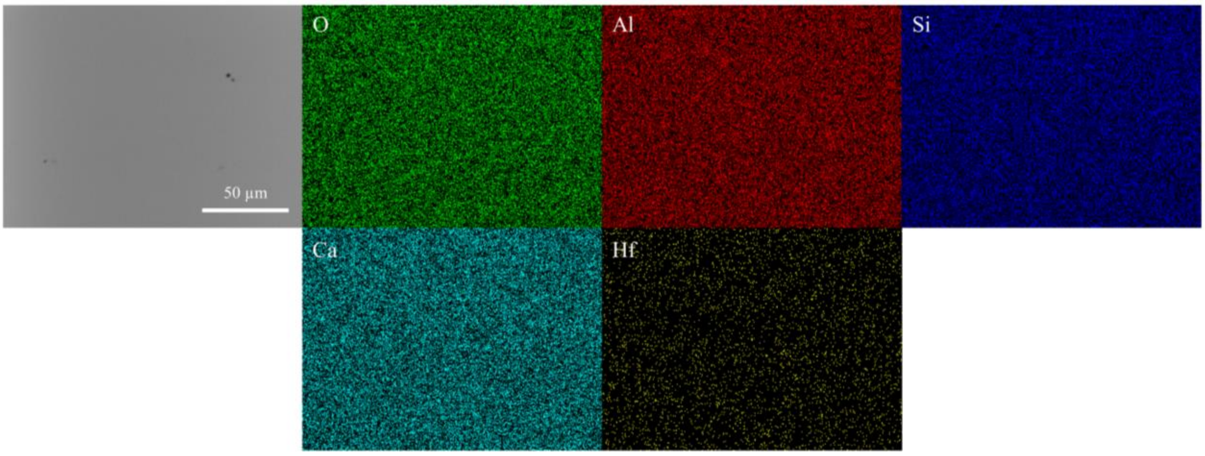

Figure 6.7 SEM image and EDS map for the Hf10 glass.

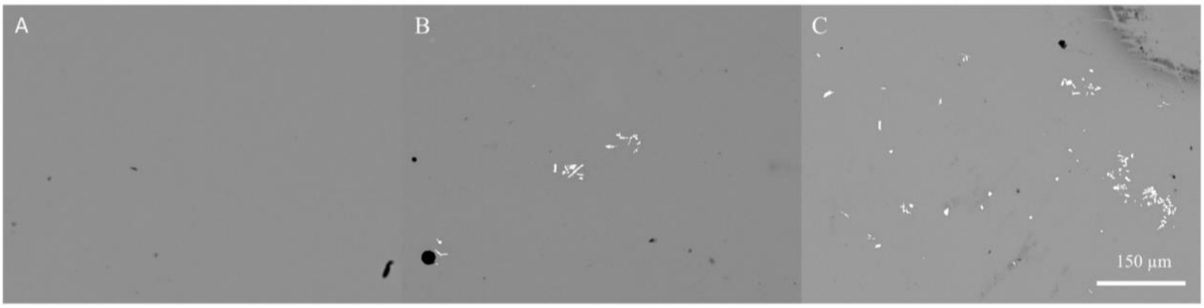

Figure 6.8 SEM images A – M1 B- M5 and C-M10.

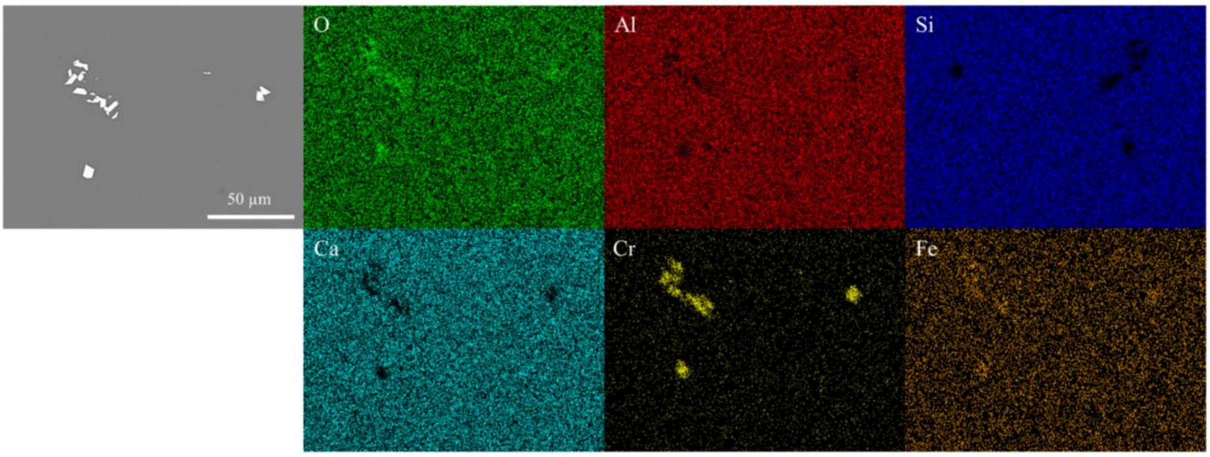

Figure 6.9 SEM image and EDS map for the M10 glass.

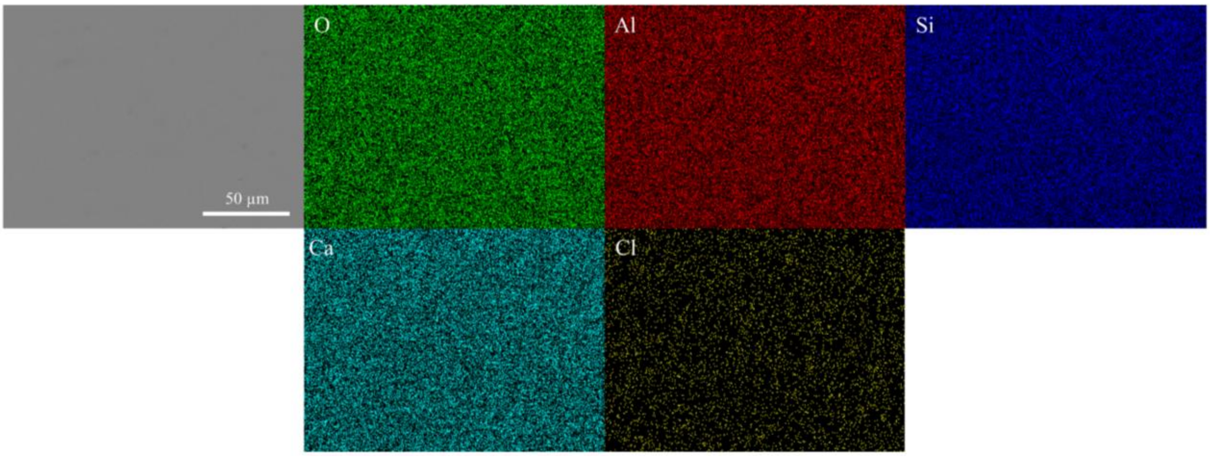

Figure 6.10 SEM image and EDS map for the PVC10 glass

6.4 Density

The density of the CAS0 glass is comparable to the PVC 1-10 and the Ce0207-1 and CASHf0207 suggesting that at lower levels the Ce and Hf surrogates don't have a major influence on density of the glass. At higher Ce and Hf and all metal (predominantly the effect of Pb) levels the addition of the waste material effects the glass density with higher levels of waste loading linearly increasing the glass density (Table 6.7).

Table 6.7 Density measurement for CAS glasses (standard deviation is in brackets)

	Density (g/cm^3)
CAS0	2.7759 (0.0069)
Ce0207	2.7347 (0.01111)
Ce1	2.7484 (0.0190)
Ce5	2.8490 (0.0214)
Ce10	2.9023 (0.0124)
Hf0207	2.7865 (0.0007)
Hf1	2.8094 (0.0042)
Hf5	2.8944 (0.0057)
Hf10	2.9702 (0.0145)
CASM1	2.8307 (0.0056)
CASM5	2.9014 (0.0004)
CASM10	3.0000 (0.0029)
CASPVC1	2.8011 (0.0005)
CASPVC5	2.7926 (0.0008)
CASPVC10	2.7918 (0.0004)

6.5 Thermal Analysis

Thermal analysis is used to identify exothermic events (crystallisation) and endothermic events (glass transition and melting) with increasing temperature (Section 3.2.4) Profiles were analysed for the full CAS series which are seen in (Figure 6.11 and 6.15) In all the profiles there are peaks that can be identified as Tg (glass transition), Tx (crystalline event) and Tm (melt event). These are outlined in (Table 6.8) and show the effects of the waste simulant additions on the CAS behaviour. Tg for the CAS glass series is within the same expected range for the composition [26] with some variation across samples but no clear trends suggesting that this relates to natural variation and show waste simulants are not having a major impact on thermal properties of the glass. In all glasses, 2 clear crystallisation events occur at ~900°C and ~1010°C and a melt event at ~1260°C it is not clear to the exact cause of these, but they most likely relate to the phase anorthite. Similar trends are seen in are also seen in industrial samples (Section 5.6) supporting the use of these lab glasses as surrogates of industrial glass behaviour.

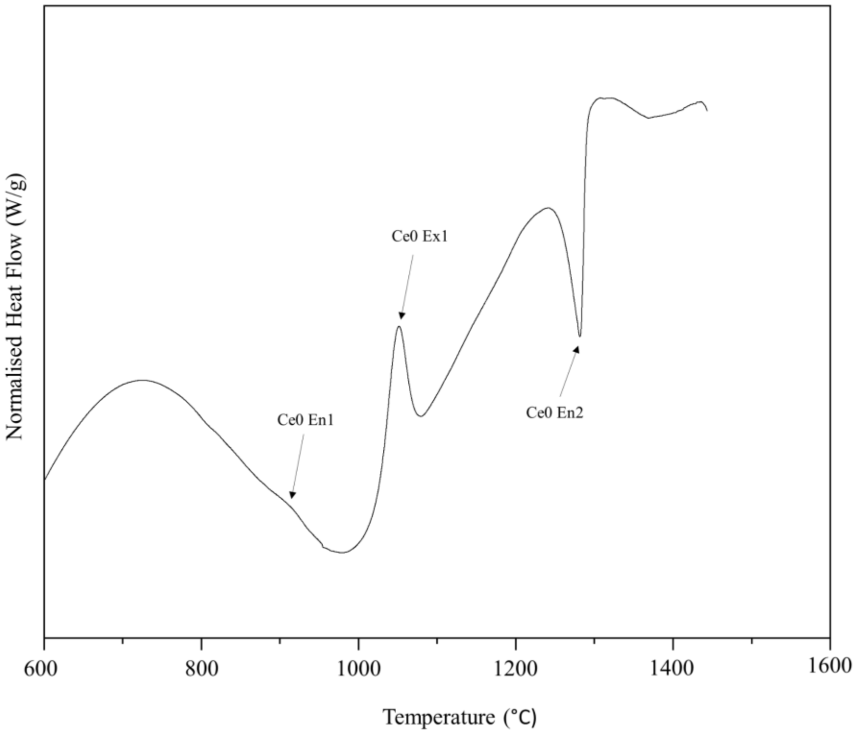

Figure 6.11 Thermal analysis profile for CAS0.

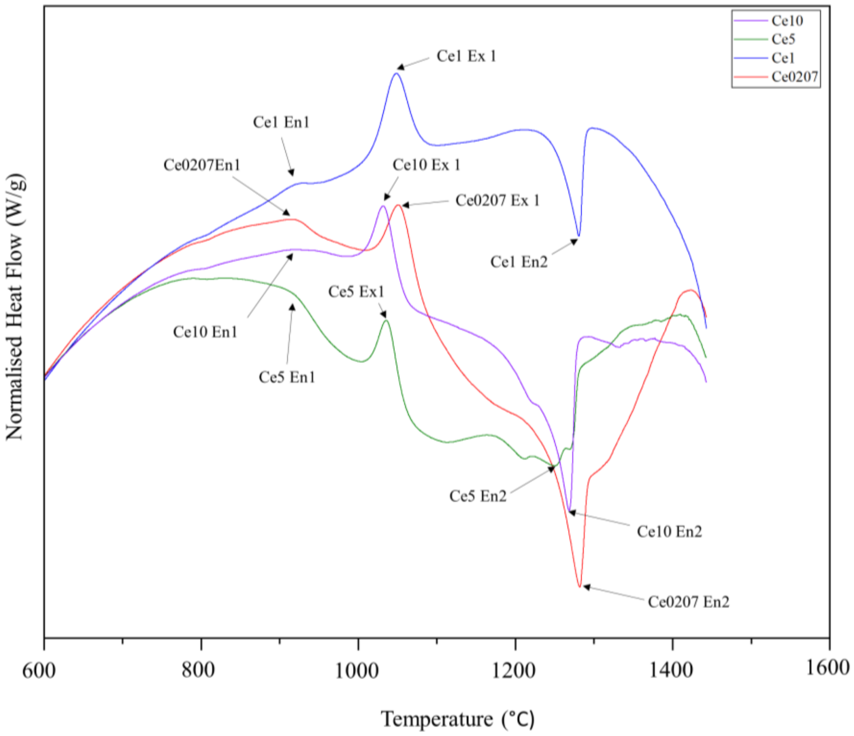

Figure 6.12 Thermal analysis for Ce 0.207-Ce10.

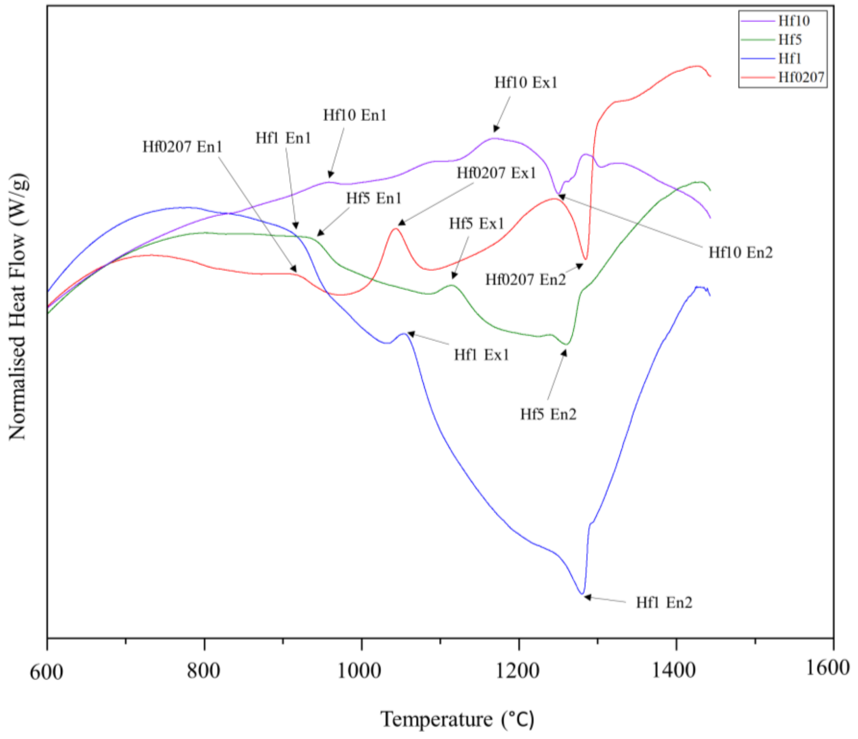

Figure 6.13 Thermal analysis for Hf0207-Hf10.

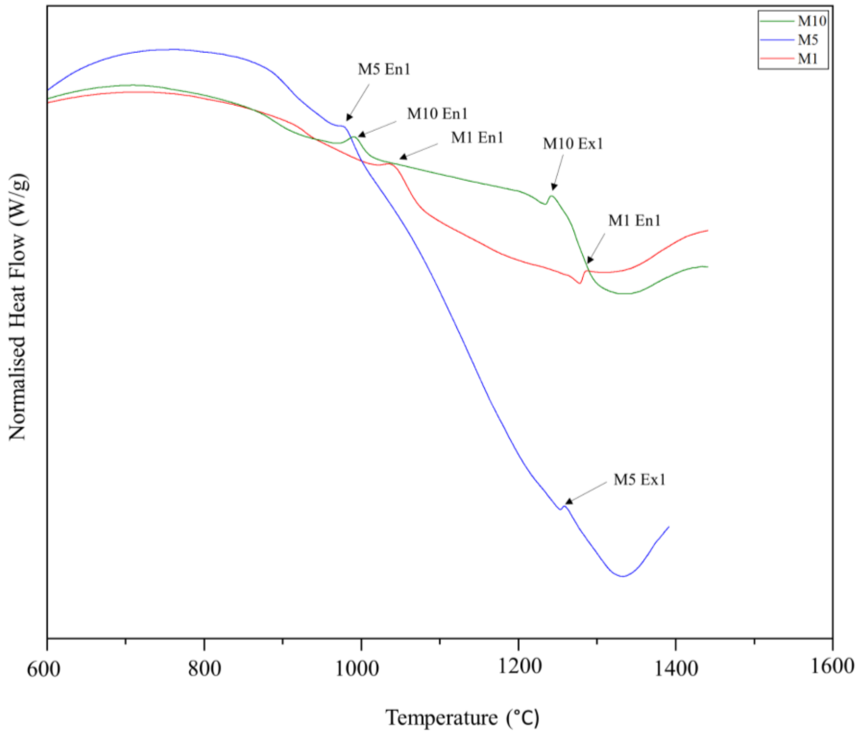

Figure 6.14 Thermal analysis for M1-M10

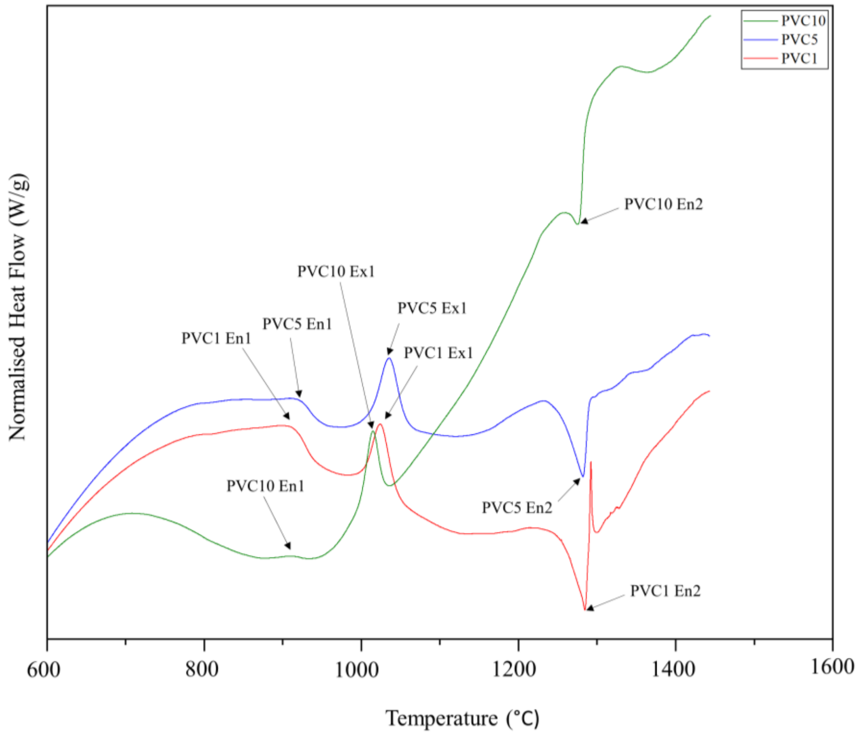

Figure 6.15 Thermal analysis for PVC1-PVC10.

Table 6.8 Estimated Tg, Tx and Tm values for CAS glasses.

	Tg (°C)	Tx(°C)	Tm(°C)
CAS0	820	915(1) and 1051 (2)	1281
Ce0207	793	922 (1) 1051 (2)	1282
Ce1	790	920 (1) and 1050 (2)	1281
Ce5	774	919 (1) and 1036 (2)	1253
Ce10	789	924 (1) and 1033 (2)	1269
Hf0207	782	922 (1) and 1044 (2)	1285
Hf1	791	917 (1) and 1055 (2)	1280
Hf5	793	943 (1) 1117 (2)	1261
Hf10	823	955 (1) 1090 (2)	1250
M1	794	919 (1) 1038 (2)	1278
M5	783	884 (1) and 979 (2)	1254
M10	738	879 (1) 992 (2)	1234
PVC1	792	912 (1) and 1025 (2)	1285
PVC5	787	914 (1) and 1036 (2)	1282
PVC10	772	908 (1) and 1017 (2)	1275

6.6 X-Ray Absorption Spectroscopy (XAS)

The features of x-ray absorption spectra can be used to investigate the structural environment of different cations in the glass.

The shape of the Ce XANES spectra been shown to very sensitive to oxidation state and is more independent of co-ordination and ligand species [27, 28]. The Ce L3-Edge is very sensitive to Ce oxidation state and as for the KBasin sample in (Section 4.6) fingerprint analysis and linear combination fitting of standards allows the determination of the Ce oxidation state in the CASCe series based upon the features in 2 standards CeO_2 (Ce^{4+}) and $CePO_4$ (Ce^{3+}) (Section 3.2). The samples in CASCe series appear to have a significant contribution of Ce^{4+} in the glass suggesting a mixture of oxidation state (Figure 6.16). There does not appear to be a significant difference between the samples with linear contribution fitting providing a quantitative measure of contribution in the samples and estimating the amount of Ce^{4+} between 24-28%. This contradicts previous work done on PCM slags [21, 29, 30] which has shown that Ce in these melts was exclusively in 3+. However, this may relate to the reducing conditions imposed by melt and crucible used, but also may relate to glass composition.

The significant Ce^{4+} contribution is potentially important as oxidation state has been shown to control solubility. In borosilicate melts Ce_2O_3 (3+) has been shown to be more soluble than CeO_2 (4+) [14, 16, 31-36] and is directly comparable to PuO_2 which has similar solubility (up to ca. 2 mol%) [31, 33, 34]. The CAS system under similar conditions appears to have different behaviour with here a minimum solubility of >3.66 mol% in a mixed 3/4+ oxidation state showing enhanced solubility compared to borosilicate's, this area requires further work to determine Ce solubility limits and behaviour. Ce in different oxidation states has been shown to act as a network modifier in aluminosilicates [20], this acceptance allows the glass composition to be more flexible opening the opportunity to accommodate more varied waste at a higher waste loading. The significant levels of Ce^{4+} also supports the increased levels oxidation seen in other metallic elements (see below). Hf only has a single oxidate state and the fingerprint technique shows that the Hf in all the glass closely matches the HfO_2 standard (Figure 6.17) however it is subtly different suggesting that the Hf in the glass may be in a different/altered co-ordination environment to the 7- fold co-ordinated Hf in the monoclinic HfO_2 [37]. The Hf^{4+} has been shown to have similar solubility to Pu^{4+} in borosilicate at roughly 0.5 mol% however the identified 4+ in CAS glasses clearly has a higher solubility of >3.55 mol% meaning potentially higher waste loading [10, 32, 33, 36]. It is not fully clear as to how the CAS framework would accommodate the Hf^{4+} but due to its similarity to Zr^{4+} ([38-45] and Section 2.3.4) it is most likely to be accommodated on an negative charge balanced octahedral Al^{3+} site. Subtle differences in the XANES spectra identifying a different coordination environment may support this but as Zr has also be reported in higher coordination environments then further work with more standards is required to confirm the co-ordination environment and confirm and calculate full solubility limits.

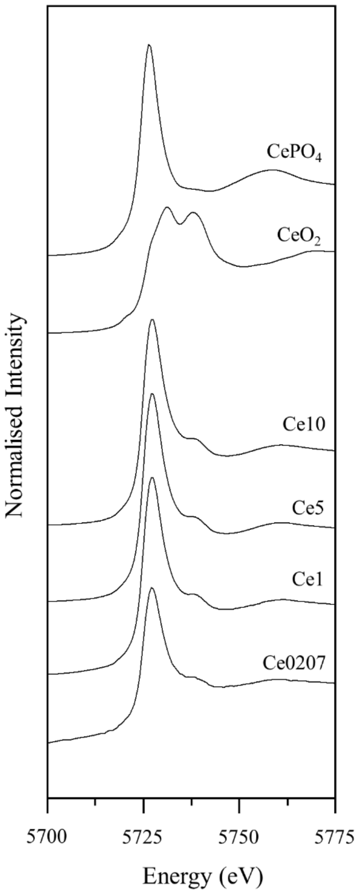

Figure 6.16 Ce L3-Edge XANES spectra for Ce0207-10 and 2 standards CeO_2 and $CePO_4$.

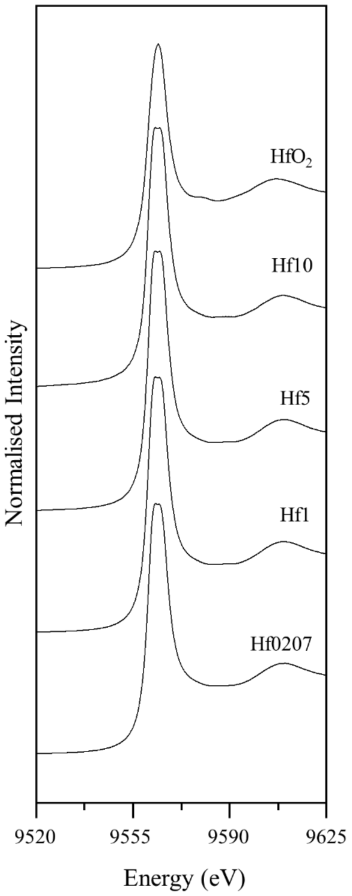

Figure 6.17 Hf L3-Edge XANES spectra for samples Hf0207-10 and the standard HfO_2.

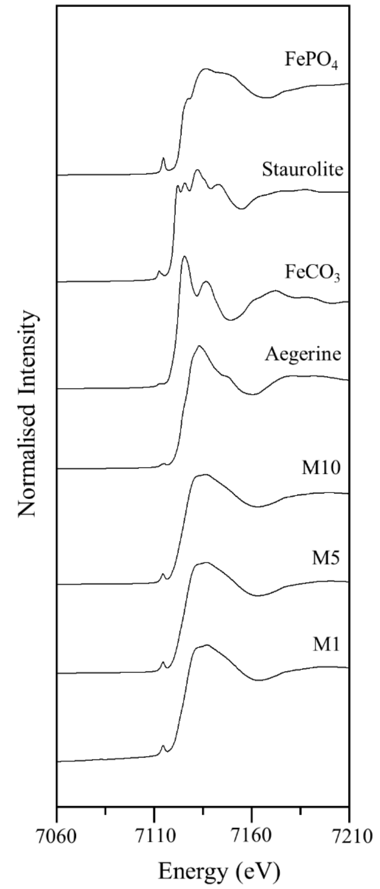

Figure 6.18 Fe K-Edge XANES spectra for the CASM samples and 4 standards staurolite, aegirine, $FeCO_3$ and $FePO_4$.

Table 6.9 E_0 positions for Fe K-Edge XANES spectra for CAS M1-M10 samples and 4 standards staurolite, aegirine, $FeCO_3$ and $FePO_4$.

	E_0 Energy (keV)
Aegerine	7119.60
Staurolite	7111.59
$FeCO_3$	7114.61
$FePO_4$	7115.40
M10	7117.79
M5	7117.8
M1	7118

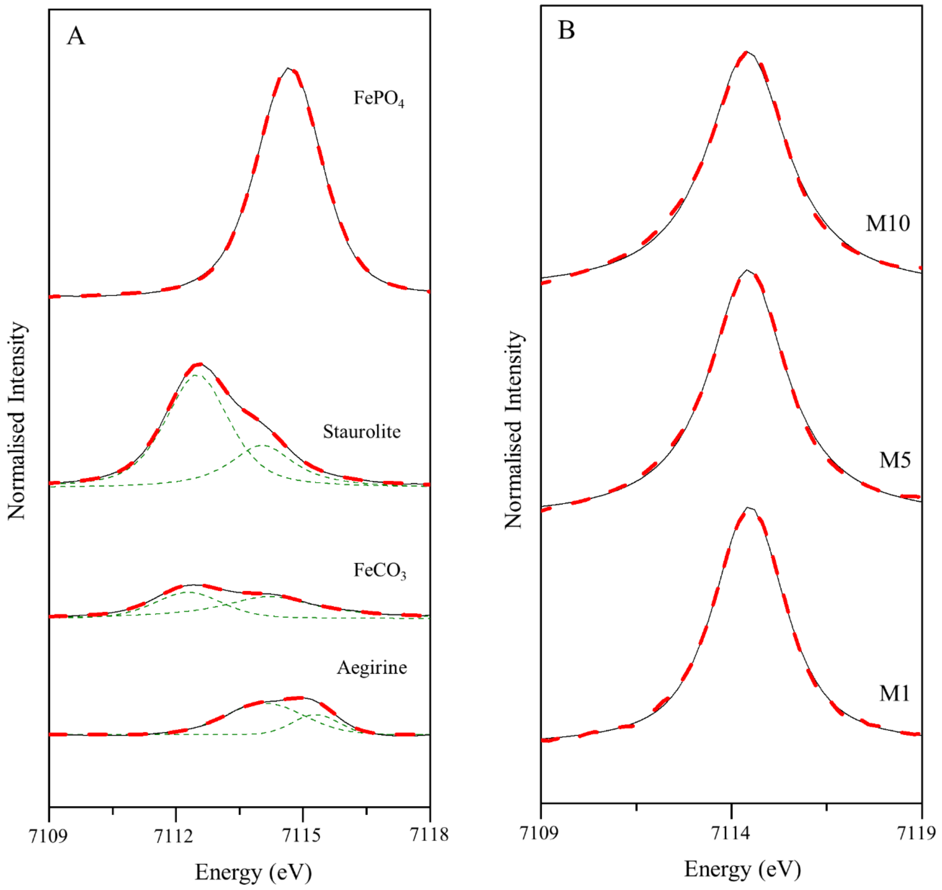

Figure 6.19 Fitted pre-Fe K-Edge for A. Fe Standards and B.M1-10.

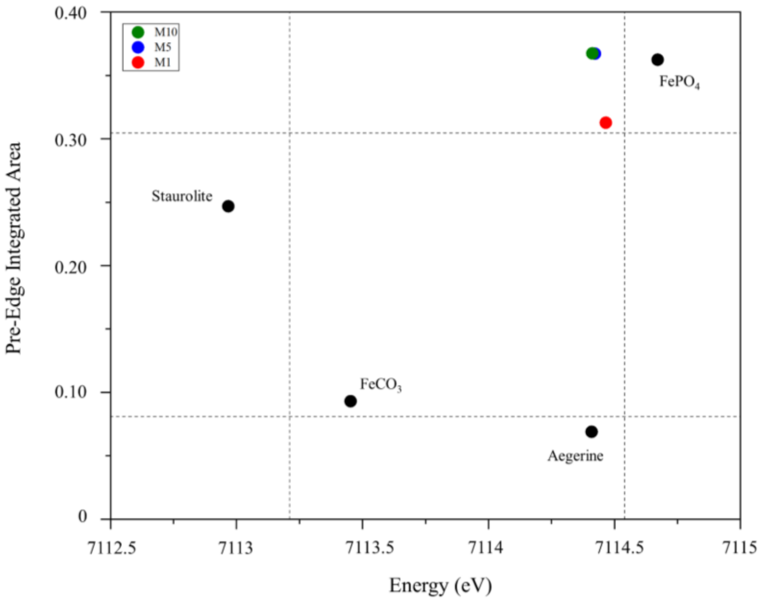

Figure 6.20 Pre-edge integrated intensities and centroid position for 4 standards and samples M1-10, shows the shift in integrated intensity related to a change in co-ordination environment and the shift in centroid position related to a change in oxidation state.

As discussed in Sections 3.2.10, 4.6 and 5.6 for Fe the fingerprint technique and E_0 position can be used to compare Fe K-Edge XANES spectra, however the complicated nature of the edge and the often-ambiguous nature of the E_0 position in the industrial samples make it difficult to discern the Fe environment. For the CASM samples the fingerprint analysis is still challenging based upon the complicated nature of the standard edge shapes, however, the E_0 position is more defined in the simpler CASM edge making the E_0 energy (Figure 6.18 and Table 6.9) more diagnostic of the Fe^{3+} environment in the glass. As in previous analysis however the most robust technique for determining Fe-environment is with pre-edge fitting using pseudo-voigt functions (Figure 6.19). Samples from CAS-M can be fitted with a single pseudo-Voigt with a centroid close to 7106 eV (Figure 6.19). This closely matches the centroid position and integrated intensity for $FePO_4$ (Fe^{3+}(IV) with near identical distribution from M5 and M10. The downshift in IS from $FePO_4$ indicates some Fe^{2+}(IV) in all the samples and the reduction in integrated intensity for M1 indicates minor Fe^{2+}(VI) (Figure 6.20). These observations indicate that the Fe is accommodated in the CASM in tetrahedral sites as a Fe^{3+} which is expected for Fe^{3+} at higher concentrations in glass (Section 2.3.4) [46, 47]. In CAS Fe in this environment will substitute for the structurally similar tetrahedral Al^{3+} as a network former in the glass structure [46, 48]. This contrasts with the Tetronics samples which were the Fe is predominantly in the Fe^{2+}, however the co-ordination in the glassy 1A_glass sample is the same with a fourfold (IV) tetrahedral environment, supporting the theory that co-ordination could be controlled crystallisation with four fold (IV) accommodation irrespective of oxidation state, in line with previous observations (Section 5.6) [46]. Fe^{3+} concentration also appears to control co-ordination, along with other factors such as modifier ionization strength, so this requires further study (Section 2.3.4) [47].

The Ca^{2+} environment along with a set of standards has been analysed as in Section 5.2 (Figure 6.22 and 6.23). As discussed previously (Section 3.2.10) the standards represent a series of co-ordination environments for the consistent Ca^{2+} cation with an apparent increasing pre edge integrated area with co-ordination/distortion, the energy seems consistent except for the outlier Labradorite. The oxidation state is constant in Ca^{2+} so it is not as clear as to the effect of the co-ordination on the energy value if any, to work this out a wider standard study is required. All the CAS glass samples are plotted in the same area which is most representative of the minerally equivalent labradorite in a distorted polyhedron with seven oxygens with a possibly high co-ordination shown by the elevated pre edge integrated area. There is no significant variation between different waste additions and amounts suggesting no change to the Ca^{2+} environment. The CAS Ca^{2+} area has been used to compare to industrial samples in Section 5.7 showing the similarity between the environments and supporting in term of Ca^{2+} environment the use of lab samples as industrial simulants.

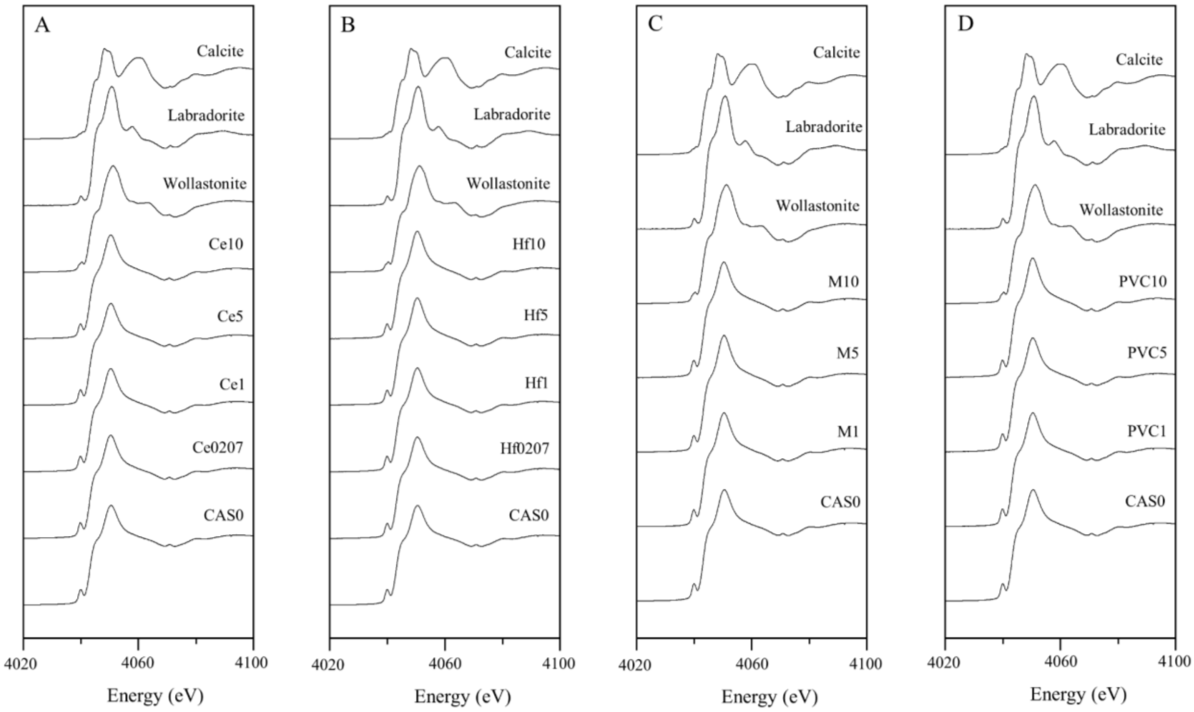

Figure 6.21 Ca K-Edge XANES spectra for the CAS samples including A- Ce B – Hf C – Metal and D – PVC and 3 standards Wollastonite, Labradorite and Calcite.

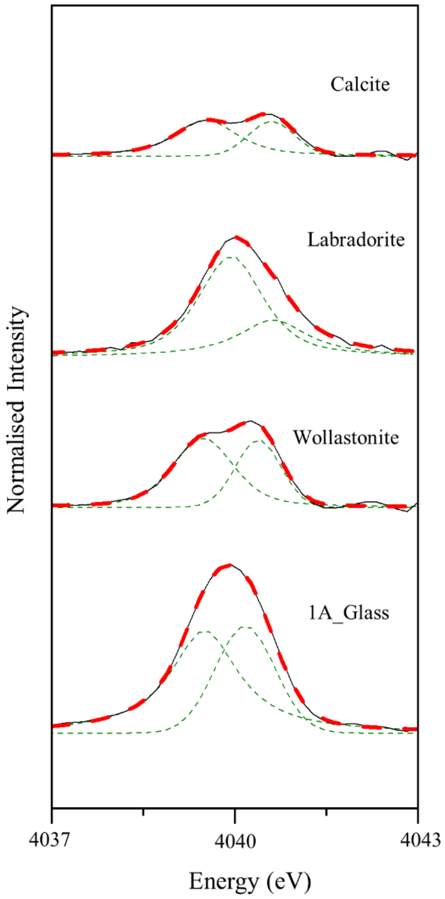

Figure 6.22 Fitted pre-Ca K-Edge for CAS0 and 3 standards Wollastonite, Labradorite and Calcite, other series fits (Hf, Metal and PVC) are very similar so are not shown but subtle shifts are represented in Figure 6.23.

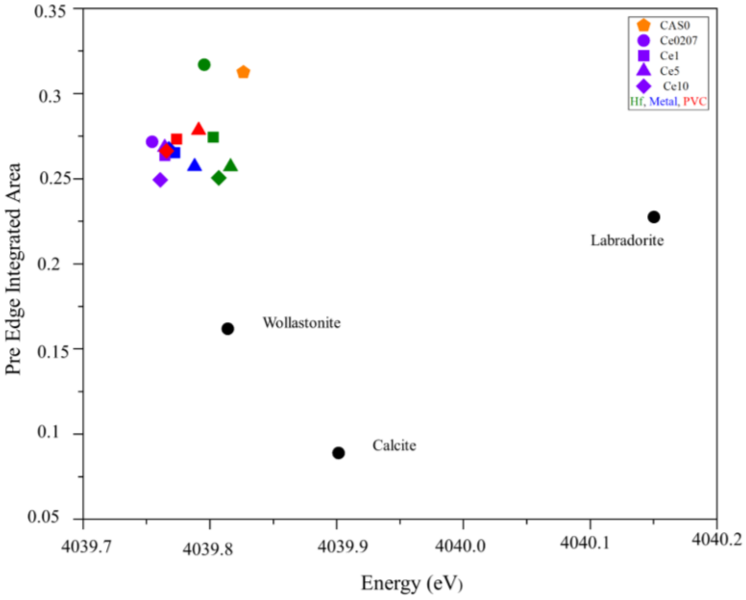

Figure 6.23 Pre-edge integrated intensities and centroid position for 4 standards and samples M1-10, shows the shift in integrated intensity related to a change in co-ordination environment and the shift in centroid position related to a change in oxidation state.

The lab glasses were created in a more oxidising environment than the industrial glasses, which is supported by there being a considerable concentration of Ce^{4+} in the Ce CAS series and Fe^{3+} environment in the CAS Metal series. This is important, because to fully represent the industry glass and understand the incorporation of waste elements in CAS glass, then the REDOX environment needs to be reproduced as variable oxidation states of elements including Fe can affect incorporation into the glass and key properties of the glass including connectivity and durability (Section 5.10).

6.7 Mossbauer Spectroscopy

Mossbauer spectra as seen in previous chapters has been used for a comparison to X-ray absorption analysis to investigate Fe environment. Spectra from sample M5 and M10 trial have been fitted with several peaks (Figure 6.24) with the position and splitting diagnostic of the Fe environments, the Mossbauer signal was too weak in sample M1 to provide a significant analysis.

Sample M5 has a dominant (0.59) doublet with an isomer shift of 0.2 mm/s and a quadrupole splitting value of 1.5 mm/s which is closest to the region of Fe^{3+} in sixfold octahedral VI co-ordination. Sample M10 has a similar dominant (0.66) doublet with analogues isomer shift (0.2 mm/s) and quadrupole splitting (1.3 mm/s) also in the region close to Fe^{3+} in an sixfold octahedral VI environment, this is analogous to the Fe^{3+} present in the Tetronics 1A_glass sample and similar higher co-ordination has been found in natural glasses (Section 2.3.4 and [46]).

These two major sites, in comparison to previous analysis (Section 4.7 and 5.8) and other sites in these samples, fall the furthest outside of the main identification windows diagram from [49] and with the values from each fit in (Figure 6.24) plotted in (Figure 6.25), with the majority other sites falling at least on the edge of the windows as a minimum. In bulk analysis, to create the environment windows [49], there are samples in this region suggesting that analysis is more complicated than simple definition into these generalised regions. Another option for the interpretation of the co-ordination in these glasses is to assume the isomer shift value is not underrepresented and that the quadrupole value is increased by Fe site distortion with a distorted fourfold tetrahedral co-ordination, this would fit with X-ray absorption analysis (see below) and is the most common co-ordination for Fe^{3+} when in high concentrations in natural glass, with increased ionization by a strong modifier like Ca^{2+} causing increased distortion (Section 2.3.4 and [46, 47]). Clearly, although confirmed as Fe^{3+} some caution is required in confidently defining the co-ordination of these major sites and it is an area that requires further analysis and confirmation to be confident of the correct interpretation.

In both M5 and M10 there is also contribution from other Fe^{3+} sites that increase the amount of Fe^{3+} as a fraction of total Fe in the samples to >0.79 (Table 6.10). M5 has two additional doublets with an isomer shift of 0.3 and 0.1 mm/s and a quadrupole splitting of 1.0 and 0.3 mm/s indicative of Fe^{3+} in an octahedral (VI) and tetrahedral (IV) with some possible distortion increasing values. M10 has an additional doublet at isomer shift of 0.4 mm/s and a quadrupole splitting of 0.6 mm/s indicative of Fe^{3+} in an octahedral (VI) with low levels of distortion (Table 6.10 and Figure 6.25).

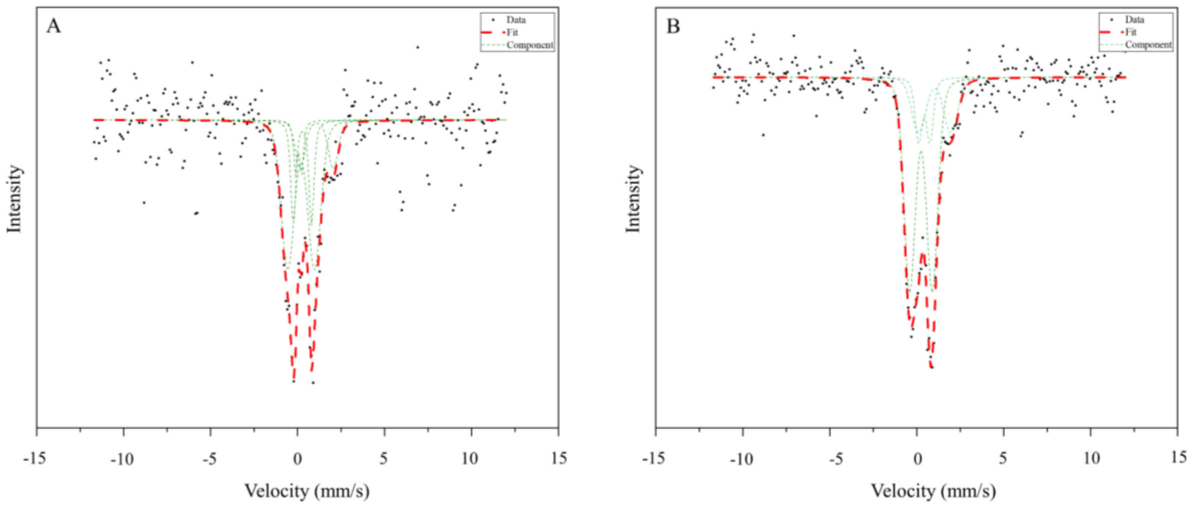

Figure 6.24 Fitted Mossbauer spectra for A - M5 and B - M10.

A minor amount (<0.21) of Fe is Fe^{2+}, M5 has doublet with an isomer shift of 1.1 mm/s and a quadrupole splitting of 1.9 mm/s and M10 a doublet with an isomer shift of 1.0 mm/s and quadrupole of 1.8 mm/s (Table 6.10 and Figure 6.25). This is identified as tetrahedral (IV) Fe^{2+} environment which matches the industrial Tetronics 1A_glass sample, M5 is slightly outside the identified region but based upon previous analysis this is seen as measurement variation rather than a change in coordination or distortion.

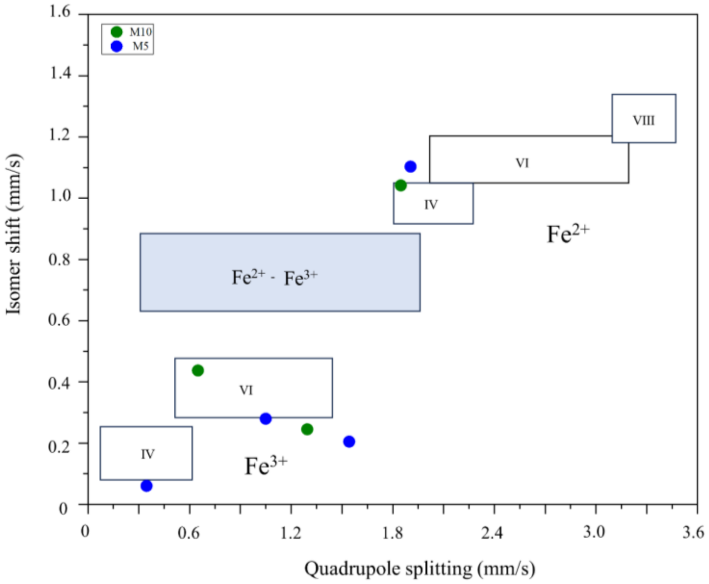

Figure 6.25 IS (Isomer shift) and QS (Quadrupole splitting) diagram from [49] with the values from each fit in (Figure 6.24) plotted.

Table 6.10 Fraction of Fe^{3+} in each sample as a fraction of the total Fe content.

Samples	$Fe^{3+/}\Sigma Fe$
M10	0.79
M5	0.85

The Mossbauer spectroscopy analysis can be compared to the x ray absorption fitting as both are indicative of the Fe environment in the samples. The two techniques in this case are not as complimentary as in previous chapters, they both support the conclusion that most of the Fe in the metallic lab CAS glass is Fe^{3+}. Unlike the 'mixed' and low levels of Fe^{3+} in the Tetronics samples, the large fraction (Table 6.10) of isolated Fe^{3+} sites in these samples dominated the average x ray absorption signal as well as the main Mossbauer site, supporting the theory of increased oxidation of the metallic iron in the laboratory melts. Comparison of the two techniques in relation to co-ordination is more complicated and the two techniques are only in agreement if it assumed that the samples in the Mossbauer analysis are in a distorted a site with four fold tetrahedral (IV) coordination. The X-ray data concludes that an average measurement from all the sites would be dominated by the main Fe^{3+} site and fourfold tetrahedral (IV) coordination is commonly seen for natural samples (Section 2.3.4 and [46]) supports the Fe^{3+} being in four fold tetrahedral (IV). This is a different coordination to six fold tetrahedral (VI) coordination seen in Tetronics 1A_glass but previous studies have shown that with increased Fe^{3+} the coordination is reduced from sixfold tetrahedral (VI) to four fold tetrahedral (IV) coordination, with high ionic elements such as Ca^{2+} causing significant distortion [47]. Although higher Fe^{3+} coordination environments have been seen in natural glasses meaning that sixfold tetrahedral (VI) is a possible environment (Section 2.3.4 and [46]) further analysis is needed to confirm its presence in these samples. As discussed in Section 5.8 this is different to the Tetronics lab melts that are dominated by Fe^{2+} indicating a lower oxidation environment possibly caused by presence of organic material, graphite electrodes, metallic drum or the size of melt and reduced accessibility and mixing of oxidants. This, as discussed in Section 5.8 highlights that although the composition of CAS M5 glass closely matches the Tetronics and industrial trial 1A_glass in Section 5.8 then care must be taken in using this as an analogue for the Tetronics glass as the Fe environment is very different that can have a major impact on the glass structure and likely, although not tested in this chapter for the CAS glass, the durability. In the following Sections a variety of different techniques are used to investigate the structure of the CAS glass, how the different additives effect the structure and how it compares to the industrial glasses.

6.8 Raman Spectroscopy

Raman spectroscopy for all the CAS glasses is visually similar with a high frequency region at 900 to 1200 cm^{-1} and a low frequency region at 200 to 800 cm^{-1} and the Boson peak at 100 cm^{-1}. The shape and position of the Raman spectra appear to show very subtle differences from the base CAS0 glass with the addition of the simulants except the Boson peak that remains constant throughout the spectra (Figure 6.26).

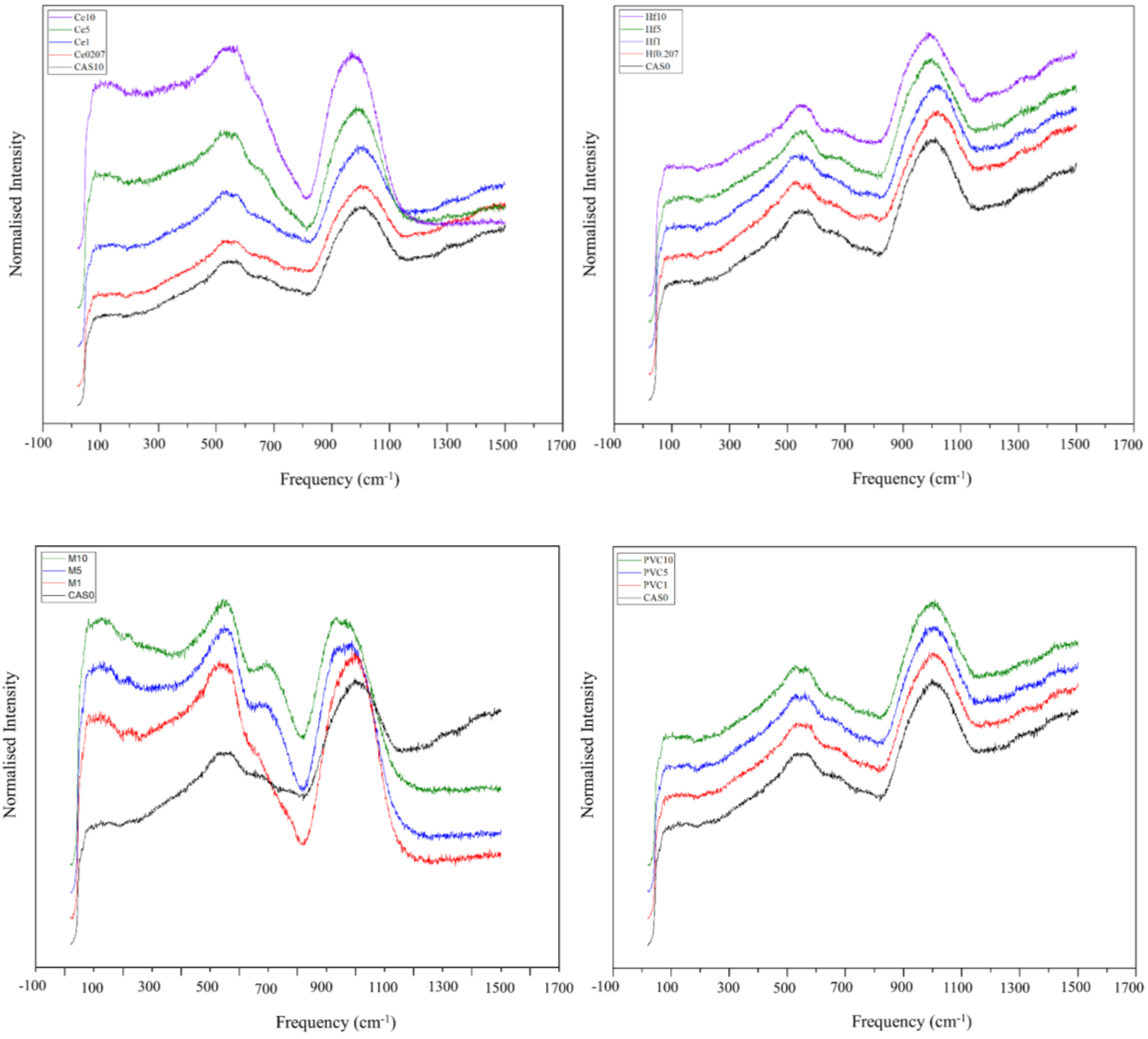

Figure 6.26 Stacked Raman spectra from -100 to 1700 cm^{-1} for the CAS series of glasses. CAS 0 is shown in all plots for comparison to CAS glasses with additions of Ce, Hf, Metal and PVC.

The addition of Ce visually shows little to no effect at very low levels (0.207) with the spectra moving to a slightly higher frequency, but the shape and structure remaining the same. With further additions of Ce there are more intense changes to the spectra. From Ce1-Ce10 the high frequency peak increases in intensity and shifts to slightly lower frequency and the lower frequency region also appears to grow in intensity, although further analysis (see below) show that the intensity changes are an illusion and are actually a function of additional higher frequency 2200 cm^{-1} peaks changing the normalisation shape of the spectra and there is relatively limited change caused to the lower and higher frequency regions by the addition of Ce.

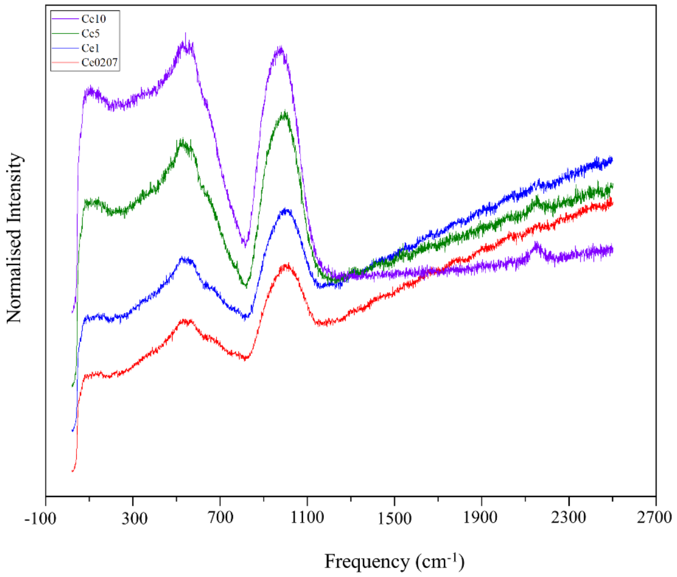

Figure 6.27 Stacked Raman spectra from -100 to 2700 cm^{-1} for Ce0207-Ce10. Note the high frequency peak present in high Ce glasses.

A peak at 2200 cm^{-1} (Figure 6.27) is attributed to Ce-O stretching that is seen in the higher (Ce5 and 10) loaded glasses and is possibly visible in Ce1 although this appears to be close to detective limits. The addition of Hf appears to visually have little to no effect on the shape or the position of the Raman spectra in relation to CAS0 with just a minor increase in frequency for the Hf0.207 and then a small decrease with additional Hf. The addition of metal causes a more significant shift in the particularly the shape of the Raman spectra with the position of common peaks roughly the same but as the metal content increases there is a clear increase in the intensity of the shoulder at 700 cm^{-1} in the lower frequency region. The addition of PVC has very little effect on shape and position of the Raman spectra suggesting that the addition of PVC has not had any major effect on the CAS0 glass structure.

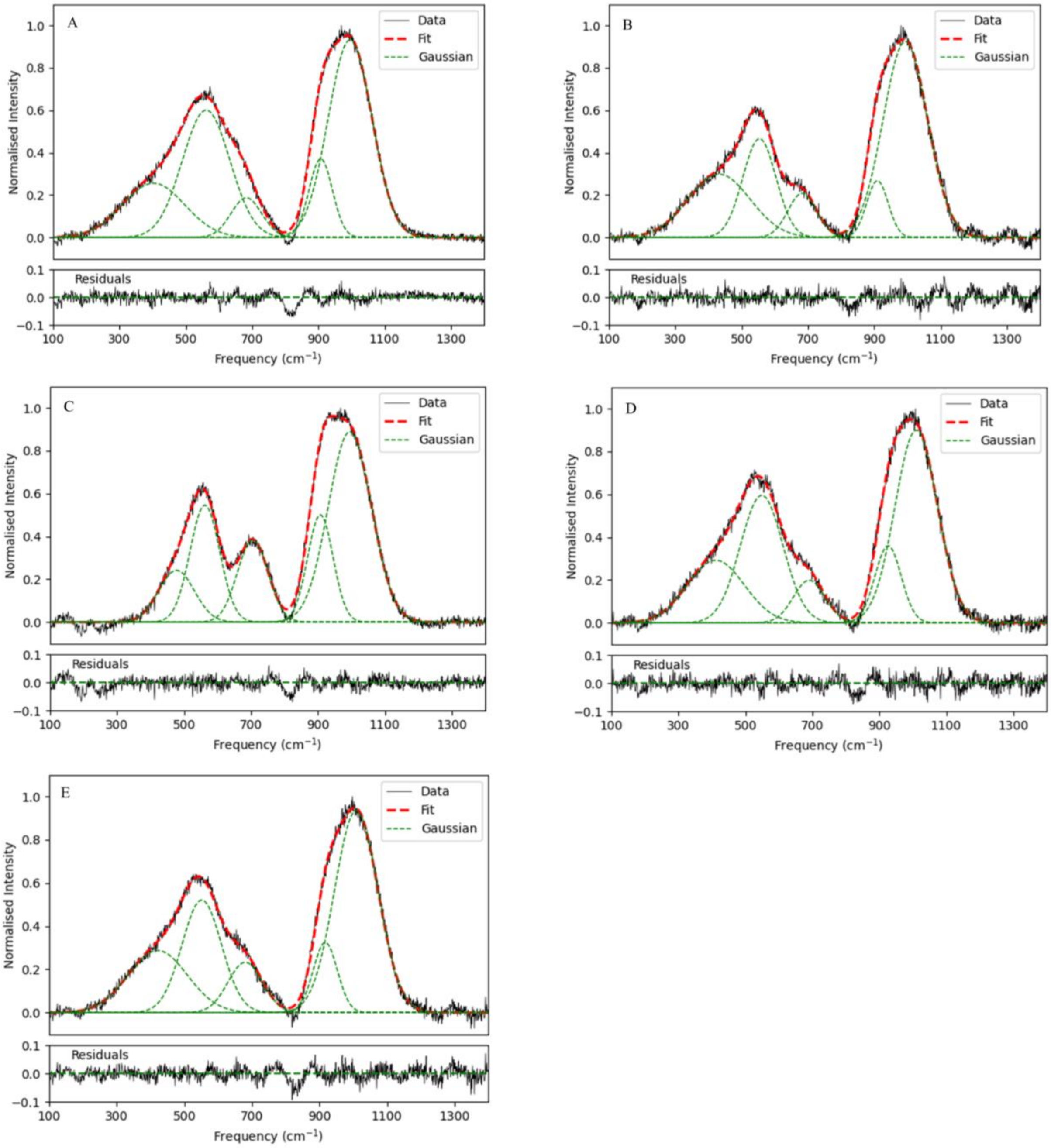

Figure 6.28 Fitted spectra for A- Ce10 B- Hf10 C-M10 D- PVC10 and E- CAS0.

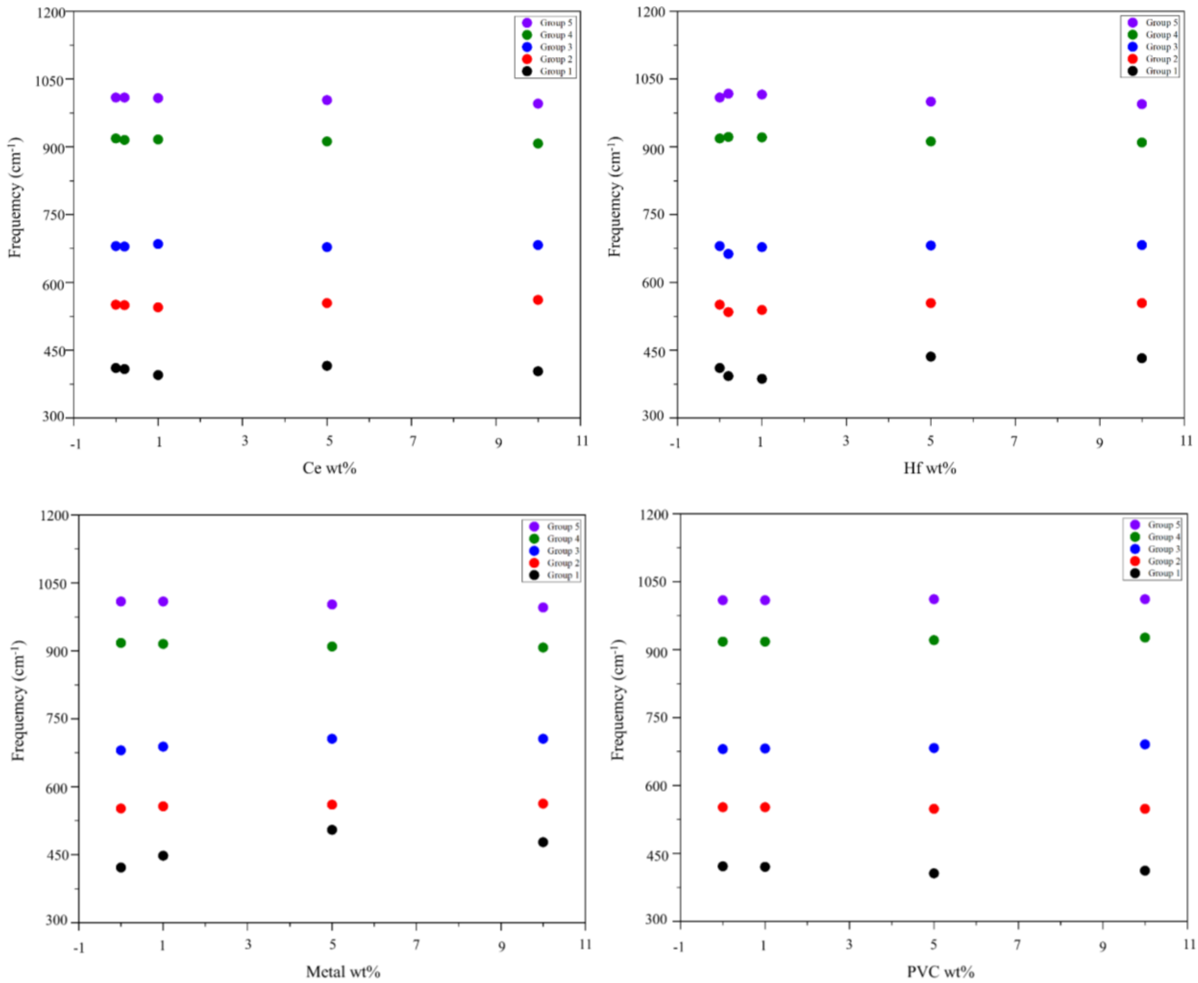

Figure 6.29 Gaussian positions for fitted spectra vs addition % for Ce, Hf, Metal and PVC for fitted spectra.

To further investigate and try to assign structural reasons to the subtle changes seen in (Figure 6.26) the Raman spectra were background removed and fitted with gaussian peaks using the Rampy code (Section 3.2.9) (Figure 6.28). There are subtle changes to the position and frequency of the gaussian peaks, these give a better indication of changes to the CAS addition. All CAS glasses can be fitted with the same range of 5 gaussians with 3 in the lower frequency at ~ 400-530, 550 and 700 cm^{-1} and two in the higher frequency region at ~900 and 1000 cm^{-1} there are some shifts of the relative intensity and position of these peaks with the addition of the waste simulants. The gaussians have been labelled Group 1-5 based on the frequency with Group 1 being the lowest frequency, based on Table 3.20 in Section 3.2.9 these groups can be attributed to the following bond vibrations; Group 1 at ~450 cm^{-1} is related to Si-O-Si (A1) asymmetric motion in 5-6 membered rings in a polymerised glass structure, Group 2 at ~550 cm^{-1} is a sign of some depolymerisation as well in the structure with it possibly representing the collapse of the D1 and D2 defect bands in Si-O° rocking motion in Q4 units or Q3 T-O-T breathing. This is analogous to the lower frequency signals seen in the 1A_glass Tetronics sample seen in Section 5.9 with intensity and positional difference showing the effects of different processing conditions and addition of simulants, this is also seen in the mid and high frequency regions. Group 3 at 700 cm^{-1} is less well defined but relates to bond motion in polymerised ring structures or potentially Al-O motion in the Al sub-network with variable Q species stretching, Group 4 at ~910 cm^{-1} relates to stretching in Q1 depolymerised units with lower frequency shifts associated with Al-Si substitution, Group 5 at ~1000 cm^{-1} is analogous of Group 4 but with more polymerised Q3 units, it is common that Q3 and Q1 units are associated in depolymerised glass due to balancing in the network modifier distribution [50]. As noted by visual observations, the addition of waste simulants doesn't significantly change the position of the Gaussian peaks with only minor changes causing shifts in the Raman spectra (Figure 6.29). There are some changes to the relative intensities caused by the addition of the different waste simulants although they are subtle with generally similar values for all glasses suggesting overall similar glass structure with small changes caused by waste loading (Figure 6.30). For the Ce series there is inconclusive evidence that there is any significant change in the groups intensity which supports the visual analysis and shows that the observed changes in (Figure 6.26) relate to the presence of the higher frequency Ce-O signal.

For the Hf series there is variable behaviour between the different groups in the glasses with different Hf loadings. Group 3, 4 and 5 are relatively constant for all levels of Hf but there is variation in the groups 1 and 2, with higher group 2 levels in lower Hf loading and higher group 1 levels in higher Hf loading, this shows that the Hf is no having major structural effects but is changing the behaviour of Si-O motion in ring structures likely due to Hf accommodation, it is unknown the frequency of the Hf-O bond but no clear evidence was seen to suggest a direct signal in the Raman spectra. For the metal series there is again some subtle shifts in the different groups. Group 5 is constant for all metal levels, but Group 4 and 3 are slowly increasing with increased metal content, with constant Group 1 and decreasing Group 2 until metal 10 when Group 1 and 2 reverse.

For the PVC series there are minor shifts and there are trends with increased waste loading suggesting that they may some structural changes associated with this rather than just natural variation. In Group 2, 3 5 there is a minor decrease, Group 1 is constant, and Group 4 there is a minor decrease with increasing levels of PVC.

It can be clearly seen that there are some subtle changes likely to the major silicate network associated with the increased waste loading, although direct attribution to structural variance is difficult and often a better measure is to look at the average structural effect of the waste loading. As discussed in Chapter 4 the Raman Polymerisation Index (RPI) is a robust method for analysing Raman spectra and investing the polymerisation of the measured glass. The RPI measures the ratio of the low and high frequency peak and can show average changes in features of increasing or decreasing polymerisation and can see that changes in the gaussians can cause to the ratio. The RPI is increasing for metal and Hf showing an increase in polymerisation of the CAS system with increased metal addition as mostly Fe^{3+} or Hf^{4+} increasing the amount of network formers in the glass. The PVC and Ce appear to show inconclusive constant levels with Ce likely replacing Ca levels in line with some natural Ca variation and PVC not adding any key elements to the glass (Figure 6.31).

In conclusion there seems to be some changes to the silicate network in the lower and upper frequency regions due to the addition of Hf and metal, these are more major for the metal addition. The Ce and PVC don't seem to have major effects on the glass structure. The changes to the Hf and metal are hard to discern but relate to the Q1 and Q3 species and variation in ring structure, which increase overall polymerisation in the metal glasses and decrease polymerisation in Hf glasses with increased waste loading. The idea of producing lab glasses is to compare and reproduce the behaviour of industrial glasses so that different behaviours can correctly investigated. Compositionally, the Tetronics 1A_glass sample in Chapter 5 closely matches CAS M5 sample however the Raman spectra more closely resemble CAS0. This difference is attributed to the different behaviour of the Fe in the CAS metal series and the Tetronics 1A_glass. The Fe oxidation states in the two glasses is different with Fe^{2+} in the 1A_glass and Fe^{3+} in the CAS glass with different co-ordination environments. Fe^{2+} is found to be in tetrahedral (IV) coordination in both 1A_glass and M5 and M10 which appears from Raman spectrum to accommodate into the CAS structure without major structural changes likely as a substitute for Ca$^{2+.}$ The Fe^{3+} is very minor in 1A_glass and in octahedral (VI) co-ordination, this appears to be structurally incorporated without majorly effecting the CAS structure, potentially on the Si^{4+} or Al^{3+} sites. At much higher concentrations in the lab glasses, it has been interpreted as supported by X-ray absorption and the Raman that the Fe^{3+} is not as easily accommodated into the structure and forms distorted tetrahedral sites that have an impact on the silicate ring structure. This illustrates the importance of consideration of the redox and melt environment, and the associated compositional and structural changes, when reproducing industrial samples in the lab.

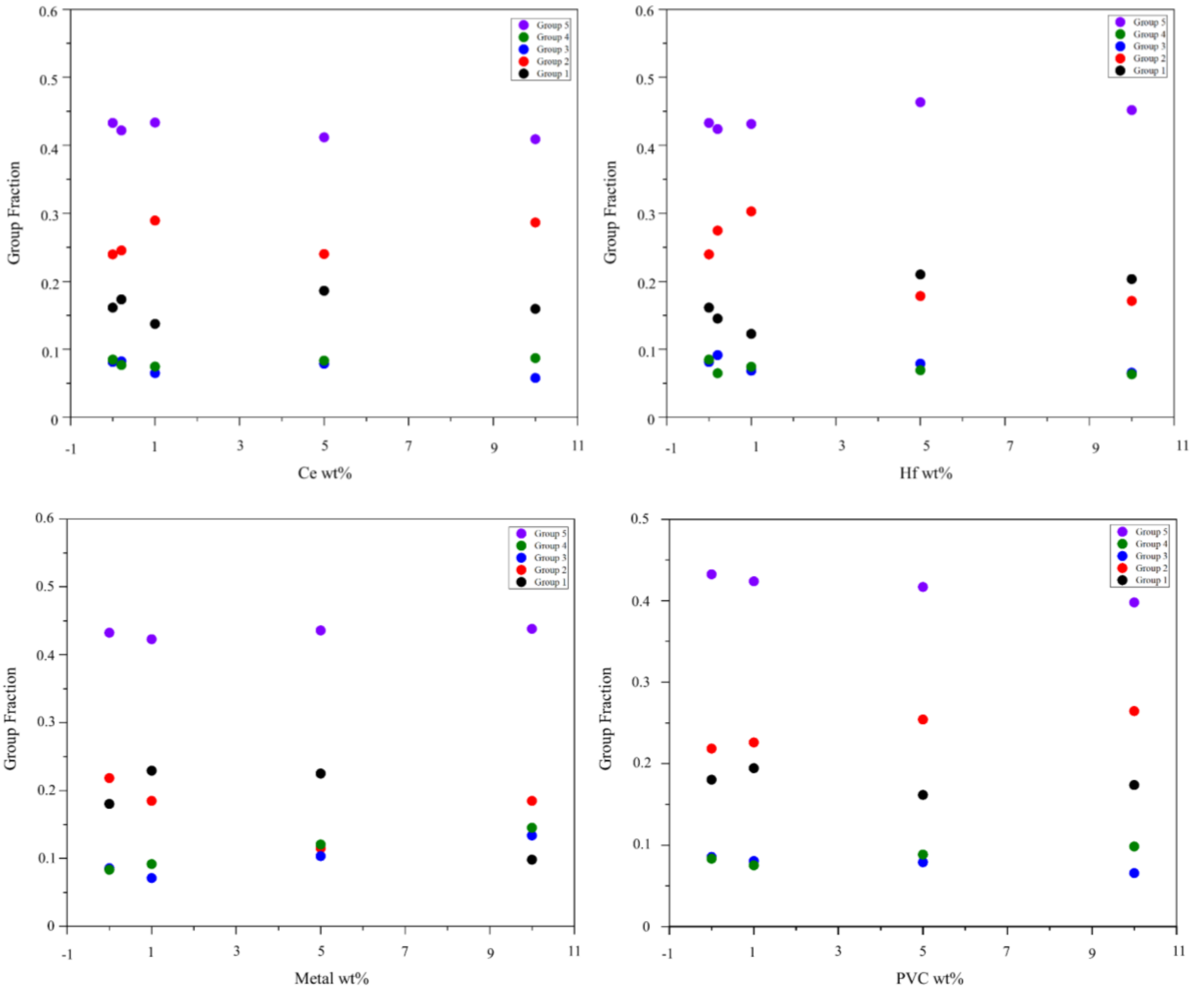

Figure 6.30 Group fractions for the Gaussians in the high frequency region of the CAS glass spectra based upon integrated area vs total integrated area for Ce, Hf, metal and PVC addition %.

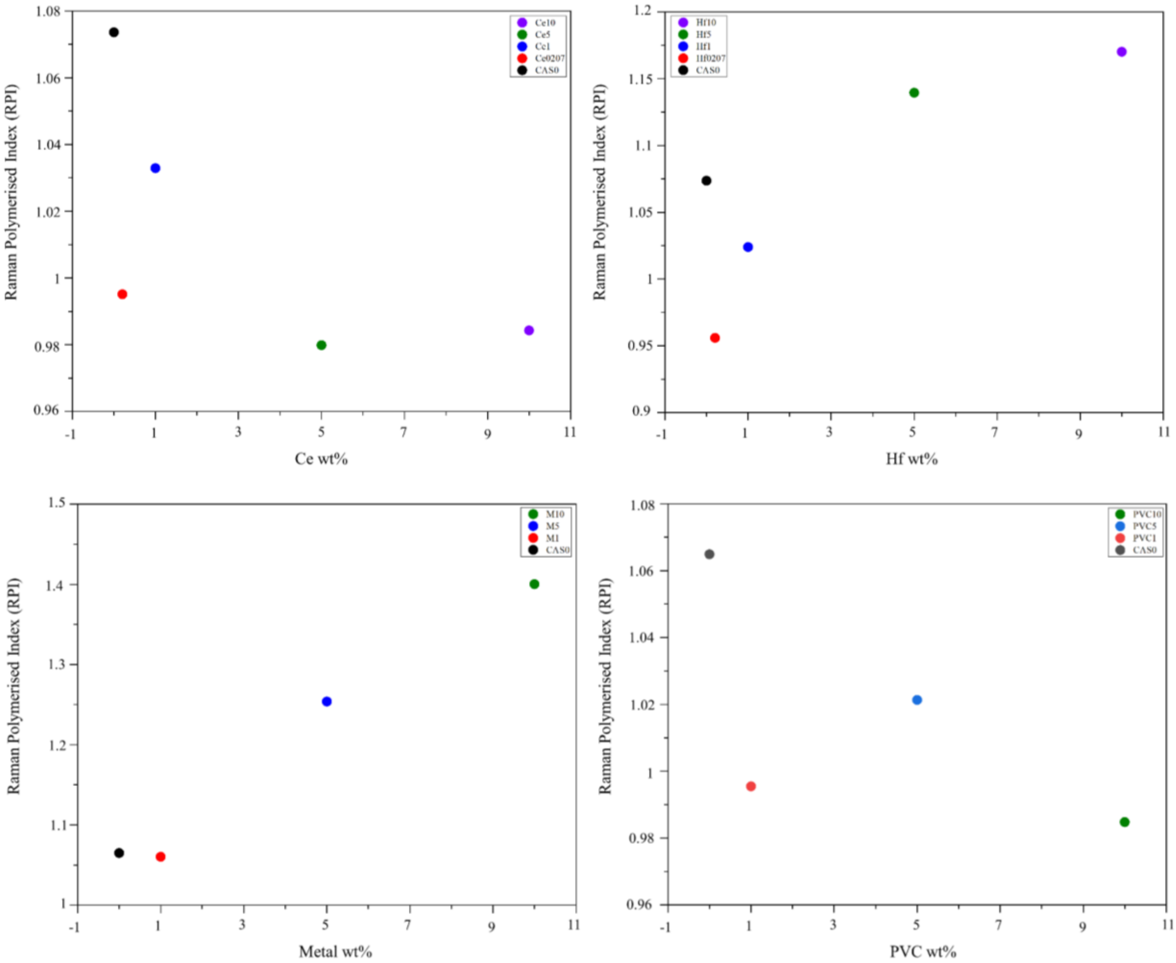

Figure 6.31 Raman Polymerisation vs addition % for Ce, Hf, Metal and PVC for fitted spectra.

6.9 NMR Spectroscopy

Si and Al NMR appear consistently similar for all samples suggesting that, like for Raman, there is only minor if any structural changes to the samples relating to the addition of the simulants (Figure 6.32 and 6.33). To further investigate subtle variations the NMR spectra for both Si and Al were fitting using either Gaussian or the CZsimple model as described in Section 3.2.7 (Figure 6.34 and 6.35). For all the Si NMR the samples there is a dominant peak at -80 to -90 ppm which is diagnostic of Q3 with minor contributions of other Q4 and Q2 species that match in with Raman studies and shows that there is minor shifts in the gaussian chemical shift (ppm) (Figure 6.36) and group fraction (Figure 6.37) relating to minor shifts in speciation caused by additions although there is no clear pattern or trend and this could be assigned to natural sample variation. In the Al NMR where there are clear peaks with centres at roughly 10, 40 and 60 ppm with Al which relate to Al [4], [5] and [6] in the structure a set of peaks at around 80 ppm are not defined and may relate to spinning side bands or an alternative undescribed contribution. Al [4] dominates the population in all CAS glasses with an average of roughly 75% which is expected for tetrahedral Al but in a lot of the glasses although not all there is measurable levels of Al [5] (15%) and [6] (5%) that is expected from historical CAS glasses (Figure 6.39) (see Section 2.1.7). There is common trend within the spectra other than what appears to be natural variation in the samples, this suggests that the addition of the waste elements is not having any major effect on the role that Al plays in the CAS glass network. This shows that if the surrogates perform in a similar way to real waste that the CAS glass can easily accommodate addition of waste elements into its structure without risking any major destabilising structural changes to the role Al plays. Based on other analytical techniques it appears that the Fe maybe having a major impact on the structure including the Si and Al framework, unfortunately this could not be analysed by the NMR due to the magnetic nature of the CAS + metal samples.

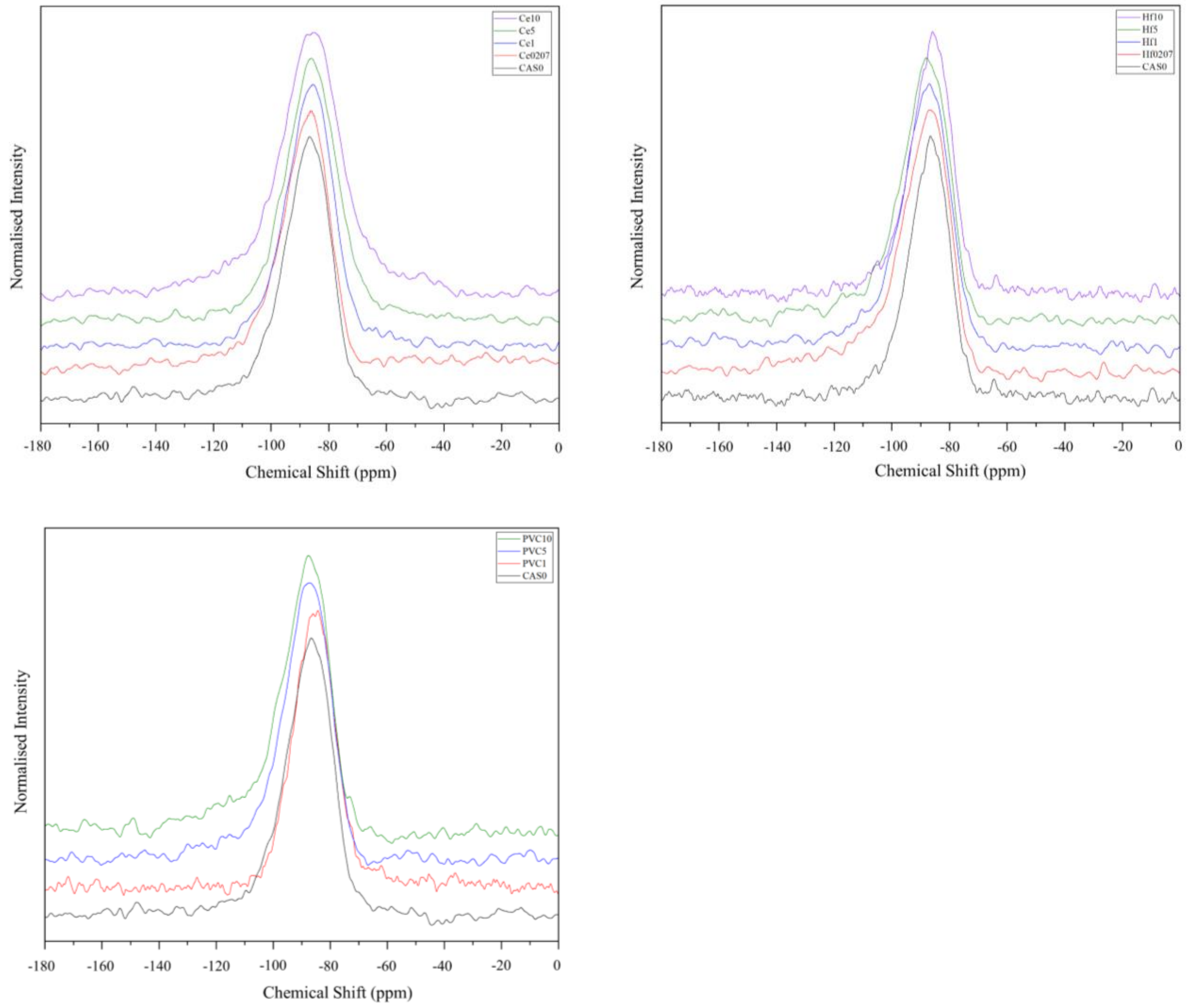

Figure 6.32 Stack Si-29 NMR plots for Ce, Hf and PVC samples.

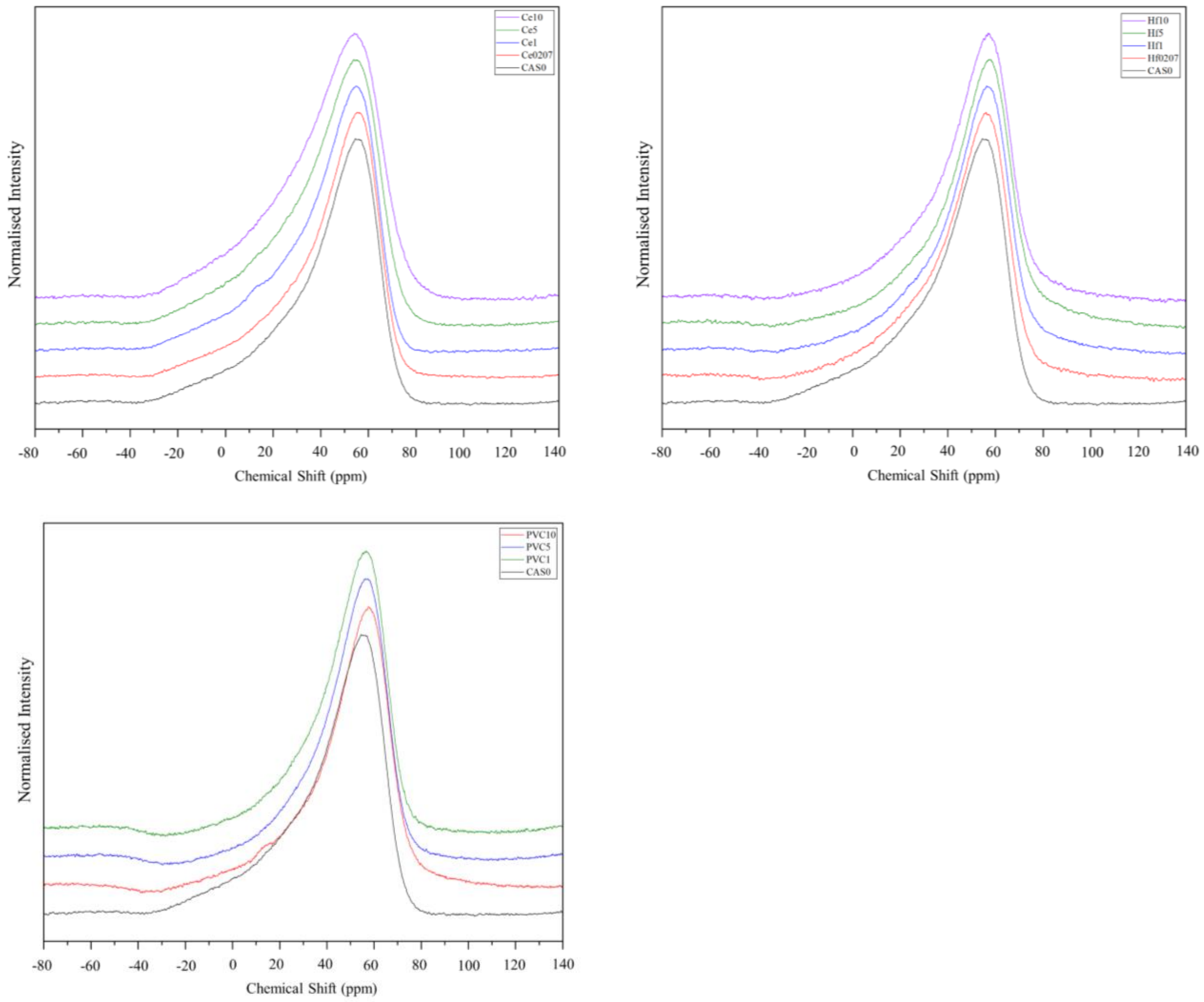

Figure 6.33 Stack Al-27 NMR plots for Ce, Hf and PVC samples.

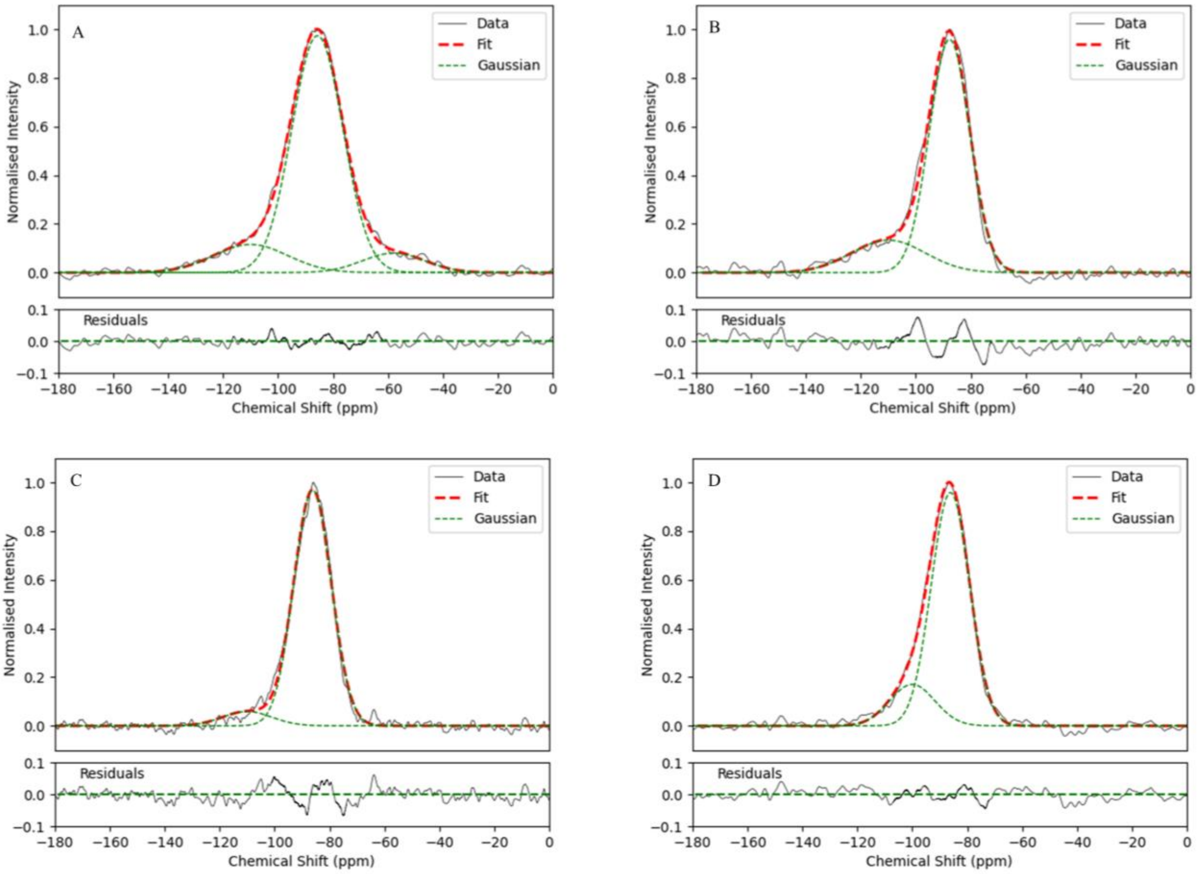

Figure 6.34 Fitted Si-29 NMR plots for A- Ce-10 B- Hf10 C- PVC10 D- CAS0

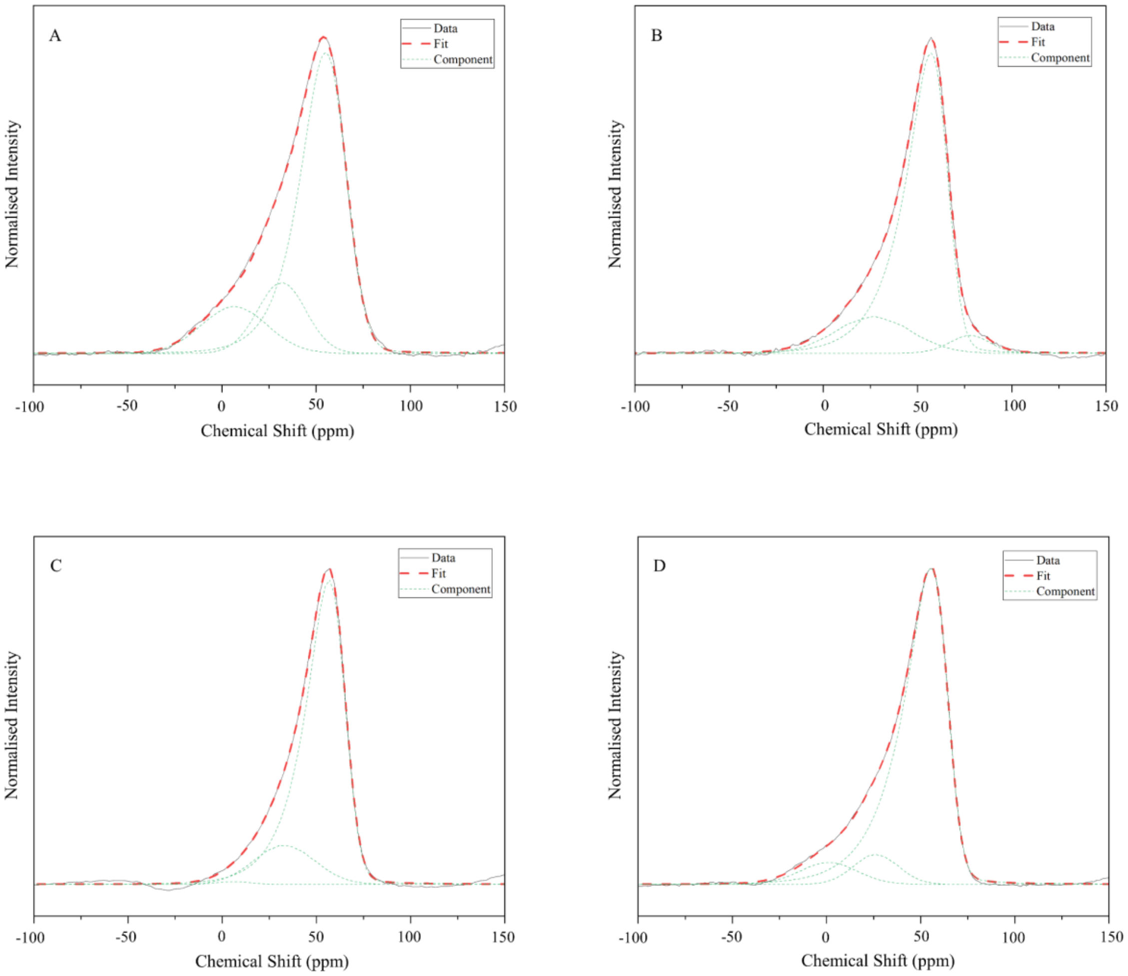

Figure 6.35 Fitted Al-27 NMR plots for A- Ce-10 B- Hf10 C- PVC10 D- CAS0

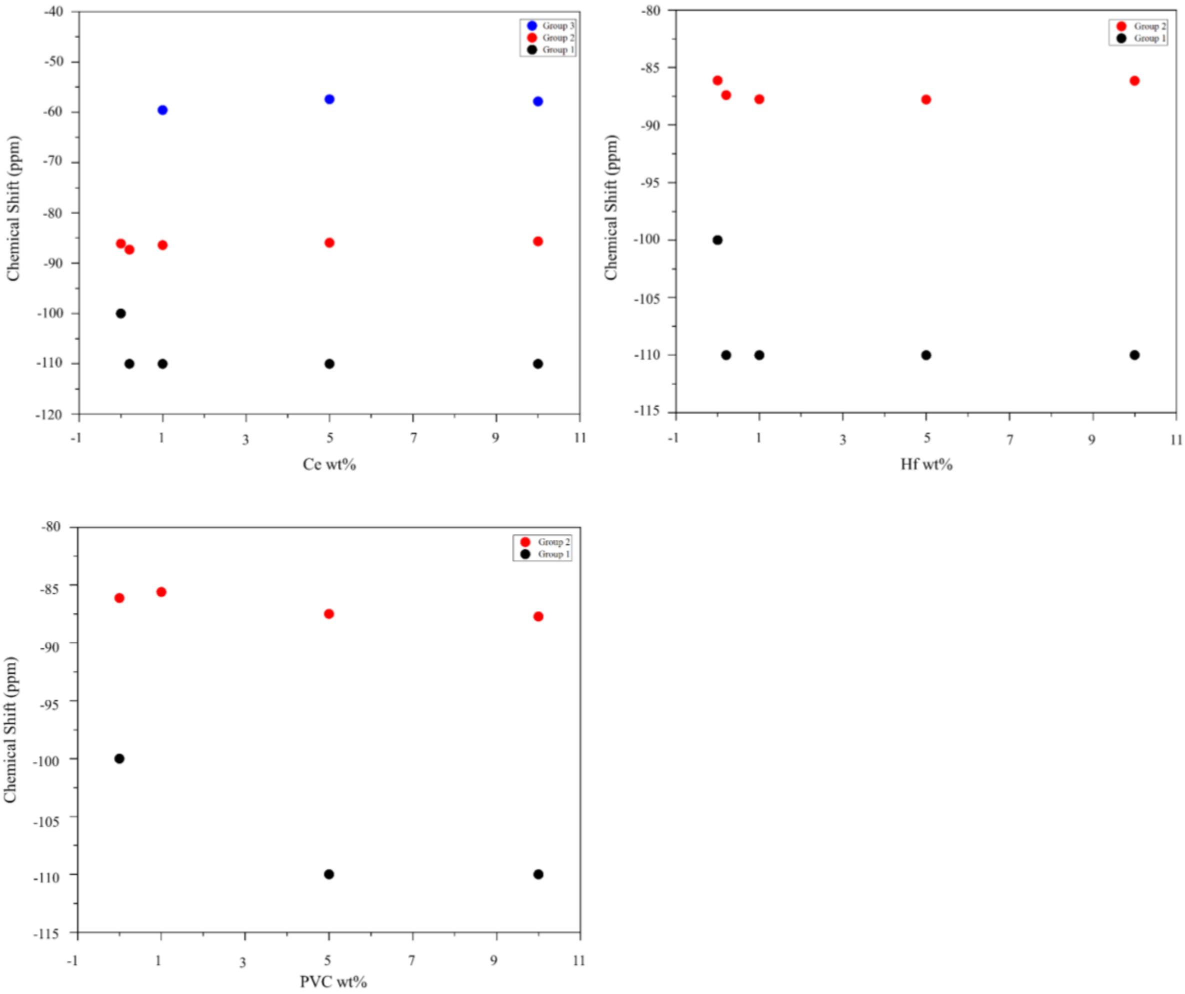

Figure 6.36 Gaussian positions for fitted spectra vs addition % for Ce, Hf, Metal and PVC for Si-29 spectra.

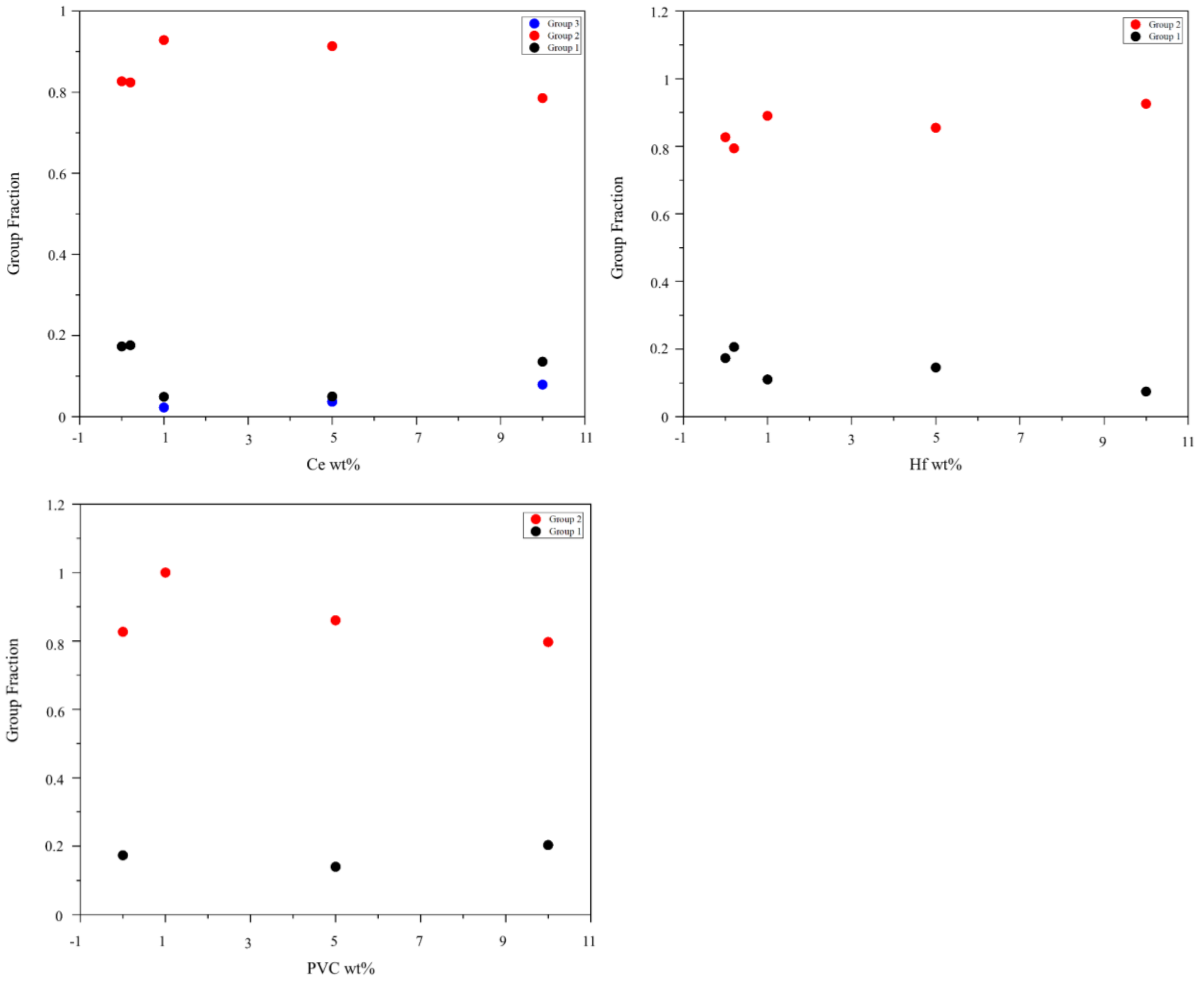

Figure 6.37 Group fractions for the Gaussians in Si-29 spectra based upon integrated area vs total integrated area plotted as a function of Ce, Hf and PVC addition %.

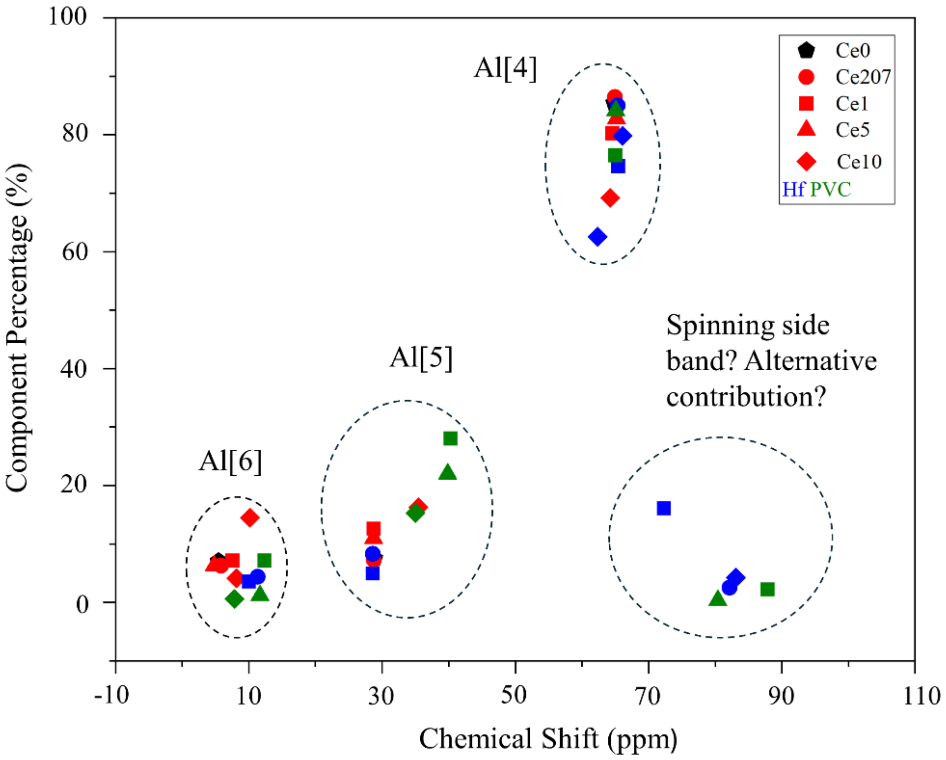

Figure 6.39 Chemical shift value for each component in the CZsimple NMR fits vs the area percentage of each component in relation to the total fit area. The different components have been grouped and identified in relation to different coordination values or Al. Components at elevated chemical shift (ppm) are found in a few of the glasses and it is unclear as to what these are attributed to.

6.10 Conclusions

A series of CAS glasses that represent a synthetic simulant for plasma produced PCM waste have successfully been produced with the addition of waste simulants. The aim was to investigate the answers to the questions posed in Section 2.2.1.2 and 2.2.2.2.

Answering question 5, pure glasses were produced in most waste additions with accommodation of the the main PCM waste components, with waste loading of up to 10 wt% excluding for Cr in the metallic CASM glass that reaches saturation at ~5 wt%, with Cr crystallisation in the form of eskoliate and Cl that shows low retention in all CAS PVC glasses. This contrasts with previous lab and industry trials (Chapter 5 and [1-4, 22, 23]) and raises initial questions about how representative the glasses presented here are of the PCM wasteform envelope. Further work required to better understand the heterogeneity in the industrial trials and the main factors effecting the type and distribution of crystalline elements. There were minor increases of Cl retention with waste loading but all Cl levels (maximum of 0.09 mol%) were well below batched values, with low retention likely linked to high Al levels supressing Cl incorporation by a yet described mechanism. There are minor increases with waste loading for the incorporation of the radionuclide simulants Ce and Hf and there solubility limits are high for both Ce and Hf (>3.55-66 mol% at 1400-1450°C), this is in line with previous studies of Hf in aluminosilicates [15] but higher than the maximum quoted values for Pu and Ce in either tri or tetravalent oxidation state in borosilicate glass [10-13]. In contrast to studies on Ce incorporation into borosilicate's glasses the solubility of Ce is still high despite there being significant amounts (24-28%) of Ce^{4+} in the CAS glass. From a scientific point of view, it would be of interest to increase the doping of the simulants to find saturation points and further investigate the incorporation mechanisms and the effects of the waste simulants. The main structural differences in relation to question 6, are represented by several techniques but with the biggest changes shown in the CASM glasses, with minor changes seen with Hf addition. XAS and Mossbauer analysis shows that the Fe in these trials is mostly Fe^{3+} likely in a distorted tetrahedral coordination in contrast to the Fe^{2+} of various coordination seen in Section 5.7. The Raman spectroscopy shows the differential incorporation of Fe^{2+} and Fe^{3+} in the CAS glass with the 1A_glass spectra from Chapter 5 closest to the CAS0 spectra despite being closest in composition to CAS M5. This shows that Fe^{2+} in the Tetronics trials has a minor effect on the CAS structure, being accommodated on the Ca^{2+} sites, whereas the Fe^{3+} has distorted tetrahedra that can be incorporated into the CAS glass structure but there is a clear effect on the silicate glass framework. The increased oxidising environment in the lab trial melts is further supported by the lack of any metallic Fe and the significant amounts of Ce^{4+} (24-28%) in comparison to previous trials. Hf addition effects the silicate ring structure with changes to the lower frequency Raman signals. PVC and Ce addition has no major effect on the glass structure. The RPI index supports these conclusions and shows the increased polymerisation of the glass as more metal as Fe^{3+} and Hf^{4+} is added increasing the fraction of network formers. NMR spectroscopy shows in all samples the dominance of Q3 speciation in the Si framework along with significant Al [4] and more minor Al [5] and Al [6]. There are no clear trends between the different CAS glasses showing that the additions of Ce, PVC and Hf are not majorly affecting the Q species and Al speciation which is expected for from Raman analysis for Ce and PVC, but the changes in Hf silicate ring structure are not seen in the Q-species or Al environment. The effect of metal addition could not be analysed by NMR due to the magnetic nature of the samples.

In relation to Section 2.2.2.1, the effect of compositional and structural changes on the density, thermal properties and viscosity of the CAS glasses was observed or measured, with some consequences for the processing parameters. Density of the CAS glasses increased as expected at higher waste loading of radionuclide simulants and metal with little to no effect at lower levels or for any addition of PVC. Generally, all the CAS glasses had high viscosity that reduced glass mobility and prevented pouring, waste additions appeared to increase viscosity with CAS0 being partially mobile. These observations were based on subjective observations and more detailed viscosity measurements would be beneficial as this trend could be expected from structural data for higher polymerised Hf and metal glasses but is unusual for Ce and PVC glasses. For operational purposes the high melt viscosity is not an issue as there are no plans to pour the PCM wasteforms and plasma operation is likely to be at much higher temperatures. Thermal analysis is inconclusive with the glasses in the correct region for CAS glass but with no clear trends for factors such as Tg that maybe expected for high polymerised Hf and metal glasses, showing that this analysis requires further attention to link structural measurements and physical properties. Interestingly, lower melt temperatures were used compared to previous industrial samples based upon the liquidus temperature of the glass rather than the melting temperature of the steel or operational plasma temperature. Incorporation of the waste elements at the lower temperature opens possibilities for reduced melt temperatures helping to lower costs and volatilisation. Some caution is required as the metallic waste was added in powder form rather than solid form this and the milling/size reduction of pre-cursors aided the melting, glass formation, reduction in crystalline material and elemental incorporation process, although it is unlikely that this will be implemented in industry with the aim for whole drum vitrification. In contrast plasma trials have shown that increased oxidation or changes to the plasma set up and operation process could help to increase metallic melting and reduce crystallisation.

All the conclusions highlight that there are some significant differences between the industrial trials and the lab trials that could make it difficult to make direct comparisons and draw conclusions on unmeasured factors such as the expected durability of the CAS glasses or the radionuclide simulant retention in the CAS glasses. The differences are interpretated to potentially relate to several factors including sample preparation, in particular size reduction, type and form of glass forming additives and melt conditions including the temperature and redox environment. A better understanding of factors would help to improve understanding of the PCM vitrification and future trials need to consider:

- restraining melt conditions particularly redox, melt temperature and waste type.
- expanding into different Pu simulants including U and Th as these offer alternative advantages to Ce and Hf (Section 3.1.2).
- mixing waste simulants to explore how they can all impact on each other.
- as there is a paucity of research on CAS durability and some issues comparing CAS glasses to results in Chapter 5, then a set of dissolution tests on the lab glasses would allow relative durability to be assessed, with tests in Section 5.10 suggesting it would be high, and the mechanism for dissolution to be better understood.

6.11 References

1. Tetronics, 1107 COSTAIN Plasma Trials Procedure for Nuclear Demonstration Furnace. 2019.
2. Boast.L, Investigation of the Thermal Treatment of Higher Activity Waste., in Material Science. 2018, Sheffield.
3. Hyatt, N.C., et al., Thermal treatment of simulant plutonium contaminated materials from the Sellafield site by vitrification in a blast-furnace slag. Journal of Nuclear Materials, 2014. 444(1): p. 186-199.
4. Schwarz.R, B.P.a., Thermal Treatment of Plutonium Contaminated Materials Phase 2: Vitrification Study Final Report. 31st May 2012.
5. Schofield, J.M., P.A. Bingham, and R.J. Hand, The Immobilisation of a Chloride Containing Actinide Waste Surrogate in Calcium Aluminosilicate Glasses, in Environmental Issues and Waste Management Technologies in the Materials and Nuclear Industries XII. 2009. p. 69-80.
6. Siwadamrongpong, S., M. Koide, and K. Matusita, Prediction of Chloride Solubility in CaO-Al2O3-SiO2 Glass Systems. Journal of Non-crystalline Solids - J NON-CRYST SOLIDS, 2004. 347: p. 114-120.
7. Schofield, J.M., Vitrification of a chloride containing actinide waste surrogate. 2011, University of Sheffield: Dpeartment of Materials and Science and Engineering.
8. Thornber, S.M., et al., Solubility, speciation and local environment of chlorine in zirconolite glass–ceramics for the immobilisation of plutonium residues. RSC Advances, 2020. 10(54): p. 32497-32510.
9. Tan, S. and R.J. Hand, Incorporation and phase separation of Cl in alkaline earth aluminosilicate glasses. Journal of Nuclear Materials, 2018. 507: p. 135-144.
10. Lopez, C., et al., Solubility of actinide surrogates in nuclear glasses. Journal of Nuclear Materials, 2003. 312(1): p. 76-80.
11. Deschanels, X., et al., Plutonium solubility and self-irradiation effects in borosilicate glass. Progress in Nuclear Energy, 2007. 49(8): p. 623-634.
12. Feng.X, e.a., Distribution and Solubility of Radionuclides in Waste Forms for Disposition of Plutonium and Spent Nuclear Fuels: Preliminary Results. 1999, PNNL.
13. Bingham, P.A., et al., The Use of Surrogates in Waste Immobilization Studies: A Case Study of Plutonium. MRS Proceedings, 2008. 1107: p. 421.
14. J.N.Cachia, et al., Enhancing cerium and plutonium solubility by reduction in borosilicate glass. Journal of Nuclear Materials, 2006. 352(1): p. 182-189.
15. Chevreux, P., et al., Hafnium solubility determination in soda-lime aluminosilicate glass. Journal of Non-Crystalline Solids, 2017. 457: p. 13-24.
16. Strachan.D, V.R.E., Shuh.K.D, Ewing.C.R, Distribution & Solubility of Radionuclides & Neutron Absorbers in Waste Forms for Disposition of Plutonium Ash & Scraps, Excess Plutonium, and Miscellaneous Spent Nuclear Fuels. 1998: Environmental Management Science Program.
17. Cachia, J.N., et al., Enhancing cerium and plutonium solubility by reduction in borosilicate glass. Journal of Nuclear Materials, 2006. 352(1): p. 182-189.
18. Feng.X, L.H., Davis.LL, Li.L, Darab.G.J, Shuh.K.D, Ewing.C.R, Wang.M.L, Vance.R.E, Allen.G.P, Bucher.J.J, and C.M.I. Edelstein.M.N, Schweiger.J.M, Vienna.D.J, Strachan.M.D , and Bunker.C.B, Distribution & Solubility of Radionuclides & Neutron Absorbers in Waste Forms for Disposition of Plutonium

Ash & Scraps, Excess Plutonium, and Miscellaneous Spent Nuclear Fuels. 1998: Environmental Management Science Program.

19. Feng, X., et al. Distribution and Solubility of Radionuclides in Waste Forms for Disposition of Plutonium and Spent Nuclear Fuels: Preliminary Results. 1999. United States.
20. Aboelwafa, M.A., et al., Influence of Cerium oxide on the structural aspects of soda-lime aluminosilicate glasses synthesized by sol-gel route. Materials Chemistry and Physics, 2023. 305: p. 127930.
21. L.Boast, Investigation of the Thermal Treatment of Higher Activity Waste., in Material Science. 2018, Sheffield.
22. Hyatt, N.C., et al., Characterisation of Plasma Vitrified Simulant Plutonium Contaminated Material Waste. MRS Proceedings, 2006. 985: p. 0985-NN10-06.
23. Boast, L., M.C. Stennett, and N.C. Hyatt, Thermal treatment of plutonium contaminated material (PCM) waste. MRS Advances, 2017. 2(13): p. 735-740.
24. Tetronics, 1107 Plasma PCM Trials Report for Nuclear Demonstration Furnace. 2020.
25. Morgan, S., Personal Communication.
26. Cormier, L., D.R. Neuville, and G. Calas, Relationship Between Structure and Glass Transition Temperature in Low-silica Calcium Aluminosilicate Glasses: the Origin of the Anomaly at Low Silica Content. Journal of the American Ceramic Society, 2005. 88(8): p. 2292-2299.
27. Bailey, D., et al., Ce and U speciation in wasteforms for thermal treatment of plutonium bearing wastes, probed by L 3 edge XANES. IOP Conference Series: Materials Science and Engineering, 2020. 818: p. 012019.
28. el Damrawi, G. and A. Behairy, Structural Role of Cerium Oxide in Lead Silicate Glasses and Glass Ceramics. Journal of Minerals and Materials Characterization and Engineering, 2018. 06: p. 438-447.
29. Bailey, D.J., et al., Ce and U speciation in wasteforms for thermal treatment of plutonium bearing wastes, probed by L3 edge XANES. IOP Conference Series: Materials Science and Engineering, 2020. 818(1): p. 012019.
30. N.C.Hyatt, et al., Thermal treatment of simulant plutonium contaminated materials from the Sellafield site by vitrification in a blast-furnace slag. Journal of Nuclear Materials, 2014. 444(1): p. 186-199.
31. Paul A, B., et al., The Use of Surrogates in Waste Immobilization Studies: A Case Study of Plutonium. MRS Proceedings, 2008. 1107: p. 421.
32. X.Deschanels, et al., Plutonium solubility and self-irradiation effects in borosilicate glass. Progress in Nuclear Energy, 2007. 49(8): p. 623-634.
33. C.Lopez, et al., Solubility of actinide surrogates in nuclear glasses. Journal of Nuclear Materials, 2003. 312(1): p. 76-80.
34. Li, H., J.D. Vienna, and P. Hrma. Borosilicate based glasses for immobilization of plutonium-bearing materials. 1996. United States: American Ceramic Society, Westerville, OH (United States).
35. X.Feng, e.a., Distribution & Solubility of Radionuclides & Neutron Absorbers in Waste Forms for Disposition of Plutonium Ash & Scraps, Excess Plutonium, and Miscellaneous Spent Nuclear Fuels. 1998: Environmental Management Science Program.
36. X. Feng, H.L., L.L.D.L. Li, J.G. Darab, M.J. Schweiger,J.D. Vienna, B.C. Bunker, P.G. Allen, J.J. Bucher, I.M.Craig, N.M. Edelstein, D.K. Shuh, R.C. Ewing, L.M.Wang,E.R. Vance, Ceramic Trans., 1999. 93: p. 409.
37. Gallington, L.A.-O., et al., The Structure of Liquid and Amorphous Hafnia. LID - 10.3390/ma10111290 [doi] LID - 1290. (1996-1944 (Print)).

38. Bergeron, B., et al., First investigations of the influence of IVB elements (Ti, Zr, and Hf) on the chemical durability of soda-lime borosilicate glasses. Journal of Non-Crystalline Solids, 2010. 356(44): p. 2315-2322.
39. Jollivet, P., et al., An enhanced resolution of the structural environment of zirconium in borosilicate glasses. Journal of Non-Crystalline Solids, 2013. 381: p. 40-47.
40. Farges, F., C.W. Ponader, and G.E. Brown, Structural environments of incompatible elements in silicate glass/melt systems: I. Zirconium at trace levels. Geochimica et Cosmochimica Acta, 1991. 55(6): p. 1563-1574.
41. Ficheux, M., et al., Structural evolution of high zirconia aluminosilicate glasses. Journal of Non-Crystalline Solids, 2020. 539: p. 120050.
42. Lu, X., L. Deng, and J. Du, Effect of ZrO2 on the structure and properties of soda-lime silicate glasses from molecular dynamics simulations. Journal of Non-Crystalline Solids, 2018. 491: p. 141-150.
43. Lu, X., et al., Structural role of ZrO2 and its impact on properties of boroaluminosilicate nuclear waste glasses. npj Materials Degradation, 2018. 2(1): p. 19.
44. Dargaud, O., et al., In Situ study of Nucleation of Zirconia in an MgO–Al2O3–SiO2 Glass. Journal of the American Ceramic Society, 2010. 93(2): p. 342-344.
45. Dargaud, O., et al., Structural role of Zr4+ as a nucleating agent in a MgO–Al2O3–SiO2 glass-ceramics: A combined XAS and HRTEM approach. Journal of Non-Crystalline Solids, 2010. 356(52): p. 2928-2934.
46. Le Losq, C., M. Cicconi, Rita, and D. Neuville, R, Iron in Silicate Glasses and Melts: Implications for Volcanological Processes, in Magma Redox Geochemistry, M. Roberto and R.N. Daniel, Editors. 2021, Wiley. p. 233 - 253.
47. Mysen, B.O., The structural behavior of ferric and ferrous iron in aluminosilicate glass near meta-aluminosilicate joins. Geochimica et Cosmochimica Acta, 2006. 70(9): p. 2337-2353.
48. Cormier, L., Glasses: Aluminosilicates. Encyclopedia of Materials: Technical Ceramics and Glasses, 2021.
49. Dyar, M.D., et al., MÖSSBAUER SPECTROSCOPY OF EARTH AND PLANETARY MATERIALS. Annual Review of Earth and Planetary Sciences, 2006. 34(1): p. 83-125.
50. Merzbacher, C.I., K.J. McGrath, and P.L. Higby, 29Si NMR and infrared reflectance spectroscopy of low-silica calcium aluminosilicate glasses. Journal of Non-Crystalline Solids, 1991. 136(3): p. 249-259.